UNIVERSITY OF SOUTHAMPTON

FACULTY OF ENGINEERING AND THE ENVIRONMENT

X-ray Computed Tomography and image-based modelling of plant, root and soil systems, for better understanding of phosphate uptake

Author:
Samuel Keyes MEng

Supervisors:
Dr Alan Marchant, Prof. Tiina Roose, Prof. Ian Sinclair

A thesis submitted in fulfilment of the requirements for the degree of Doctor of Philosophy

December 31, 2013

Abstract

A major constraint to crop growth is the poor bioavailability of edaphic nutrients, especially phosphate (P). Improving the nutrient acquisition efficiency of crops is crucial in addressing pressing global food-security issues arising from increasing world population, reduced fertile land and changes in the climate. Despite the undoubted importance of root architecture and root/soil interactions to nutrient uptake, there is a lack of approaches for quantifying plant roots non-invasively at all scales. Mathematical models have allowed our understanding of root and soil interactions to be improved, but are almost invariably reliant on idealised geometries or virtual root growth models. In order to improve phenotyping of advantageous traits for low-P conditions and improve the accuracy of root growth and uptake models, more sophisticated and robust approaches to *in vivo* root and soil characterisation are needed. Microfocus X-ray Computed Tomography (μ-CT) is a methodology that has shown promise for non-invasive imaging of roots and soil at various scales. However, this potential has not been extended to consideration of either very small (rhizosphere scale) or large (mature root system scale) samples. This thesis combines discovery experiments and method development in order to achieve two primary objectives:

- The development of more robust, well-described approaches to root and soil μ-CT imaging. Chapters 2 and 3 explore the potential of clinical contrasting methods in root investigation, and show how careful consideration of imaging parameters combined with development of user-invariant image-processing protocol can improve measurement of macro-porous volume fraction, a key soil parameter.

- Chapter 4 develops an assay for first-time 3D imaging of root hairs *in situ* within the rhizosphere. The resulting data is used to parameterise an explicit P uptake model at the hair scale, suggesting a different contribution of hairs to uptake than was predicted using idealised geometries. Chapter 5 then extends the paradigm for root hair imaging and model generation, building a robust, modular workflow for investigating P dynamics in the rhizosphere that can accommodate non-optimal soil-water states.

Contents

List of Tables

List of Figures

Author's declaration

Academic Thesis: Declaration Of Authorship

I,

declare that this thesis and the work presented in it are my own and has been generated by me as the result of my own original research.

I confirm that:

1. This work was done wholly while in candidature for a research degree at this University.
2. Where any part of this thesis has previously been submitted for a degree or any other qualification at this University or any other institution, this has been clearly stated.
3. Where I have consulted the published work of others, this is always clearly attributed;
4. Where I have quoted from the work of others, the source is always given. With the exception of such quotations, this thesis is entirely my own work;
5. I have acknowledged all main sources of help.
6. Where the thesis is based on work done by myself jointly with others, I have made clear exactly what was done by others and what I have contributed myself. Dr Richard Boardman assisted with coding of the seeded region growth algorithm developed in Chapter 2. Dr Neil Gostling assisted with development of the chemical contrasting protocol for μ-CT imaging developed in Chapter 3. Dr Gostling also collaborated on developing the plant growth assay in Chapter 5, as well as the SRXCT imaging and hair segmentation in the chapter. Dr Keith Daly collaborated on Chapter 5, assisting with post-processing of numerical modelling data and the streamline analysis work. Prof. Matthias Wissuwa

provided rice genotypes for comparison, and helped set up the growth protocol in rhizoboxes in Appendix 8.3. Peter Talboys carried out the soil P assay in Appendix 8.2.1.

7. Parts of this work have been published as:

   - SD Keyes, RP Boardman, A Marchant, T Roose, I Sinclair, (2013), *A robust approach for determination of the macro-porous volume fraction of soils with X-ray computed tomography and an image processing protocol*, **European Journal of Soil Science**, Volume 64, Issue 3, pp 298-307
   - SD Keyes, KR Daly, NJ Gostling, DL Jones, P Talboys, BR Pinzer, R Boardman, I Sinclair, A Marchant, T Roose, (2013), *High resolution synchrotron imaging of wheat root hairs growing in soil and image based modelling of phosphate uptake*, **New Phytologist**, Volume 198, Issue 4, pp 1023-1029

Signed:..... Date:.....

Acknowledgements

I would like to thank my supervisors Alan Marchant, Tiina Roose and Ian Sinclair. I have been afforded both the independence to shape my own ideas, and as much wise and good-humoured counsel as I ever wanted. I am aware this is a rare privilege. I owe a particular debt of gratitude to Prof. Roose, who has been an exceptional mentor throughout, helping shape the way I think and work as a scientist, and always offering an open door to my ideas and concerns.

It has been a great blessing to work in a department surrounded by such generous-spirited people. Multidisciplinary work has many challenges, but the opportunity to share in research with people from different backgrounds has never failed to be deeply inspiring. Much of my work would have been impossible without the collaboration and advice of my colleagues at the μ-VIS Centre for Computed Tomography. In particular, my working partnerships with Drs Richard Boardman, Keith Daly and Neil Gostling have led to much of the work presented in this thesis. Their expertise and gladness to collaborate have inspired me in my own work, and they deserve ample credit for all their generosity. Drs Mark Mavrogordato, Dmitry Grinev and Anna Scott have also been a constant source of support, technical advice and friendship. I doubt whether there can be a better bonding experience than a $48\mathrm{h}$ shift on a synchrotron beamline.

Research affords unrivalled opportunities to work with colleagues from around the world, and I am particularly grateful to Prof. Matthias Wissuwa of the Japan International Research Centre for Agricultural Sciences for his friendship, generosity and experience. Two weeks as a visiting researcher in Japan was invaluable for developing my knowledge of rice genotypes and agriculture, as well as allowing me to gather data that complemented my μ-CT work in Southampton. Seeing the very best side of what international research can be was a wonderful experience, and I was humbled by the hospitality of Prof. Wissuwa and his colleagues during my stay.

I would like to thank my family, who have never been anything short of sacrificially supportive. My parents have always fostered my curiosity, and believed in my potential even when my school reports didn't. This often-exasperating son owes them so much. My botanist grand-

father the late Dr Bob Lucas was a great inspiration in younger years. An authority on fungal mycorrhizae (and, so it seemed, almost everything else), Dr Bob would surely be amused to see this mechanical engineer grandson working on rhizosphere visualisation.

Submitting a PhD thesis days before one's wedding cannot be recommended. Lastly, and most importantly, I would like to thank Colette. For all your understanding and patience with a scientist's frustrating 'habits.' For your encouragement during the tough days. For everything. I have always been certain of your love and support, and I cannot thank you enough. We got there together.

Chapter 1

Understanding the roles of roots and soils in relation to plant nutrient acquisition

The literature review in this chapter serves as a broad introduction to domain challenges and hypotheses that form the basis of this thesis. More detailed literature pertaining to particular experimental work is found in relevant chapters.

1.1 The importance of agriculture to global food security

Over 200 years ago Thomas Robert Malthus wrote an essay, in which he predicted that left unchecked, a continuously growing global population would eventually face famines, disease and widespread mortality [Herder et al., 2010; Malthus, 1798]. In the present day these concerns remain, as the global population continues to increase, whilst the area of viable agricultural land available for food production is contracting [Godfray et al., 2010]. During the 1960's, Asia, Africa and Latin America were thought by many to be on the brink of political and humanitarian crisis, as growth in agricultural yields failed to keep pace with population increases driven to a great extent by rapidly declining infant mortality rates [Khush, 2001]. A widely read book of the time, *Famine 1975!* predicted that by 1977 parts of the underdeveloped world would be suffering famines, by 1982 these famines would have reached catastrophic proportions, and that soon thereafter, revolutions, economic upheaval and social turmoil would ravage large areas as a result [Khush, 2001; Paddock and Paddock, 1968]. That these predictions failed to materialise is due almost entirely to what is now known as the 'Green Revolution,' in agriculture, through which new approaches for genetic improvement of crops were implemented to bring about profound yield increases [Khush, 2001]. The objective impact of this revolution cannot be overstated. Despite a doubling in the population of densely

populated, low-GDP nations in the period 1966-2000, food production increased by 125% over the same timescale, averting many of the socio-economic disasters that had been predicted to result from severe food shortages.

The declining per-capita food production in Asia in the preceding years of the century had directly resulted from a failure to develop increasingly efficient varieties of rice (*Oryza sativa*) [Khush, 1999]. The backbone of the agricultural revolution in this region, improved germplasm, was made possible in large part by work at the International Rice Research Institute (IRRI) in the Philippines, which remedied some of the more obvious shortcomings of contemporary rice varieties [Khush, 2001]. Their work focused on improvement of above-ground traits, producing new varieties that generated less non-grain biomass and had short stems that were less prone to damage by inclement weather conditions. Following this breakthrough, a range of other factors that had previously been uneconomical, such as improved irrigation and intensive fertilisation, were able to help provide viable yield improvements [Sanchez et al., 1997]. Similar advances for the other major global crops, wheat (*Triticum aestivum*) and maize (*Zea mays*) occured across the developed world following similar breeding programmes by institutions such as the International Maize and Wheat Improvement Centre (CIMMYT) in Mexico [Khush, 2001].

Despite the impact of this agricultural revolution in the latter half of the 20th Century, global staple crop production *per capita* is once again falling, and the threat of severe food shortfalls exists once more [Khush, 1999]. In the present day, three cereal species; rice (*Oryza sativa*), wheat (*Triticum aestivum*) and maize (*Zea mays*) are responsible for meeting 75% of human crop-food requirements [Coudert et al., 2010]. Based on UN estimates of global population growth, production of these cereals will need to increase by $> 40\%$ in order to meet projected demand by 2030, an increase which will have to be achieved against the backdrop of diminished fertilizer availability, a contraction in absolute fertile land area and reduced irrigation [Coudert et al., 2010]. In addressing the crisis of the 1960's, the dominant strategy had been the breeding of short-stature and lodging-resistant varieties with high sensitivity to inputs of fertilisers. In the present day, new increases in yield must be achieved without widespread possibility of recourse to intensive fertilisation, particularly in the developing world [Khush, 1999; Lynch, 2007]. Rather than focusing on optimising the useful biomass and seed yield as previously [Gonzalez et al., 2009; Xing and Zhang, 2010], an obvious approach to this challenge is to focus on the often-neglected influence of root system characteristics on yield potential [Herder et al., 2010].

1.2 Plant root systems and their inherent complexity

The growth and resource acquisition processes of plant root systems exhibit a multi-faceted complexity significantly exceeding that of the aerial plant. Above ground, the primary objectives of plants are the interception of light and CO_2, maintenance of water homeostasis, and reproduction. Detrimental environmental constraints to aerial growth include heat exposure, competition for light, and damage resulting from both weather and herbivorous attack [Postma et al., 2013]. By comparison, necessary resource capture by roots extends to more than 14 essential nutrients (in addition to water) as well as several others that are non-essential but beneficial for growth [Postma et al., 2013]. The list of detrimental environmental factors affecting roots includes aluminium, sodium, chloride and manganese toxicity, low water availability, soil saturation, low temperature, herbivore attacks and excessive mechanical resistance [Postma et al., 2013]. Furthermore, compared to the above-ground plant, the below-ground portion is involved in far more complicated biochemical processes and a large number of biotic interactions with the wide array of fauna present in agricultural soils [De Deyn and Van der Putten, 2005; Watt et al., 2006]. Given the inherent complexity of plant root systems and the soils in which they grow, improving understanding of root development and linking architecture to resource acquisition are highly non-trivial objectives.

As a direct result of root complexity, our present knowledge of many fundamental processes related to mature plants (such as uptake kinetics and root senescence characteristics) is limited [Darrah et al., 2006; Lontoc-Roy et al., 2006]. A review by *Gregory et al.* argues that due to the difficulty of measuring root systems, little attention has been given to specific characteristics that may prove pivotal in facilitating more efficient nutrient and water uptake [Gregory et al., 2005]. Partly responsible for this is the extraordinary extensivity of mature plant root networks, which makes accurate quantification of even simple characteristics extremely difficult and time consuming [Taiz and Zeiger, 2002]. A study by *Dittmer* of winter rye (*Secale cereale*) plants used extensive manual sampling to estimate the size of a single root system after 16 weeks growth, finding 13.8×10^6 roots with a total length of over $620\mathrm{km}$ and surface area of almost $250\mathrm{m}^2$ [Dittmer, 1938]. The number of root hairs was estimated to be 14×10^9 with a total length of over $10 \times 10^3\mathrm{km}$ and surface area of $400\mathrm{m}^2$. Such extensiveness poses clear challenges to reliable characterisation at the entire plant scale, even discounting the added complexity of the soil environment in which roots grow.

The complexity of root systems is not limited to architecture or morphology alone, since plants exert mechanical and biochemical influences upon their environment, mediating soil properties in order to optimize uptake of essential nutrients [Lambers et al., 2006]. A few of these processes are shown in schematic form in Figure 1.1. An important example is the enhanced mobilisation of PO_4 ions in dry soil horizons by the transfer of water to superficial layers from

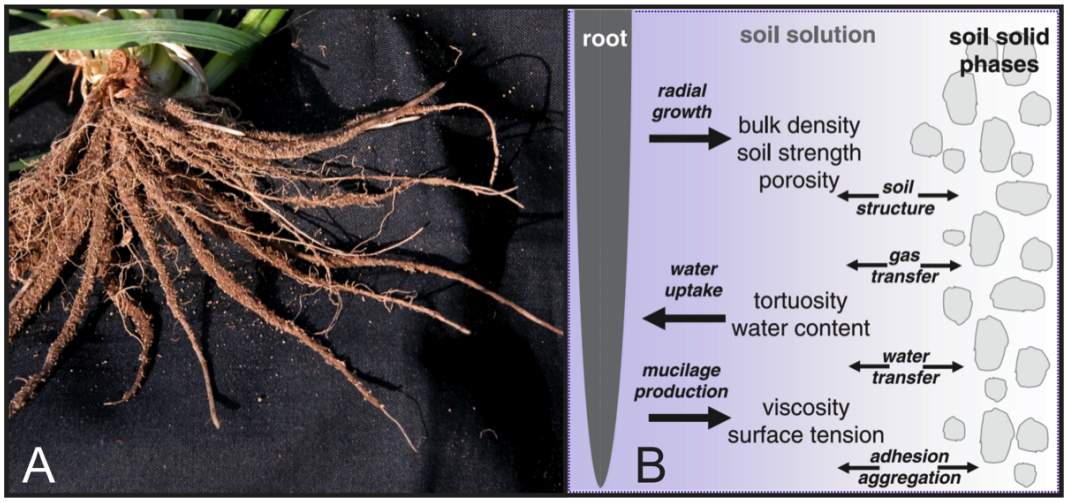

Figure 1.1: (A) Roots are engaged in a complex array of interlinked processes with rhizosphere soil [Brady and Weil, 1996]. Roots respond plastically to soil nutrient and water status, as well as the mechanical impedance presented by the complex physical structure. In turn, roots influence the soil through mechanical interference, water uptake and redistribution, and exudation of numerous compounds including polysaccharides and surfactants which influence soil fauna and soil water characteristics [Hinsinger et al., 2005].

deep in the root system - a mechanism termed *hydraulic redistribution* or *hydraulic lift* [Burgess et al., 1998], but which has proven complicated to quantify experimentally [Lambers et al., 2006]. Better understood is the exudation of mucilage and organic compounds through which plants establish the *rhizosphere* (Figure 1.1-A), a key zone of biochemical activity surrounding plant roots, improving the mobility of phosphate and other nutrients [Gahoonia and Nielsen, 1998; Peterson and Farquhar, 1996]. *Zoysa et al.* found that root exudates were able to exert profound effects on soil phosphate chemistry, though this effect was limited to a small soil volume extending a maximum of 3mm from the root surfaces. This places the influence of exudation at the length scale of the rhizosphere rather than that of the bulk soil, and demonstrates that comprehensive root system characterisation must consider processes at the single root scale as well as the root system scale. [Zoysa et al., 1997].

1.3 Phosphate, a key growth-limiting nutrient in agriculture

Alongside mechanical anchoring the most significant role of the root system is the acquisition of key resources, of which the inorganic nutrient phosphorus (P) is one of the most important. In plants, P forms a component of nucleic acids and phospholipids, assists in the activation of many enzymes, and plays an important role in carbon metabolism. As such, it is second only to nitrogen (N) in its importance for growth [Dery and Anderson, 2007].

Low P availability limits agricultural productivity (Figure 1.2), a limitation which can usu-

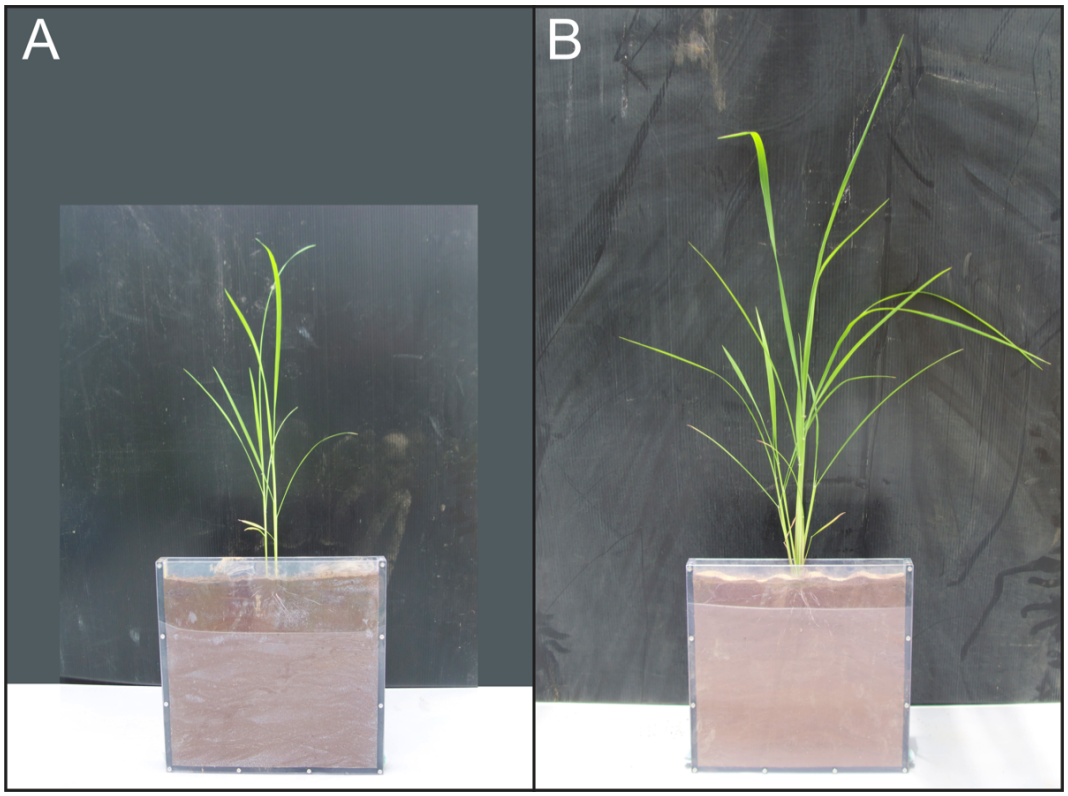

Figure 1.2: Low nutrient status affects plant vigour. Frames (A) and (B) show the same genotype of rice (*Oryza sativa* cv. *KAS*) after ($30\mathrm{d}$) growth. The soil in (A) is in a low-P condition, and the soil in (B) has been treated with P fertiliser to an equivalent P level of $50\mathrm{kg.ha}^{-1}$. The greater above-ground biomass of the plant grown in P-treated soil is evident.

ally only be overcome by supplying fertilizer to the soil [Vance et al., 2003]. Unlike nitrates, phosphate cannot be synthesised industrially or generated by other soil organisms, a situation that has led to rapid depletion of global rock phosphate reserves [Lambers et al., 2006]. Despite this, many agricultural soils subject to intensive, long-term fertiliser application have over time accumulated high concentrations of P that is unavailable to most plants. This unavailability results from strong sorption of the nutrient with soil, as well as the poor adaption of many plants to access these forms, which can account for the fate of $80 - 90\%$ of applied P [Jones, 1998]. Along with others, *Krasilnikoff et al* propose that low soil availability of P is one of the most significant factors contributing to poor food availability in equatorial Africa, with phosphate application often having little effect on yields due to rapid chelation by iron (Fe) and aluminium (Al) oxides in the soil [Krasilnikoff et al., 2003]. As discussed, the revolution of global agriculture during the 20th Century was largely possible due to the increased availability of mined rock phosphate, but many farms worldwide still do not receive adequate supplies [Dery and Anderson, 2007]. As it is often applied carelessly, waste and environmental pollution frequently result [Dery and Anderson, 2007].

Recently, a predictive paradigm from the oil industry known as *Hubbert peak theory* has been applied to data for known P reserves in order to forecast depletion rates of mineable stocks, with the estimated period for near-total exhaustion of global P predicted at between 50 and 130 years [Dery and Anderson, 2007]. Given the reliance of global food supplies on P, depletion at this rate is of acute significance, as unlike other essential nutrients there are no effective substitutes for mined P fertiliser in intensive agriculture [Survey, 2011]. The joint problems of P reserve depletion, poor uptake efficiency and off-site pollution place a great impetus on two areas; the development of new crop varieties which can acquire soil P more efficiently, and improved soil management protocols which minimise waste [Lambers et al., 2006].

Phosphate dynamics at the rhizosphere scale

Phosphate acquisition is primarily a function of three processes;

- The movement of PO_4 ions from soil (source) to roots and root hairs (sinks).
- The mechanism and rate of absorption once ions reach a sink surface.
- The binding and solubilisation reactions on aggregate surfaces and intra-aggregate regions.

Mass flow typically accounts for less than 5% of total P uptake by plants, such that transport of the ions is limited by the diffusion coefficient (D), the value for which is very low in soil

[Lambers et al., 2006]. Numerical modelling has suggested that increasing the maximum inflow rate of P at the plant root surfaces has little effect on total uptake, due to the governing influence of diffusion rate [Jungk, 2001; Silberbush and Barber, 1983]. This limitation leads to zones of local P depletion which are commonly observed in rhizosphere studies, and were first visualised using radiographic methods which allowed quantification of ^{32}P gradients around roots [Lewis and Quirk, 1967]. Such gradients arise when the root or root-hair uptake rate exceeds the rate at which mass flow or diffusive transport are able to replace P being lost from the rhizosphere at the uptake surfaces [Jungk, 2001]. In such cases, the rate of replenishment in depletion zones is predominantly governed by the buffer power (b) of the particular soil in which the plant is grown [Zoysa et al., 1997]. In response to low P availability, the plant may be able to actively mobilise ions by modifying soil water status through hydraulic redistribution, or by altering the chemistry of the rhizosphere through release of exudates containing carboxylates and phosphatases [Lambers et al., 2006]

Accurately determining how far the rhizosphere extends from root surfaces is difficult, since the various plant nutrients have different diffusion coefficients, and hence different depletion profiles in the soil [Hinsinger et al., 2005]. There is thus no easily defined single boundary between the rhizosphere and bulk soil, and the zone for N may be many tens of times greater in diameter than that for P, which typically extends less than $1\mathrm{mm}$ from the root surface [Hinsinger et al., 2005]. Figure 1.3 shows such a depletion gradient for a root of maize (*Zea mays*), measured using a ^{33}P tracer. The existence of these small length-scales of depletion for such a key nutrient has led to the suggestion that only a very small percentage of the total soil volume within the boundaries of root growth ($< 1\%$) can truly be termed the rhizosphere [Hinsinger et al., 2005].

Though the rhizosphere is clearly a vitally important zone for understanding nutrient uptake, accurately quantifying the movement of $[PO_4]^{3-}$ ions close to the root surfaces is a non-trivial task. Because the region of soil in which the plant can exert influence lies in such close proximity to root surfaces, accurate sampling is extremely difficult [Hinsinger et al., 2005]. Even where aggregates directly adhering to roots (as in Figure 1.1-A) can be selectively sampled, rhizosphere effects may be underestimated, since the length scale of these aggregates is often greater than that of P depletion gradients [Hinsinger et al., 2005]. In the face of these challenges, an important refinement in measurement of rhizosphere processes was achieved by applying an approach in which roots are grown against a porous, planar membrane housed within a laboratory growth chamber [Kuchenbuch and Jungk, 1982; Wenzel et al., 2001]. Soil can then be sampled in planes parallel to that of the membrane in order to quantify depletion and exudation profiles, though it must be considered that the root geometry represents a substantial oversimplification of the unconstrained state, and does not allow any spatial

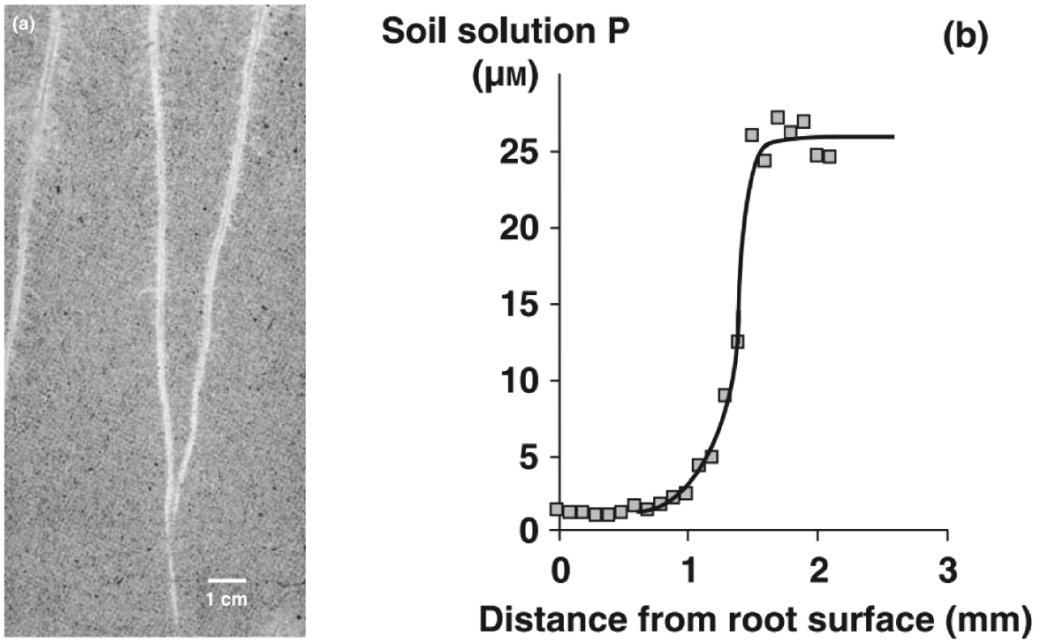

Figure 1.3: Figure from *Hinsinger et al.* showing characterisation of P depletion profiles around a maize (*Zea mays*) root. (a) Roots are grown in a rhizobox, in soil treated with a ^{33}P tracer. Measuring radioactivity allows P concentration to be estimated at discrete points on the viewing plane. (b) Shows the concentration of P in soil solution plotted with respect to distance from the root surface.

heterogeneity of uptake along individual roots to be quantified [Hinsinger et al., 2005]. Uptake processes also exhibit temporal heterogeneity due to changing environmental conditions, not least the diurnal variation of light (which governs photosynthesis rates) and the coupled heterogeneity of nutrient and water demands [Hinsinger et al., 2005]. Further complexity is introduced in that certain other soil fauna also uptake soil P, including microbes, which have been observed to contain a great diversity of different P compounds, not all of which are available to plants [Hedley and Stewart, 1982]. Additionally, the homogeneity of soil P distribution assumed as an initial condition in many models has been shown to be erroneous, with a significant variation in concentration observed over a range of length scales [Darrah et al., 2006; Hedley and Stewart, 1982].

It is clear that many different rhizosphere states can potentially develop, and that these are dependent on a potentially enormous number of possible specific combinations of soil, plant, fauna and environmental conditions [Darrah et al., 2006]. Since the efficiency of fertiliser utilisation in agriculture is presently $< 50\%$ for all the major plant nutrients, there is a clear need to understand the most dominant processes governing P acquisition in agricultural systems, and thus how plant breeding and soil management might improve yield efficiency [Postma et al., 2013].

1.4 Targeted breeding of root traits for enhanced P acquisition by crop plants

It is well known that genotypic variations among plant species are responsible for widely differing nutrient acquisition by roots, and utilisation by the plant [Marschener, 1998]. Since one route to enhanced P uptake is increased total soil exploration, there are a wide range of morphological and architectural root adaptations that could potentially improve uptake efficiency, including modified branching angles, branching rates, and specific root length [Haling et al., 2013; White et al., 2013]. Degrees of variation in individual traits can be substantial due to the highly plastic nature of plant development, with intra-species variations in root size and growth rates potentially varying by orders of magnitude [Callaway et al., 2003]. Given the number of interlinked processes involved in root function, it is very difficult to define the concept of an 'optimum' root architecture [Fitter et al., 1991; Robinson, 1988]. Nonetheless, there is increasing consensus that cultivars can and should be developed with root systems tailored for optimal nutrient and water efficiency, and thus enhanced yield, given a specific set of environmental parameters [Ao et al., 2010; Bingham and Wu, 2011; Chen et al., 2011; de Dorlodot et al., 2007; Dunbabin et al., 2005, 2013; Gregory et al., 2009; Lynch, 2007; Lynch and Brown, 2012; WU et al., 2005]. A recent review by *Brown et al.* suggested an extensive list of possible root adaptations from the RSA to the hair scale, though the observation was made that all adaptions entail certain drawbacks (such as high carbon cost, or increased susceptibility to pathogens) [Brown et al., 2012]. In order to generate greater yield with fewer inputs, plant breeding approaches are needed which can incorporate advantageous traits into new germplasm, but this in turn will require substantially better understanding of plant growth and phenomics than is currently available [de Dorlodot et al., 2007; Lynch, 2007; Postma et al., 2013]

1.4.1 The key link between plant root architecture and nutrient acquisition efficiency

The characterisation of plant roots can be broadly divided into two domains; one concerning architecture and morphology, and the other concerning biochemical soil mediation processes [Darrah et al., 2006; Lynch, 1995]. *Lambers et al.* have proposed that in particularly extreme nutrient-deficient environments, it is the optimised combination of RSA and biochemistry which most strongly determines the success of plant development [Lambers et al., 2006]. Although traits in both domains make an interlinked contribution to overall plant performance, previous studies have tended to investigate these domains independently of one another [Darrah et al., 2006]. This is in large part due to the extensiveness, diversity and plasticity of root architecture, which have posed a daunting challenge in attempts to develop methodological approaches to root classification [Dittmer, 1938; Lynch, 1995]. It is also extremely difficult to

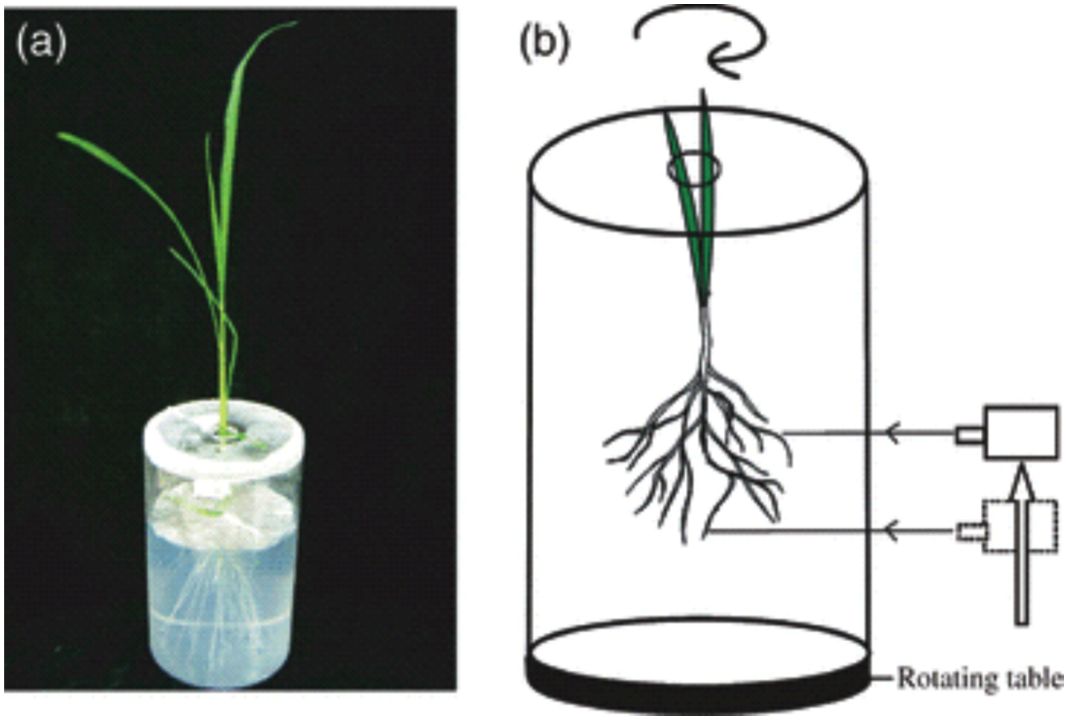

Figure 1.4: Protocol used by *Fang et al.* to non-destructively image root architecture in gel culture. Roots are grown in gel (a) and scanned periodically using a laser-scanning apparatus which allows reconstruction of root paths in three-dimensions [Fang et al., 2009].

accurately measure release rates and chemical compositions of root exudates in the soil environment, leading the bulk of recent studies to focus on plants grown hydroponically or in gel culture (Figure 1.4); conditions which allow little interpolation with the field environment [Gregory and Hinsinger, 1999; Heeraman et al., 1997; Pierret et al., 2005]. Exudates are predominantly composed of carboxylates (citrate, malate, malonate etc) which solubilise organic and inorganic phosphate via ligand exchange [Lambers et al., 2006]. Phenolics and mucilage, also found in exudates, are capable of mobilizing phosphate, but to a lesser extent [Lambers et al., 2006]. Because the interactions of such compounds are complex and numerous; competitive and synergistic processes occur in the rhizosphere which do not lend themselves to straightforward experimental observation [Hinsinger et al., 2005].

Aside from exudation and absorption processes, roots can be characterised with respect to spatial distribution and branching, with substantial investigative effort having recently been focused in this area [Gregory et al., 2003; Heeraman et al., 1997; Jenneson et al., 2003; Kaestner et al., 2006; Perret et al., 2007; Turcotte et al., 1998]. A review by *Lynch* describes different domains under which structural root characteristics can be classified [Lynch, 1995]. The *morphology* of the system refers to the surface features of individual root axes, including the presence of root hairs and secondary roots, as well as epidermal characteristics [Lynch, 1995]. The *distribution* of roots describes system features such as length and biomass topologically with respect

to variables such as soil horizon, distance from a seminal root, and distance to neighbouring plants; without taking into account the spatial orientation of network elements [Lynch, 1995]. *Root system architecture* (RSA) is a term used to describe the spatial configuration of a root system, and whilst not accounting for morphology, is superior to either topology or distribution, since both these components may themselves be derived from a comprehensive description of the root architecture [Lynch, 1995]. The heterogeneous distribution of nutrients and water in real soils means that plant RSA is a significant factor in the effectiveness with which resources can be acquired by the plant [de Dorlodot et al., 2007].

Alongside RSA, the structure of the soil in which crops grow is also highly correlated with their development, and thus is of significant agricultural importance [Lipiec et al., 2006; Pagliai and De Nobili, 1993; Stewart et al., 1999]. Optimal crop development is strongly linked to the aeration, water transport and root penetration characteristics of the soil [Hinsinger et al., 2009; Perret et al., 1999; Pires et al., 2005; Stewart et al., 1999]. However, the complexity of the medium has necessitated that much work be descriptive, concerned with differences between soils rather than the linking of structural parameters decisively to their functional relevance for growth [Hinsinger et al., 2009]. Further relevant literature regarding soil structure is found in Chapter 2, which considers a new method for porosity quantification in soils.

Important architectural traits are not limited to the root system scale, or even the single root scale. Root hairs, single-cell extensions of the root surface, can contribute substantially to P uptake, in some conditions accounting for up to 80% of total P acquisition [Gahoonia and Nielsen, 1998; Jungk, 2001]. It has been suggested that root hairs enhance uptake by accessing resources isolated from the root surface by air-filled voids, increasing root-soil contact and anchoring roots into the soil matrix, aiding mechanical penetration [Bengough et al., 2011]. Extensive consideration is given to the role of root hairs in Chapter 5, but at all scales it is evident that an over-reliance on *in vitro* methods of characterising both architectural and biochemical root traits has blinded investigators to quite how complex an array of biochemical and physical processes is present in real soil systems [McCully, 1999]. Full consideration of the literature relating to root-hairs is found in Chapter 5.

1.5 Canonical methods for quantifying root traits, soil characteristics, and their influence on nutrient acquisition

It has been demonstrated from the pertinent literature that RSA and soil structure are both key elements in understanding the fundamental bases of nutrient uptake efficiency in plants. Because of the known importance of such characteristics, a wide variety of methods has been developed in order to allow investigation of roots and the soils in which they grow, and facil-

itate comparison of relevant traits through genotyping and phenotyping work. The following section reviews some of the most significant extant methodologies for root system elucidation.

1.5.1 Destructive and direct-observation methods

Due to the fact that roots grow in an opaque soil medium, traditional methods for investigating both biomass and topology necessarily involved disturbance or artificial constraint of the soil-plant system [Perret et al., 2007]. Before the relatively recent emergence of tomographic methods as tools for the characterisation of subterranean plant growth, the most commonly used techniques had been variations of either direct observation (rhizoboxes and minirhizotrons) or destructive root washing approaches [Pierret et al., 2005].

Root washing methods

The general approach to destructive root observation begins with the extraction of either cores or monolithic soil samples, from which roots are separated via careful washing before being subjected to manual or computer-assisted analysis techniques [Pierret et al., 2005]. Variations of this generalised approach include simple washing under a fine stream of water [Berntson and Woodward, 1992], soaking for $24 - 48\mathrm{h}$ in a clay-dispersant solution (sodium pyrophosphate) followed by washing using fine sieves and filter paper [Pagliai and De Nobili, 1993], washing in a succession of sieves of decreasing mesh diameter [Sierra et al., 2003], and use of commercially available root washing equipment based on the design of *Smucker et al.* [Pierret et al., 2005; Smucker et al., 1982]. Though the use of these techniques is extensive in the literature, it is clear that in addition to being time-consuming, the separation of roots from rhizosphere soil through conventional destructive techniques unavoidably introduces experimental artefacts by damaging the roots and root hairs [Wenzel et al., 2001]. There is much evidence in the literature to support this view, with suggestions made that the widespread use of such techniques is a function of pragmatic considerations such as low cost and rapidity, rather than verifiable accuracy and reproducibility [Pierret et al., 2005].

Many studies have drawn attention to the fact that biomass and root length data obtained through root washing are sensitive to relatively small changes in methodological approach. In a destructive study of cores containing tree roots, *Livesley et al* found that measured root length was highly dependant on the mesh-size of the sieves used to retrieve root material from the washing solution [Livesley et al., 1999]. *Sierra et al.* proposed that loss of root material during washing and sorting is among the most significant sources of error in the experimental estimation of root mass [Sierra et al., 2003], whilst in a review of root investigation methods, *McCully* estimated that fine roots (diameter $< 0.8\mathrm{mm}$) of *Zea mays* plants lost during conventional washing methods could account for more than 50% of total root length [McCully, 1999].

A study by *Amato et al.* has also drawn attention to the significance of mesh size in estimating total root length, reporting that sieving at a mesh diameter of $2\mathrm{mm}$ recovered only 10% of the total root length that could be recovered at a mesh diameter of $0.2mm$ [Amato and Ritchie, 2002]. Such findings correlate with the those of a review spanning more than six decades of plant root research, in which *Pierret et al.* concluded that over 50% of total root length in *Brassica napus L.* is comprised of roots with diameter $< 0.2\mathrm{mm}$. When it is considered that the standard version of the commercially available *Delta-T* root washing apparatus uses a $0.5\mathrm{mm}$ mesh, it appears likely that studies undertaken using such equipment will significantly underestimate total root length [Pierret et al., 2005].

Comparison of the root recovery rates obtained using different methodologies yields somewhat surprising results. A review by *Pierret et al* ranked the average values of *root density* (L_v) derived from various studies representing the full range of current techniques, and found that whereas the recent studies utilising root washing generally estimated L_v values that were higher than those in minirhizotron studies and lower than those for X-Ray CT studies, the highest values of all were from washing studies conducted in the 1930's by *Dittmer* and others (see Figure 1.5) [Dittmer, 1938; Pierret et al., 2005]. This suggests that in addition to the known influence of mesh size on measured values of L_v, root washing techniques are also highly dependant on human factors, such as the care taken in separation of soil and root matter. These factors are proposed as a likely reason for the significantly higher L_v values estimated by *Dittmer* when compared to those of later studies utilising less tedious but also less meticulous separation methods [Pierret et al., 2005].

1.5.2 *In vivo* methods

Despite being of certain use in quantifying biomass, length density and topology of root systems, destructive root characterisation methods such as washing usually fail to provide useful information about RSA [Tracy et al., 2010]. The extrication of roots from soil unavoidably introduces artefacts such as damage or root loss, destroys the native architecture of the system, and negates the opportunity to analyse the same plant at a later developmental stage [Lynch, 1995]. Moreover, methods involving the washing of soil cores are not only time consuming, but also spatially and temporally discontinuous, with the difficulty of interpretation and comparison with other studies providing substantial disincentives to their use [Gregory et al., 2003]. For these reasons, the ability to observe roots and soil biota *in vivo* is highly desirable, and the development of such techniques has brought with it the promise of an improved understanding of soil-root interactions [Lynch, 1995]. Direct observation of the soil environment is also advantageous in determining how soil fauna such as earthworms both colonise and modify their surroundings, and the effect of such interactions on soil structure and root behaviour [Lussen-

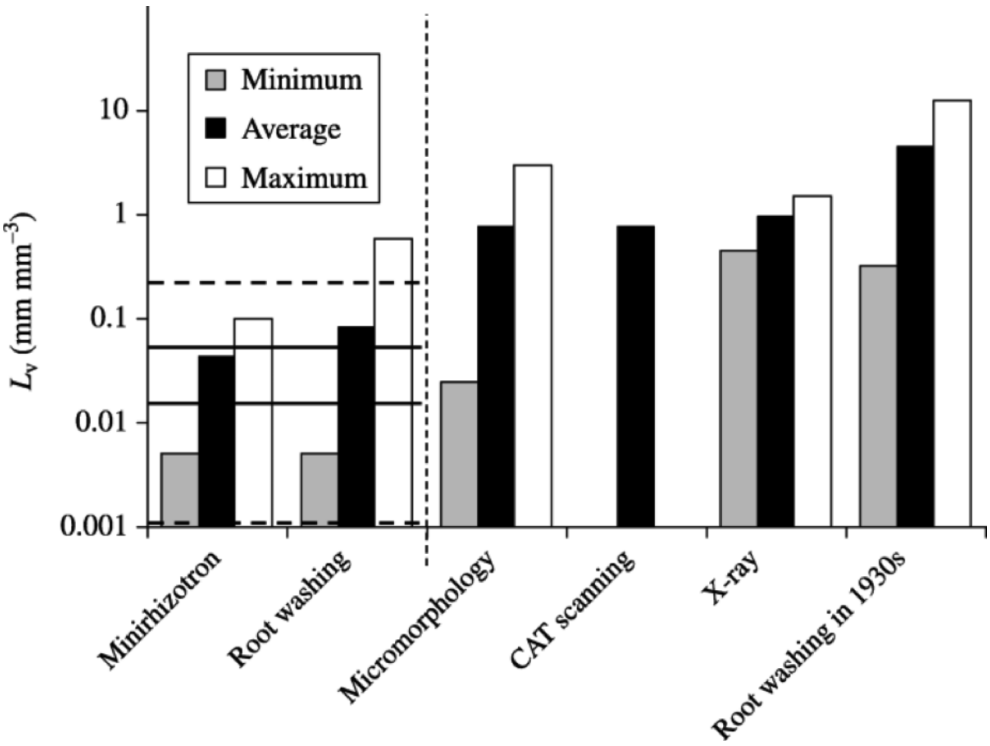

Figure 1.5: Comparison of L_v values achieved by different characterisation methods [Pierret et al., 2005].

hop and Fogel, 1993]. In their simplest form, direct observation methods require simply that plant roots are able to be grown against some form of sampling surface through which they can be sampled by the investigator, either by eye using image capture devices, or via chemical assay. The following protocols are all variations on this philosophy.

Rhizoboxes/Rhizotrons

Minirhizotrons are an extremely simple direct-observation tool for studying growing roots *in situ*. A minirhizotron setup comprises clear polymer tubes implanted at a field site, into which a specially adapted camera may be periodically inserted to record development of adjacent roots [Johnson et al., 2001]. Though the technique has allowed the application of demographic methods to roots in the field environment, facilitating the tabulation of developmental stages from initial growth to senescence, it has proven difficult to convert root counts into more useful data such as length densities or biomass [Lussenhop and Fogel, 1993; Pierret et al., 2005]. Since digital root extraction of root positions from minirhizotron images is in practice very difficult, the accuracy of the method is reliant on the ability of the user to recognise root material in scanned images [Pierret et al., 2005]. Moreover, there is evidence that due to the rapid turnover rates of fine roots, a significant proportion of such material is likely to be missed if the sampling frequency of the study is longer than one week [Johnson et al., 2001]. Further

complications in the use of minirhizotrons arise when estimating root densities, since installation unavoidably causes local compaction in the soil around the tube. Moreover, soil or tube movement can result in an air gap between the tube and soil, forming a preferential growth path that will cause bias when root data is upscaled to generate whole-plant estimates of root density [Lussenhop and Fogel, 1993].

Alternatives to minirhizotrons include rhizotrons and rhizoboxes, the former designed for the direct observation of plant roots, and the latter for the characterisation of rhizosphere biochemical properties including hydration, pH, and exudate concentration at varying distances from a root mat [Wenzel et al., 2001]. Rhizotrons most commonly comprise a plexiglass box filled with soil and fitted with a suitable system to provide hydration in accordance with desired parameters [Wenzel et al., 2001]. Light is generally occluded in order to simulate field conditions and prevent algal growth, with a hinged flap allowing periodic viewing of roots adjacent to a certain plane [Gibeaut et al., 1997; Heeraman et al., 1997]. In practice this plane is often oriented at an angle which exploits root gravitropism to provide favourable root-to-glass contact, with characteristic figures of 45° [Dinkelaker et al., 1993] and 55° [Berntson and Woodward, 1992] to the horizontal being characteristic [Wenzel et al., 2001]. Methods for qualitative assessment of root growth in rhizotrons are similar to those utilised in minirhizotrons, though the comparatively easier access and more favourable geometry provided by a flat viewing plane offer greater scope for quantitative measurements to be made. At a simple level, a study by *Berntson et al.* made use of acetate sheets to trace root systems by hand at different intervals [Berntson and Woodward, 1992], whilst a more refined methodology implemented by *Schmidt et al.* among others examined roots of rice plants using a flat-bed scanner fixed in front of a rhizotron window (see Figure 1.6) [Schmidt et al., 2011]. The use of commercially available flat-bed scanners in this application is still widespread in root and rhizosphere research [Dannoura et al., 2012; Schmidt et al., 2011].

Other more specialised methodologies based on the rhizobox concept have been developed for the investigation of specific processes. One example is an agar-based bioreporter assay recently developed for quantification of inorganic arsenic mobilisation and release in rhizosphere soil [Kuppardt et al., 2010]. Roots of maize (*Zea mays*) were grown in a planar geometry, and agar plates containing bioreporter bacteria *E. coli DH5*α *1598* applied directly to the root system for a $2\mathrm{h}$ incubation period. Following a further incubation interval post-removal, fluorescence measurements were taken in order to quantify arsenite and arsenate concentrations. Such novel methodologies are presently limited to investigation of planar root systems, but do allow spatially-resolved quantification of chemical speciation around roots, at resolutions well into the $< 1\mathrm{mm}$ range.

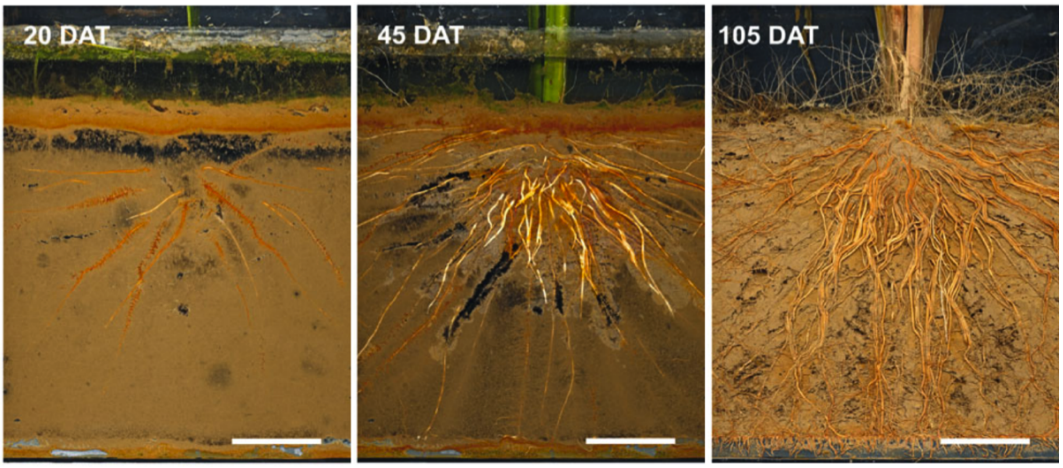

Figure 1.6: Figures from *Schmidt et al.*, showing scans of *Oryza sativa* roots grown in a standard rhizotron setup [Schmidt et al., 2011]. Soil is a standard paddy medium (Anthraquic Cambisol), and Fe oxidation can clearly be seen around roots (orange and black regions). Images are shown at 20, 45 and 105 days after transplanting (DAT), and scale bar is 5cm.)

Tomographic imaging methods

Destructive characterisation and rhizotron-based direct observation approaches have been insufficient in satisfactorily capturing the architectural and morphological complexity of root systems [Heeraman et al., 1997]. Reviews have pointed to the clear need for development of non-destructive techniques allowing study of the rhizosphere in-situ, and in recent years a number of innovations in non-invasive imaging appear to have shown significant promise in meeting this requirement [Gregory and Hinsinger, 1999]. Two families of techniques, X-ray Computed Tomography (XCT) and Nuclear Magnetic Resonance Imaging (NMRI), represent a step-change in this regard, both allowing three-dimensional, non-invasive and non-destructive imaging of a wide range of biological materials [Heeraman et al., 1997; Stuppy et al., 2003]. These methods hold significant promise for the study of root systems [Moran et al., 2000], soil structure [Mooney, 2002], and water movement in the rhizosphere [Aylmore, 1993], all of which have until recently been hampered by the destructive or spatially diffuse nature of the methods previously available [Gregory and Hinsinger, 1999]. As well as providing the capacity to qualitatively assess root and soil characteristics, non-invasive imaging entails the possibility of employing digital image analysis techniques to measure roots as they appear in-situ [Pierret et al., 2005].

The latest generation of X-ray CT scanners provide superior spatial resolution to that afforded by NMRI, with the additional benefits of largely density-proportional attenuation and imperviousness to paramagnetic elements leading to increasing adoption in plant and geosciences [Gregory et al., 2003; Perret et al., 2007]. These techniques have been used in the field of plant science for around 20 years, in optimum conditions allowing non-destructive geometric clas-

sification of roots in real soils, but interpretation of the resulting data remains a serious and ongoing challenge [Dunbabin et al., 2013].

1.5.3 The role of numerical modelling in predicting nutrient acquisition characteristics

Alongside root observation methods, and partly due to the difficulty of measuring root characteristics and related processes in situ, mathematical modelling methods have long proven to be a useful tool in plant and soil sciences. By considering root and soil structure virtually, and approximating biochemical processes using mathematical equations, simulated 'experiments' into the influence of different conditions, traits and parameters can be conducted without the need for time-consuming growth trials [Dunbabin et al., 2013]. The modelling of root systems gives investigators an opportunity to investigate the influence of geometric root parameters which are non-trivial to investigate experimentally [Dunbabin et al., 2013]. Modelling can be broadly considered as existing across two overlapping domains, one concerned with the simulation of physical root growth at scales from the root hair to the entire root system scale, and the other concerned with simulating biochemical transport, reaction and uptake processes at the same range of scales.

Methods for modelling nutrient uptake by plant roots

Current approaches to modelling the transport and uptake of nutrients are varied, but the foundations were laid in in the 1960's in work by *Barber*, *Nye* and others who developed early models for the uptake of poorly-mobile nutrients and water by plant roots [Bagshaw et al., 1972; Barber et al., 1963; Drew et al., 1969; Nye, 1966]. These early models considered the uptake rate of ions by a small, idealised root section giving a cumulative total per unit length which could then be integrated over the entire root length (determined by destructive root-washing methods) to provide a whole-plant estimate. This early approach, now commonly known as the *Nye-Tinker-Barber* model, assumes that uptake occurs only from the fluid phase, that soil is structurally homogeneous, and that the matrix is at 100% water saturation [Barber and Silberbush, 1984; Nye and Tinker, 1977; Roose et al., 2001; Tinker and Nye, 2000]. Furthermore, plant mediation of the kinetics of nutrient uptake and diffusion (by processes such as exudation) are neglected [Drew et al., 1969]. In the model, the standard diffusion equation describes ion kinetics in the fluid phase:

$$\frac{\partial C_l}{\partial t} = D\nabla^2 C_l, \tag{1.1}$$

where C_l ($\mathrm{mol.m^{-3}}$) is the concentration of P in pore water, and D ($\mathrm{m^2.s^{-1}}$) is the diffusion constant for P in water.

Flux across the root surface is defined by some suitable expression, usually an experimentally-informed *Michaelis-Menten* law (describing catalysis of adsorption and desorption processes by enzymes). The flux of ions into solution from the soil surfaces is governed by a boundary condition which approximates the influence of soil chemistry on absorption and desorption [Murray, 1993]. Though the Nye-Tinker-Barber model can be considered mechanistic (in that it explains constituent processes in terms of physical laws), the lack of understanding required to accurately describe processes below the rhizosphere scale means that it ceases to be truly mechanistic below this scale [Darrah et al., 2006].

More recent work by *Roose and Fowler*, *Ptashnyk et al.*, *Leitner et al.*, *Zygalakis et al.* and others has built upon this model, gradually reducing the number of assumptions made by the minimal approach. *Roose and Fowler* re-derived the equations used in the classical model by considering two mobile forms of soil P; one in solution, and one in the solid phase [Darrah et al., 2006; Roose and Fowler, 2004]. The technique of *non-dimensionalisation* allowed for identification of processes which could be excluded during upscaling of the model [Roose and Fowler, 2004]. Others have added the influence of root hairs to this model using a *homogenisation* method to transform spatial heterogeneities at different scales into a single, computationally tractable description [Leitner et al., 2010b; Pavliotis and Stuart, 2008]. In this manner the root-hair functions were integrated into the larger-scale model [Leitner et al., 2010b]. It was assumed that soil was quasi-homogenous at the scale considered, and a compound diffusion coefficient was defined in order to include both the buffer power (b) and an impedance factor (representing the effect of pore tortuosity in the soil matrix) [Leitner et al., 2010b]. As with earlier models, Michaelis-Menten kinetics were used to describe the relationship between concentration at the root hair surface and the rate of influx across the surface [Leitner et al., 2010b]. This represented an improvement upon earlier approaches which had either expanded the effective root radius by the hair length (to form a 'virtual' root cylinder with a greater diameter) [Passioura, 1963], or modified the transport continuity equation for transport to the root surface to include a second sink term accounting for nutrient flux into hairs [Bhat et al., 1976]. Though some studies have attempted to explicitly consider the root hairs as part of a three-dimensional model [Geelhoed et al., 1997], this is highly challenging computationally, and most workers have instead chosen alternative approaches [Leitner et al., 2010b].

By taking the previously outlined approach, *Leitner et al.* were able to predict how quickly depletion gradients are likely to form in the soil, and thus inform the timescale over which such processes ought to be experimentally investigated [Leitner et al., 2010b]. Alongside this work, *Zygalakis et al.* have also developed a model of nutrient uptake by root hairs. This approach removes the assumption of soil quasi-homogeneity at the hair scale by instead considering the soil in terms of two domains (following *Ptashnyk et al.*) [Ptashnyk et al., 2011; Zygalakis

et al., 2011]. In this model, the continuity equation contains separate terms describing fast and slow reactions *within* the aggregates, and both fast and slow sorption are also considered at the particle surfaces [Zygalakis et al., 2011]. As in previous models, the uptake function is described in terms of a Michaelis-Menten type law. Two transport zones are considered - an extra-hair zone (with no sink terms) and a hair zone (in which the equation governing the inter-aggregate space includes a sink term representing the influence of root hairs) [Zygalakis et al., 2011]. Root-hair influx rates were based on those determined experimentally for root surfaces, an assumption made on the basis that similar trans-membrane transport mechanisms govern uptake in both cases [Mudge et al., 2002]. Once defined, this dual-porosity model was compared to the single-porosity model of *Leitner et al*, with substantial differences discovered in estimated uptake. Greater cumulative uptake was predicted for the dual-porosity case, since nutrient release from the intra-aggregate space was able to replace nutrients lost at the soil/fluid boundary [Zygalakis et al., 2011]. Furthermore, given a constant total length, increasing root hair lengths enhanced uptake to a greater degree than increasing their distribution density; a difference that was not predicted by the single-porosity model [Zygalakis et al., 2011]. Uptake in the dual-porosity model was also less sensitive to changes in soil moisture content [Zygalakis et al., 2011].

As previously discussed, the invasive measurement of rhizosphere soil for the purpose of validating parameters at the root hair scale is extremely difficult, and hence such parameters are difficult to validate experimentally [McCully, 1999; Zoysa et al., 1997]. Headway is being made in certain areas, such as the more accurate quantification of ion fluxes across root membranes (*in vitro*) using the microelectrode ion flux estimation (MIFE) technique pioneered in plant applications by *Shabala et al.* [Shabala et al., 2006]. Despite this, there is a lack of knowledge in other areas such as that required to allow nutrient spatial heterogeneity to be non-invasively and accurately determined. Though this heterogeneity has been mapped for very small thin-section soil samples ($40 \times 30 \times 2.5\mu\mathrm{m}$) by combining spatially-resolved X-Ray fluorescence (XRF) and X-ray absorption near-edge structure (XANES) techniques, there are substantial caveats with such a approaches. The sample sizes are extremely small when compared to the length scales of rooted soil volumes, samples must be resin-infused, and both techniques require use of synchrotron radiation sources [Lombi et al., 2006]. Such studies suggest that it is not presently possible to characterise spatial distribution of nutrients at larger scales in three dimensions. This shortfall reiterates the need for more multidisciplinary approaches, combining the joint efforts of theoreticians and experimentalists, in order to synthesise accurate parameter determination with explicitly considered, mechanistic models in order to advance understanding.

Methods for modelling physical growth of plant roots

Nutrient uptake models in the literature most often use idealised simplifications of the root/-soil environment as the architecture upon which equations for nutrient kinetics are solved. In the simplest case, this can be a cylinder representing the root, within a larger cylinder representing the soil, perhaps with a cylinder of intermediate radius representing the root hair zone [Darrah et al., 2006]. Later models have considered more sophisticated geometries, in which soil and air phases are represented as an ordered array of spheres in a water matrix, with roots or root hairs arranged among them in a repeating pattern (Figure 1.7) [Zygalakis et al., 2011]. Ultimately it is desirable to consider the entire root system within a modelling environment, allowing the investigator to compare functional tradeoffs between different rooting strategies [Dunbabin et al., 2013]. Due to the difficulty of extracting real 3D root architecture from plants in soil, a range of computational environments have been developed allowing the virtual growth of quasi-realistic root systems, which can then be imported into finite element software for nutrient or water uptake modelling [Dunbabin et al., 2013]. SimRoot [Lynch et al., 1997], ROOTMAP [Diggle, 1988], RootTyp [Pagès et al., 2004] and RootBox [Leitner et al., 2010a] all allow the user to virtually 'grow' entire root systems according to a large number of input parameters. The dependence on user-defined parameters varies, with some environments making more use of stochastic processes, and others heavily dependent on detailed input of experimental or literature-derived data for branching rates, branching angles, growth rates and other traits [Dunbabin et al., 2013]. *Schnepf et al.* parameterised the RootBox model in a recent study using detailed root drawings acquired from field sectioning of crops during the 1950's [Kutschera and Lichtenegger, 1960; Schnepf et al., 2012]. The models also differ substantially in their accounting for the physical and biochemical properties of soil and their influence on root growth. ROOTMAP places particular emphasis on responsive plasticity in root hair growth and nutrient uptake based on soil conditions [Dunbabin et al., 2013].

Unavoidably, the number of parameters required to approximate the different plant and soil processes and interactions is large, a factor that introduces limitations not only in accuracy, but also in validating whether or not unintended consequences have resulted from parameter interaction [Dunbabin et al., 2013]. To make finite element models at the whole-plant scale tractable, polygon meshing must also be at a coarse scale compared to the hair and single aggregate scale. Added to the fact that most models do not consider any soil property differences between rhizosphere and bulk soil, rhizosphere-scale activity is clearly likely to be under-accounted for [Carminati et al., 2010]. Only two of these simulation environments, SimRoot and ROOTMAP have the facility to take into account the influence of root hairs at all [Dunbabin et al., 2013].

The accuracy of growth models are limited by a paucity of mathematical descriptions of cer-

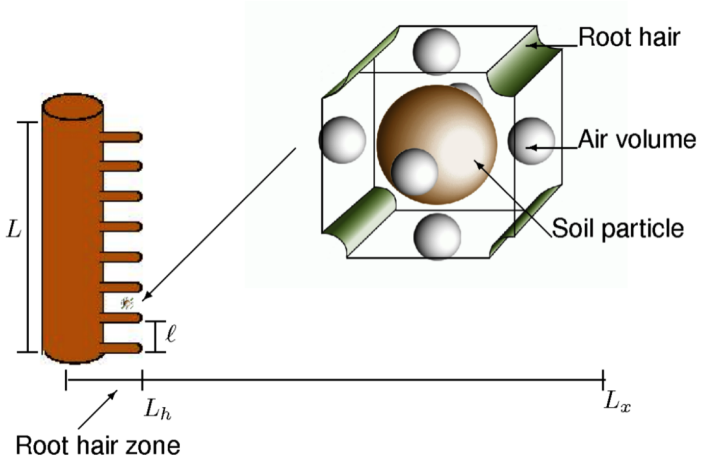

Figure 1.7: Figure from *Zygalakis et al.* showing the periodic geometry used in their model of root-hair P uptake. At least one soil particle is assumed to lie between adjacent hairs [Zygalakis et al., 2011].

tain more complex physical processes on the one hand, and a lack of experimentally-derived parameterisation data on the other [Dunbabin et al., 2013]. Root morphological features such as hair structure and aerenchyma are also usually overlooked. In order to be more widely integrated into plant breeding efforts, the influences of the environment on phenotypic plasticity will have to better predicted [Lynch and Brown, 2012]. Though such models can currently provide relatively good approximations to plant-scale root structure, an improved ability to investigate root systems *in situ* at a range of scales will not only allow explicit nutrient uptake modelling to be achieved on real geometry, but also help parameterise virtual models, particularly with the aid of upscaling regimes such as homogenisation [Schnepf et al., 2008].

1.6 Key requirements for progress towards improved nutrient uptake efficiency in crops

Towards better-informed targeted breeding and soil management for improved crop P efficiency, a number of aims can now be summarised which shape the work in this thesis.

1.6.1 The explicit consideration of rhizosphere-scale processes in numerical regimes

Current modelling approaches almost always neglect the explicit consideration of root hairs [Leitner et al., 2010b]. Nonetheless, some numerical studies have investigated the influence of root hair traits on uptake of P at the single root scale using a variety of methods [Ma et al., 2001]. Though these have allowed functional tradeoffs between traits such as length and density to be investigated to some degree, the soil is considered structurally and biochemically as

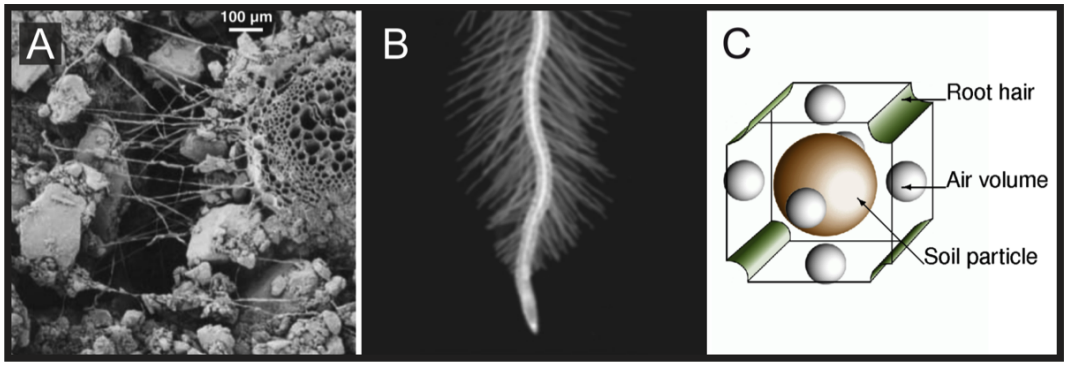

Figure 1.8: (A) Cryo-SEM studies reveal a degree of morphological complexity in hair and soil interactions that is unaccounted for in (B) agar-grown studies [Müller and Schmidt, 2004] or (C) hair-scale numerical models [Zygalakis et al., 2011].

a bulk medium, and the hair architecture is highly ordered, both of which are serious over-simplifications [Ma et al., 2001]. It is known from cryogenic scanning electron microscopy (cryo-SEM) studies that hairs in real soil are likely to experience much more complex physical interaction with rhizosphere soil than is suggested either by these models or by agar plate studies [Hinsinger et al., 2005; Van Noordwijk et al., 1993] (See Figure 1.8). It would be sensible to consider rhizosphere and hair complexity as fully as possible in models at the appropriate scale in order to establish the fundamental processes and timescales governing uptake, allowing these findings to be incorporated during careful mathematical upscaling to the root-system scale [Roose and Fowler, 2004]. Considering both hairs and soil explicitly would allow the removal of certain assumptions currently necessary to account for a lack of understanding, such as the definition of a compound diffusion coefficient into which the influence of soil buffer power (b) is incorporated, along with the averaged influence of pore tortuosity effects in the form of a simple, scalar 'impedance factor' [Leitner et al., 2010b]. Since the physical and biochemical properties of the rhizosphere differ markedly from those of bulk soil [Carminati et al., 2010; Gregory et al., 2005; Hinsinger et al., 2009], it seems most prudent to visualise them non-destructively, and to expend experimental effort to make such advances possible.

1.6.2 Conclusion - extending the scope of X-ray CT imaging in plant science

The complexity of coupled plant and soil processes has in large part been underestimated due to an over-reliance on *in vitro* investigation methods [McCully, 1999]. μ-CT imaging (reviewed in Chapter 2) potentially offers the possibility to non-destructively investigate root architecture, morphology, anatomy and the structural characteristics of the surrounding soil and water at a range of scales, but work is needed to extend its utility in the field of plant science. The following developments are considered to be particularly timely and relevant for investigation.

Imaging the RSA of large-scale plant samples

Of particular interest for investigation using μ-CT are root scales that are absent from previous work, yet known to be highly relevant to understanding of development and function, with particular emphasis on traits implicated in phosphate uptake. One of these is the realistic length scales of mature root-systems, as opposed to the $< 10\mathrm{cm}$ sample diameters at which virtually all previous work has been focused. By extending beyond juvenile samples to investigation of more mature crops at the root-system scale, it is likely that quantification of field-relevant architecture for trait phenotyping as well as parameterisation of nutrient uptake and growth models can be improved.

Imaging root hairs and soil at the rhizosphere scale

There have been few attempts to image root systems at the $> 10 - 15\mathrm{cm}$ scale, but a similar paucity of work also exists at the microscale. At present, no studies have used non-destructive tomographic imaging to investigate the rhizosphere or the micro-scale plant and fungal structures that colonise it. Root hairs and mycorrhizae are both known to be highly implicated in the uptake of immobile nutrients [Lambers et al., 2006], but the nature of their interaction with real soils is poorly known. The overwhelming majority of studies into root hair development, trait differentiation between species, and responses to abiotic stress have been carried out *in vitro* using agar or phytagel plates. Though these make observation straightforward, such conditions allow little interpolation with the conditions of the field environment [Gregory and Hinsinger, 1999; Heeraman et al., 1997; Pierret et al., 2005]. It is unclear whether such data can in fact be meaningfully translated to the much more complex context of real soil at all, and unfortunately such considerations are usually absent from such studies [Herder et al., 2010]. Since μ-CT methods now allow investigation down to the $< 1\mu\mathrm{m}$ scale, it is important to utilise such capabilities to unravel the actual structure of soil, hairs and mycorrhizae in the rhizosphere zone, in order to improve our understanding of their morphology and development, but also to facilitate the acquisition of more accurate statistical data than is available through destructive sampling or *in vitro* approaches. The ability to directly investigate hair and rhizosphere traits between different soil states and genotypes may generate data that will enhance breeding efforts to generate germplasm tailored for low-P environments. Since a great deal of our knowledge about root hairs comes from samples grown in mechanically and chemically homogenous phytagel [Causin et al., 2012; Maizel et al., 2011; Yang et al., 2013; Yi et al., 2010], it is important to develop more sophisticated approaches that can detect plastic responses to the physical and biochemical complexity of the real soil environment [McCully, 1999]. If this is achieved, existing models can then be parameterised with real hair and rhizosphere soil geometry, allowing the influence on nutrient uptake of differences in genotypic/phenotypic hair traits, soil structure and water content to be compared using explicit regimes at unprecedented

levels of accuracy.

Improving and standardising workflows for μ-CT imaging

Interpretation of μ-CT data still remains a difficult task within the plant and soil science communities [Dunbabin et al., 2013]. An in-depth review of μ-CT imaging in plant and soil sciences, found in Chapter 2, reveals the wide range of parameters and protocols used for imaging of roots in soil, often without justification for their use [Keyes et al., 2013b]. In addition, a high degree of user-based variation is known to exist in quantification of even simple soil and root parameters from μ-CT data [Baveye et al., 2010]. There exists a clear need for standardisation of imaging procedures and reporting of imaging parameters in a manner that allows increasing optimisation of protocols for maximum root retrieval. Furthermore, a move away from imaging in sands or very sand-rich media should be made in order to more accurately capture the behaviour of the root in the much more complex biochemical and mechanical environment represented by real soil [McCully, 1999]. One way to achieve this is the development of methods such as those existing in clinical X-ray CT to treat samples using radio-opaque media for artificial contrast enhancement. Such methods have not been applied in plant science, despite low-contrast being a perennial issue.

Further to acquisition, analysis of soil and root μ-CT data has traditionally been *ad hoc* and heuristic, either failing to be carried out according to well-validated protocols, or failing to link observed characteristics to important plant and soil processes [Houston et al., 2013]. As well as improving methods to visualise the architecture and morphology of undisturbed plants in real soil, it will be increasingly important to use such information both to compare genotypic and phenotypic trait differentiation, and to link traits to uptake and other key processes using modelling and other multidisciplinary approaches.

1.7 Rationale and major hypotheses

These key areas of investigation suggested by the literature give shape to a number of governing hypotheses for experiments. This thesis considers the use of μ-CT as a technique for the non-destructive investigation of roots and soil at a number of scales. The technique holds promise for the phenotyping of important P uptake traits, and the parameterisation of root and growth uptake models which can be used to predict the influence of different soil and root factors on P efficiency. However, given continued drawbacks in the form of a limited sample-size range and availability of well codified paradigms for interpretation of data, there is a clear need for progress before μ-CT begins to realise its considerable potential as a method in plant and soil sciences. Though detailed sub-hypotheses appear in the course of relevant chapters, the major guiding hypotheses shaping this body of work are as follows:

- Novel methods and robust workflow development can be combined to address problems affecting the reproducibility of soil/root parameter measurement, such as an intrinsic lack of root/soil contrast in root/soil μ-CT.
- Development of new protocols for large-sample imaging can allow the un-constrained, non-invasive, *in vivo* quantification of key root system parameters at the scale of the mature plant, allowing phenotyping and model parameterisation from roots free from heavily constrained geometries (rhizoboxes) or non-field growth media (*i.e* gels, sands and nutrient solutions).
- μ-CT can be applied to plant and soil morphology at the rhizosphere scale in order to understand the interactions of hairs with the real soil environment in a manner that facilitates both novel qualitative insights, and the parameterisation of explicit numerical P-uptake models for the first time at the hair scale.

The following chapters consider experimental approaches to validation of these hypotheses, through a multidisciplinary combination of targeted discovery experiments and systematic method development.

A detailed review of the μ-CT imaging method at a level accessible to the non-specialist is found at the beginning of Chapter 2. μ-CT imaging methods form a substantial component of the thesis, such that the reader may regularly be referred back to the methods and definitions within this section.

Chapter 2

Addressing measurement accuracy and contrast issues in μ-CT studies of roots and soil

Two canonical issues affecting the use of μ-CT imaging in soil and plant sciences are the low contrast classically attainable between roots and their surrounding environment, and the high degree of user-bias and variation in measurement of even simple soil and root parameters. Soil porosity is one such parameter which correlates with many soil and plant processes, such that accurate quantification is of known importance. This chapter considers present issues with the estimation of soil porosity using μ-CT, arising in both the imaging and image processing domains. It is then shown how an informed tuning of imaging parameters can be used to maximise image contrast, with a novel algorithm used to automate the process of soil *segmentation* into macropore and aggregate regions. Segmentation is an important step in image-based porosity measurement and preparation of geometric soil representations for use in numerical models, but is often performed either using simplistic global thresholding tools or using highly user-dependent approaches. The results generated using the algorithm are compared to results from both gravimetry and canonical image-based segmentation approaches. The algorithm is later applied in Chapter 5 to prepare μ-CT data for numerical modelling at the hair scale.

2.1 A comprehensive review of μ-CT imaging methodology in the fields of plant and soil science

2.1.1 The history of X-ray Computed Tomography in plant and soil sciences

X-ray CT imaging (XCT) originated in 1971, initially as an exclusively medical diagnostic tool,

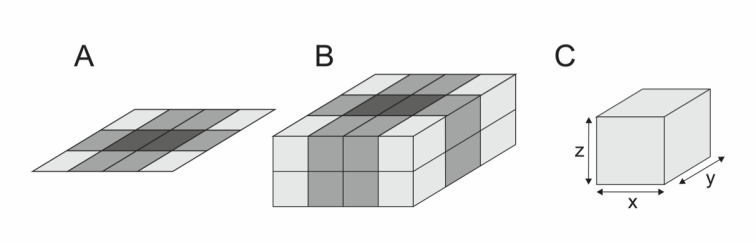

Figure 2.1: (A) 2D images are composed of discrete elements (usually of square geometry) called (pixels), (B) 3D datasets are composed of similar elements called *voxels*, which have an x, y and z dimension (C). In most cases, $x = y = z$.

designed for scanning of human-sized objects, and operating at non-lethal X-ray doses [Stuppy et al., 2003]. It allows the non-invasive 3D reconstruction of objects, where image contrast is predominantly determined by the differences in X-ray attenuation of different sample constituents. Though it can be viewed as single, 2D planar 'slices', XCT data is predominantly presented as a 3D array of image elements known as 'voxels,' analogous to pixels in 2D images, but with a cuboidal geometry (see Figure 2.1). The edge length of the voxels is one factor determining the *spatial resolution* of the data, thus influencing the smallest observable feature size (Figure 2.1-C).

Early XCT studies of soil structure [Hainsworth and Aylmore, 1983; Hamza and Aylmore, 1992] explored the potential of using medical devices, and concluded that it was possible to acquire insight beyond the scope of traditional soil/root investigation methods [Gregory et al., 2003]. The spatial resolution of the images was ($\approx 1.5 \times 1.5 \times 10\mathrm{mm}$); too coarse to distinguish all but the coarsest scales of soil porosity [Gregory et al., 2003]. Later, *Watanabe et al.* explored the potential of medical scanners to quantify plant roots, and were successful in detecting the coarse roots of Chinese yam (*Dioscoria oppositifolia L.*) [Watanabe et al., 1992], whilst *Tollner et al.* were able to distinguish roots in samples of the significantly finer-rooted soybean (*Glicine max L.*), though only the seminal roots were visible at the system resolution of ($1.14\mathrm{mm}$) [Perret et al., 2007; Tollner et al., 1994]. A study by *Heeraman et al.* was the first to use a non-medical device, obtaining images of common bean (*Phaesolus vulgaris L.*) plants at a resolution of ($160 \times 160 \times 200\mu\mathrm{m}$), and detecting roots with a diameter of ($350\mu\mathrm{m}$) using a high-energy industrial unit with a $420\mathrm{kV}$ accelerating potential and a scan time of $4.1\mathrm{h}$ per sample [Heeraman et al., 1997]. Such resolution offered a substantial improvement over that attainable using medical systems, and though the latter offer faster acquisition times, their usefulness is still limited by comparatively poor resolution, as well as the fact that scanning parameters are optimised for the human body rather than soils or root tissue [Jenneson et al., 2003; Lontoc-Roy et al., 2006]. By comparison, *micro-focus* X-ray CT (μ-CT) uses significantly higher-resolution monochromatic or polychromatic X-ray sources and static flat-panel or linear detector arrays, which allow for up to a 100-fold increase in spatial resolution compared

to most medical systems [Stuppy et al., 2003]. The increasing affordability and prevalence of such scanners has meant ever-increasing use of μ-CT within the fields of soil and root research. Examples of extracted root architectures acquired using the technique are shown in Figure 2.2.

The first use of a system specifically designed for the observation and quantification of roots in soil was in a study by *Jenneson et al.*, who built a bespoke scanner capable of a voxel resolution of $(100 \times 100 \times 100 \mu\mathrm{min})$, with scan times of around $40\mathrm{m}$ for samples with diameter $(25\mathrm{mm})$ and height $(30\mathrm{mm})$ [Jenneson et al., 2003]. Though representing an improvement in terms of scan time and resolution, the results of the study shared the limitations of earlier investigations in that detection of finer roots was limited, and the pore space of the growth media was finer than could be resolved at the resolution available [Kaestner et al., 2006]. The sample diameters in this study (and those in a further study using the same device by *Gregory et al.* [Gregory et al., 2003]) were limited by the low source energy and the small detector size, resulting in conditions whereby roots came into contact with the growth chamber walls and became indistinguishable in data soon after germination [Perret et al., 2007]. In the present day, despite the relative maturity of μ-CT technology, it is clear that there is significant work to be undertaken in developing effective imaging protocols which facilitate subsequent extraction and characterisation of root architecture and morphology [Heeraman et al., 1997; Perret et al., 2007].

Even rudimentary representation of feature morphology within μCT image data requires a system resolution that is at least twice as fine as the feature of interest, but in images with a significant degree of noise, or where surrounding material is markedly heterogeneous, successful detection may require a higher relative spatial resolution [Kaestner et al., 2006]. As well as spatial resolution, the contrast between phases is an important property of a CT image, with maximisation of contrast being an important prerequisite for effective feature extraction [Heeraman et al., 1997]. With respect to X-ray attenuation coefficient (the measure of how strongly X-rays are attenuated by the material), theoretical contrast (C_{th}) between materials in a CT image is defined as,

$$C_{th} \approx \frac{|\mu_f - \mu_b|}{\mu_b} \times 100\%, \tag{2.1}$$

where (μ_f) and (μ_b) are attenuation coefficient of feature and background respectively [Sivers and Silver, 1990]. Because of the influence of image noise on feature detection, it is often helpful to consider the *contrast to noise ratio* (CNR) instead of the idealised contrast, defined as,

$$\mathrm{CNR} = \frac{|\overline{\mu_f} - \overline{\mu_b}|}{N_{ROI}}, \tag{2.2}$$

where ($\overline{\mu_f}$) and ($\overline{\mu_b}$) are the mean attenuation coefficients in sampled feature and background

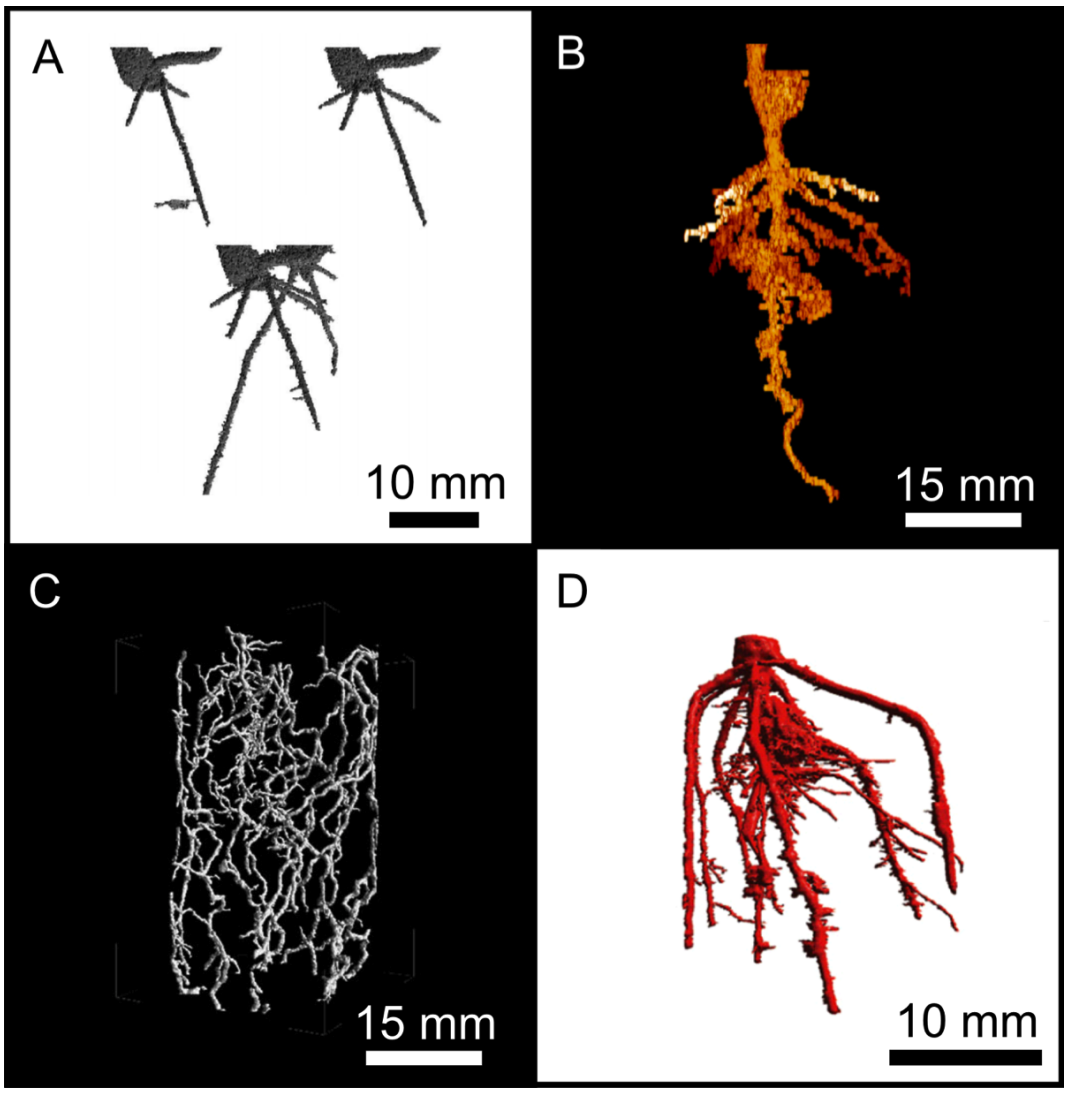

Figure 2.2: Example geometries of root systems obtained from X-Ray CT data. (A) Compound image showing growth over time of wheat (*Triticum aestivum*) roots [Gregory et al., 2003]. (B) Early rooting of chickpea (*Cicer arietinum*) [Perret et al., 2007]. (C) Roots of 29 day old wheat [Flavel et al., 2012]. (D) Roots of maize (*Zea mays*) extracted from CT data using a novel root tracking algorithm [Mairhofer et al., 2012]. Note the small scale of samples.

regions, and (N_{ROI}) is the *noise of interest*, equivalent to one standard deviation in the sampled values of μ_f. In addition to CNR, the *signal to noise ratio* (SNR) of reconstructed μ-CT images is also an important quality parameter that is used to assess image quality and compare datasets. SNR is simply calculated as,

$$\mathrm{SNR} = \frac{\overline{\mu_f}}{N_{ROI}}, \tag{2.3}$$

Attenuation of X-rays at photon energies of $< 1\mathrm{MeV}$ is dominated by *photoelectric absorption* and *Compton scatter*, for which attenuation is proportional to the inverse of the third and first power of photon energy respectively. Reducing beam energy is thus a means of improving contrast, though because photon emission, atomic interactions and detection are all probabilistic events, this is achieved at the expense of a reduced signal-to-noise ratio. The easiest way to mitigate against this problem is to increase acquisition time, thus improving the detector counting statistics, but though inherent detector and electronic noise can be minimised, they cannot be eliminated [Heeraman et al., 1997]. For samples with good spatial stability over time, this is often unproblematic, but in the case of roots and soils, the inherent instability of the structures involved means that longer scans risk generating increasingly severe movement *artifacts* in the data.

2.1.2 The operation of a 3rd generation $\mu - \mathrm{CT}$ system

The use of conventional X-ray CT as a means to characterise the structure of a sample relies on two fundamental physical processes:

- The differential attenuation experienced by an X-ray beam, dependent on the density and chemistry of phases in the sample.
- The ability to acquire 2D radiographs at different angles through an object in order to reconstruct the attenuation coefficient at discrete points in 3D space [Gregory and Hinsinger, 1999].

The following section will elucidate the components required to transform these principles into a useful instrument for scientific investigation, and hence describe the basic operation of a third-generation μ-CT scanner.

Figure 2.3 shows a simplified schematic of imaging operation. The pertinent output of a contemporary μ-CT scanner is a large number of *angular projections*; 2D transmission radiographs acquired sequentially as a sample rotates through 2π radians (π radians for synchrotron CT) [Gregory and Hinsinger, 1999]. Sampling theory indicates that for optimum image quality, the number of projections (n_{proj}) should be kept in the range $n_{proj} > (\frac{\pi}{2}) \times n_{det,x}$, where $n_{det,x}$ is the number of detector elements in the x direction. During the *reconstruction* process that

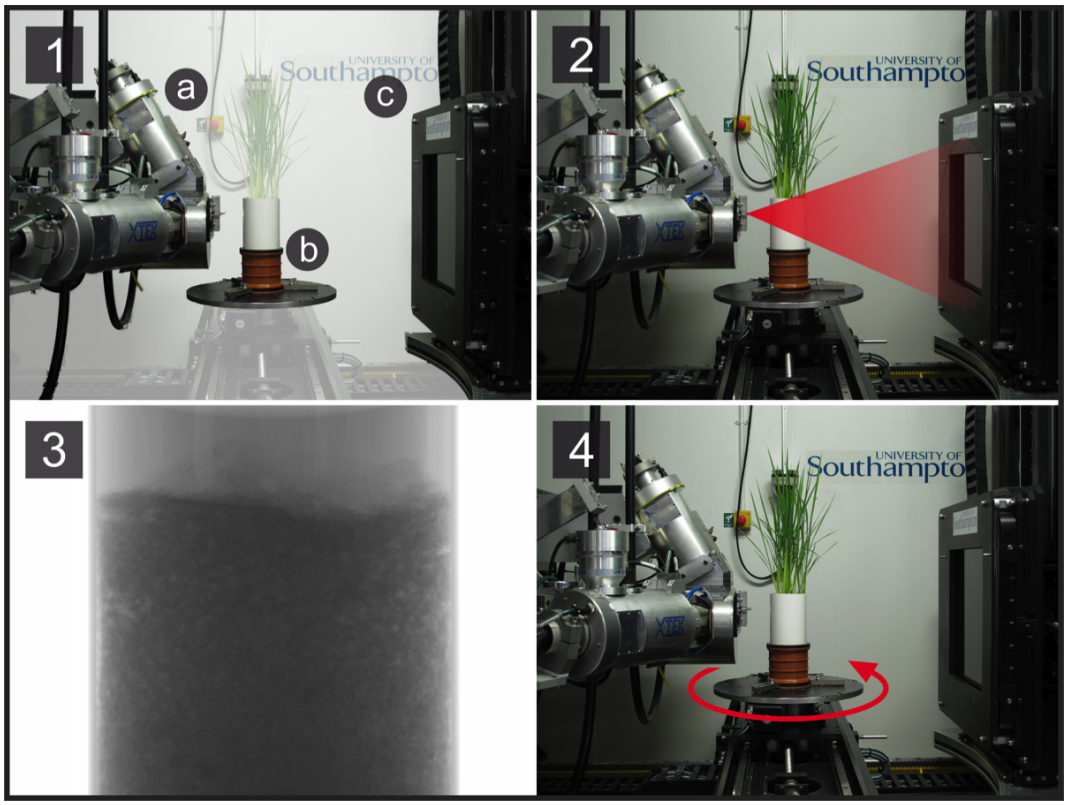

Figure 2.3: Schematic of μ-CT scanner operation. (1) The basic hardware elements of a bench-top scanner are a polychromatic X-ray source (a), a rotating sample stage (b) and a flat-panel or linear-array (CLDA) detector (c). (2) The source generates a cone beam of photons, which are attenuated as they pass through the object on the stage. (3) The detector acquires a 2D radiograph (projection) for this angular step. (4) The sample stage rotates by $\frac{2\pi}{n_{proj}}$ radians, ready for the next radiograph acquisition.

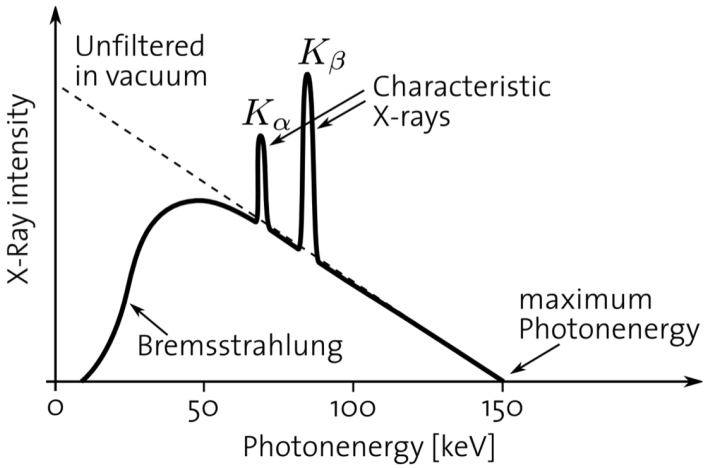

Figure 2.4: Representative X-ray emission energy spectrum. The photon beam comprises low energy *bremsstrahlung*, and higher energy 'K' peaks, the energy of which is characteristic of the target material.

follows image acquisition, a three-dimensional volume is generated from these projections, often using a numerical back-projection algorithm, which allows a three-dimensional matrix of attenuation coefficients to be generated by reconstructing x, y planar 'slices' for all positions along the z axis [Gregory and Hinsinger, 1999; Heeraman et al., 1997].

In the case of bench-top $\mu-\mathrm{CT}$ scanners, the X-ray photon beam is generated by bombarding a metal target with thermionically emitted electrons in a vacuum tube, producing photons with an initial energy spectrum that is a function of element voltage, target material and beam filtering [Heeraman et al., 1997]. The different components of this spectrum are the broad energy *bremsstrahlung*, emitted when an incident electron is diverted by a nucleus, along with characteristic high-energy peaks arising from photons re-emitted when electrons in target atoms are knocked to lower atomic-energy levels by incident electrons (see Figure 2.4). The transmitted intensity of the X-ray beam through the object can be approximated using Beer's Law:

$$I = I_o \exp\left(-\mu X\right), \tag{2.4}$$

Where I_o is the source intensity of the X-ray beam, μ is the linear attenuation coefficient (assuming here that the material is homogenous), and X is the distance travelled through the sample. μ is a function of material density (ρ) and mass attenuation coefficient (μ^*), a relationship given by:

$$\mu = \rho\mu^*, \tag{2.5}$$

The mass attenuation coefficient (μ^*) is itself a function of both the atomic number (Z) of the

material and the photon energy of the X-ray beam. The previous equations assume that the absorbing material is homogeneous in density and composition over the distance X. However, for heterogeneous materials the attenuation coefficient will vary along the beam path, requiring the initial equation for I to be rewritten as an integral with respect to the variable of integration along the beam (ξ):

$$I(X) = I_o \exp\left[-\int_0^x \mu(\xi) d\xi\right], \tag{2.6}$$

This equation can be rearranged to give:

$$\ln\left(I_o / I(X)\right) = \int_0^x \mu(\xi) d\xi, \tag{2.7}$$

[Heeraman et al., 1997]

CT characterisation of materials using such an X-ray source is achieved by computation of the linear attenuation coefficient (μ) of the beam between the source and detector [Lontoc-Roy et al., 2006]. μ is a measure of the proportion of incident X-rays which are absorbed or scattered within the material, which in the case of hard X-rays in the Compton domain is linearly related to material density [Heeraman et al., 1997; Lontoc-Roy et al., 2006; Perret et al., 2007]. In medical imaging, calculated values of μ are often normalised with respect to water and air by the following expression, which yields a *CT number* (CTN), expressed in dimensionless *Hounsfield* units:

$$CTN = \frac{(\mu_{subject} - \mu_{water})}{(\mu_{water} - \mu_{air})} \times k, \tag{2.8}$$

Where $\mu_{\text{air}} = 0$, and $k \approx 1000$ [Lontoc-Roy et al., 2006]. Unlike a synchrotron X-ray source which typically produces a coherent, monochromatic photon beam, the X-ray beam emitted by bombardment of a target by electrons is clearly polychromatic [Jenneson et al., 2003]. The varying attenuation of different-energy photons by the sample material leads to preferential absorption of those with lower energy, which due to varying path-lengths through the sample results in *beam hardening* artefacts in the output image [Gregory et al., 2003]. This is often visible in CT data in the form of a 'cupping' effect, where attenuation coefficient increases radially from the centre of the object outward (Figure 2.5). To mitigate against this phenomenon, the beam can be filtered to produce a quasi-monochromatic spectrum, characterised by a single, prominent peak at an energy which is particularly well suited to imaging of the sample in question [Jenneson et al., 2003]. In their study of plant roots, *Jenneson et al.* used a beam with peak energy of 22keV filtered using 2mm of aluminium (Al) and $50\mu\text{m}$ of palladium (Pd) [Jenneson et al., 2003], exploiting the preferential low-energy X-ray absorption of the Al, and element-specific *k-edge* filtering of high energies by the Pd. Most modern μ-CT systems typ-

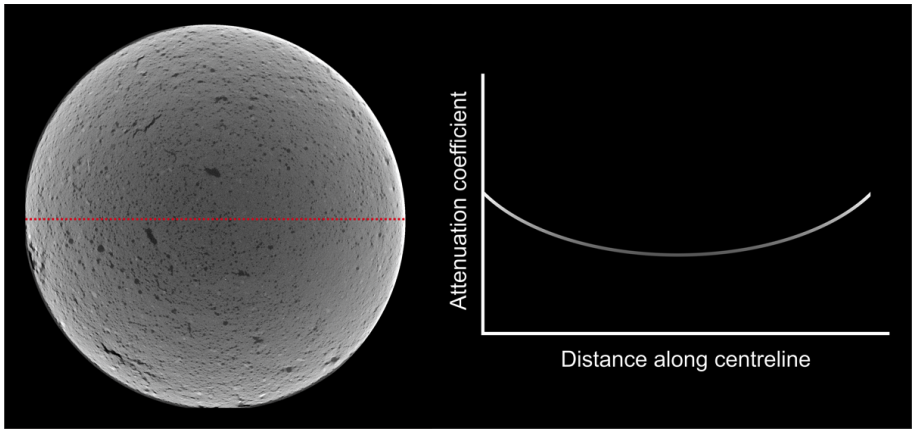

Figure 2.5: The beam hardening artifact presents in x, y slices as an increase in attenuation coefficient from the centre to the fringes of the image. The plot shows the influence of the effect. The presence of moderate to severe beam hardening makes successful segmentation of phases based on greylevel difficult, since the attenuation coefficient of materially identical regions will vary as a function of distance from the sample centre in addition to the expected influence of density and atomic number.

ically offer a range of target material for X-ray generation, which along with filters can help optimise beam characteristics for refinement of image quality [Gregory and Hinsinger, 1999].

Along with beam hardening, another detrimental effect regularly encountered in μ-CT images is ring artefacts (Figure 2.6). These present as concentric rings of spurious attenuation coefficient, and arise from fluctuation in the output of individual detector elements during a scan [Jenneson et al., 2003]. Ring artifacts can be mitigated against by introducing a linear translation of the stage between projections, thus using different detector elements to acquire each projection, but introducing a corresponding penalty in increased acquisition time [Gregory et al., 2003; Jenneson et al., 2003].

Despite the similar anatomy of most commercially available μ-CT units, different studies of roots and soil have used a distinct range of different parameters in their respective experiments. Table 2.1 shows a subset of widely-cited CT studies of plants and soils from the literature, along with imaging parameters and relevant details regarding sample preparation and data-processing. Tellingly, in a liminal space between artificial media and field soils, the majority have either used sand or soil with a high sand content, sieved to very fine aggregate sizes in the range $0.1 - 2\mathrm{mm}$.

2.1.3 Issues affecting characterisation of organic materials using μ-CT

Despite advances in the ability to visualise roots in three-dimensions using μ-CT, the resulting datasets nonetheless present the researcher with a three-dimensional geometric entity which

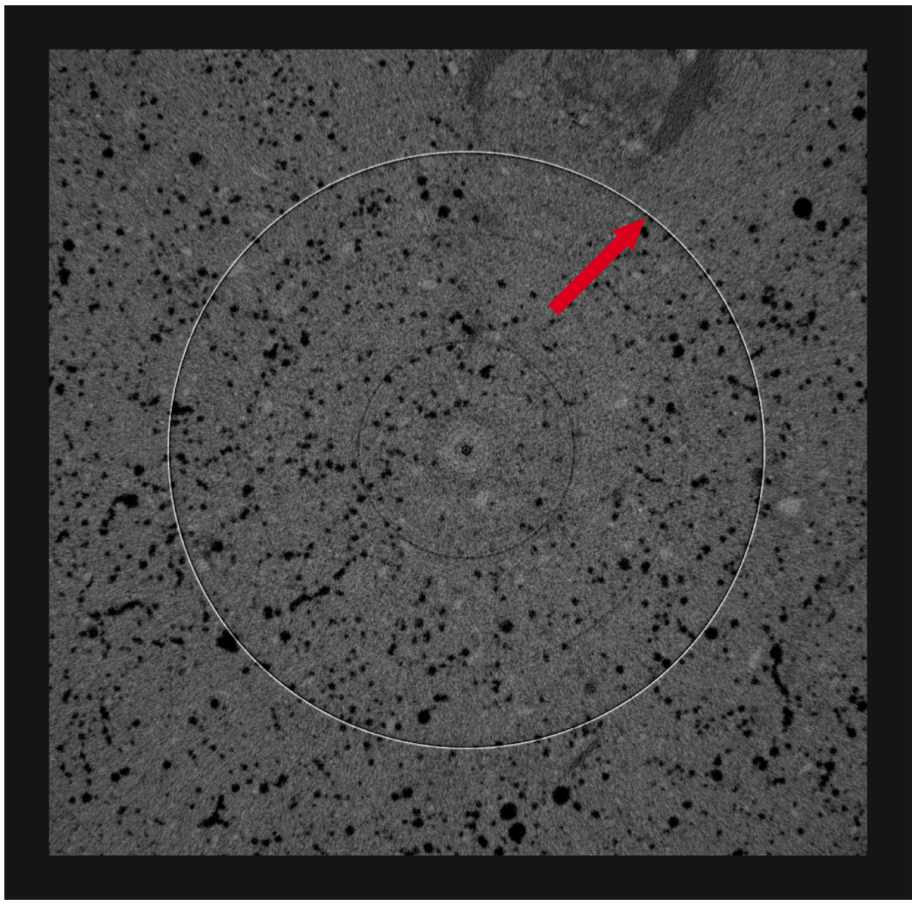

Figure 2.6: Ring hardening artifacts present as concentric rings of spuriously high or low attenuation coefficient relative to the range of values in the image. Frame-averaging and lateral shifts of the sample during scanning can mitigate against the artifact, but at the cost of increased acquisition times.

Table 2.1: Scan Parameters used in literature studies. Energies for polychromatic sources are measured as the mean value of the spectrum.

Reference	Year	Plant	Dia (mm)	Soil	P.S (mm)	kV	mA	S.D (mins)	x,y (μm)	Software
Heeraman et al.	1997	*Phaseolus vulgaris L*	50	Sand	$0.1 - 0.25$	420	3	30	160	VIS-5D
Pierret et al.	1999	*Aesculus hippocastanum*	200	Sandy clay	Resin	140	1.4	-	500	Rotate v1.13
Jenneson et al.	2003	*Triticum aestivum*	25	Sandy loam	< 0.25	50	0.5	30	100	IDL 5.2
Gregory et al.	2003	*Triticum aestivum*	25	Sandy loam	< 0.25	50	0.5	100	100	IDL 5.2
Lontoc-Roy et al.	2006	*Zea mays*	100	Sandy loam	< 2	130	100	12.5	120	MATLAB/Java
Kaestner et al.	2006	*Alnus incana*	37	Quartz sand	0.063-0.355	50	0.114	8.7	36	-
Hamza et al.	2007	*Lupinus augustifolius*	45	Sandy clay	-	-	-	-	500	-
Perret et al.	2007	*Cicer arietinum*	230	Sand	0.5	130	160	8	275	PV-WAVE
Han et al.	2008	*Solanum tuberosum*	≈ 200	Sand	< 2	120	150	-	350	MATLAB
Seignez et al.	2010	*Arabidopsis halleri*	10	Dredged sludge	-	130	-	-	10	Aphelion/ImageJ
Aravena et al.	2011	*Helianthus annus*	14	Clay loam	$0.5 - 0.8$	SYNC	-	-	4.4	AVIZO 6.0
Tracy et al.	2012	*Triticum aestivum*	29	Sandy loam	< 2	100	100	60	17.4	RootViz3D
Flavel et al.	2012	*Triticum aestivum*	3	Sand/Ferrosol	$0.5 - 1$	100	270	≈ 4	68	VGStudio MAX

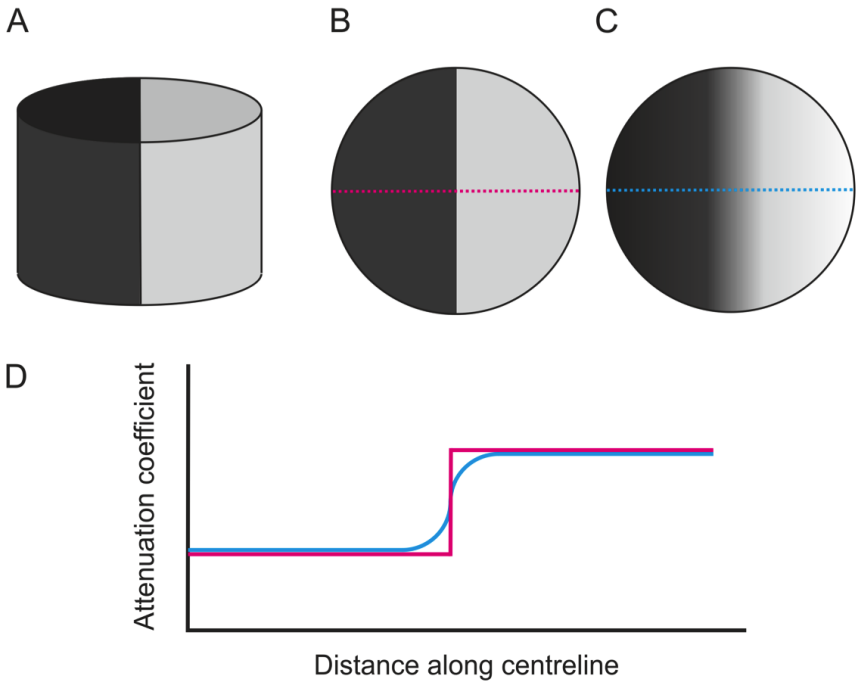

Figure 2.7: Schematic illustrating the partial volume effect. (A) A 3D object composed of two perfectly homogenous phases of different density is scanned using μ-CT. (B) In the ideal case, x, y slices through the reconstructed data would reveal two regions of discrete attenuation coefficient, with an abrupt inter-phase transition. (C) In reality, the transition between phases is blurred as a result of averaging effects. (D) Attenuation coefficient plotted along the dotted lines in frames (A-B).

can be challenging to quantify and interpret [Dunbabin et al., 2013; Lynch, 1995]. It must be remembered that features in data are of course only *representations* of real structure within the physical sample. Spurious image entities introduced by beam hardening, streaking around high-density phases, and ring artefacts all complicate the task of drawing accurate conclusions regarding physical characteristics [Lontoc-Roy et al., 2006]. Even in the virtual absence of such artifacts, the often similar attenuation coefficients of root, soil and fluid phases make the task of segmenting *regions of interest* (ROI) a particular problem in plant imaging [Heeraman et al., 1997; Lontoc-Roy et al., 2006]. The issue of poor contrast is particularly significant when attempting to differentiate between root material and surrounding soil, and likely results from one or both of two different phenomena [Lontoc-Roy et al., 2006]:

1. The similar attenuation coefficients of water and roots frequently results in poorly contrasted images when a disadvantageous combination of soil structure and hydration protocol have led to substantial water content in the soil matrix [Gregory et al., 2003]. In some soils, the water content can cause these issues even at normal field capacities [Heeraman et al., 1997].

2. At the boundaries between phases of different density, (typically soil and air), attenuation coefficients of voxels become averaged leading to values of attenuation coefficient which fall between the averages for the two adjacent phases [Gregory et al., 2003]. (See Figure 2.7). This so-called *partial volume effect* can lead to small air-filled pores within the soil structure being spuriously assigned similar attenuation coefficients to those of the root matter in the image, a problem which has generally been countered in studies by using coarse media of a single aggregate size [Gregory et al., 2003; Perret et al., 2007].

These two problems have led many researchers to avoid the use of real soils in μ-CT studies of plant root growth, despite such soils being ideal (and necessary) for representing more closely the field environment [Gregory et al., 2003].

A further drawback with the use of μ-CT in plant sciences lies in the tradeoff between field of view (FOV) and image resolution. Though it is desirable to investigate larger and more mature plants, increasing the sample size carries associated issues regarding resolution and beam hardening [Aylmore, 1993]. Though increasing the beam energy reduces image contrast, larger samples necessitate such an increase, improving X-ray penetration in order to avoid detrimental beam hardening artefacts [Heeraman et al., 1997; Lontoc-Roy et al., 2006].

Certain upper limits to sample size arise naturally due to the detector size and both the volume and mass-handling capabilities of the manipulator stage, but increasing the sample size also necessitates a change in magnification in order to situate the sample in the detector FOV [Gregory et al., 2009]. Because the x, y size of the detector array is subject to practical limitations, bringing more of the sample into the FOV reduces the spatial resolution [Gregory et al., 2009]. Since some root features (such as root hairs) are known to be in the same order of magnitude as the current resolution limit of most μ-CT scanners, the decrease in resolution resulting from an increase in sample size clearly entails challenges in segmenting such features from resulting images [Gregory et al., 2009].

One of the major aims of this thesis is to extend the use of μ-CT imaging techniques to scales outside the current range of sample sizes, plant species and soil conditions most commonly used in the well-cited studies from the literature. Given the challenges of acquiring data of plants in real soil at the root-hair scale and the mature root-system scale, particular attention to optimisation of imaging parameters is an imperative.

2.2 Development of a user-invariant approach to quantification of soil porosity using μ-CT

2.2.1 Introduction

Soil is the growth medium of all agriculturally relevant plants, with key soil characteristics known to correlate strongly with plant growth performance [Dexter, 2004; Lipiec et al., 2006]. Soils are commonly described with respect to two domains; a textural domain, characterizing the intra-aggregate region, and in the case of well-aggregated soils, the structural domain that exists between constituent aggregates [Dexter, 2004]. Whereas the textural domain is thought to be little affected by soil management processes, the structural domain, comprising micro-cracks, cracks, bio-pores and tillage-induced macrostructures is reported to be sensitive to external factors such as tillage and irrigation [Dexter, 2004]. The equivalent pore radius marking the crossover between domains has been quantified between ≈ 2 to $10\mu\mathrm{m}$ [Kutilek and Nielsen, 2006; Lipiec et al., 2006], with the structural domain often further taxonomically divided between storage pores of 1 to $100\mu\mathrm{m}$ and transmission pores of 200 to $400\mu\mathrm{m}$ [Greenland and Pereira, 1977]. Transmission pores are seen to be particularly significant for the penetration of feeding roots [Pagliai and De Nobili, 1993]. Furthermore, a study of various clay sub-soils has shown distribution of wheat roots to be spatially associated with soil macro-pore networks [Pierret et al., 1999; Stewart et al., 1999], potentially due to roots bypassing regions of high mechanical impedance [Lipiec et al., 2006]. With regards to plant development, a thorough classification of soil porosity in both domains is seen to be important for understanding and modeling phosphate transport [Darrah et al., 2006]. Recent work in this field has moved towards increasingly realistic soil models by seeking to describe both structural and textural domains. This allows models to be built incorporating a dual porosity regime which draws a distinction between mobile and immobile soil water fractions [Kodesôova et al., 2009; Zygalakis et al., 2011]. A robust, quantifiable understanding of soil porosity characteristics is thus key to furthering quantitative bio-physical understanding of many significant and dependent processes [Grevers et al., 1989].

The heterogeneity of soils, and the difficulty of linking structural characteristics to soil-specific processes has hindered progress in accurately and reproducibly defining soil structural parameters [Young et al., 2001]. Characterisation has predominantly been built upon a framework which describes soils in terms of well-defined aggregates separated by pores, combining to form aggregate packings on a higher-magnitude length scale [Kaestner et al., 2008; Young et al., 2001]. This model has been used as a basis for the approximation of diffusion-reaction processes, though it fails in the case where macro-pores and aggregates cannot be clearly differentiated [Young et al., 2001]. Various approaches have been applied to the classification of dif-

ferent aspects of soil structure, including, but not limited to; representative aggregate models generated using *Boolean random sets* [Glasbey et al., 1991], prediction of soil-moisture retention characteristics using *neural networks* and *pedo-transfer functions* [Koekkoek and Booltink, 1999], *bounded fractal approximations* [Crawford et al., 1997], simplification of aggregates to representative bodies [Rappoldt, 1990], and use of a *disector* for estimation of *Euler-Poincaré* characteristic [Vogel and Kretzschmar, 1996]. Though such approaches have yielded valuable results, the relative lack of interaction between experimentalists and modelers across disciplines has diminished the applicability of results [Young et al., 2001]. Progress has also been hindered due to the complexity and high micro-scale heterogeneity of real soils as well as the lack of techniques to suitably confront such complexity [Lombi and Susini, 2009].

Despite the existence of a considerable and growing body of research, literature on the use of μ-CT in soil-structure characterisation reveals a paucity of robust, well-tested methods, addressing issues such as operator influence and stability to repeat measurement. This has been highlighted by a recent round-robin study by *Baveye et al.*, in which three test images of soils were thresholded by 13 experts worldwide and comparison made between structural measurements based on their individual approaches. Findings showed that for a two-dimensional μ-CT image, porosity estimates made by the experts varied from $12.92 - 72.71\%$, with a standard deviation of 14.36%. The study concluded that such variation was in large part due to user bias and the the very different approaches used by the individuals involved [Baveye et al., 2010]. The absence of a standardized, methodological framework for acquisition and processing of images for soil quantification can thus be seen as a pressing problem for the community, impeding satisfactory exploitation of the potential of μ-CT imaging [Thompson et al., 1992]. Moreover, there has been very little development in assessing how imaging and reconstruction settings can be optimised to improve image quality [Houston et al., 2013].

This chapter illustrates how an established and computationally efficient image processing approach, seeded region growth (SRG), can be applied in an automated and systematic manner to the determination of basic structural parameters in samples of real soils. A protocol is laid out for segmentation of connected macro-pore regions from $\mu-\mathrm{CT}$ data from five highly-aggregated soil samples, obtained under reasonably standard laboratory conditions (varying X-ray target and filtration conditions). The macro-porous volume-fractions elucidated by the approach are compared with results derived from traditional global-thresholding of image data as well as a direct gravimetric approach.

2.3 Materials and methods

2.3.1 Soil selection and preparation

Five soils were selected for porosity investigation using μ-CT and a gravimetric method. Three were procured from fields involved in phosphate trials at an agricultural site in Suffolk, UK. Of these, two (both Calcic Vertisols of the Newmarket series, hereafter referred to as Soils 1 and 2), were sampled from different positions in a single field, whilst the third (a Calcic Vertisol of the Hanslope series, Soil 3), was sourced from another location at the same site (FAO, 1990). A Chromi-Abruptic Luvisol of the Dunnington Heath series (hereafter referred to as Soil 4) was sourced from a University of Nottingham field site at Sutton Bonington, UK ($52°49'52'', -1°15'13''$), and a Eutric Cambisol of the Denbigh series (hereafter referred to as Soil 5) was sourced from a field site at the University of Bangor, Gwynedd, UK ($53°13'54'', 4°0'54''$).

Though it is desirable to quantify samples which closely represent field conditions, in view of the requirement to calibrate results against gravimetric data, soils were prepared in a manner which allowed fine control of hydration and structure. Benchmarking the image-based quantification of porosity against a gravimetric method necessitated a number of repeats, for which sample preparation had to be as closely controlled as possible. Larger mineral phases were removed from all samples using a soil sieve with a $4\mathrm{mm}$ aperture mesh, after which all material was desiccated in an oven for $48\mathrm{h}$ at $74°\mathrm{C}$. Following desiccation, soils were passed through a $1.8\mathrm{mm}$ mesh, with the resultant material sieved a second time at $1.18\mathrm{mm}$. Material passing through the second mesh was discarded, such that the approximate diameter of aggregates was from $1.18 - 1.8\mathrm{mm}$. Sample material was stored in airtight containers to prevent moisture uptake.

Sample containment

To facilitate efficient imaging, soils were contained within separated, interlocking polymer tubes assembled into a stack to simplify batch acquisition. Tubes were manufactured from circular-section, extruded acrylic with an internal diameter of $19\mathrm{mm}$ and wall thickness of 3mm. A line corresponding to a fill volume of $9\mathrm{cm}^3$ was marked on each sample holder using the meniscus of a $9.00\mathrm{g}$ mass of de-aired water hand-pipetted into each sample holder as a reference.

Sample preparation

Desiccated soils were introduced to sample tubes up to the $9\mathrm{cm}^3$ demarcation line. Samples were immediately weighed to determine the soil bulk density. Due to the difficulty of accurately applying a repeatable compaction process to all samples, no such treatment was implemented. Samples were prepared immediately before imaging to minimise settling before

image acquisition.

2.3.2 μ-CT Imaging

All CT data for this study was generated using a bespoke Nikon/Metris hutch μ-CT scanner at the $\mu - \mathrm{VIS}$ X-ray imaging centre, University of Southampton, UK. Images were acquired with a Perkin Elmer 1621, 2096×2096 element flat-panel detector (Perkin Elmer Inc., Cambridge, UK) with a cesium iodide (CsI) scintillator, with a total of 2101 projections generated for each sample. Two datasets were acquired per sample, using tungsten (W) and molybdenum (Mo) reflection X-ray targets at a $60\mathrm{kV}$ accelerating potential. Further data were acquired for the Soil 4 and Soil 5 samples using a W target at $40\mathrm{kV}$ with a $0.1\mathrm{mm}$ tin (Sn) filter, selected to produce a narrower X-ray spectrum via k-edge filtration (Figure 2.8). The accelerating potential was constrained to $40\mathrm{kV}$ by the requirement to overlap the dominant energy peak of the target with the k-edge of the filter material, (further details regarding k-edge filtering can be found in [Crotty et al., 2007]). Mean energy, simulated using the SpekCalc utility [Poludniowski et al., 2009], was $\approx 23\mathrm{keV}$ for the unfiltered case, and $\approx 24\mathrm{keV}$ for the filtered case (including $0.5\mathrm{mm}$ beryllium (Be) exit window in all cases). As a consequence of reduced flux, projection exposure times were increased from $1\mathrm{s}$ to $4\mathrm{s}$ for the filtered beam condition, necessitating an increase in total scan time from 35 to 140 minutes.

Volumes were reconstructed from raw projection data using a standard filtered Feldkamp back-projection algorithm implemented in Nikon Metrology CT Pro 3D, producing $32\mathrm{bit}$ datasets for analysis [Feldkamp et al., 1984]. Isotropic voxel resolution of all reconstructed data was $21.6\mu\mathrm{m}$. A comprehensive overview of acquisition, reconstruction, and image quality parameters is available on page 49 of Section 2.1, and in the relevant literature and standards [ASTM, 2008; Ketcham and Carlson, 2001].

2.3.3 Gravimetric pore-volume estimation

Post-imaging, the porosity of samples was estimated directly using a reversal of a standard, simple gravimetric approach for estimation of water content in soil cores [Dane, 2002]. Deionised water was hand-pipetted to the $9\mathrm{cm}^3$ demarcation on each tube, and samples were weighed to determine the mass of water at saturation. Samples were sealed to prevent evaporation and left for $12\mathrm{h}$ for any further absorption to occur. After this time, menisci remained constant on all samples, and no additional water was introduced. Four repeat measurements were made for each soil type.

2.3.4 Feature extraction from reconstructed data

Reconstructed data were down-sampled to $16-\mathrm{bit}$ format, and grey-levels normalized (linear

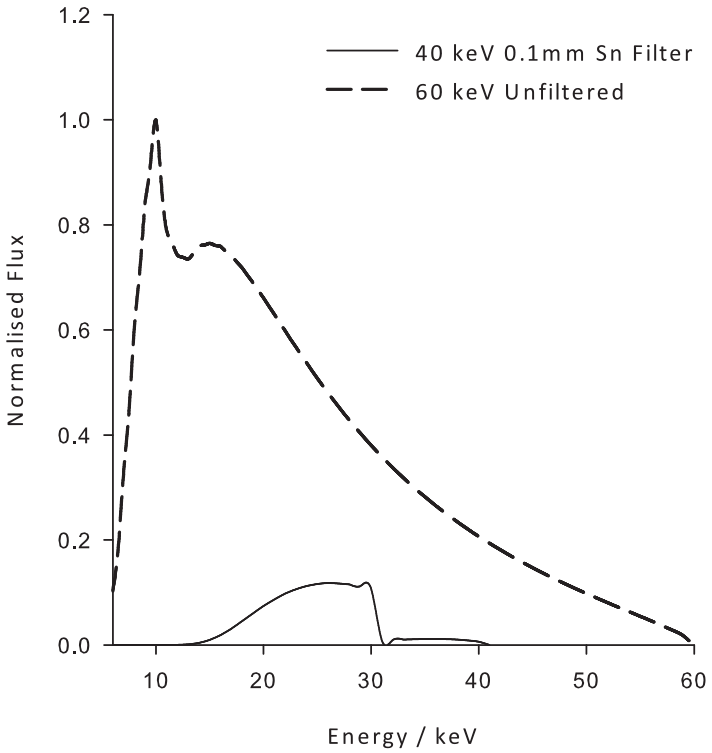

Figure 2.8: Comparison of an unfiltered X-Ray beam from the hutch μCT scanner, generated with a W target, with a quasi-monochromatic beam from the same target, produced through k-edge filtering using $0.1\mathrm{mm}$ of Sn.

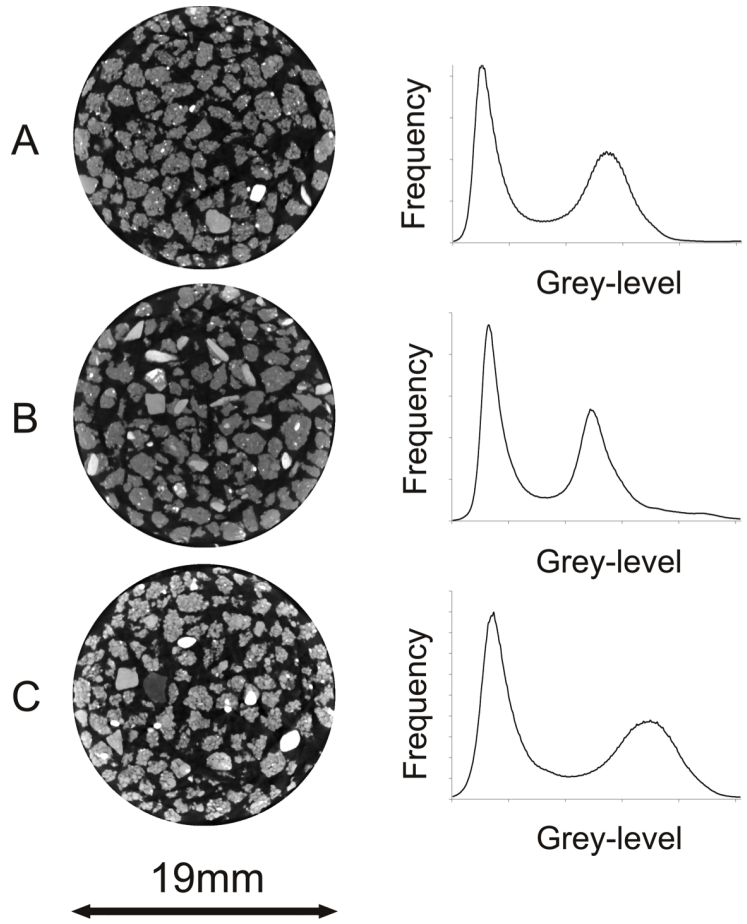

Figure 2.9: Example slices from data-sets, and grey-level histograms (with regard to entire volumes) of A) Soil 1, B) Soil 5, C) Soil 4, obtained using FIJI, demonstrating the bimodal distribution in grey-levels.

re-scaling for equivalent attenuation of surrounding air and the acrylic polymer of the sample tube; -1000HU and 118.2HU respectively [Prionas et al., 2010]) for convenience of visualization and comparison. Down-sampling from 32 to 16bit produced images with 65536 discrete grey-levels; providing a level of accuracy more than appropriate to the application, particularly considering that 8bit images (with 256 discrete levels) are the norm [Baveye et al., 2010]. All procedures were implemented using the *FIJI* open-source, image processing package [Schindelin et al., 2012].

9cm^3 cylindrical regions of interest were extracted from the datasets, with noise reduction being carried out via a 3×3 pixel median filter applied to each slice. The influence of seed point selection and threshold tolerance for seeded region growth (SRG) segmentation of contiguous macro-pore space was then determined via a new hybrid protocol. Seed points for region growth segmentation (five in the first instance) were automatically selected from the central slice of each dataset according to the following procedure. Since the datasets all returned a

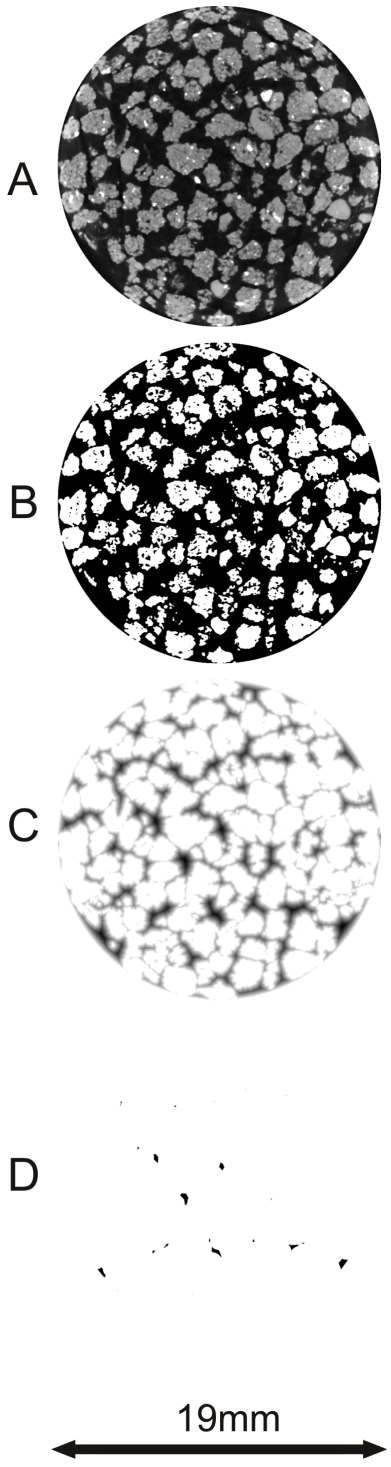

Figure 2.10: Seed selection routine for seeded region-growth method A) original image, B) data-set binarised with a minimum-error filter, C) distance map generated for porous domain and D) seed selection voxel set.

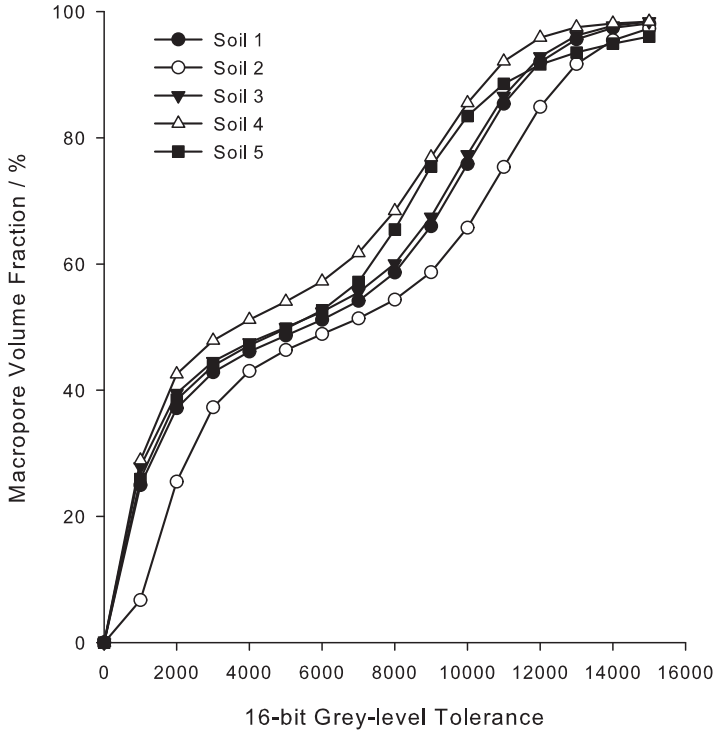

Figure 2.11: Plots of connected porosity against tolerance value for each soil, calculated by seeded region-growth. Values are the means of porosities derived from five randomly selected seed points.

clearly bimodal histogram (Figure 2.9), a minimum error filter [Kittler and Illingworth, 1986] was used to generate an approximate threshold between the air and soil aggregates for the entire volume. This output was then used to produce a binarised dataset of the porous domain, from which a distance transform was computed, such that lower intensity voxels in the resulting volume were indicative of a greater distance from the initially estimated soil aggregate boundaries. A global threshold was applied to the distance map, excluding all voxels with distances less than 80% of the maximum value in each image (Figure 2.10). For each dataset, five seed points were then randomly selected from this set for input into a 26-neighbour, static SRG algorithm, implemented in the C# programming language. The algorithm was run twice from each seed point; once taking into account the entire volume, and once constrained to the middle 200 slices of each dataset, as defined along the z axis. The influence of tolerance parameter on connected-volume output was then determined by varying the tolerance value in steps across the entire grey scale range. The mean input/output characteristics thus determined for the five soils are shown in Figure 2.11.

2.3.5 Beam hardening estimation

Due to the heterogeneity of attenuation coefficients within soils, grey-level variations in the homogenous polymer wall of each tube were used to indicate the magnitude of the beam-hardening artifact. Within the z-axis mid-slice of each dataset, vectors were defined radially from the tube centre-line at $0°$, $45°$ and $90°$ to the y-axis, being constrained to the plane of the slice, normal to the z-axis. For the vector segments pertaining to the tube walls, voxel intensity values were plotted with respect to distance from the tube midpoint. The gradient of a line fitted through these points provided an approximate measure as to the degree of beam hardening.

2.3.6 Sensitivity of SRG to seed location

A typical large macro-pore with a quasi-circular cross-section was selected from within the middle slice of the Soil 3 dataset, for which a further seed set was generated. A line was manually specified across this pore, the start and end points of which were situated within the visually determined partial volume between the voxels of the pore and those of the neighbouring aggregates (Figure 2.12). 10 evenly spaced points along this vector were selected as seed points for SRG, using a tolerance step magnitude of 1000 over the entire grey-level range.

2.3.7 Histogram thresholding

In addition to segmentation using the SRG method, data were generated for comparison using two histogram thresholding methods; Otsu's method [Otsu, 1979] and the minimum-error filter [Kittler and Illingworth, 1986].

2.4 Results and Discussion

2.4.1 Image processing rationale

Though SRG is a well-defined method in the literature of a number of fields, this work demonstrates how such standard techniques may be combined into a hybrid approach which reduces the degree of user bias inherent in present image-based soil quantification routines. Discussion of this protocol will be followed by a discussion of the image-quality parameters relevant to success of thresholding methods, and the effectiveness of various strategies in improving image quality at the data-acquisition stage.

2.4.2 SRG detected volumes

For samples of Soils 1-5, plots of connected porosity volume with respect to tolerance values produced an S-shaped curve with a stable linear region surrounding the inflection point. For

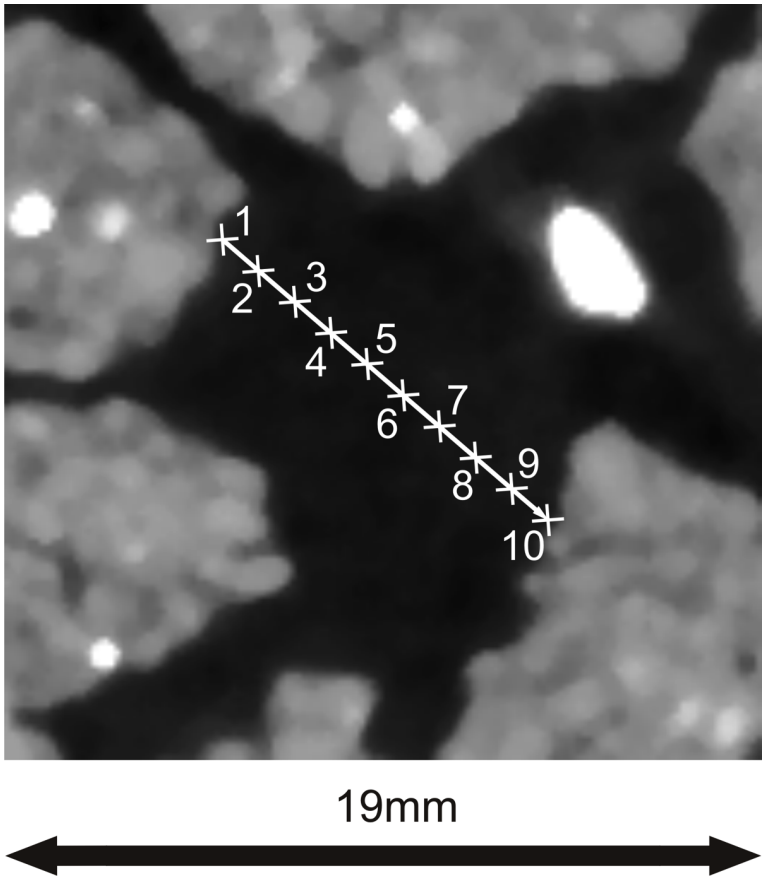

Figure 2.12: Typical pore space sampled for influence of seeded region-growth seed point location. Seeds were evenly distributed along the vector between 1 and 10. SRG data are found in Figure 2.14.

all samples, output curves generated using both entire datasets and 200-slice sub-volumes correlated with no observable deviation, suggesting that the mid-sample sub-volumes are representative inputs from which meaningful inferences can be made regarding the larger volumes.

Existing SRG approaches typically require the user to manually specify either seed point (or points), a homogeneity criterion (usually as a function of a threshold value), or both. According to the findings of *Baveye et al.* regarding user bias, development of a more robust, stable and unsupervised approach necessitates automated, intervention-free methods for selection of these input parameters [Baveye et al., 2010]. Though the homogeneity criterion has often been tuned using trial and error [Adams and Bischof, 1994], a common approach to automating its selection is to develop some parameter (W) which is a function of image properties (i.e. standard deviation, contrast-to-noise ratio) derived from the entire volume and/or a sample seed-region [del Fresno et al., 2009; Sivewright and Elliott, 1994]. In this paper, the homogeneity criterion was based on tolerance value alone, and the characteristic S-shaped curve obtained by plotting connected volume for a range of tolerances, as produced by the SRG algorithm, provided the basis for final tolerance value selection (Figure 2.11. The S-shape of the tolerance/volume characteristic for these soils is largely due to the partial volume effect between the quasi-homogenous soil and air regions, which introduces non-linearity in the tolerance/volume relationship. A tolerance value coinciding with the inflection point correlates with a condition where the boundary of the connected region lies within the partial volume between the two dominant material phases. The existence of identifiable inflection points thus provides a route to estimation of a user independent tolerance value from the SRG data.

Positions of inflection points were determined using a finite-difference method to approximate the 2nd derivative of each output curve. In each case, linear interpolation between tolerance values either side of the sign change was used to more accurately approximate the tolerance at the inflection point. In this manner, user-independent tolerance values were derived for the 5 randomly selected seed points drawn from the set generated by the distance mapping procedure. For all datasets, these values were then used to generate final SRG output data from which macroporous volume fractions were derived. (Figure 2.13).

2.4.3 Sensitivity of SRG algorithm to seed location

Whilst automated selection of SRG seed points via the distance transform is effectively designed to reduce the probability of unrepresentative seed point grey-values due to local artifacts (such as beam hardening streaks, edge streaks and partial volumes), the potential influence of such artifacts has been tested on a small sub-region of a dataset. SRG data were generated according to the previously outlined method using seed points that were linearly

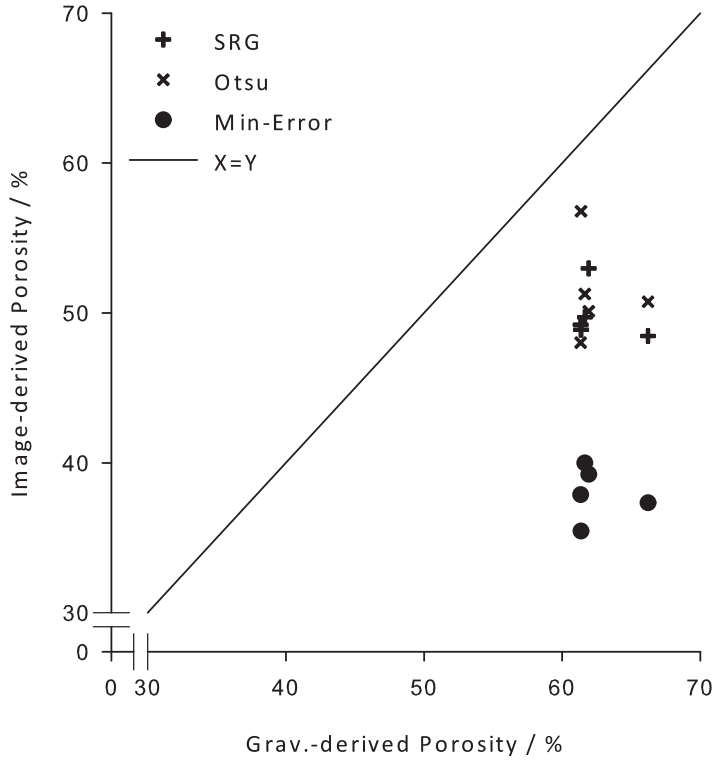

Figure 2.13: Macro-pore volume fractions (%) as estimated by seeded region-growth, gravimetrically, Otsu's filter [Otsu, 1979] and minimum-error filter [Kittler and Illingworth, 1986].

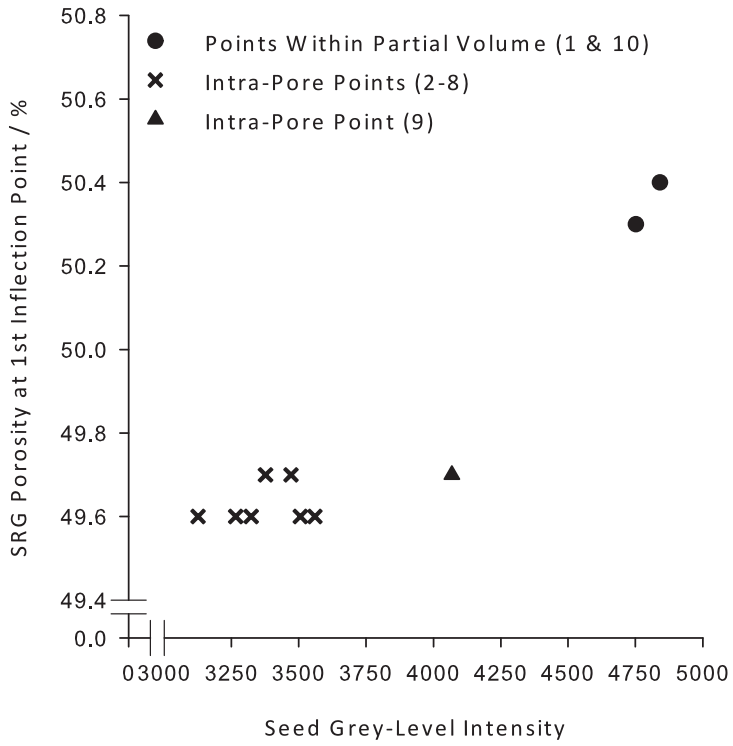

Figure 2.14: Seeded region-growth connected porosity (%) plotted against seed grey-level intensity for each of 10 seed points along the vector shown in Figure 2.12.

distributed across a single pore (Figure 2.12). Comparison of detected volumes allowed the sensitivity of the algorithm to changes in seed position and grey-level intensity to be determined, since low variability of volume output despite differing seed position and/or grey-level intensity correlates with stability. Figure 2.14 shows that output volumes correlated well for intra-pore points, despite the range in grey-level intensity values of the seed voxels (indicated on the x axis). Outlying grey-level intensities, and visual inspection of seed position demonstrated that vector end-points 1 and 10 lie within the partial volume region between aggregate and pore domains, accounting for the slightly elevated estimation of macro-pore volume when compared to the other points ($\approx 1.4\%$). Though point 9 also displayed an elevated grey-level value compared to the range of the other intra-pore points, there was no consequent increase in SRG output volume calculated using the inflection-point tolerance. The elevated grey-level intensity of this point as compared to other intra-pore seeds suggests particular influence of artifact effects (i.e. streaks, noise) in the seed locality, however such effects appear not to have impacted the stability of the method. Nonetheless, seed points this close to the aggregate boundaries would be rejected anyhow during the distance transform pre-processing stage of the overall SRG workflow, reducing the potential for error.

2.4.4 Gravimetric and global thresholding results

The gravimetric method yielded four results for each soil type, and total water mass at saturation was used to estimate porosities, which were 61.6%, 61.4%, 61.4%, 61.9% and 66.2%respectively for Soils 1, 2, 3, 4 and 5. The macro-pore volumes estimated using the SRG approach for each sample were compared with these results, as well as those derived from the histogram-thresholding methods (Figure 2.13). Good correlation between SRG derived macro-pore regions and the reconstructed image data was visually established for all datasets (Figure 2.15).

For all soil samples, macro-pore volume estimations derived from approaches in the image-processing domain were smaller than those estimated using the gravimetric method, demonstrated by their position below the $x = y$ line in Figure 2.13. Dilating the boundaries of the SRG determined macropore region of the Soil 5 dataset by 2 voxels to simulate a region with a volume fraction lying on the $x = y$ line results in a clearly visible overestimation of the macro-pore domain, as compared to the result derived using the inflection-point tolerance value (Figure 2.16). This strongly suggests that the increase in porosity estimated using the gravimetric method is not due to underestimation of macro-pore boundaries. This supports the hypothesis that the SRG method provides a more accurate classification of the macropore space than gravimetry, with the difference in porosity determined by the two methods being accounted for by the intra-aggregate textural porosity. Since $\mu-\mathrm{CT}$ only allows inference to be made regarding structures at a scale of at least the voxel resolution, it is likely that the difference in porosity estimate between image-based and gravimetric methods is due to textural porosity of a length scale too small to be detectable at the imaging resolution [Horgan, 1998]. Furthermore, due to its intrinsic connectivity constraint, the SRG approach does not account for any pores which are connected to the macro-pore domain by micro-pore networks of undetectably small size.

The varying volume fractions estimated using the histogram thresholding approaches can be accounted for by the feature-independence of the methods used [Adams and Bischof, 1994]. In both cases, threshold is determined using the grey-level distribution alone. Thus, where contrast allows, intra-aggregate porosity may be classified, but equally, there may be underestimation of the macro-pore region. This latter effect was visually verifiable in the case of the minimum-error filter.

2.4.5 Influence of imaging parameters on image quality

All artifacts, though different in their identifying characteristics, introduce local error into the direct proportionality between voxel intensity and material attenuation coefficient. Seed-based

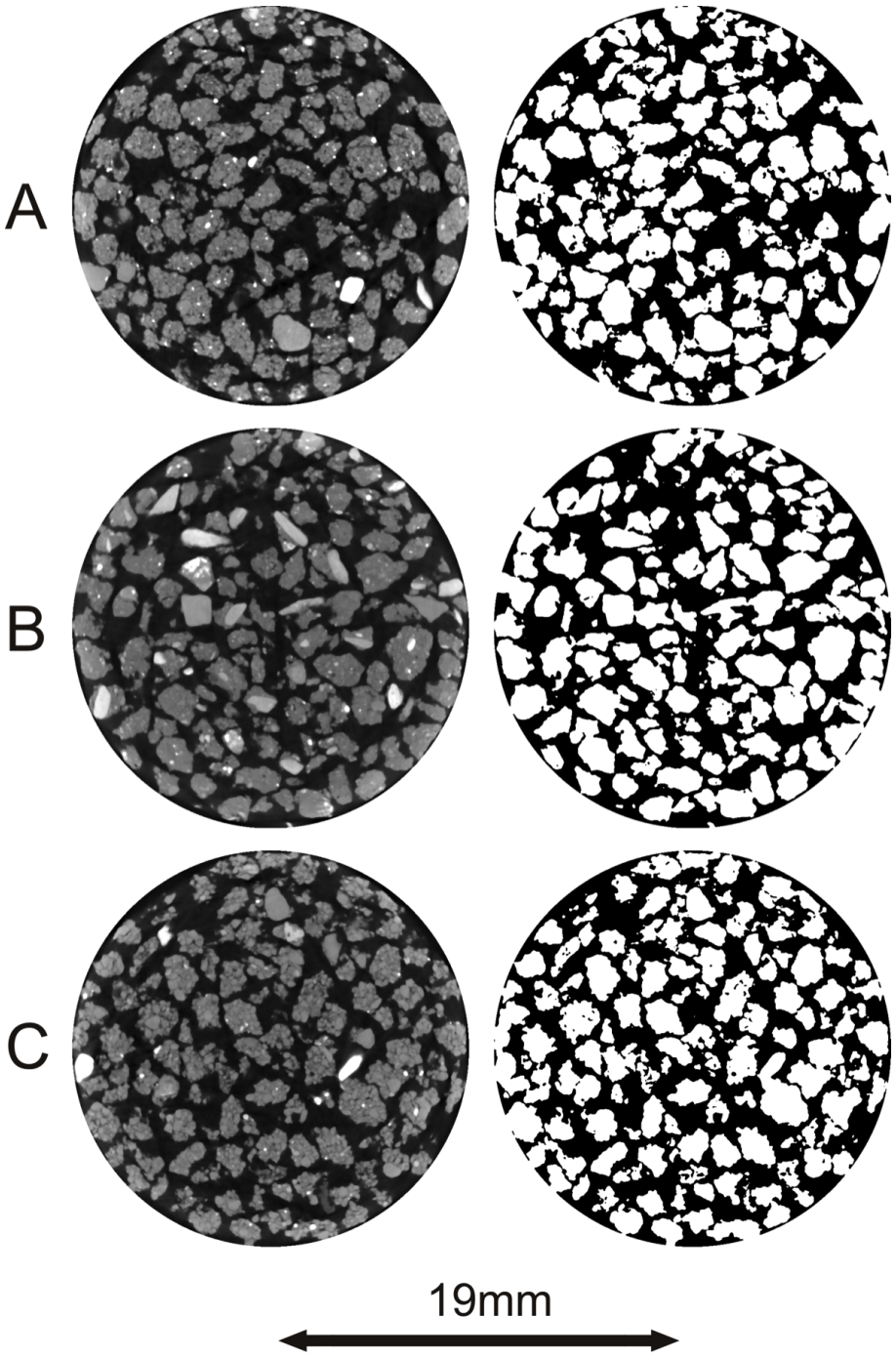

Figure 2.15: Comparison of original data with the binary representation of connected volume produced by the automated method for A) Soil 1, B) Soil 5 and C) Soil 4 samples.

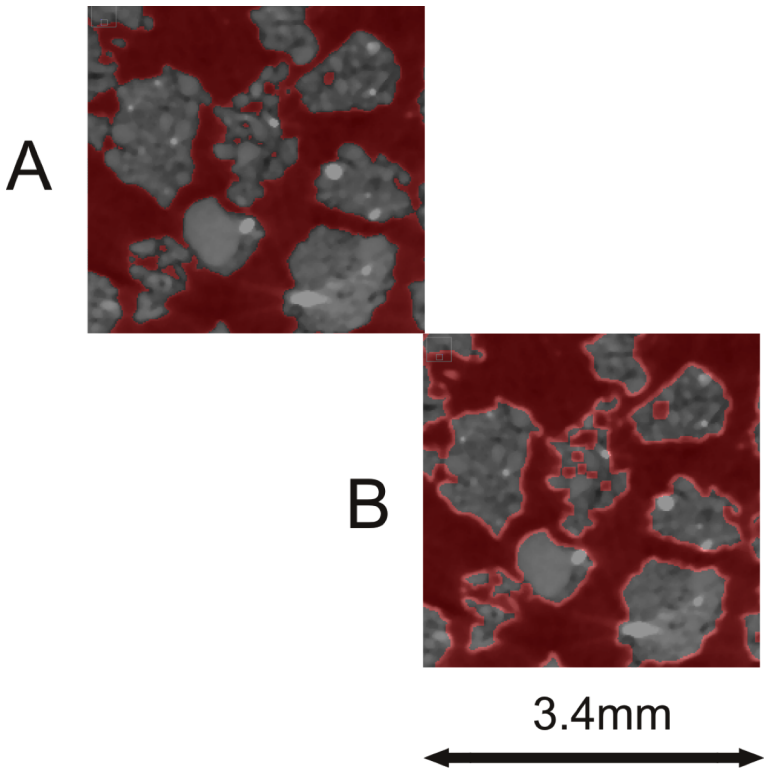

Figure 2.16: Reconstructed Soil 5 data showing an overlay of A) seeded region-growth region at estimated tolerance, B) the same region dilated to lie on the $x = y$ line in Figure 2.12, demonstrating resultant over-estimation of macro-pore region. This suggests that undetectably small pores are responsible for the difference in porosity derived by the image-based and gravimetric methods.

methods are known to be particularly sensitive to noise, since a single atypical voxel chosen as a seed point will potentially skew the entire region classification [Adams and Bischof, 1994]. In view of such sensitivities, the effectiveness of different artifact reduction strategies in the imaging domain was investigated.

2.4.6 Target and filter materials

Voxels pertaining to the polymer tube wall were used to provide an estimate of the degree of beam hardening present in each image. Though beam-hardening effects can be localized, the global *cupping* artifact arises as a result of the preferential absorption of lower energy photons in sample objects when using a polychromatic X-ray source. Plotting the variation in greyscale intensities along a radially aligned vector through a polymer region (with homogenous attenuation coefficient) allowed the effects of filtering on the severity of this artifact to be compared. Filtering the X-ray beam with $0.1\mathrm{mm}$ of Sn provided a substantial reduction in the magnitude of the beam-hardening artifact in all 3 samples; consistent with the quasi-monochromatic conditions achieved by k-edge filtering (2.2).

Table 2.2: Normalized beam-hardening for individual samples, as demonstrated by normalized greyscale gradients across the thickness of the polymeric (acrylic) wall of the sample container. Grey scale gradients are shown for scans with the W target, with and without a $0.1\mathrm{mm}$ Sn filter

Soil ID	Unfiltered	With $0.1\mathrm{mm}$ Sn	Reduction using filter (%)
Soil 5	0.085	0.0467	45.1
Soil 4	0.018	0.002	88.9

Matching the emission spectrum of the target to the X-ray absorption characteristics of a suitable filter can produce a beam with much narrower energy peak than in the unfiltered condition (Figure 2.8), however substantial reductions in available photon flux occur, requiring greatly increased scan times and/or increased X-ray source power, with a consequent reduction in spatial resolution due to increased spot size. The benefit of reducing beam hardening through filtration is thus dependent on the sensitivity of the SRG method to local changes in voxel intensity within the macro-pore space. The comparison of returned volumes from seed points along a single pore showed that the method is resilient to small changes in seed intensity, suggesting that the more than fourfold increase in imaging time when using the filter is an inefficient use of resources in this instance. In other imaging scenarios, particularly those where grey-levels are calibrated against a phantom and used to measure density, such an approach to reduce beam hardening would potentially be justifiable.

2.4.7 Influence of X-ray target material

In the case of simple thresholding strategies, accurate differentiation of phases within data requires the existence of sufficient contrast so that grey-level distributions of such regions do not substantially overlap. Classification of phases within soils using X-ray CT data is often associated with difficulties in obtaining adequate contrast between air, water and solid regions [Kaestner et al., 2008]. Whilst the accelerating potential (keV) provides a primary means of controlling the X-ray spectrum, and hence the effective image contrast, the chosen target material will vary the characteristics of the spectrum obtained. Calculation of key image quality parameters allowed the influence of these differences to be quantified. Calculation of signal to noise and contrast to noise ratios (SNR, CNR respectively) showed that there is also a modest improvement in noise performance obtained via use of a W target instead of Mo for an equal scan duration. Use of the W target improved the mean SNR across the samples from 13.4 to 14.8, and the CNR from 12.9 to 15.0, as compared to the Mo target.

2.5 Conclusions

A seeded region growth (SRG) algorithm has been used to provide the basis for a robust, automatable approach to the segmentation of interconnected macro-porous domain from μ-CT images of well-aggregated soils. Identification and quantification of artifacts and image quality parameters has demonstrated that image quality (in terms of beam hardening and noise characteristics) can be improved through well-informed use of filters and X-ray target materials, although influence on segmented macro-pore space was found to be small in the present work. The SRG algorithm, using a range of tolerances to explore the dynamic range of the dataset, was found to produce characteristic S-shaped curves of tolerance value against returned volume. A finite-difference approximation of characteristic curves allows determination of turning points, and thus tolerance value, which represent a repeatedly determinable characteristic. It was possible to automatically select seed points for the SRG algorithm in a robust manner using distance maps generated from regions segmented via an initial histogram-derived threshold. This method was found to be stable to changes in seed location, and variation in grey-level intensity of the order found within the macro-pore domain of the datasets. The difference in porosity determined using SRG and the gravimetric method is directly attributable to the textural porosity volume fraction of the intra-aggregate domain. SRG is thus seen to be a useful approach for segmenting out macropore space in mineral soils, however there are likely to be limitations imposed in quantifying soils with more heterogeneous density distributions. Organic matter will produce variation in grey-level gradients between different air/aggregate boundaries, possibly leading to over or under-estimate of the macro-pore region. A possible refinement envisaged to the protocol is to use the boundary determined between macro-porous and aggregate domains as a seed region for a local gradient-search, using additional image-processing operators to differentiate better between material phases, particularly in the

presence of water.

Chapter 3

The application of clinical contrast media for enhanced contrast in μ-CT imaging of plant roots

As discussed in Chapter 2, poor root-to-soil contrast in reconstructed data is a fundamental issue in root and soil μ-CT. Though a number of imaging domain approaches can be used to improve the CNR and SNR of data (as described in Section 2.4.7), the application of chemical contrasting methods such as those used in clinical XCT has not as yet been assessed in plant μ-CT. In this chapter, two commonly used, iodine-based medical contrast media were trialled to assess performance in elucidating RSA, physiology and flow processes in roots of pea plants (*Pisum sativum*). A loading protocol was developed, and a dilution series of each medium tested in order to characterise the relationship between iodine concentration and contrast enhancement. Quantification of attenuation coefficient down the contrasted steles of seminal roots allowed contrast profiles to be plotted with respect to root length. Calibrating attenuation coefficient against concentration allowed a relationship to be derived. This suggested that in addition to enhancing contrast for architecture extraction, the technique may have potential in temporally-resolved tracing of phloem flow processes.

3.1 Introduction

The degree of contrast in μ-CT data is determined by differential X-ray attenuation of different sample constituents, with attenuation being a function of material mass density and effective atomic number (see Section 2.1). Problematically for the imaging of plants in field conditions, roots are regularly in contact with water and soil organic material (SOM), both of which have an almost identical attenuation coefficient to plant tissues. Consequently, regions pertaining to roots, water and SOM are often challenging to distinguish in μ-CT data, making extraction of

continuous root architecture unfeasible, particularly for fine roots [Menon et al., 2006].

In μ-CT studies of plant root and soil systems, mitigation of these problems has typically been achieved through optimising soil composition and/or hydration profile. A review of previous studies has shown that the growth media used have almost exclusively been rich in sand, with a low SOM content [Gregory et al., 2003; Pierret et al., 2005; Tracy et al., 2010]. Close control of soil hydration in samples has also been a common means by which to improve the detection rate of roots during post-processing [Lontoc-Roy et al., 2006]. Though careful manipulation of soil composition and hydration can improve extraction of root architecture from data, an over-reliance on these approaches means that numerous realistic field conditions are at present excluded from examination using μ-CT methods. There is a clear need for imaging approaches that are tolerant to a wider range of soil and water conditions, particularly those found in the field, allowing root structures to be characterised. In human and mammalian soft-tissue imaging, radio-opaque contrast media are routinely used to enhance feature identification [Hallouard et al., 2010]. The local contrast improvement in perfused tissues occurs due to the high attenuation coefficients of these media, and in clinical applications, there now exists a wide range of water-soluble, iodine-based compounds with high effective atomic number and low-reactivity, suitable for a variety of different XCT imaging protocols [Christiansen, 2005].

A mature field in medical science, the potential use of contrast media is as yet virtually unexplored within plant radiology. Though the clinical contrast agent Gastrografin has been used in one study to identify locations on the roots of cabbage (*Brassica oleracea capitata*) that had been affected by verticilium wilt, the study only examined plants *in vitro*, and did not investigate root architecture [Kemmochi and Maru, 2004]. In clinical XCT, the scanning of tissue regions at different time intervals after infusion of a contrast medium allows dynamic fluid behaviour such as preferential flow paths and perfusion rates to be quantified [Fournier et al., 2004; Roberts and Stewart, 2002]. Though Nuclear Magnetic Resonance imaging (NMR) has been used to non-invasively quantify water velocity in aerial plant tissues [Windt et al., 2009], the use of suitable tracers to characterise the dynamics of delivery of photosynthesis products and foliar-applied compounds to plant roots has not been attempted using μ-CT. Since plant roots possess extensive vascular systems for water, solute and carbon transport, it was hypothesised that development of a chemical-contrasting protocol for plant μ-CT might be feasible. Assessment could then be made of the following potential applications:

- The improvement of general root-to-soil contrast, according to Equation 2.1 in Section 2.1, allowing enhanced extraction of continuous RSA from μ-CT data.
- The characterisation of flow in the vasculature of plant roots, with the possibility of trac-

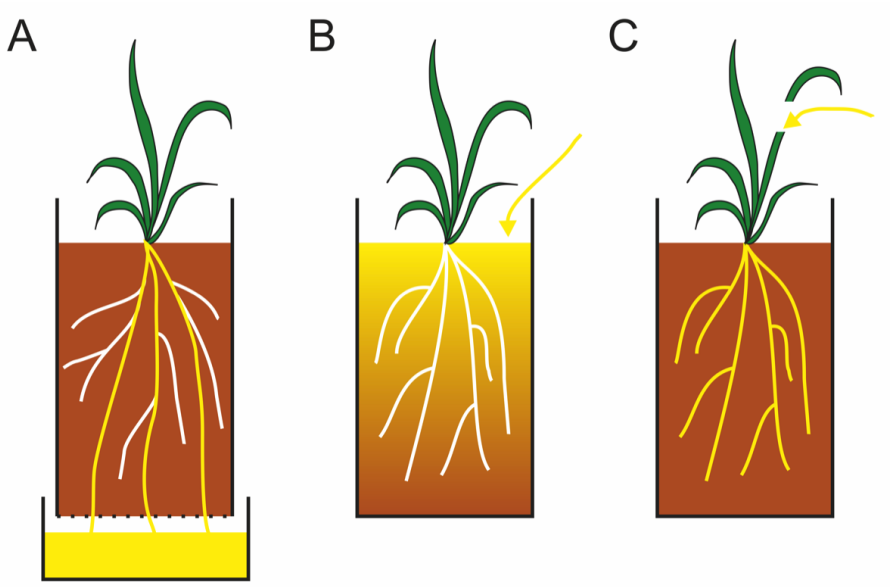

Figure 3.1: Schematic showing three proposed methods for introducing media in order to improve root/soil contrast. (A) Xylem contrasting via root tissues (B) Negative (soil) contrasting via saturation of soil with a medium impervious to absorption by roots, (C) Phloem contrasting via aerial tissues. In each case, contrast medium is shown in yellow.

ing phloem demand, in a manner analogous to flow characterisation in clinical XCT.

- The identification of intra-root physiology that is normally not visible in μ-CT due to the very similar attenuation coefficients of the different regions within the root cross-section.

3.1.1 Methods for delivery of contrast media to target regions

The use of contrast media in clinical XCT is made possible by the existence of a vascular transport system in the mammalian body. The vasculature of higher plants comprises two connected but functionally distinct networks; the xylem, which transports water from the roots towards transpiration surfaces, and the phloem, which transports photoassimilates from the tissues in which they are produced towards sinks where they are required to support growth. The distinct characteristics of the two systems largely determines the most suitable manner in which to introduce contrast media to each. Further to these two loading routes, it is conceivable that negative contrasting of roots could be effected by introducing a contrast agent to soil and pore water which was impervious to plant uptake. Figure 3.1 shows a schematic of these three posited methods.

3.1.2 Loading media into plant xylem

The xylem network is the structurally simpler of the vascular systems, consisting of long

strings of dead cells whose cell walls have broken down at the connecting surfaces, forming long conducting tubes. Water entering the roots is carried along these tubes towards aerial tissues by a negative pressure gradient, maintained by stomatal transpiration on the leaf surfaces. Provided that the roots of the plant permit uptake of the iodinated compound across the epidermis, loading of the xylem system would be most straightforwardly effected by isolating particular roots from the soil. The most obvious way to achieve such isolation of roots is a modification of the air-gap apparatus developed by *Gahoonia et al* in order to verify the role of root hairs in phosphate uptake [Gahoonia and Nielsen, 1991]. By allowing roots to cross an air gap into a chamber containing contrast agent, the possibility of soil contamination would be negated, though this approach would necessitate the plant reaching a stage of maturity at which the roots had reached the boundaries of the growth chamber. The problematic aspect of this approach is that by the point where root development was sufficient for growth across an air gap to a secondary chamber, the root system would likely have developed a mat against the mesh, constricting the architecture to an artificial geometry. Furthermore, in the absence of hydraulic redistribution processes, only those roots with access to the iodinated solution would become contrasted, with the result that lower-order laterals with no access to the medium may remain undetectable during post-processing.

3.1.3 Loading media into plant phloem

Since the work of *Hartig* in the mid 19th Century, it has been known that phloem plays a major role in plant translocation of organic solutes [Hartig, 1858]. As well as fulfilling a different role in terms of transport, the phloem network differs structurally from the xylem. Whereas xylem cells are dead at maturity, the transport cells of the phloem system are living [Taiz and Zeiger, 2002]. These individual elements are linked by *sieve pores* which range in size from $5 - 15\mu\mathrm{m}$, forming long strings of conducting cells known as *sieve tubes*. The major sinks for photosynthesates during plant development are the root and shoot apices, with the leaves closest to the emergence of the primary stem preferentially supplying the bulk of the root requirements, and those furthest from the root system supplying the requirements of aerial tissues [Taiz and Zeiger, 2002]. Though this is the general case, there exists a certain degree of plasticity in supply characteristics, and the plant can adapt to resupply tissues from different sources when preferred sources are lost (as a result of mechanical damage or disease) [Joy, 1964].

Wheareas xylem loading would necessarily take place near the apices of the roots (in order to maximise contrasted length), the oppositely oriented principal direction of phloem transport (from photosynthesising sources to root sinks) indicates that loading of the phloem should be achieved through the aerial tissue. There is precedent in the literature for this approach, since introduction of P^{32} to the phloem system of small plants has been achieved previously by

excising flaps in leaf tissues to expose the cut ends of sieve tubes [Watson, 1976]. Provided that the osmolality and viscosity of the contrasting solution are kept within a range that permits uptake and transport within the sieve tubes, it is proposed that a similar approach to that of *Watson et al* might be a successful means to contrast the root tissues.

3.1.4 Controlling factors in experimental design

Within the body, the successful use of contrast agents to visualise structures is dependent, among other factors, on the velocity with which the solution or suspension is transported to the target region, the local concentration (and thus radio-opacity) which can be attained in the region of interest, and the chemotoxicity of the compound [Christiansen, 2005; Singh and Daftary, 2008]. In medical applications, intravenous administration of $100 - 200\mathrm{ml}$ of intravenous iodinated contrast agent is generally necessary in order to produce adequate contrast for visualisation of vascular tissues [Christiansen, 2005]. For an average-sized adult, this equates to a volumetric concentration of iodinated solution of 2-4% in the blood during imaging. Assessing the loaded volume required in a plant of a given size is difficult to estimate, given a paucity of data for total phloem volume as a function of biomass. Thus, it was necessary to assess a variety of dilutions of the candidate media in order to characterise performance.

In addition to medium delivery volume and concentration, the timescale over which the contrasting solution will be transported throughout the plant is also an important factor in developing an experimental protocol for contrast-assisted μ-CT imaging of roots. Transport of photosynthesate solution along phloem sieve tubes is many orders of magnitude greater than can be accounted for by diffusion alone [Taiz and Zeiger, 2002]. Velocity measurements have been conducted using various techniques, primarily either by tracing of radioactive isotopes, or via nuclear magnetic resonance (NMR) imaging. Velocities determined through these methods were found to range from $0.3 - 1.5\mathrm{m.h}^{-1}$ [Taiz and Zeiger, 2002]. A study of 35 day old sunflower (*Helianthus annus L*) plants using P^{32} tracer introduced to leaf phloem measured average velocity in the main stem at $0.5\mathrm{mh}^{-1}$, with radioactivity (proportional to tracer concentration) continuing to increase for $> 24\mathrm{h}$ [Watson, 1976]. NMR-based measurements of phloem velocity in 40 day old *Ricinis communis L* from two studies range from $0.94 - 1.44\mathrm{mh}^{-1}$ [Peuke et al., 2001; Rokitta et al., 1999]. These findings suggest that for phloem loading, a duration at the $\geq 24\mathrm{h}$ scale is most suitable.

3.2 Materials and methods

A winter pea variety (*Pisum sativum L. cv. frisson*) was chosen for investigation, owing to a relatively rapid growth rate and coarse roots (as compared to other commonly investigated plants such as *Arabidopsis thaliana*). Growth containers were $50\mathrm{ml}$ polypropylene centrifuge tubes,

and hydration was facilitated via 16 perforations of approximately $1\mathrm{mm}$ diameter around the base of each tube. The growth medium was a Denbigh series Eutric Cambisol from the Ah horizon of a lowland-grassland environment at Bangor University ($53°13'54''$, $4°0'54''$), which was freeze-sterilised for $16\mathrm{h}$ and sieved to $< 2\mathrm{mm}$ particle size. Seeds were pre-germinated at $21°\mathrm{C}$ for 96h on moist filter paper, before being surface planted at a density of one seed per tube, the seeds being covered with a $5\mathrm{mm}$ layer of soil. Soil was treated with a rhizobium culture, in order to promote root nodulation. Growth was conducted in a controlled growth environment (Fitotron ECR), under fluorescent lights on a simulated diurnal cycle, with $16\mathrm{h}$ light at $23^{o}\mathrm{C}$ and 60% humidity, and $8\mathrm{h}$ darkness at $18°\mathrm{C}$ and 55% humidity with $0.5\mathrm{h}.°\mathrm{C}^{-1}$ temperature and $0.5\%.\mathrm{h}^{-1}$ humidity ramp rate. Sample tubes were initially top-watered via pipette, then kept in a $5\mathrm{cm}$ depth of water to allow capillary hydration of the soil.

Two iodinated contrast agents were used, both of which are used gastrologically and intravenously in medical X-Ray CT imaging. Gastrografin (a mixture of $100\mathrm{mg}.\mathrm{ml}^{-1}$ sodium amidotrizoate and $660\mathrm{mg}.\mathrm{ml}^{-1}$ meglumine amidotrizoate) is a high-osmolality, ionic iodinate, and was supplied at an iodine concentration of $370\mathrm{mg}.\mathrm{ml}^{-1}$ and osmolality of $\approx 2150\mathrm{mOsm}.\mathrm{kg}^{-1}$. Niopam (iopamidol) is a low-osmolality, non-ionic iodinate, and was supplied at an iodine concentration of $300\mathrm{mg}.\mathrm{ml}^{-1}$, and osmolality of $\approx 800\mathrm{mOsm}.\mathrm{kg}^{-1}$. The contrast media were mixed with de-ionised water to form a dilution series, with Niopam concentrations of 100%, 50%, 25% and 1%, and Gastrografin concentrations of 66%, 50%, 25% and 1%.

For $24\mathrm{h}$ prior to imaging, Gastrografin and Niopam were loaded into the phloem of the plants using a modification of a leaf-flap approach following *Watson* [Watson, 1976]. A single branched stem axis was cut with a scalpel, near a leaf sheath on each plant, following which the cut surface of the stem was submerged in an Eppendorf tube containing a single dilution-step of a particular contrast medium. Tubes were foil-wrapped to occlude sunlight and avoid denaturing of the contrast media, and stems were fastened securely with small lengths of autoclave tape to ensure complete submersion of the cut surfaces throughout the infusion period. After $24\mathrm{h}$, the plants were transported for μ-CT imaging, and the stem of each sample removed from the contrast agent immediately prior to imaging.

Scans were acquired using an X-TEK/Nikon Metrology HMX ST225 at the $\mu - \mathrm{VIS}$ Centre for Computed Tomography at Southampton University. A total of 3142 angular projections were acquired for each sample using a W target in reflection mode, with 2 frames-per-projection, and an exposure of $0.5\mathrm{s}$. The beam accelerating potential was $110\mathrm{kV}$ and tube current was $120\mu\mathrm{A}$. Each plant was scanned once, generating a total of 8 datasets, one for each dilution step. Volumes were reconstructed using a Feldkamp back-projection algorithm implemented in the Metris CT Pro software package (Nikon Metrology, Tring, UK), generating $32-\mathrm{bit}$ datasets

with an isotropic voxel resolution of $16.3\mu\mathrm{m}$. A beam-hardening correction was applied during reconstruction to compensate for a modest beam-hardening artifact present in the data (see Section 4.3.2 for a full description). The datasets were scaled down to $16-\mathrm{bit}$ for more tractable image processing, using the same transformation on each dataset. Data were checked for slope and offset normalisation using the polymer and air regions of the data, but variation proved negligible due to the identical scan parameters, and none of the samples required any adjustment.

Measurements of attenuation coefficient were made using the open source image-processing software FIJI [Schindelin et al., 2012]. Examination of root cross sections in each sample revealed that the internal structure of the seminal root was clearly distinguishable, with the phloem vessels evidently contrasted by the infused media. In single data slices normal to the root axis, a Cintiq 22HD graphical tablet was used to manually define a *poly-line* at the boundary between the contrasted vascular bundle in the stele and the un-contrasted tissue of the cortex (see Figure 3.2). Only the innermost discrete bundle was considered in each case, and mean grey-level intensity (I) was reported for the voxel set enclosed by the polyline. A series of such measurements was made, beginning in a plane normal to the root axis, defined at the point where the seminal root exited the seed. Measurements were taken at intervals of 100 voxels ($1600\mu\mathrm{m}$) down the root length, until the phloem region became indistinguishable.

Root architectures were also extracted as three-dimensional entities, following the procedure of *Flavel et al.*, using a seeded region-growth (SRG) procedure within the post-processing software package VGStudio MAX 2.1 [Flavel et al., 2012]. This process was carried out separately for the un-contrasted tissue and the contrasted region, using an adaptive tolerance and a variety of user-defined seed points.

In order to calibrate iodine concentration against attenuation coefficient in the resulting data, a phantom containing a dilution series of Gastrografin 370 was prepared for imaging. Gastrografin solution was pipetted into a clean beaker and made up to concentrations of 100%, 50%, 25%, 10%, 5%, 1% by volume using pure RO H_2O at RT. A control sample of 100% RO H_2O was also prepared. At each dilution step, $1\mathrm{ml}$ of solution was drawn up into a $1\mathrm{ml}$ polymer syringe barrel, following which all syringe barrels were clustered into a single sample for imaging. The resulting cluster was imaged and reconstructed using the same parameters used for the root samples. In the reconstructed data, FIJI was used to find the mean attenuation coefficient (I) of the fluid region in each syringe.

3.3 Results

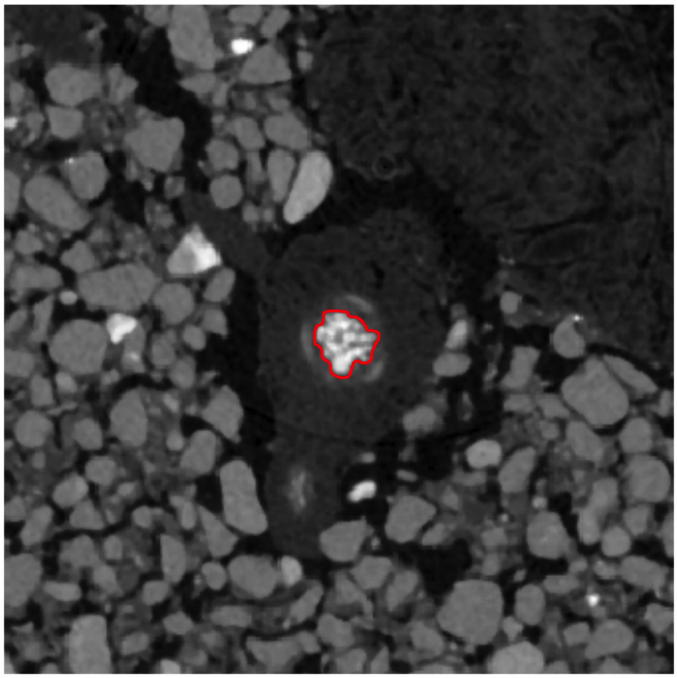

Figure 3.2: Intensity of contrasting was quantified by defining a poly-line around the innermost bundle of the stele (shown in red). The mean value of enclosed voxels (I) was used as an intensity measure.

3.3.1 Comparative effectiveness of Niopam and Gastrografin

All plants except those treated with 1% concentrations showed clear evidence of root contrast enhancement. Figure 3.3 shows reconstructed x, y sections through the seminal root of the plant treated with 25% Niopam 300, showing a substantial elevation of attenuation coefficient in the stele as compared with the un-contrasted cortical tissue. In frames (1-4) of Figure 3.3, simple visual inspection confirms that the attenuation coefficient of the phloem region is higher than the mean value for the surrounding soil. Over this region, the contrasted phloem could be extracted automatically in a user-invariant manner using global histogram-based segmentation methods [Otsu, 1979] . Figure 3.4 shows the mean intensity (I) with distance in the contrasted vascular bundle for all samples (with the exception of the 1% concentration solutions). A red line indicates the mean soil attenuation coefficient, estimated by sampling small regions at 20 randomly selected points in the central slice of each sample. In root regions for which I falls below this threshold, global histogram segmentation will fail as a reliable architecture-extraction method. Comparing the intensity plots in Figure 3.4 clearly reveals that for equivalent dilution steps, Niopam 300 was more effective than Gastrografin 370 at enhancing contrast between roots and the surrounding soil, and that both media provided the most extensive contrast enhancement at a concentration of 25%.

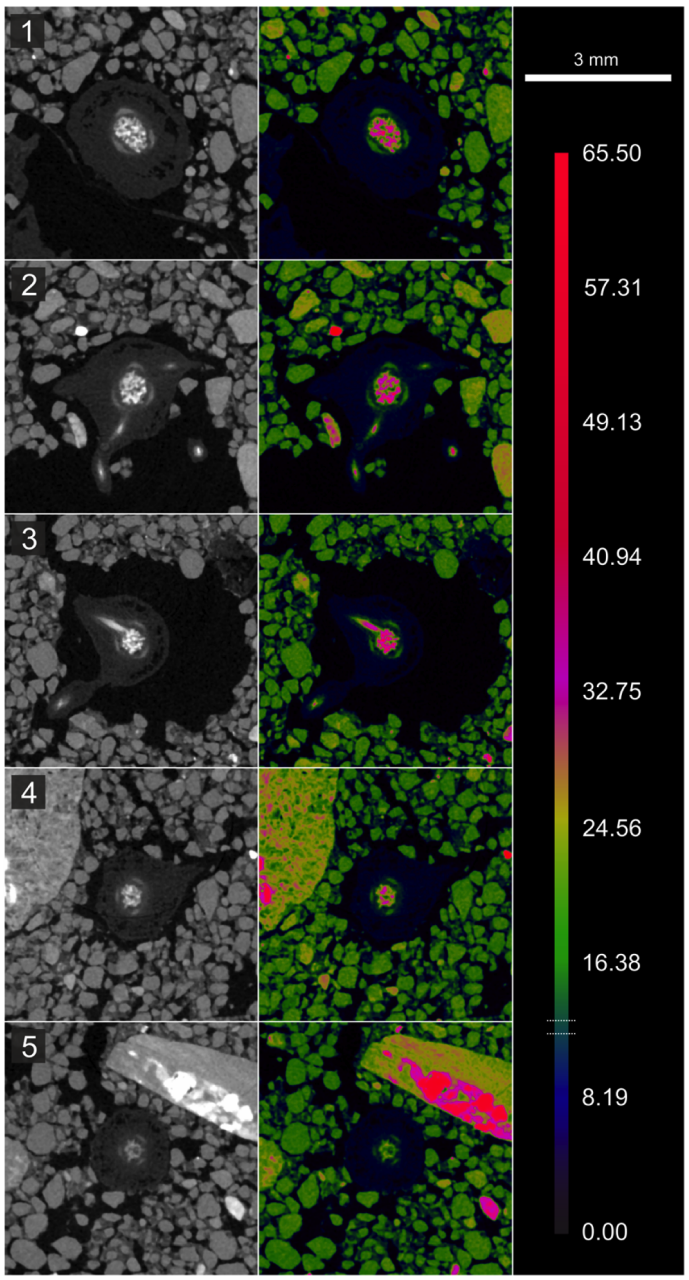

Figure 3.3: Cross sections through $\mu - \mathrm{CT}$ data of a seminal root, treated with a 25% solution of Niopam 300. Greylevel data is shown in the left column, along with corresponding colour-map of attenuation coefficient. The band indicated on the legend represents one standard deviation centred on the mean value for the surrounding soil. Frame (1) represents the emergence of the seminal root from the seed, with frames (2-5) situated at $4.9\mathrm{mm}$ intervals down the root.

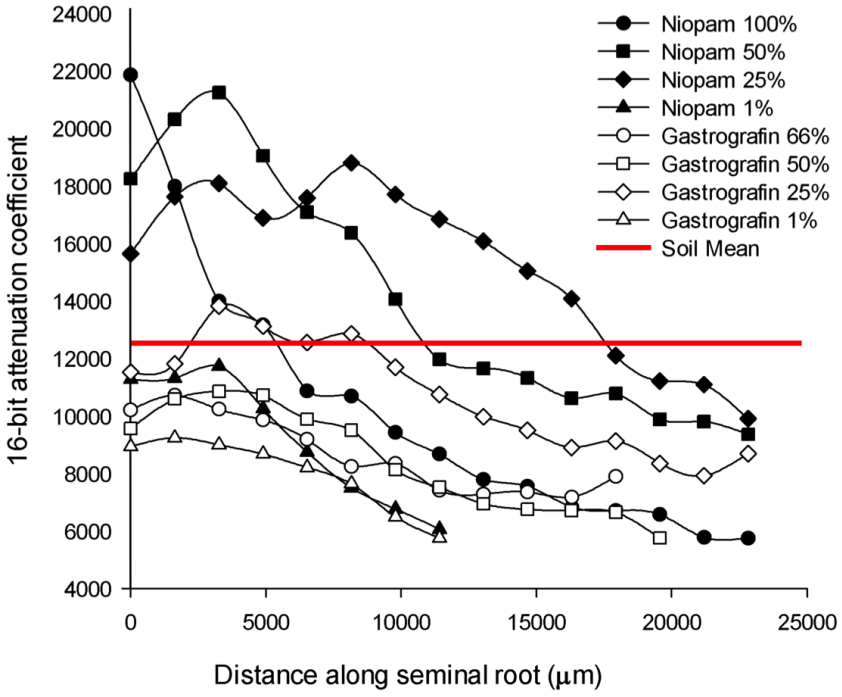

Figure 3.4: Plots showing mean attenuation coefficient of contrasted region with respect to distance from seed, comparing all dilution steps for Niopam 300 and Gastrografin 370. The red line indicates the mean attenuation coefficient of the surrounding soil.

3.3.2 Use of attenuation to map vascular iodine concentration

Figure 3.5-A shows the architecture of the contrasted phloem region, extracted via SRG from the 25% Niopam dataset. The range of attenuation coefficients in the phloem is shown using a colour-map, with the legend indicating the mean value of soil attenuation (including one standard deviation centred on this value). It was possible to extract phloem regions using SRG even where the mean attenuation coefficient had fallen well below that of the surrounding soil phases. This is the case because voxels (discrete 3D image elements) in the data pertaining to the contrasted stele region are 'insulated' from those of the surrounding soil by the un-contrasted tissue of the cortex. The SRG algorithm classifies regions based on both attenuation coefficient and connectivity of voxels, hence regions of similar attenuation coefficient isolated from each other by regions of distinctly different attenuation coefficient will not be co-classified. Figure 3.5-B shows a comparison of the resulting phloem region with the un-contrasted tissue region extracted using SRG. Evidently, there were some regions where un-contrasted tissue architecture was extractable but where the phloem had not been adequately contrasted to allow extraction. Conversely, some regions were only extractable via SRG segmentation of the contrasted phloem. The observation of different intensities suggests a possible variation in phloem demand between different lateral roots.

3.3.3 Extraction of vascular physiology within root tissues

In Figure 3.5, the macrostructure of a number of rhizobial nodules is clearly visible. Figure 3.6 shows detail of a nodule from the sample treated with 100% Niopam, showing both the external structure and the vasculature. Figure 3.6-A clearly shows the seminal root, the remains of the seed casing, and a nodule situated on a first order lateral root. Figure 3.6-B shows the structure of the phloem vasculature, with a colour-map representing corresponding attenuation coefficient. In addition to revealing the intricate, branched structure of the phloem vessels within the nodule, the heterogeneity of contrast enhancement across the phloem volume is clearly visible. Since attenuation coefficient in this region is a function of iodine concentration, the substantial spatial heterogeneity of attenuation coefficients within the phloem indicates corresponding heterogeneity in iodine concentration. As discussed previously, such observations raise the hypothesis of whether suitable contrast media might have an application as tracers for investigation of flow processes.

3.3.4 Exudation of contrast agents into soil

In the sample treated with a 25% dilution of Gastrografin 370, highly attenuating phases were observed surrounding lateral roots at a number of positions. The attenuation coefficient of this phase exceeded those of the surrounding soil phases, but was similar to that of the root stele, suggesting that it originated from the root. Though a number of examples of this phenomenon

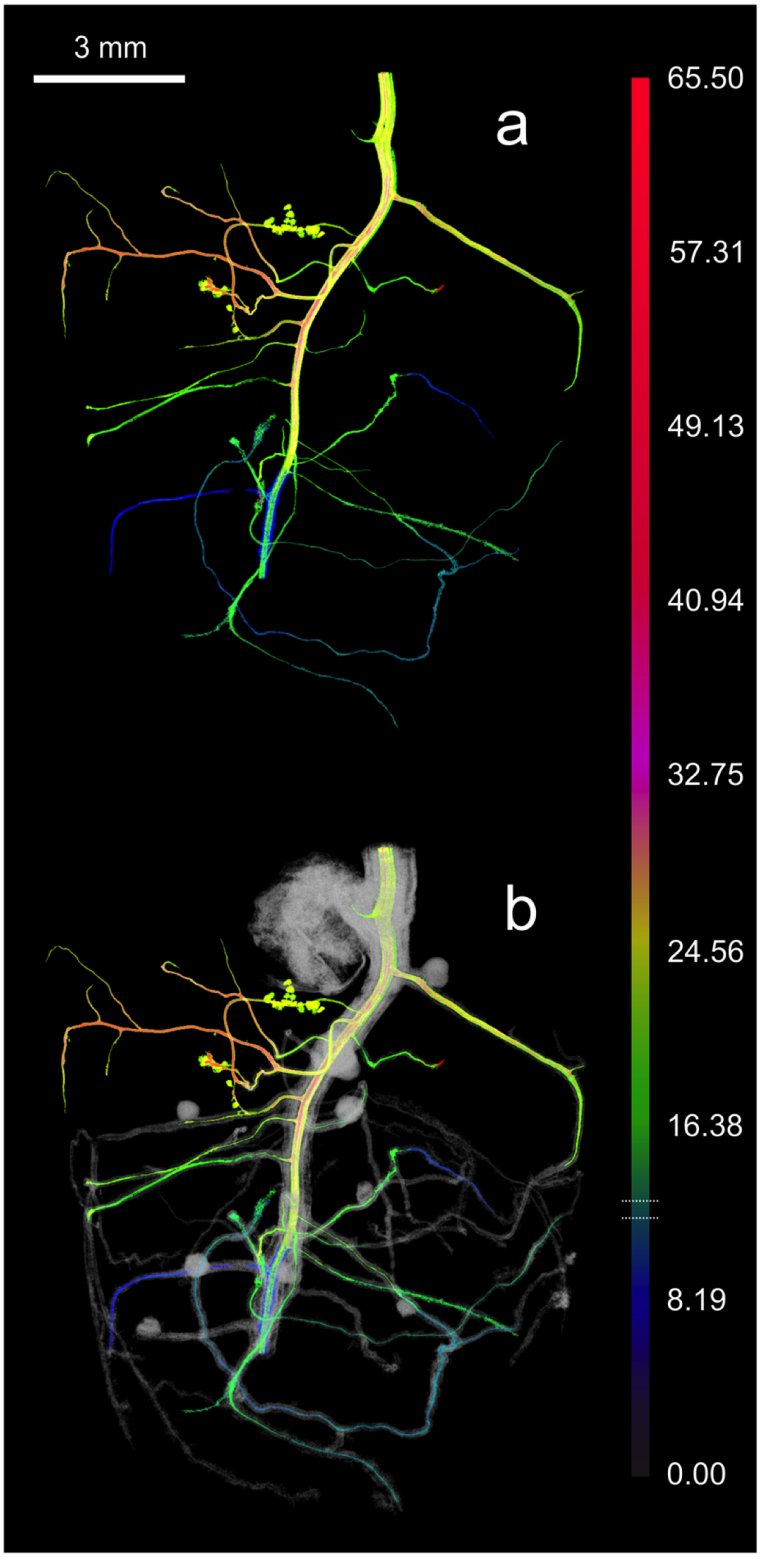

Figure 3.5: The root system of juvenile *Pisum sativum*, treated with a 25% solution of Niopam 300. (A) The contrasted phloem vasculature is shown with a colour-map representing attenuation coefficient. Variation in attenuation coefficient over the contrasted region can be seen. (B) The same region is shown overlaid with the un-contrasted tissue of the root cortex. Root nodules are clearly visible.

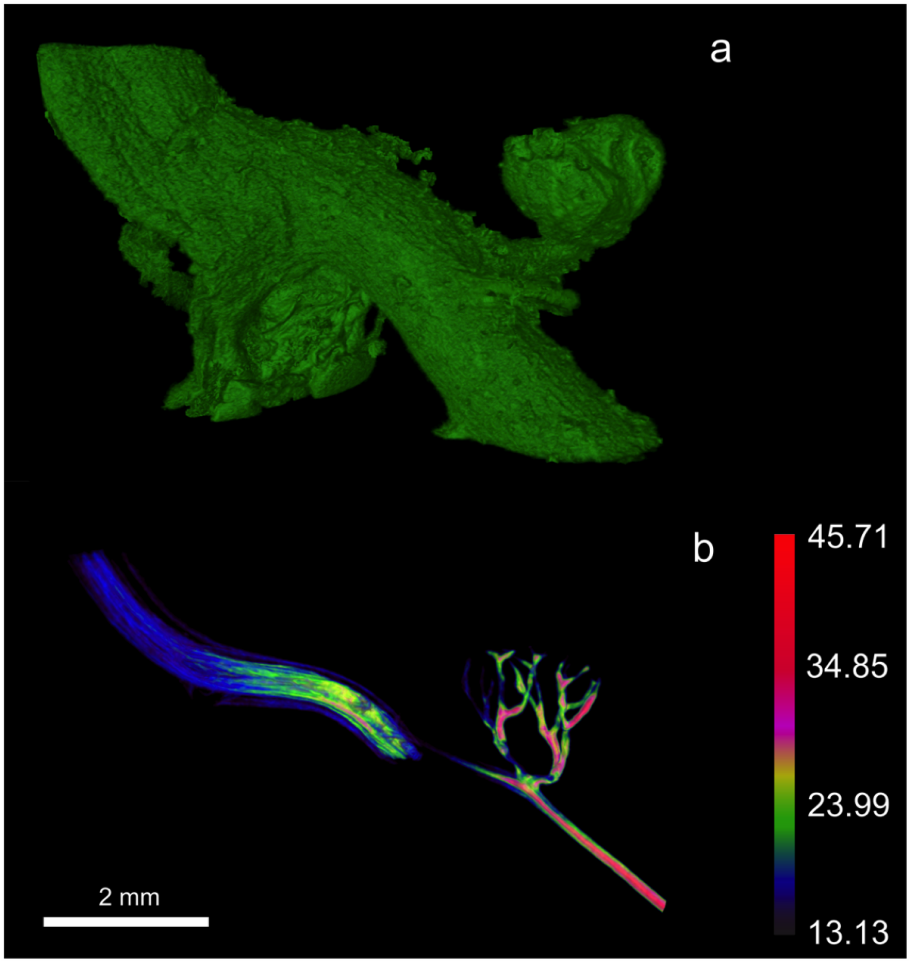

Figure 3.6: A rhizobial nodule situated on a lateral root of *Pisum sativum*, treated with a 100% solution of Niopam 300. (a) The external morphology of the nodule, with seminal root and seed remnants visible. (b) The contrasted vasculature of the nodule. The vessel arrangement is clearly visible, and the colour-map shows the heterogeneity of attenuation coefficients. Regions of high local attenuation coefficient, resulting from high iodine concentration are clearly discernible.

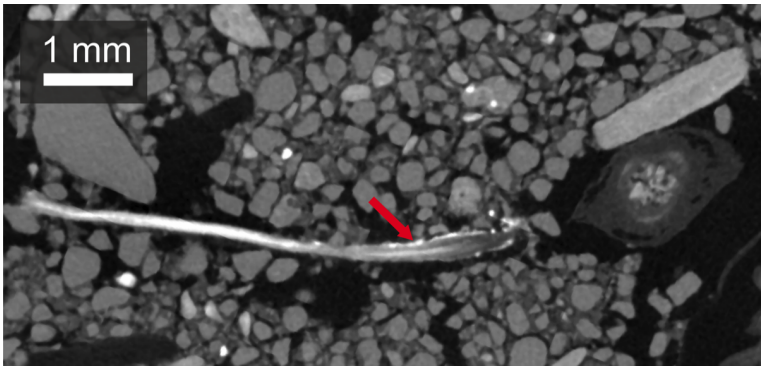

Figure 3.7: A lateral root (LR) of *Pisum sativum*, treated with a 25% solution of Gastrografin 370. Highly attenuating phases are visible within the LR with an attenuation coefficient range substantially higher than the mean level of both the soil phases and the stele of the seminal root. The surface of the LR also shows evidence highly attenuating phases, as indicated by the arrow, suggesting that the contrast media has been transported across the epidermis.

(shown in Figure 3.7) were found within the data for the roots treated with 25% Gastrografin 370, it was not evident in any of the other datasets. It should also be noted in Figure 3.7 that the attenuation coefficient in the LR is much greater than for higher order root from which it originates. This suggests either that a bolus of locally high iodine concentration was in the process of moving through the lateral root during the scan, or that molecules of sodium amidotrizoate and diatrizoic acid had locally accumulated within the root as an end-fate.

3.3.5 Use of a phantom to calibrate iodine concentration to attenuation coefficient

Figure 3.8 shows $16-\text{bit}$ attenuation coefficient plotted as a function of Iodine concentration for all dilution steps in the phantom. A third order polynomial ($y = -4e^{-12}x^3 + 4e^{-7}x^2 + 0.0082x - 35.892$) was fitted to the data with an accuracy of $R^2 = 1$. The correlation justifies the use of the function as a conversion factor between iodine concentration and attenuation coefficient in the contrasted root data.

3.4 Discussion

The results confirm the hypothesis that clinical contrast media can provide meaningful insight into plant root architecture and transport processes that extends beyond the scope of conventional μ-CT protocols. By enabling the phloem to be visualised distinctly from surrounding tissues, physiological detail can be discerned that is not usually conducive to investigation using bench-top devices. At present, only synchrotron beam-lines and certain very high resolution laboratory X-ray imaging facilities allow access to the sophisticated suite of phase-contrast techniques that can provide substantial imaging-domain contrast enhancement between re-

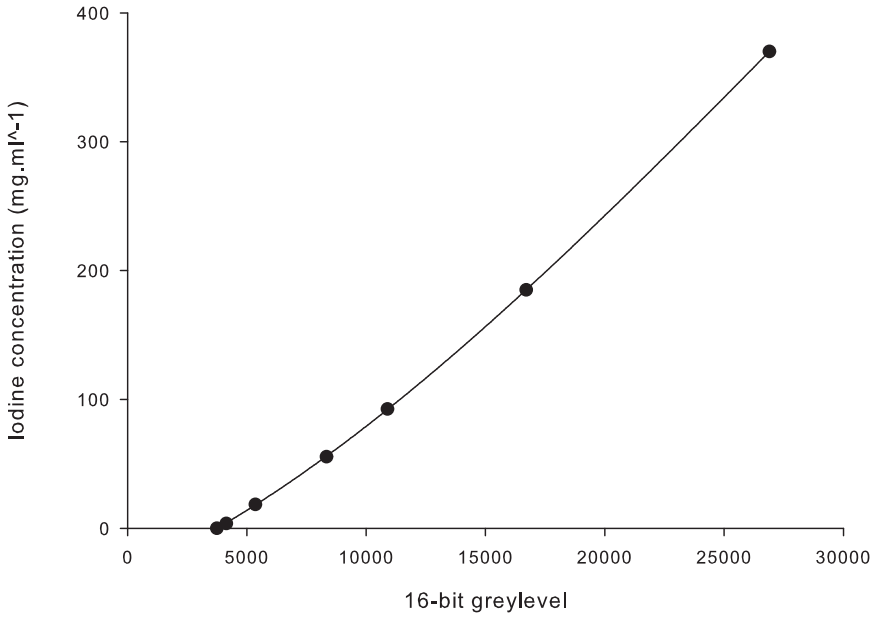

Figure 3.8: Plot showing the relationship between attenuation coefficient (represented by 16-bit grey-levels), and the iodine concentration of the contrast medium in $\mathrm{mg.ml^{-1}}$. The equation for the best-fit line is shown in Section 3.3.5.

gions of very similar attenuation coefficient, such as plant tissues and bulk water [Stampanoni et al., 2006]. However, sample sizes for these systems are typically limited to the $< 1\mathrm{cm}$ range, making these methods suitable only for studies at the single root and root hair scales [Keyes et al., 2013a]. The use of contrast media allows normally indistinguishable features to be identified in soil, *in vivo*, with a standard bench-top scanner of the type most commonly used for root and soil CT imaging. Because the technique depends upon phloem translocation rather than any intrinsic contrast between soil and root tissues, we predict that effectiveness should be largely invariant to soil water and SOM status. It will be noted that in the data presented, the water content of the soil was low, such that macro-pore space was gas-filled. Under these hydraulically favourable conditions, it was possible to extract a large degree of the RSA without using the contrasted stele regions (see Figure 3.5 on page 3.5). Further development of the method will assess the hypothesis that in conditions of high soil water content, even a moderate chemical contrasting effect within the roots may allow extraction of otherwise invisible RSA

For both contrast media used, a dilution of 25% provided the most extensive enhancement of attenuation coefficient in the phloem. Because higher concentrations of I should always result in higher attenuation, it is evident that there exists an optimum balance between iodine concentration and detrimental factors such as viscosity and osmolality of the medium. Gastrografin, which has a higher viscosity, osmolality and ionicity, was significantly less effective than

Niopam at comparable dilutions, despite a 23.3% higher I content per unit volume. Within the human body, matching the osmolality of a contrast agent to that of the blood is known to result in a better tolerance and thus fewer adverse side effects. Toxicity to the plant at higher concentrations might be responsible for reduced uptake of the medium, and thereby reduced contrasting of phloem tissue. It is possible that in plants, uptake might be improved by careful matching of the medium to important physical and chemical parameters of the phloem. In a study by *Fu et al.* which experimentally determined the osmolality of sap from the phloem of both herbaceous and woody plants, values were found to range from $400 - 800\mathrm{mOsm/kg}$ [Fu et al., 2011]. Whereas the osmolality of Gastrografin is substantially higher at $2150\mathrm{mOsm/kg}$, the osmolality of Niopam 300 at $37°C$ is $\approx 640\mathrm{mOsm/kg}$, resulting in likely iso-osmolar conditions in the $50 - 100\%$ dilution range. This property matching may have been implicated in the superior performance of Niopam when compared to Gastrografin at similar dilutions.

Other contrast media might also be suited to applications in root μ-CT. The composition of *clinical* contrast media is optimised for low reactivity, binding-affinity and viscosity, as well as closely plasma-matched osmolality, all of which correlate with a reduction in detrimental side-effects in mammals [Christiansen, 2005; Wynn et al., 2011]. However, in extracting root architecture, the main experimental requirement is to achieve a maximal attenuation coefficient differential between root and soil, for which purpose other properties, such as binding, might in fact be advantageous. It is evident from the attenuation profiles in Figure 3.4 that Niopam and Gastrografin concentration in phloem regions can diminish once loading of the medium at the infusion point ceases. This is possibly why a number of the attenuation coefficient profiles in Figure 3.4 reach a maximum further along the seminal root than the initial datum, even though the datum is closer to the infusion point. Once the infusion through the stem ceases, un-contrasted phloem is apparently able to move down behind the contrasted bolus, reducing the attenuation coefficient in the trailing region. Though this has promising implications for the quantification of *flow* processes, alternative media with a binding affinity for starch (such as elemental iodine) should be assessed for their performance in contrasting roots specifically for RSA extraction.

As seen in Figure 3.7, it appears that in some cases, contrast media is able to be transported across the root epidermis and into the rhizosphere soil. Very highly attenuating phases are seen to coat root surfaces in several regions of the root system treated with a 25% dilution of Gastrografin 370. No similar phenomena were observed in the data for any other dilutions of either contrast medium. Though there is insufficient data to draw empirical conclusions, the most obvious candidate mechanism for this phenomenon would appear to be transport of constituent molecules from the contrast medium via root exudation. As described in the literature review, plants exude a variety of compounds which alter the physical and chemical

properties of rhizosphere soil, thereby influencing a host of transport mechanisms and faunal interactions. The range of compounds exuded by roots includes proteins, amino acids, organic acids, monosaccharides and polysaccharides [Hinsinger et al., 2005]. A study of mucilage from roots of maize (*Zea mays*) has found that (94% w/w) was composed of carbohydrates, of which the major monosaccharides were galactose (26%, molecular volume $155.8\mathring{A}^3$), arabinose (20%, molecular volume $130.69\mathring{A}^3$) glucose (18%, molecular volume $155.8\mathring{A}^3$), fucose (18%, molecular volume $147.56\mathring{A}^3$) and xylose (15%, molecular volume $130.96\mathring{A}^3$) [Bacic et al., 1986]. It is conceivable that the constituent molecules of Gastrografin (sodium amidotrizoate, molecular volume $276.2\mathring{A}^3$, and diatrizoic acid, molecular volume $278.9\mathring{A}^3$) might be transported along with these constituents, whereas the substantially greater molecular volume of iopamidol ($424.5\mathring{A}^3$) renders the molecules too large to be transported via exudation. If roots are to be contrasted for extraction of RSA, the leaching of contrast media into the soil represents a deleterious phenomenon. However, media that are able to be transported across the root epidermis might have a role in allowing root exudates to be visualised in-situ using μ-CT, if a suitable protocol could be developed and validated.

3.5 Conclusions and future work

Clinical contrast media such as Niopam and Gastrografin evidently hold potential for the investigation of fluid flow in plant tissues, and potentially as a surrogate marker for key solutes. The initial results presented in this work have demonstrated that Iodine concentration profiles can be quantified and visualized. By determining the mathematical relationship between iodine concentration and attenuation coefficient via μ-CT of a suitable dilution series, it is possible to directly report iodine concentration from data of contrasted plants. A methodology based on this principle could be used to investigate the variability of phloem demand to different roots and the end fate of species delivered from aerial tissues, in a manner analogous to methods already used to quantify perfusion and flow rates in the clinical domain [Fournier et al., 2004]. The suitability of particular contrast media for use as tracers for photosynthesis products or foliar-applied species will depend on the similarity between flow kinetics of the molecules. Future work will use phloem flow modelling to characterise the transport behaviour of different iodinated molecules in the phloem, in order to screen candidate media for these applications.

Chapter 4

Imaging at the root-system scale using novel acquisition and reconstruction approaches

The literature review demonstrated that the majority of μ-CT studies of plants have been both small-scale ($\approx 2-12\mathrm{cm}$ diameter) and made use of idealised soil states in order to enhance soil to root contrast. This chapter explores the potential for extending the scale of feasible studies up towards sample diameters more representative of mature root systems, in realistic soil conditions. Extracting root features at reduced voxel resolution necessitates a compensatory increase in the attenuation coefficient differential between roots and soil. Unfortunately this is difficult without either modifying the soil away from common field conditions, or chemically increasing the X-ray attenuation of the roots (as discussed in Chapter 3). Roots of certain plants, such as rice (*Oryza sativa*), present a third possibility for enhanced contrast. By exploiting the naturally occurring attenuation difference between root aerenchyma and flooded soil, the ability to detect RSA can be maintained even at comparatively lower voxel resolutions than found in existing μ-CT studies. This chapter develops a robustly optimised protocol for RSA extraction of primary rice roots grown in field soil in large ($> 20\mathrm{cm}$) chambers. By extracting root paths from reconstructed data, rooting length and angles can be compared between genotypes, in real soil conditions requiring neither quasi-planar growth constraints or homogenous gel media.

This chapter considers sequentially:

1. Validation of the contrast between root aerenchyma and flooded soil in reconstructed μ-CT data.
2. Development of a robust protocol for large-sample imaging and subsequent extraction of RSA parameters

3. Use of the protocol to compare two contrasting genotypes with differing performance in low-P soil

4.1 Introduction

Table 2.1 on page 59 tabulates scan metadata from studies spanning 15 years, showing certain clear trends in the use of X-ray CT to investigate plants. Of the 13 studies reviewed, the majority made use of idealised media, and 10 investigated plants grown in pots of diameter $< 10\text{cm}$. Of the studies at the largest pot diameters (200 and 130mm), one investigated resin-impregnated tree roots, and the others both investigated species of only modest agricultural interest, grown in pure, homogenous sand [Han et al., 2008; Perret et al., 2007; Pierret et al., 1999]. 9 of the studies did not investigate either of the major three staple crops, maize (*Zea mays*), rice (*Oryza sativa*) and wheat (*Triticum aestivum*), with the remaining 4 all investigating wheat.

A number of observations may be made regarding these trends. Firstly, the known importance of real soil in influencing root plasticity means that the architecture and morphology of roots grown in an inert and physically homogenous sand medium cannot be expected to correlate with those found in the field [McCully, 1999]. Secondly, the relatively small sample sizes used preclude the investigation of more mature (and agriculturally relevant) plant samples, since roots quickly reach and interact with the walls of the growth chambers, introducing artifacts to the extracted RSA data [Perret et al., 2007]. Thirdly, rice (*Oryza sativa*) and maize (*Zea mays*) are conspicuously absent from root μ-CT studies, despite their major global importance as staple cereals [Coudert et al., 2010]. In the case of rice, drought stress and poor soil fertility present particularly major barriers to necessary improvements in per-capita yield [Champoux et al., 1995; Wissuwa et al., 2006]. Growth is constrained by drought stress across large swaths of Asia, Africa and Latin-America, which are entirely reliant on rain for irrigation [Champoux et al., 1995]. It has been estimated that around 28% of global ricelands are affected by alternating flooding and drying, causing stresses which constrain yield [Champoux et al., 1995]. In addition to lowland agriculture, 11% of global production is accounted for by upland rice, which is almost always exposed to water stresses [Champoux et al., 1995]. Clearly, even small improvements in drought resistance would have a substantial impact on food security in the developing world. As for other crops (see Section 1.4.1) changes in RSA are known to confer benefit in such environments, with increased rooting depth and branching correlating particularly strongly with yield improvement [Asch et al., 2005; Lorens et al., 1987; Mambani and Lal, 1983; Wright et al., 1983]. Rooting angles in many crop plants are known to be influenced by the P status of the soil, with attenuation of the gravitropic response commonly attenuated in low-P conditions, resulting in shallower rooting [Dunbabin et al., 2013; Postma

et al., 2013]. However, this trait is not universal, with some species and genotypes displaying a steeper-rooting phenotype under low-P conditions [Bonser et al., 1996]. The ability to quantify and compare root angle distributions between genotypes is thus of interest for genotyping and phenotyping, but because root-angle information is lost if roots are destructively sampled from the soil, non-invasive methods are required. *Bengough et al.* demonstrated a methodology for the estimation of soil-grown root angles in $9\mathrm{d}$ old barley samples (*Hordeum vulgare*), grown in quasi-planar, rhizobox-type geometries [Bengough et al., 2004]. By pressing a board with a grid of metal pins into the soil-filled rhizoboxes, then gently washing the roots free of soil matter, the growth angles of the soil-grown plants could be measured (see Section 4.5 for further detail and example images.) Problematically, rooting angles of plants grown in quasi-planar soil volumes will almost certainly be influenced by mechanical interference with the chamber walls (as shown in Figure 4.1). This poses the hypothesis as to whether μ-CT methods can be applied to samples at significantly large diameter to allow the measurement of mechanically unconstrained rooting angles of mature plants.

Rice presents a favourable candidate species for investigation with μ-CT, not only because of its global importance as a staple crop, but as a result of innate root morphology characteristics. Cellular respiration in plants is limited by oxygen availability, but advantageous genetic adaptation allows certain plants to respond to saturation-induced reduction in O_2 supply to root surfaces by generating continuous internal gaseous pathways, known as *aerenchyma* [Aulakh et al., 2000; Taiz and Zeiger, 2002]. The poor contrast usually available between root and fluid regions in reconstructed μ-CT data results form their closely matched attenuation coefficients (μ_f for the root, and μ_b for the background), such that the theoretical contrast (C_{th}) between two regions, given by,

$$C_{th} \approx \frac{|\mu_f - \mu_b|}{\mu_b} \times 100\%, \tag{4.1}$$

is low. A database of attenuation coefficients maintained by the National Institute of Standards and Technology (NIST) gives values for (μ) of $1.37\mathrm{cm}^2.\mathrm{g}^{-1}$ and $1.36\mathrm{cm}^2.\mathrm{g}^{-1}$ for pure water and human soft tissue respectively, given a characteristic accelerating potential for root μ-CT imaging of $200\mathrm{keV}$. This equates to a theoretical contrast of ($C_{th} = 0.8\%$) between features and background in reconstructed data. (X-ray absorption in human soft tissue is assumed to be a reasonable analogue for plant tissue). By comparison, the theoretical contrast between pure water and air at the same accelerating potential is more than 10 times greater, at ($C_{th} = 10\%$). Thus, it was hypothesised that the gas-filled aerenchyma of rice roots might provide an advantageous degree of contrast in flooded soil conditions of the type used for rice culture across Asia [De Datta and Sharma, 1985].

The following hypotheses were proposed:

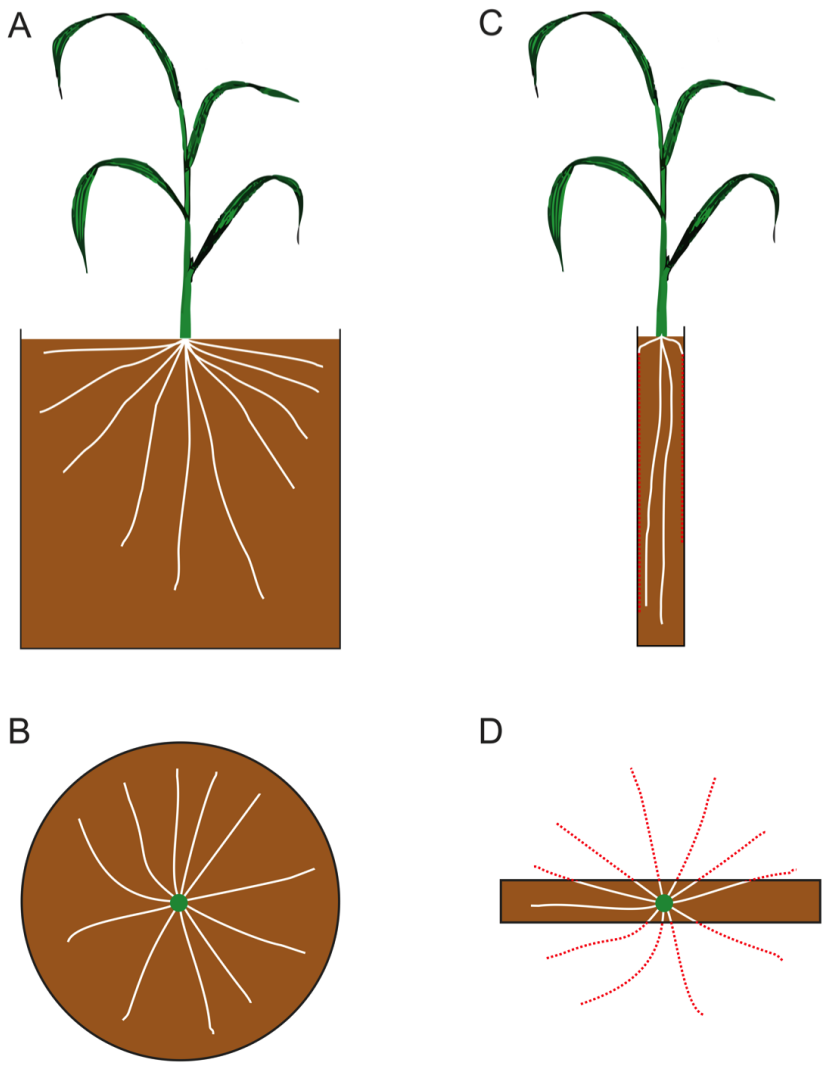

Figure 4.1: Assuming a quasi-radial distribution of roots, interference with the walls of a cylindrical growth chamber will begin to occur for multiple roots at the same growth period (if at all). Frames (A) and (B) show side and top-view schematics of this condition. By contrast, in a quasi-planar growth chamber such as a rhizobox), roots emerging parallel to the short axis will quickly be constrained by physical interaction with chamber walls. Frames (C) and (D) show affected roots in red. Such roots will necessarily exhibit significant deviation from the growth paths expected in an unconstrained condition.

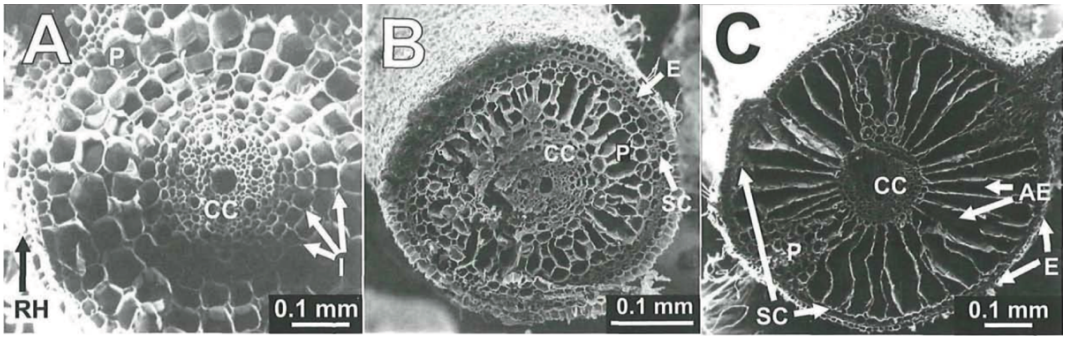

Figure 4.2: Figure from *Butterbach-Bahl et al.* showing SEM microscopy images of aerenchyma in roots of *Oryza sativa* [Butterbach-Bahl et al., 2000]. (A) Root section close to a root tip of a 13 day old specimen. (B) Cross section of a young basal root section of a 39 day old specimen. (C) Cross section of a mature basal root section of a 39 day old specimen. Degeneration of cortical cells to aerenchyma is much more pronounced in the basal region. (P - cortical cells, CC - central cylinder, RH - rhizodermis, SC - sclerenchymatous cylinder, E - exodermis, AE - aerenchyma.)

- The aerenchymous gas continuum of rice root systems provides sufficient image contrast with surrounding fluid and soil phases to be used as a means for extraction of RSA in flooded soil conditions.
- The aerenchyma-contrasting principle can be exploited and combined with robust selection of suitable imaging parameters in order characterise key RSA parameters of plants at sample scales considerably in excess of those used in literature studies ($\approx 10\text{cm}$).

4.2 Characterising contrast between root aerenchyma and flooded soil in reconstructed μ-CT data of rice (*Oryza sativa*)

4.2.1 Materials and methods

In order to assess the degree of contrast between the gas continuum of rice roots and saturated soil phases in reconstructed μ-CT data, a validation experiment was carried out. A polymer growth chamber of 105mm internal diameter and 200mm height was constructed, allowing flooded soil conditions to be maintained throughout the growth period. The growth medium was a Eutric Cambisol of the Denbigh series, sourced from a field site at the University of Bangor, Gwynedd, UK ($53°13'54'', 4°0'54''$), desiccated at $23°\text{C}$ for 72h before sieving manually at a mesh diameter of 5mm in order to remove larger mineral phases which might cause scattering artifacts in reconstructed data. Water was added to the sieved soil until 100% saturation was reached, following which the flooded soil was manually stirred for 10min to remove structure, homogenising the medium. This process approximates the *puddling* procedure used across Asia to prepare soil for rice agriculture [De Datta and Sharma, 1985]. After a 1h settling

period, standing water was removed from the surface of the soil, and the saturated soil and water mixture introduced to the growth chamber. The chamber was filled to a level $\approx 5\mathrm{cm}$ below the opening, with a surface water layer of depth $\approx 2\mathrm{cm}$ maintained throughout the growth period. Seeds of *Oryza sativa cv. Nipponbare* were pre-treated at $55^{\circ}\mathrm{C}$ in order to break dormancy, following which 8 seeds were planted to the surface of the soil. Plants were grown in a glasshouse for 35 days, maintained at a temperature range of $25 - 28^{\circ}\mathrm{C}$, following which the growth chamber was transported for imaging.

Images were acquired using a Nikon/Metris hutch $\mu-\mathrm{CT}$ scanner, with a Perkin Elmer 1621, 2096×2096 element flat-panel detector (Perkin Elmer Inc., Cambridge, UK) and cesium iodide (CsI) scintillator. A total of 3142 projections were generated at an accelerating potential of $160\mathrm{kV}$ and a tube current of $186\mathrm{mA}$ using a tungsten (W) target, (in order to satisfy the requirement for $> 10\%$ X-ray transmission). Volumes were reconstructed using a Feldkamp back-projection algorithm implemented in the Metris CT Pro software package (Nikon Metrology, Tring, UK), generating $16-\mathrm{bit}$ datasets with an isotropic voxel resolution of $58.8\mu\mathrm{m}$.

Root structures were segmented using a global thresholding routine in the image-processing package FIJI. Upper and lower values of attenuation coefficient were adjusted in order to maximise the visibility of root material whilst avoiding classifying soil phases. In order to remove voxels representing gas bubbles, which had been co-classified with aerenchyma due to a near-identical attenuation coefficient, a sphericity constraint was applied using the *analyse particles* plugin in FIJI to filter out discrete, quasi-spherical voxel sets.

4.2.2 Results and discussion

Figure 4.3 shows a magnified x, y slice through the reconstructed data, showing clearly the cross-sections of numerous roots, with a magnified sub-frame clearly demonstrating the visibility of internal structure, including the central stele. Beneficial contrasting is apparent between the aerenchymous region of the cortex and the surrounding phases. Figure 4.4 shows a 3D rendering of the RSA extracted using simple global thresholding methods, with the tiller positions of each plant superimposed for reference. It was evident that some root regions were not extracted using the global thresholding protocol, and that moreover, the high planting density had led to constraint by chamber walls, as well as extensive inter-growth of roots from different plants. Nonetheless, given the relatively large diameter of the growth chamber compared to other studies (see Table 2.1), the extensivity of extracted RSA compares very favourably with the results of other studies (see Figure 2.2 in Chapter 2). This is particularly notable given the simple global thresholding routine used, a class of segmentation approach that is generally considered significantly too simple for root segmentation [Flavel et al., 2012].

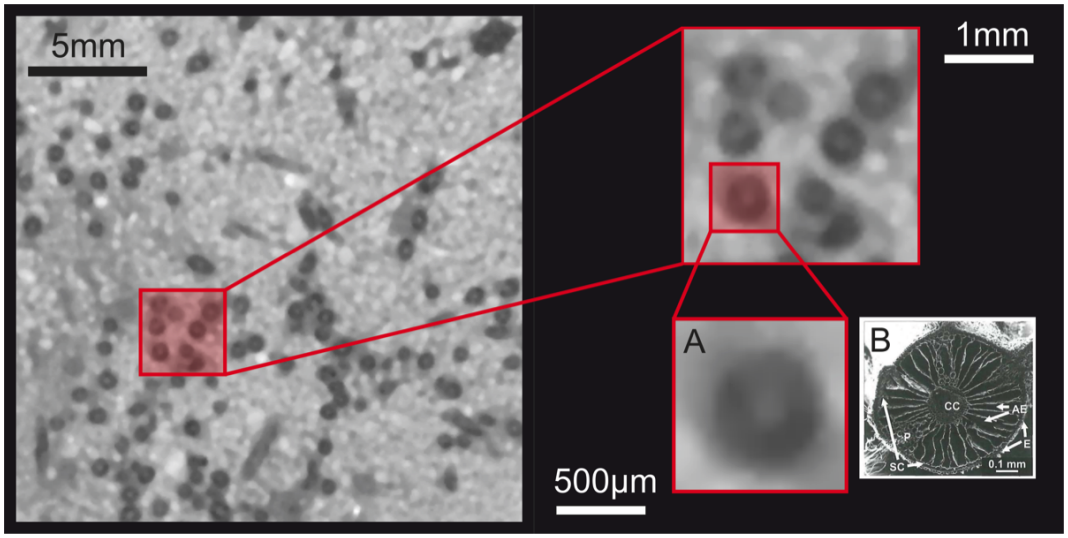

Figure 4.3: Figure clearly shows root cross-sections, well-distinguished from the surrounding soil phases. Frame (B) shows an SEM image of a mature rice root cross section, with aerenchyma (labelled AE) clearly visible surrounding a fluid-filled stele (reproduced from *Butterbach-bahl et al.* [Butterbach-Bahl et al., 2000]) Comparing the image with the single root cross-section for the CT data shown in (A), it is evident that the gas phase is responsible for the favourable contrast with the soil. By comparison, the stele region has a very similar attenuation coefficient to the surrounding soil.

4.3 Optimisation of imaging parameters for quantification of RSA traits using a large-sample μ-CT protocol

Given the favourable performance of aerenchymal contrasting in growth chambers of $\approx 11\text{cm}$ diameter, an experiment was designed to benchmark the performance of different imaging and reconstruction modes at larger sample sizes ($\approx 21\text{cm}$). The aim was to robustly determine a set of parameters for imaging and reconstruction, in order to optimise image quality and root extraction rate against scan time. With optimal protocol parameters, and the extraction rate validated against values from destructive sampling, the final objective was to apply the protocol to two contrasting rice genotypes, assessing the potential of large-sample imaging for non-destructive phenotyping of root angle traits in low-P soil.

4.3.1 Materials and methods

Rice was planted to growth chambers according to the protocol described in Section 4.2.1. For this experiment, the chamber diameter was increased to 21cm, giving a full-field image resolution of $\approx 100\mu\text{m}$ using the 2096×2096 element flat-panel detector available. A rice variety (*Oryza sativa cv Varyla*) was provided by collaborators at the Japan International Research Centre for Agricultural Sciences (JIRCAS), being a comparatively poor-performing genotype in low-P conditions. A single pre-germinated seed was planted to the soil surface of the chamber

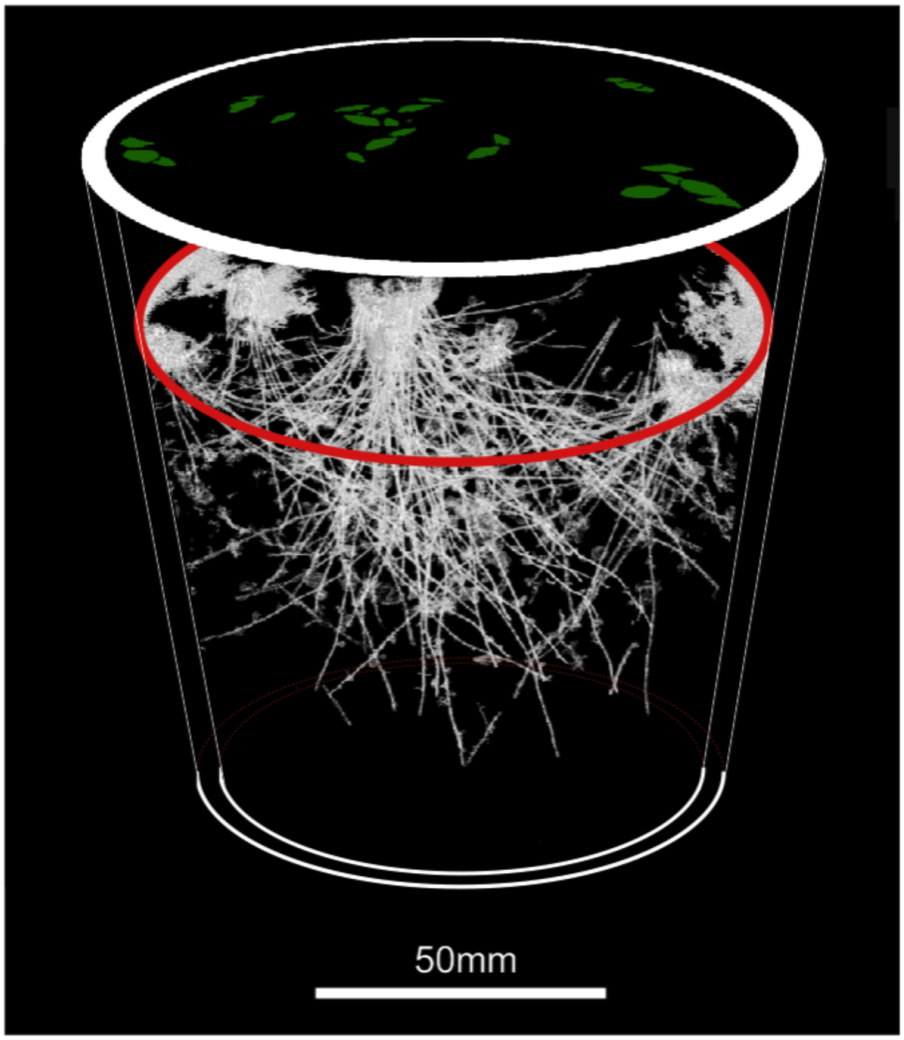

Figure 4.4: 3D root architecture of rice *Oryza sativa cv Nipponbare* extracted from raw data using global greylevel thresholding. Positions of tillers are shown in green, with the soil surface indicated in red.

in a central position.

The growth period was 5 weeks, after which the chamber was imaged using the $445\mathrm{kV}$ Nikon Hutch μ-CT scanner at the $\mu - \mathrm{VIS}$ centre.

Benchmarking μ-CT imaging modes

The following contrasting imaging modes were compared:

- **Full-field** imaging of the entire chamber, using a 2096×2096 element flat panel detector, for a voxel resolution of $106.2\mu\mathrm{m}$. 3142 radiographs were acquired at 8 frames per projection (FPP), representing a modest compromise between scan duration and artifact reduction, for a total scan time of $0.94\mathrm{h}$.
- **ROI** imaging of a central sub-region with diameter $\approx 10.5\mathrm{cm}$, situated concentric to the chamber circumference and extending down $\approx 9\mathrm{cm}$ below the soil surface, for a voxel resolution of $53.8\mu\mathrm{m}$. 9000 radiographs were acquired at 16 frames per projection (FPP), representing a heavy weighting towards image quality at the penalty of long scan time of $5.4\mathrm{h}$.
- A 27-slice scan acquired using a **curved linear detector array** (CLDA). The curved design of the CLDA ensures an isometric source-to-detector distance for all detector elements, allowing deeper elements to be used which effectively eliminate the deleterious sampling of scattered photons. For imaging of higher density samples, for which scatter-related artifacts such as noise and streaks can negatively impact upon resolution, CLDA detectors increase CNR and SNR relative to flat-panel scans. However, because a complete set of angular projections yields only a single x, y slice, acquisition times for entire volumes can be many orders of magnitude greater than for flat-panel scans. For this reason, only 27 slices were acquired, with 2001 radiographs and no frame averaging representing a heavy weighting towards scan-time reduction. Nonetheless, the scan time was still $3.9\mathrm{h}$

Table 4.1: Scan metadata for scans of *Varyla* in $21\mathrm{cm}$ diameter growth chambers.

Scan type	Spatial res. (μm)	kV	mA	Filter	Duration (h)	Projections	FPP
Full-field	106.2	320	279	1mm copper	0.94	3142	8
ROI	53.8	320	279	1mm copper	5.4	9001	16
CLDA	120.16	320	312	2mm copper	3.9	2001	1

Scan metadata for all scans are shown in Table 4.1. For each dataset, a single slice situated $\approx 25\mathrm{mm}$ below the soil surface (Figure 4.6) was reconstructed using the Metris CT Pro FDK

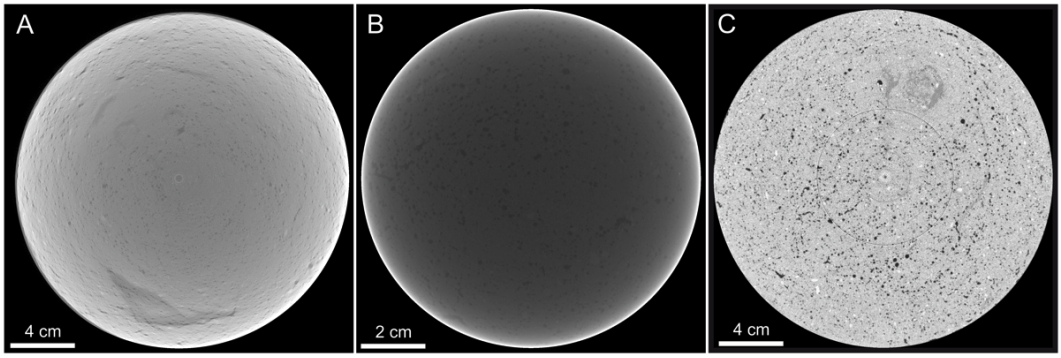

Figure 4.5: Slices through raw data with no beam hardening correction or grey-level normalisation applied. (A) Full-field, (B) ROI, (C) CLDA. The beam-hardening artifact is clearly visible in frames (A) and (B).

algorithm, according to 5 progressively greater degrees of beam-hardening correction. Representative slices of raw data with no correction applied are shown in Figure 4.5. The degree of correction was determined by discrete presets within the software. The magnitude of the beam hardening correction for each reconstructed slice was quantified in a similar manner to Section 2.3.5 on page 69. Because in this instance, no homogenous polymer region was present in reconstructed data, the beam hardening artifact was quantified by averaging the attenuation coefficient profiles along lines bisecting the data at $0°$, $90°$, $45°$ and $135°$ to the x axis. Curves were fitted to the data in order to better visualise the artifact and compare severity between reconstruction presets. 3^{rd} and 6^{th} order polynomials were fitted to data for the CLDA data and ROI/full-field datasets respectively. Plots and fits are shown in Figure 4.7. Plots showing the relationship between CNR and SNR are found in Figures 4.8 and 4.9. CNR and SNR were estimated according to Equations 2.2 and 2.3, with values of mean gas and soil/fluid attenuation coefficient ($\overline{\mu_f}$ and $\overline{\mu_b}$ respectively) sampled using 10 circles of 20 voxel diameter sited in randomly selected gas bubbles, and 10 randomly situated in the soil/fluid phase. All sampling regions were constrained within a central circle of 200 voxel diameter, where variance in attenuation coefficient due to the beam hardening artifact was at a minimum (see Figure 4.7).

Extracting primary RSA from reconstructed μ-CT data

Samples were reconstructed with optimal parameters based on quantification of the beam hardening artifact, and the values of CNR and SNR (see Section 4.3.2). The spatial resolution of the resulting data was insufficient for the application of global thresholding method used in Section 4.2.1, with root cross-sections difficult to differentiate from gas bubbles of similar diameter within static x, y slices. However, by *rastering* through x, y slices of reconstructed data in the z direction, the positions of primary root cross sections were easily identified. Figure 4.11 explains the concept of rastering, demonstrating schematically how the method fa-

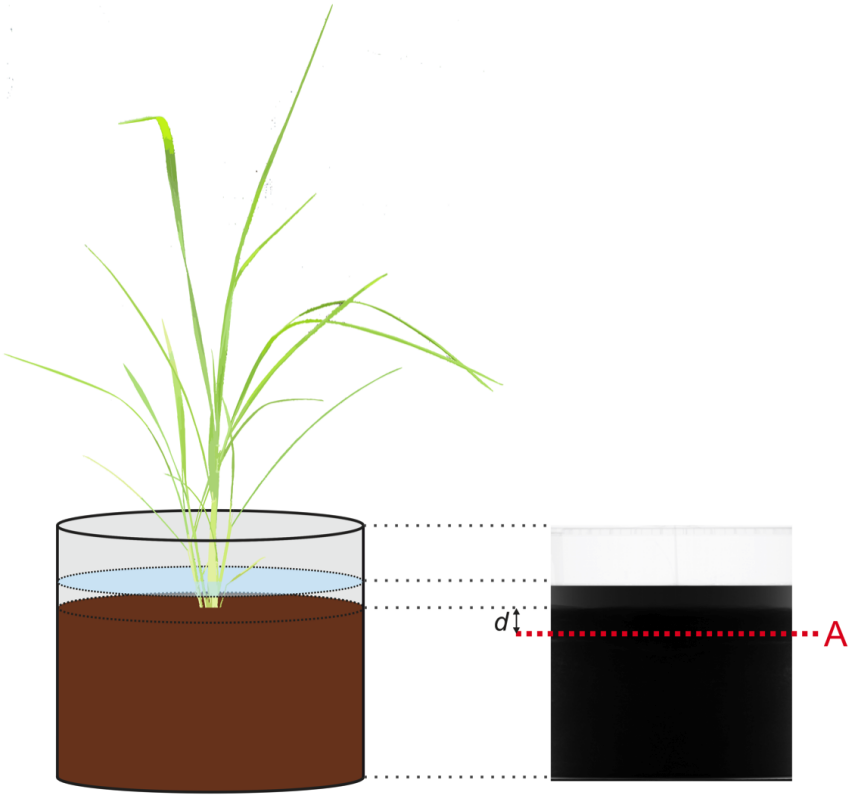

Figure 4.6: The xy slices used for quantification of the beam-hardening artifact were defined at $d \approx 2.5\text{cm}$ below the soil surface in each sample. The figure shows a schematic of the growth chamber, with corresponding 2D radiograph. Line (A) shows the approximate position of the slice.

cilitates user-identification of root cross-sections and rejection of gas bubbles. Because global thresholding and SRG methods were found to be unsuitable, a semi-manual protocol was applied to segment the root architecture. Using AVIZO 6 image-analysis software, the positions of root cross-sections were user-defined at intervals of $\approx$ 20 voxels along the z axis of the dataset until, each root became indistinguishable from the soil and fluid phases. An interpolation algorithm was then used to fit curves through the indicated points, generating continuous root pathways. This protocol was carried out for ROI and full-field datasets. With only 27 slices, the z dimension of the data acquired using the CLDA was not sufficient allow root detection.

Skeletonising root architectures in FIJI allowed root lengths to be estimated. Each skeletonised root was quantified by both total voxel count (n_{voxels}) and a straight-line trignometric approximation between the seed position and the furthest extent of each root. Figure 4.13 illustrates considerations in selecting a suitable scaling parameter (τ_s) to convert voxel count to root length, using a simple function ($L_{root} = \tau_s \times n_{voxels}$). If voxels in a skeletonised root pre-

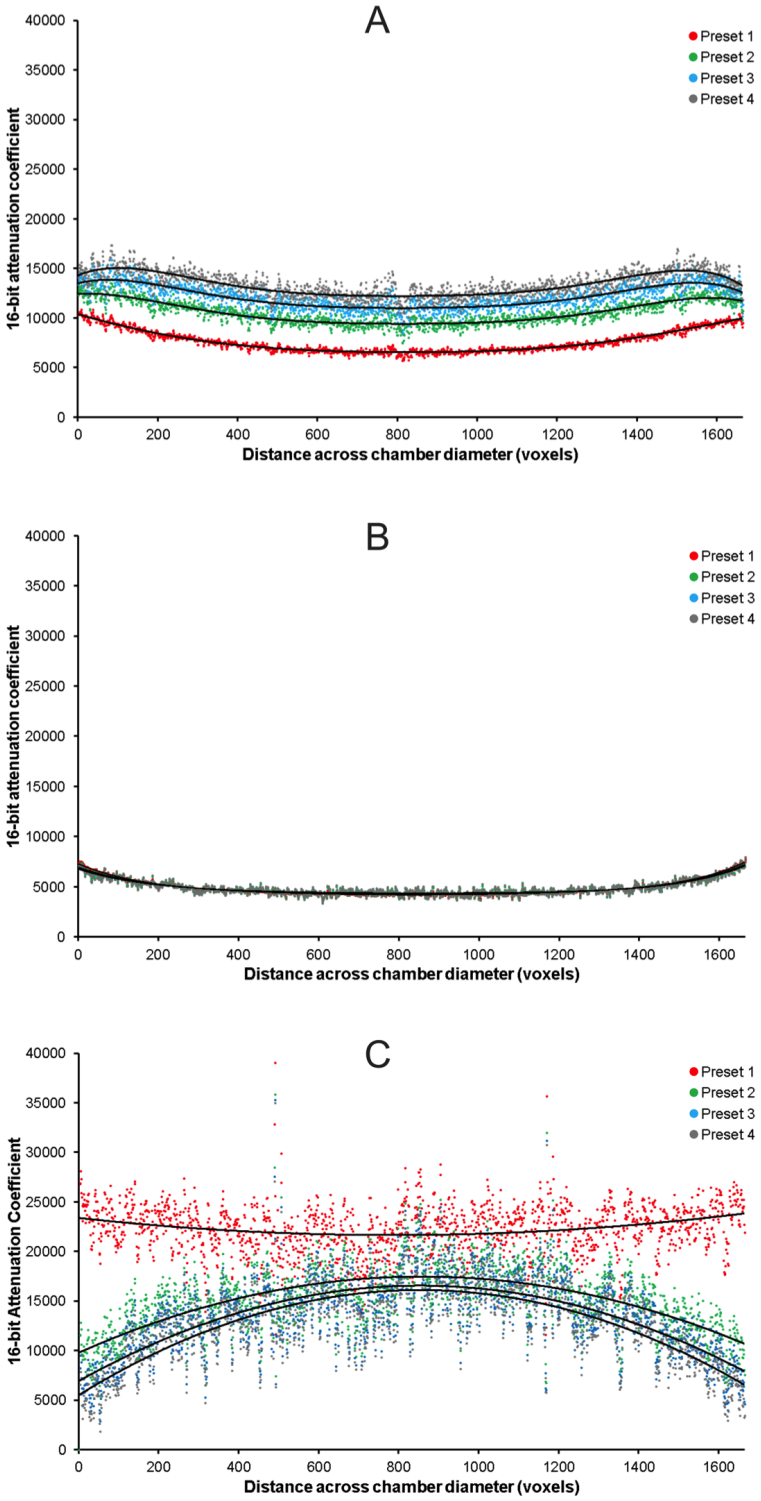

Figure 4.7: Scatter plots of attenuation coefficient along lines bisecting raw, un-normalised $16-\mathrm{bit}$ reconstructed data. Plots are shown along the same line for four beam hardening correction presets, with intensity of the correction increasing from 1 (uncorrected) to 4. Also shown are lines of best fit, demonstrating the characteristic cupping artifact. (A) Full-field, (B) ROI, (C) CLDA.

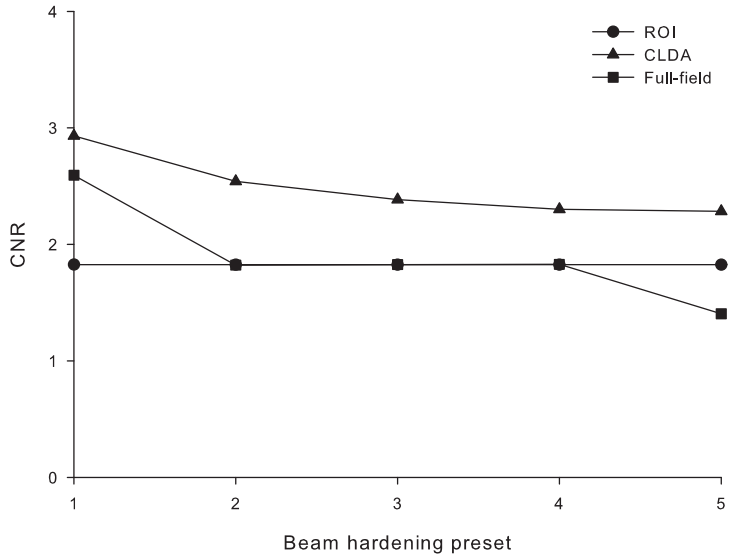

Figure 4.8: Figure showing the relationship between CNR and the degree of beam-hardening reduction for ROI, full-field and CLDA data

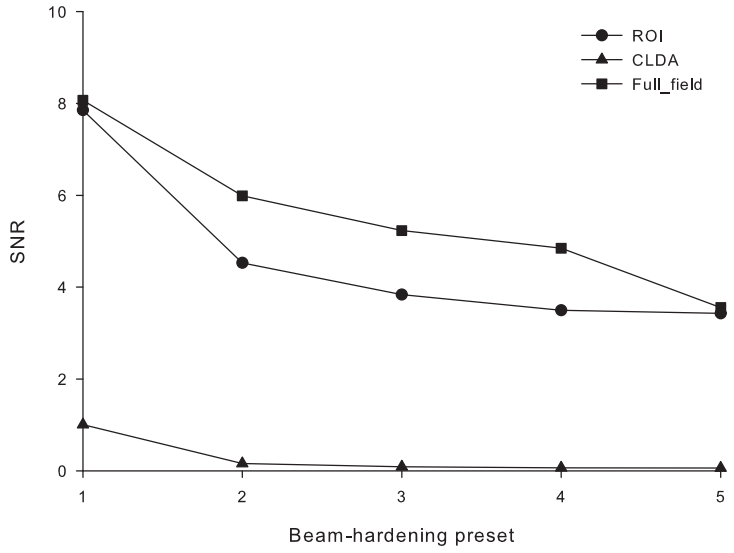

Figure 4.9: Figure showing the relationship between CNR and the degree of beam-hardening reduction for ROI, full-field and CLDA data

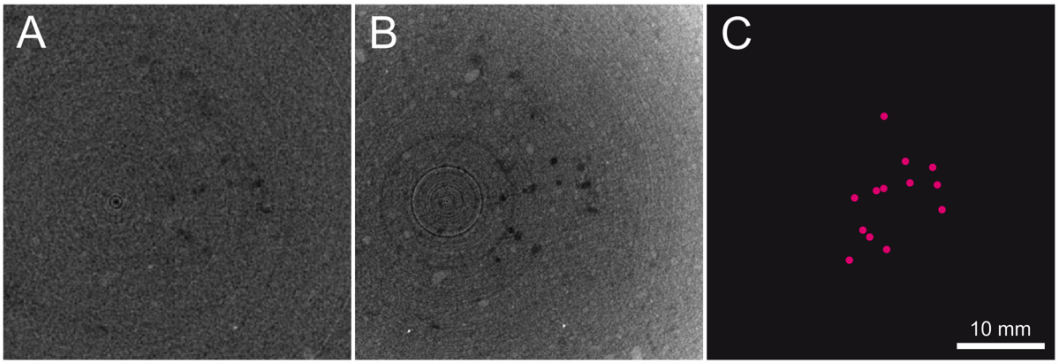

Figure 4.10: Sub-regions of reconstructed slices from (A) full-field data and (B) ROI data, showing root cross sections at a position $\approx 6\text{mm}$ beneath the seed position. Positions are shown schematically in (B).

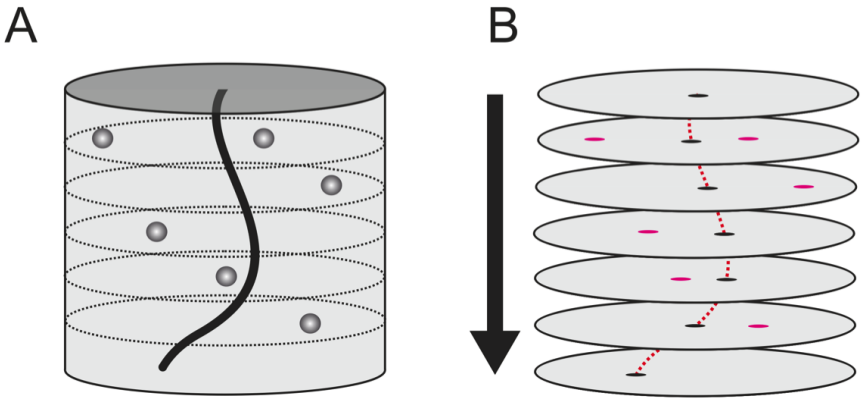

Figure 4.11: (A) Gas bubbles (represented in grey) of similar diameter to primary roots (represented by the black line) are often indistinguishable from root cross sections in static x, y slices of reconstructed data. (B) The connectivity of the root (represented by the red line) over many slices allows the root positions to be differentiated from those of the gas bubbles (represented in pink) by rastering through the data.

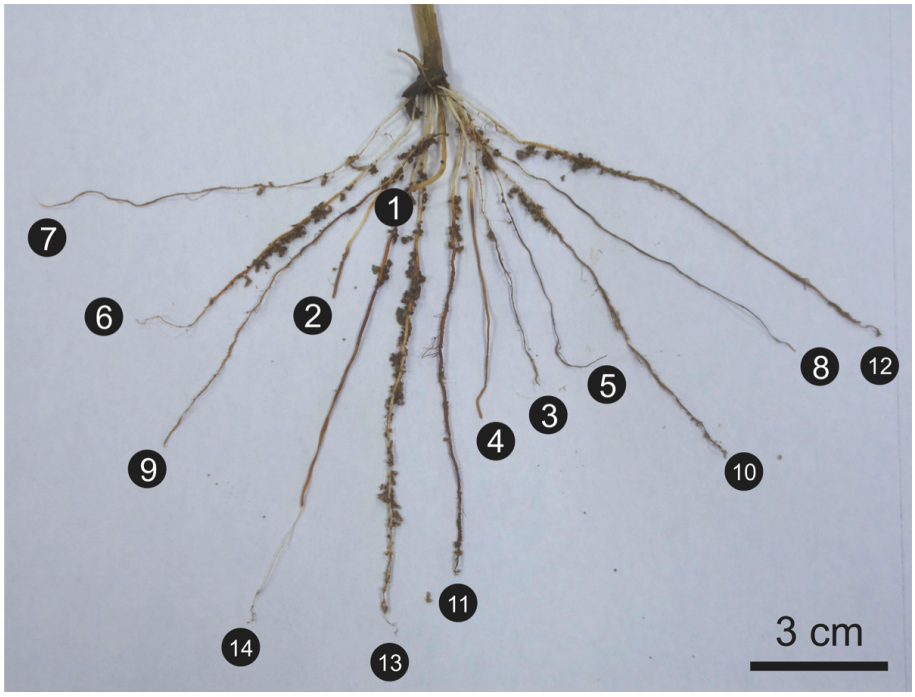

Figure 4.12: Root system of 5-week old rice plant *Oyyza sativa cv Varyla*, following post-scan root washing. Labels indicate the length order (increasing from 1-14).

dominantly mate face-to-face, then the most suitable scaling parameter would be ($\tau_s = l_{x,y,z}$), where ($l_{x,y,z}$) is the isotropic voxel resolution, such that the root length (L) is approximated by,

$$L_{root} = l_{x,y,z} \times n_{voxels}, \tag{4.2}$$

however if the majority of voxels mate corner-to-corner, a more suitable value would be,

$$\tau_s = \sqrt{(3 \times {l_{x,y,z}}^2)}, \tag{4.3}$$

Since in practice, both face-to-face and corner-to-corner mating occurs in the skeletonised root filaments, a generally appropriate general scaling factor is given by,

$$\tau_s = \frac{\sqrt{(3({l_{x,y,z}}^2))} + (l_{x,y,z})}{2}, \tag{4.4}$$

These values were compared against lengths measured following careful washing of root architecture from surrounding soil (see Figure 4.12. Photographing the root system orthogonal to the plane in which they were carefully arranged allowed lengths to be measured using FIJI by manually tracing the roots with the aid of a graphical tablet. Figure 4.12 shows the washed root system, with roots labelled according to length

4.3.2 Results

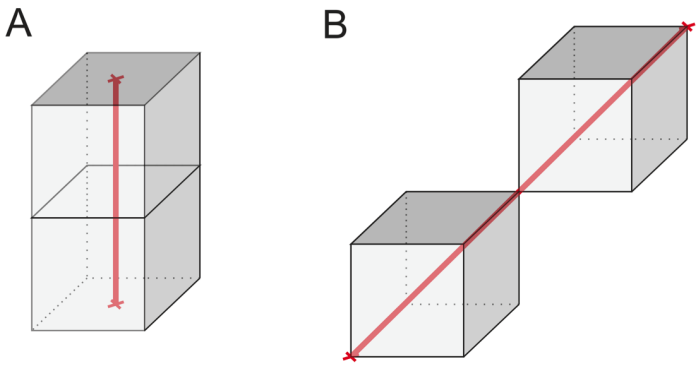

Figure 4.13: The accuracy of voxel count as an estimator of length in a skeletonised filament depends on the length scaling factor (l_s) used, and the morphology of the filament. (A) In straight filaments of connected voxels aligned with the x, y or z axes, the length is best approximated by multiplying the voxel count (n_{voxels}) by the voxel edge length ($l_{x,y,z}$) (assuming isometric voxels). (B) However, if voxels exhibit a high degree of tortuosity, such that most voxels make contact on corners rather than faces, the use of $l_{x,y,z}$ as a scaling factor will result in length underestimation.

Figure 4.14 shows extracted RSA revealed by ROI and full-field scans. Overlaying the two regions (Figure 4.14-C) demonstrates the congruence of the RSA determination between the two imaging modes. Despite the user-supervised nature of the segmentation method, it appears to be an accurate means by which to determine the growth paths of primary roots. 14 roots were detected in the ROI and full-field data, a figure validated by the washing study. Evident in Figure 4.14-C is the greater root length revealed by the full-field scan. The percentages of the total validated length estimated using voxel-counting and straight line methods were 92.0% and 87.1% respectively.

Lateral roots were not observed in the μ-CT data, but the washed roots (shown in Figure 4.12) show scarce evidence of lateral root development. It was thus not possible to determine whether or not lateral root material could be detectable in data acquired using the parameters and spatial resolutions utilised in this study.

4.3.3 Discussion

The study was extended to consider a growth chamber of $\approx 21\text{cm}$ diameter, revealing that primary roots were still detectable as a consequence of the aerenchymous gas continuum. Of the three imaging modes benchmarked to assess performance, the CLDA detector generated data with the highest CNR, though the SNR was high compared to scans acquired using the flat-panel detector (Figure 4.8). This was expected, since to prevent excessive acquisition times, no frame averaging was applied to the radiographs, compared with 16 frames-per-projection gen-

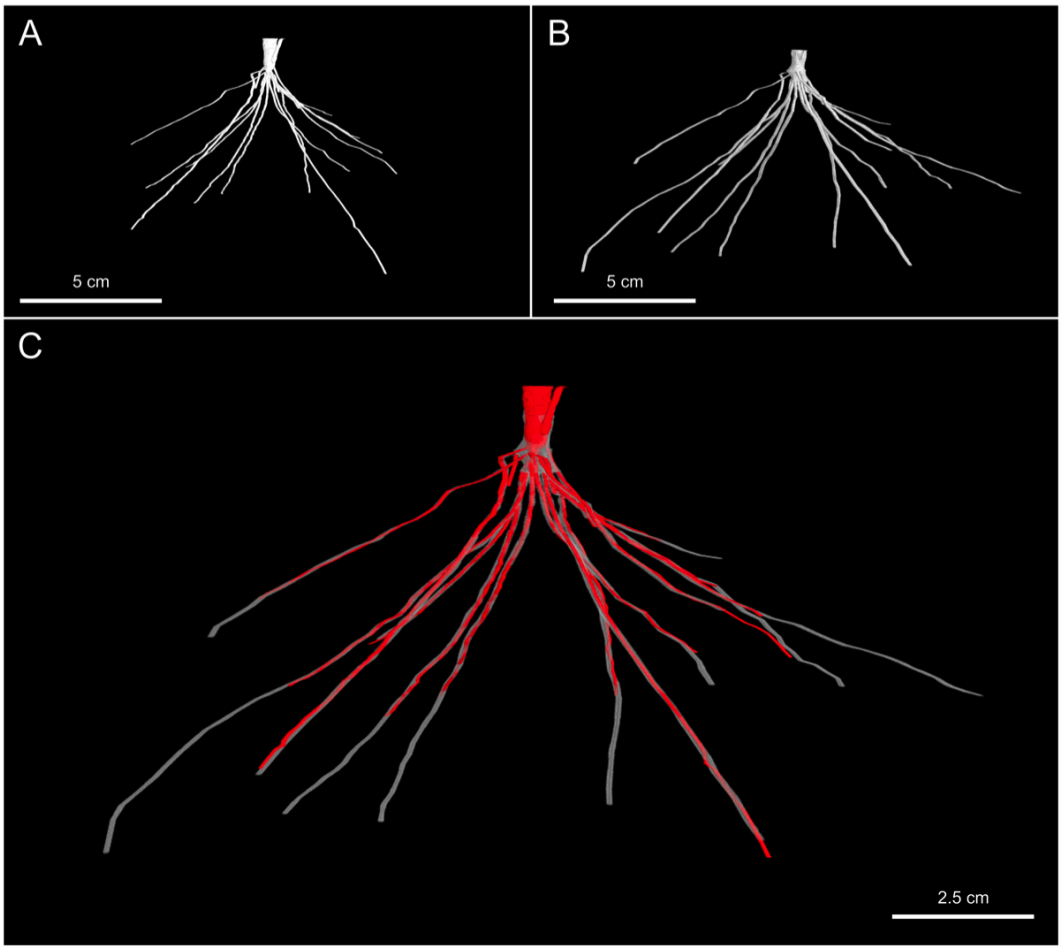

Figure 4.14: Figure shows segmented primary root paths of *Varyla* grown for 5 weeks in $21\mathrm{cm}$ diameter growth chambers. (A) Root architecture extracted from ROI scan, (B) architecture extracted from full-field scan, (C) overlay showing both congruence of extracted root paths between the two conditions, and the enhanced capture of root length in the full-field data.

erated during the ROI scan and 8 for the full-field data. Despite the comparatively high CNR achieved using the CLDA, the limitation of low-slice count, resulting from the 1D precluded the use of rastering. As a result, it was not possible to reliably differentiate between root cross sections and gas bubbles.

Quantification of the beam hardening artifact for all beam hardening reconstruction (BHR) presets is shown in Figure 4.7 on page 109. Figure 4.7-C shows clearly the comparatively greater image noise for the CLDA data, due to the lack of frame averaging during acquisition. The beam hardening characteristic of the CLDA data demonstrated the classical parabolic 'cupping' artifact, with the BHR presets only serving to invert the characteristic, resulting in a more severe artifact. Figure 4.7-B shows the data for the ROI scan, with the large number of projections and averaged radiographs having minimised image noise. The beam hardening artifact was also mild compared to the other data, with the same parabolic characteristic. None of the presets appreciably reduced the artifact. Figures 4.8 and 4.9 demonstrate that in general, beam hardening corrections are achieved at the expense of decreased CNR and SNR, such that correction should only be considered if the artifact is severe, or if calibration of attenuation coefficients is a prerequisite of the experiment. Figure 4.7-A shows data for the full-field scan, demonstrating a parabolic beam hardening characteristic, which became bimodal with the application of beam hardening correction. The optimisation of BHR against SNR and CNR should be made with respect to the analysis which is to be applied to the data. For this application, where maximum image contrast for RSA extraction was the key requirement, the SNR and CNR cost of using BHR was unjustified.

Extraction of RSA from reconstructed full-field and ROI data using a semi-supervised protocol revealed good agreement between the two scans. The full-field scan had twice the field of view used for the ROI scan, resulting in a greater captured root length. Comparison of two digital root length estimation methods revealed it was possible to capture $> 90\%$ of the washed length using the full-field data. Failure to extract regions near root tips was expected, since aerenchyma formation is less advanced in younger root tissue [Butterbach-Bahl et al., 2000]. Because RSA extracted from the full-field data correlated well with that from the higher-resolution ROI scan, with a greater root length capture rate, the full-field parameters were deemed to be most suitable for assessment of root angles between genotypes. Since the acquisition times increase more than five-fold for ROI imaging, only the ability to detect fine roots would justify the use of this protocol.

4.4 The application of an optimised imaging and RSA extraction protocol to comparison of rice genotypes with differing performance in low-P soil

4.4.1 Introduction

Following establishment of a μ-CT imaging and image-processing protocol for large cylindrical samples, the methods were applied to measurement of rooting angles in two contrasting genotypes supplied by collaborators at JIRCAS. Extensive field trials at a JIRCAS field site in Tsukuba, Japan have determined one of the genotypes (*Oryza sativa cv Mudgo*) to be high yielding in low-P conditions, with a large explored root volume, whereas the other (*Oryza sativa cv Varyla*) is a comparatively poorly yielding variety under the same conditions. Destructive field-sampling suggests that *Mudgo* has a larger root volume than *Varyla*, but such sampling has not allowed quantification of root angles. In this section, the validated and robustly optimised large-sample imaging protocol is applied to the estimation of unconstrained root angle distributions.

4.4.2 Materials and methods

Seeds were prepared and planted to $21\mathrm{cm}$ diameter growth chambers according to the protocol described in Section 4.3.1, using the same low-P soil. The growth period was 5 weeks, following which both chambers were imaged using the full-field scanning and reconstruction parameters that were optimised as part of the same protocol. Figure 4.15 shows the samples in the as-scanned condition. Following imaging, the root systems were carefully washed (Figure 4.16). Data were reconstructed and analysed using parameters and protocols described for full-field data in Section 4.3.1. By defining a straight line between seed and root tip, the z length between the two points was used to trignometrically estimate the angle of each root to the horizontal.

4.4.3 Results

Figure 4.17 shows the primary RSA of the two genotypes. As indicated from field trials, the *Mudgo* sample had a greater root number, with 54 primary roots, compared to 29 for the *Varyla* sample. The scan data also revealed contrasting root angle characteristics. Plotting histograms of angle revealed the unimodal character of the *Mudgo* root angle distribution as compared to the more multimodal distribution of the *Varyla* sample. Total root lengths estimated using the rescaled voxel-counting method were $557\mathrm{cm}$ and $282\mathrm{cm}$ respectively. The two genotypes were thus non-destructively observed to possess very different primary rooting traits.

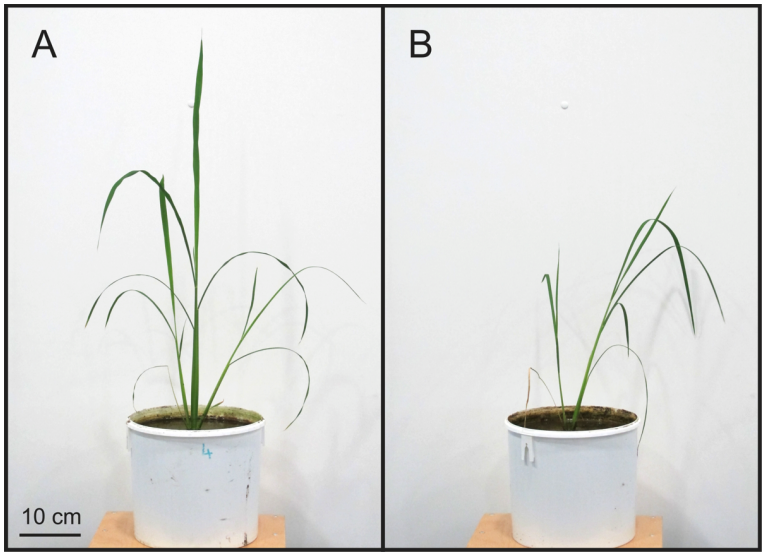

Figure 4.15: Aerial growth of 5-week old rice plants (A) *Oyyza sativa cv Mudgo* and (B) *Oyyza sativa cv Varyla* in the as-scanned condition.

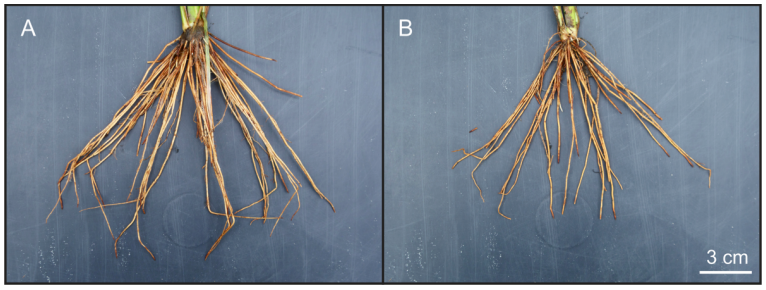

Figure 4.16: Root system of 5-week old rice plants (A) *Oyyza sativa cv Varyla* and (B) *Oyyza sativa cv Mudgo* following post-scan root washing. The greater root length of the *Mudgo* specimen is evident.

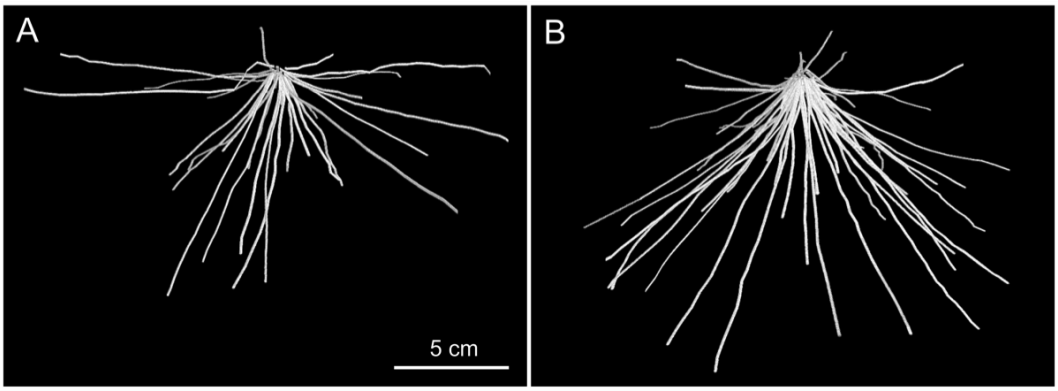

Figure 4.17: 3D root architecture of 5-week old rice plants (A) *Oyyza sativa cv Varyla* and (B) *Oyyza sativa cv Mudgo* grown in 22cm diameter growth chamber, as revealed by X-ray CT imaging. Differences in root number, length and angle distribution are clearly distinguishable.

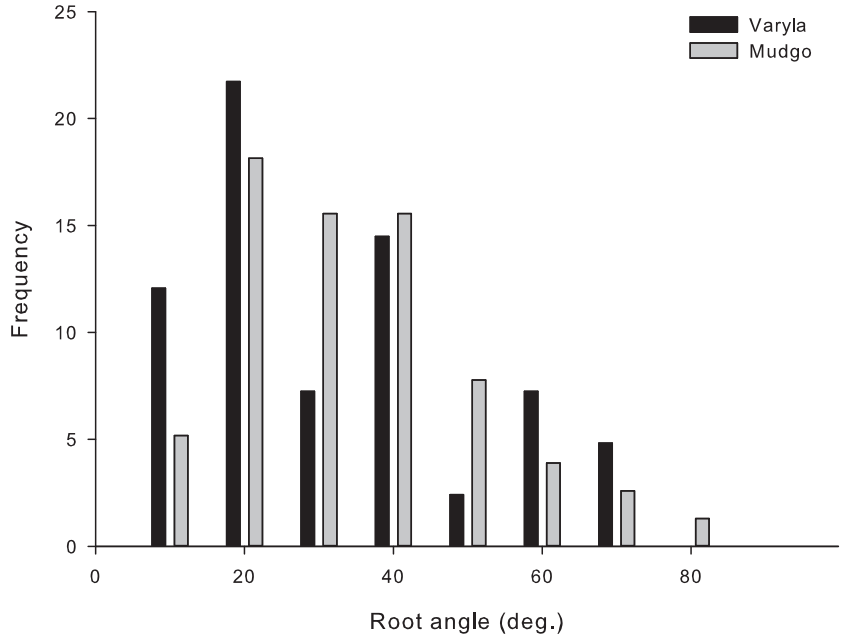

Figure 4.18: Normalised histograms of primary root angle for *Oyyza sativa cv Varyla* and *Oyyza sativa cv Mudgo* derived from analysis of CT data (plotted with bin-width of 10°). Angles are measured from a plane aligned with soil surface. Compared to the unimodal distribution of angles for *Mudgo*, the architecture of *Varyla* displays a more multi-modal characteristic, as suggested visually in Figure 4.17

4.5 Conclusions and future work

In this section, the use of a favourable attenuation-coefficient differential between aerenchyma and a saturated soil phase was validated for imaging at large sample scales in real soil. The well-cited domain literature suggests that the sample size of ($\approx 21\mathrm{cm}$) represents a new benchmark for real-soil imaging of RSA. The method was validated for path accuracy, and achieved a primary-root length extraction rate of ($> 90\%$) as compared to a root-washing method. Due to the low tortuosity of the primary roots, a straight-line approximation of root path was used to estimate root angles between two genotypes with contrasting low-P performance. The results corroborated with visual observations of the extracted RSA, revealing that the higher-yielding genotype (*Mudgo*) had a unimodal distribution of root angles, with most roots at $\approx 30^\circ$ to the horizontal, whereas (*Varyla*) had a more multi-modal characteristic, with peaks at $\approx 20^\circ$, $\approx 40^\circ$ and $\approx 60^\circ$. It was also determined that the total primary root length of the *Mudgo* sample was 97% higher than for *Varyla*.

The focus of this study was on validation and development of an optimised protocol for root angle measurement. The obvious extension of the presented work is the application of the protocol to genotypes of interest, in order to screen for a correlation between root angle and performance in low-P conditions. Through ongoing collaboration with JIRCAS, the opportunity exists to down-select genotypes from extensive field trials in low-P trials for this purpose. Appendix 8.3 outlines a protocol for the estimation of rice root angles in rhizoboxes, which was applied to four promising genotypes provided by JIRCAS. The results suggested characteristic genotypic angle distributions, which as in μ-CT data were detectable both visually and by plotting histograms. With the exception of *Oryza sativa cv Sadri tor Misri*, the measured angle distributions for the genotypes were all steep-weighted, as compared to the distributions for *Mudgo* and *Varyla* determined using μ-CT, which were both shallow-weighted. It is hypothesised that in rhizoboxes, shallow roots growing normal to the rhizobox faces are constrained by mechanical impedance to grow more steeply than would be accounted for by root gravitropism alone. This result indicates that quantification of angles in field conditions will be best achieved using μ-CT method of the kind detailed in this chapter.

A future large-scale study will compare repeats of $\approx 6 - 8$ genotypes suggested by field trials at JIRCAS to have distinctly different low-P root characteristics. Further to use in phenotyping, RSA data acquired using large-scale μ-CT imaging will be used to assess the influence of different traits on uptake of both P and zinc (Zn), in collaboration with both JIRCAS and the University of Cranfield.

Chapter 5

Synchrotron X-ray CT imaging combined with a novel root growth assay for *in vivo* elucidation of undisturbed root hairs in real soil

This chapter considers the application of μm-scale synchrotron X-ray computed tomography (SRXT) imaging to investigate the intact rhizosphere of living roots for the first time. A novel workflow is demonstrated for sample preparation, imaging, image processing and computational modelling of data, not only showing root hair structure in unprecedented detail, but suggesting via explicit nutrient uptake simulation the comparative influence of hairs and roots in different conditions.

The work is split into two sections:

- In the first, a literature review considers canonical methods of root hair characterisation. The first time imaging of wheat root hairs is then described, detailing the protocol used to grow and image hairs, the post-processing methods used to extract salient features from data, and the application of numerical modelling to real hair and soil interactions for the first time.
- The second section considers an array of secondary hypotheses raised by the first experiment, then demonstrates a number of novel approaches in order to improve the sophistication of the methodology.

5.1 Introduction

Root hairs are single-cell extensions initiating from the root epidermis, and are thought to increase uptake of poorly mobile nutrients from soil by increasing the absorptive surface area of the root network [Ma et al., 2001]. It is posited that the very small diameter of these structures allows them to forage the soil particularly efficiently for poorly mobile nutrients [Jungk, 2001]. Their particular significance for the uptake of P was suggested in seminal work by *Lewis and Quirk*, who observed depletion zones of the radioactive isotope ^{32}P around root hairs [Lewis and Quirk, 1967]. In addition to their contribution to P uptake, root hairs are known to act as sites for symbiotic interactions with organisms such as rhizobacteria [Mylona et al., 1995], and it has also been suggested that they may assist in the mechanical anchoring of plants into the soil matrix [Sieberer et al., 2005].

In the plants that form them, root hairs are generated in vast numbers. Early root-washing studies by *Dittmer* estimated that for a single, developing *Secale cereale* plant, each 24 hour period was responsible for the growth of 118 million hairs with a total length of 55 miles [Dittmer, 1937]. These lateral, tubular extensions of certain epidermal cells can reach extremely great lengths compared to their diameters [Sieberer et al., 2005]. As seen in Table 5.1, the mean diameters and lengths of root hairs vary substantially by species, with no particular correlation existing between the two dimensions. The later work of *Dittmer* found hairs of $370\mu\mathrm{m}$ length and $5\mu\mathrm{m}$ diameter in *Franxinus lanceolata*, whereas despite a substantially greater diameter of $14\mu\mathrm{m}$, root hairs of *Convolvulus arvensis* were on average only $80\mu\mathrm{m}$ long [Dittmer, 1949]. The spatial arrangement of hairs in the soil matrix also varies depending on species and environmental conditions, and paths can be tortuous as a result of root-soil interaction and the influence of mucilage [Peterson and Farquhar, 1996]. Though hairs investigated under the microscope are occasionally observed to be branched, the work of *Dittmer*, despite examining millions of hairs from hundreds of plants, never found evidence of a septate hair [Dittmer, 1949].

Root hairs reach maturity after a relatively short period compared to the lifecycle of the main roots. Early work by *McElgunn and Harrison* observed that the interval from emergence to cell death in root hairs of month old *Secale cereale* plants was of the order of two days [McElgunn and Harrison, 1969]. Later work by *Fusseder* indicated that the internal cytoplasmic structures of root hairs of *Zea mays* had begun to decay after the same period [Fusseder, 1987]. However, the cell walls were seen to remain in place for many days, despite the probable termination of uptake related to the decay of internal structures.

5.1.1 Root hair plasticity in response to abiotic stress

Table 5.1: Table following *Dittmer*, showing mean root hair diameters and lengths for a variety of different plant species [Dittmer, 1949].

Species	Avg. hair diameter on main root (μm)	Avg. hair length on main root (μm)
Equisetum arvense L.	15	1200
Agropyron elongatum	12	800
Agrostis astoriana	13	600
Avena sativa	14	1400
Eragrostis curvula	8	270
Secale cereale	15	1500
Cerastium arvense	12	750
Descurainia pinnata	7	350
Parosela dalea	15	110
Soya maz	17	240
Trifolia repens	8	250
Euphorbia albomarginata	9	300
Sium suave	8	150
Nepeta cataria	8	410
Plantango major	12	220
Tagetes patula	14	180

The environmental plasticity of roots and root hairs in soil has traditionally made it difficult to accurately measure branching characteristics and the chronology of developmental events [de Dorlodot et al., 2007]. It has long been known that RSA is a highly plastic trait, with genotypically identical specimens exhibiting large phenotypic diversity in response to differing nutrient stresses; a mechanism known as *trophomorphogenesis* [Müller and Schmidt, 2004]. In the case of P stress, a number of potential adaptions are possible, as seen in Figure 5.1. Of these adaptions, it was the observation that root hair density increases under low P conditions which first led to speculation that hairs primarily exist to enhance the efficiency of immobile ion uptake [Gilroy and Jones, 2000]. Since nutrients such as P and K are as immobile in the soil as they are essential for growth, the ability to respond plastically to pools of these nutrients is a highly beneficial trait for the majority of plants [Peterson and Farquhar, 1996]. The interception of immobile nutrients such as P can be greatly improved by upregulating the frequency and length of root hairs, as well as increasing overall root proliferation [Lambers et al., 2006]. Though such proliferation is generally thought to occur preferentially towards nutrient-rich patches, conflicting findings exist regarding whether the rhizosphere represents a zone of local depletion or increased concentration of essential nutrients, since both situations have been observed in studies [Hinsinger et al., 2005]. *Schottelndreier and Falkengren-Grerup* have suggested that this variability could either be the result of rhizosphere effects, or of preferential growth into nutrient rich regions [Schottelndreier and Falkengren-Grerup, 1999].

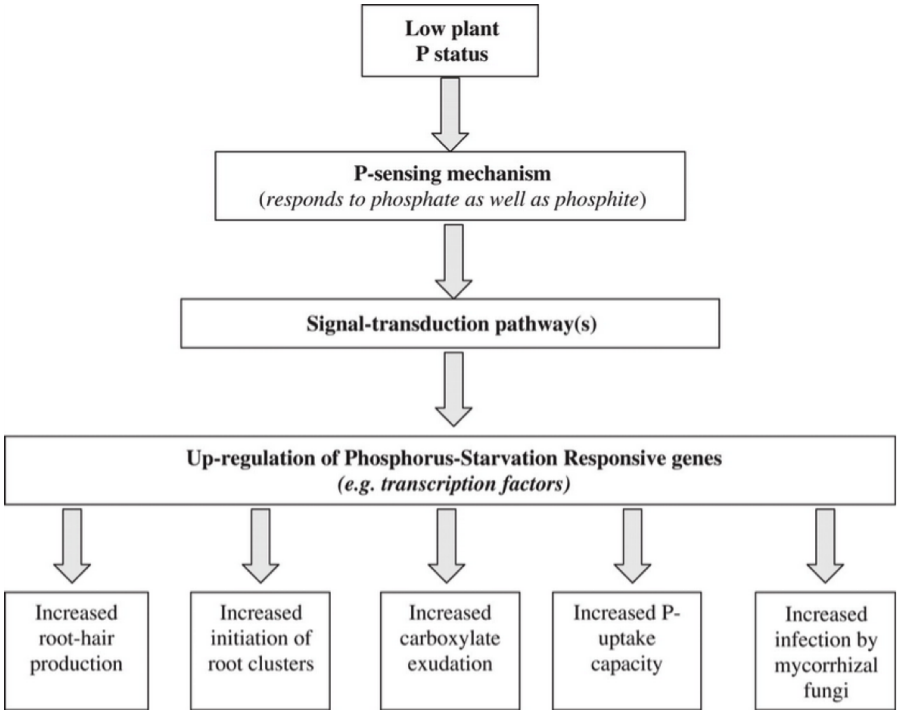

Figure 5.1: Figure from *Lambers et al.* showing plant responses to P limitation [Lambers et al., 2006]. Low P conditions result in a low plant-P status, which is sensed by the plant, resulting in up-regulation of a variety of species-specific P-starvation responses.

Studies of phosphate-driven plasticity have elucidated an array of physiological responses existing in both the morphological and architectural domains [Lynch, 1995]. The work of *Ma et al*, growing *Arabidopsis thaliana* in phytagel, found that during early developmental stages (< 7 days) root hair density did not differ significantly between low and high P conditions. However, by the 9 day point, it was seen that plants in low-P media displayed substantially higher root hair density, and that this density decreased logarithmically with increasing P concentration (see Figure 5.2 and Figure 5.3) [Ma et al., 2001]. Furthermore, there was found to be a uniquely strong relationship between P availability and root hair density, as compared with responses to all other nutrients in the study (see Figure 5.4) [Ma et al., 2001]. Work with mutants of the model plant *Arabidopsis thaliana* has also shown the profound contrast between hair formation in high and low P conditions (see Figure 5.5). Other studies have found root hair formation to be influenced by soil pH and Ca^{2+} concentration [Ewens and Leigh, 1985], as well as bicarbonate [Bergmann, 1958] and iron deficiency [Romheld and Marschner, 1981], but it is clear that the most dominant factors in trophomorphogenesis are availability and distribution of the essential nutrients N and P [Jungk, 2001; Osmont et al., 2007].

In controlling such adaptions, two way signalling via hormones and sugars between roots and the aerial tissue ensures that growth in both domains remains balanced [Jones and Ljung, 2011]. Nutrient homeostasis is regulated systematically, but evidence suggests that signalling

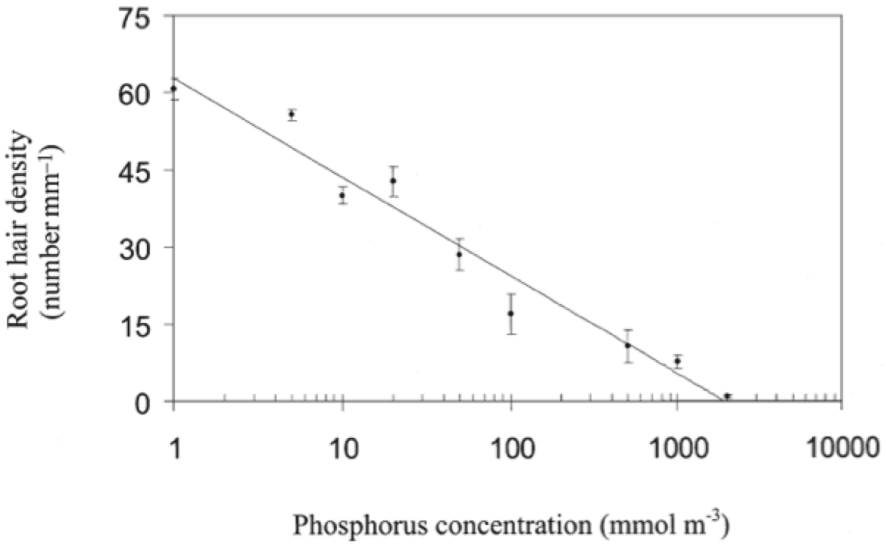

Figure 5.2: Figure from *Ma et al.* showing the regulation of root density in *Arabidospis thaliana* as a function of P concentration in the growth media. Hair counts are the means for six plants, and error bars represent SE [Ma et al., 2001].

responsible for morphological plasticity is controlled locally [Raghothama, 2000]. This has led to the hypothesis that external levels of certain specific nutrients (P and Fe) are sensed in tissues or individual cells, and not with respect to the systemic nutrient status of the plant [López-Bucio et al., 2003; Müller and Schmidt, 2004]. By contrast, other work has suggested that P concentration at root surfaces does *not* regulate hair formation, with systemic concentration instead being the significant parameter [Jungk, 2001]. Work by *Fohse and Jungk* demonstrated via split-root experiments that different root hair densities could be formed over regions with identical surface P concentrations, depending on the fraction of the surface to which the concentration was applied [Fohse and Jungk, 1983]. This strongly supports the hypothesis that up or down-regulation of hair density is not primarily a response to locally sensed P levels [Jungk, 2001]. Such experiments have established the necessity of a shoot-derived signal in order for root hairs to lengthen, but found that there can be additional enhancement in lengthening as a result of low root-P status [Jungk, 2001]. Though work is ongoing to trace the signalling pathways involved, it has been suggested that auxin is a leading candidate for the shoot-derived signal transporter [Lambers et al., 2006].

In *Arabidopsis thaliana*, the mechanism of root-hair response to low soil P is through increasing the number of files of trichoblasts (cells from which hairs initiate) in the developing roots, as seen in Figure 5.6 [Ma et al., 2001]. Individual trichoblasts do not necessarily always develop a root hair, with a study by *Ma et al.* showing that in high P media, the non-formation rate was 76%, and even in low P conditions, 10% of trichoblasts failed to produce hairs [Ma et al., 2001]. The development of extra trichoblast files in preference to 100% utilization of pre-existing tri-

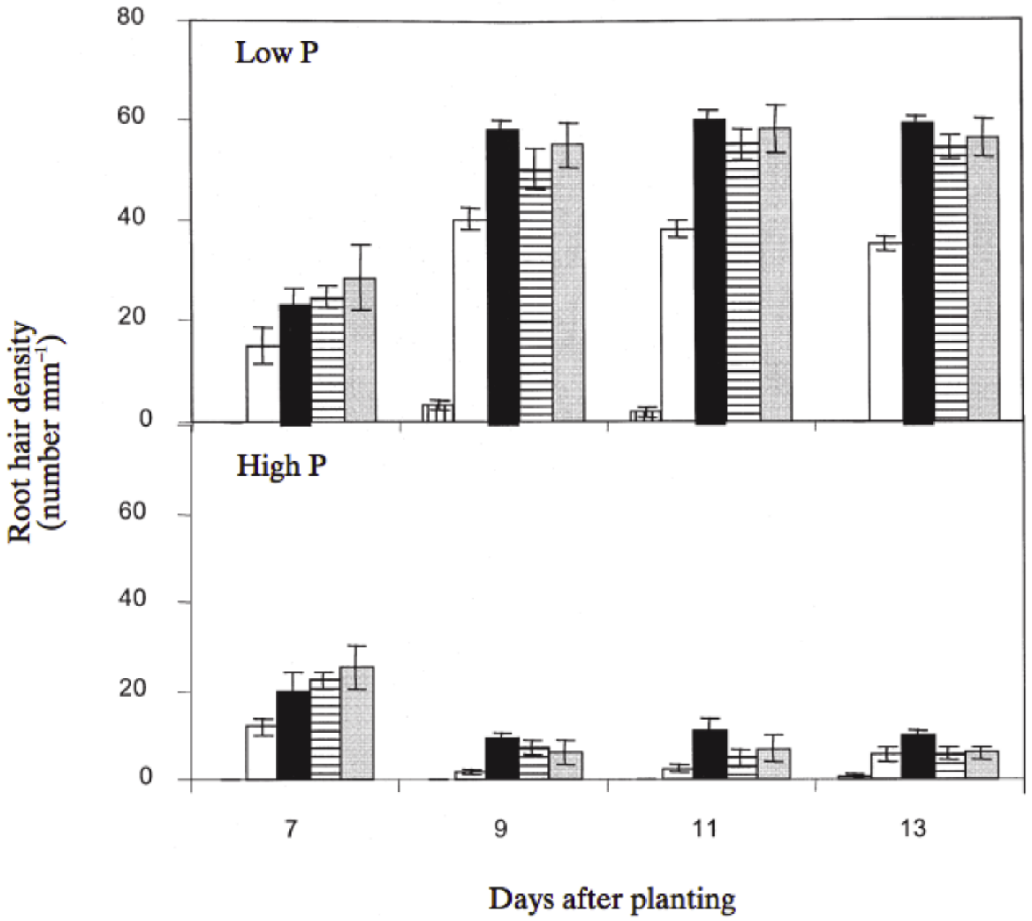

Figure 5.3: Figure from *Ma et al.* showing changes in root hair density of *Arabidopsis thaliana* over time. Plants were grown in either low P (1mmol.m^{-3}) or high P (1000mmol.m^{-3}) media, and hair density was measured over time on five 1mm root segments. The five bars at each time point (from left to right) represent the segments between $0-1$, $1-2$, $2-3$, $3-4$ and $4-5\text{mm}$ from the root tip respectively. Each bar is the mean for six plants, and error bars show SE.

choblast cells appears to confer an advantage in that greater longitudinal spacing lowers the competition for nutrients between neighbouring hairs [Ma et al., 2001]. Though much remains to be discovered about regulation of hair growth, it is apparent that the local cell response (elongation), and the developmental response (hair density) work together as part of an efficient P scavenging strategy in low-P environments [Ma et al., 2001].

It is not only soil nutrient concentrations that are responsible for trophomorphogenesis. Contact of roots with micro-organisms can significantly alter branching and elongation characteristics, a particular example of which is the infection of petunias with the bacterium *Ralstonia solanacearum*, which inhibits elongation and enhances branching of LRs [Zolobowska and Van Gijsegem, 2006]. Symbiotic relationships with ectomycorrhizae also suppress elongation whilst inducing branching of LRs which are markedly shorter than those of uninfected plants

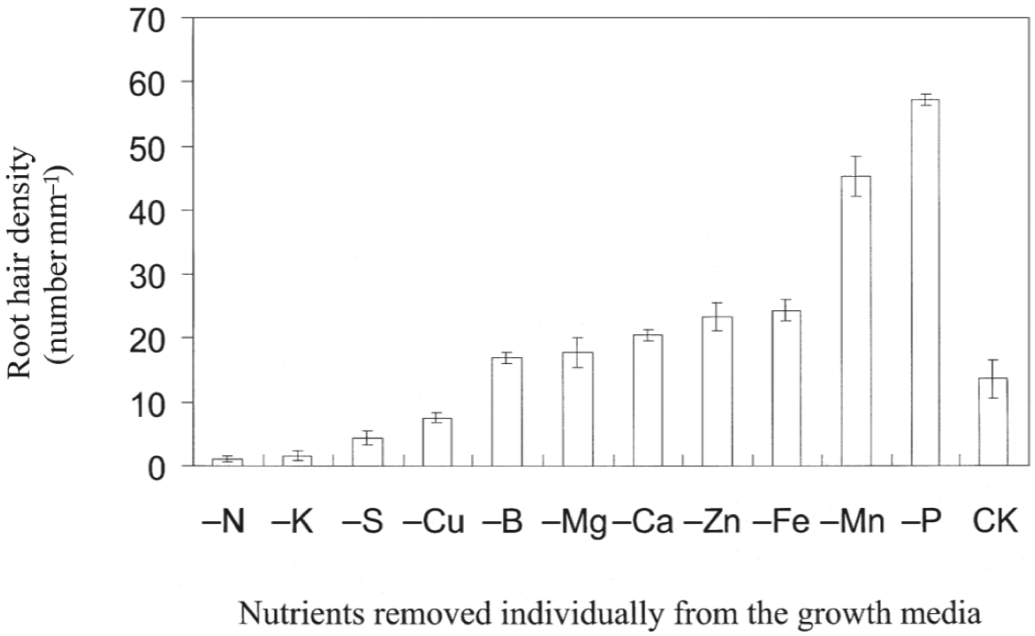

Figure 5.4: Figure from *Ma et al.* showing the effect on root hair density in *Arabidopsis thaliana* arising from removal of single nutrients from the growth media.

[Osmont et al., 2007]. Soil heterogeneity also controls root growth to a certain degree, in that preferential proliferation usually occurs into soil macropores. Such can be the extent of this correlation that in one study, 80% of roots were found to be situated within a 1mm distance of macropores [Hinsinger et al., 2005]. Many studies have found that root hairs also appear to preferentially infiltrate the pore spaces of soils [Michael, 2001] (though the difficulty of in-situ imaging requires cautious acceptance of such findings). One proposed mechanism behind this correlation is aeration-related dehydration, leading to water stress, increased metabolic activity, upscaling of ethylene synthesis and resultant root hair formation in response [Michael, 2001].

5.1.2 Canonical methods for investigating root hairs and their role in P acquisition

The length to which hairs can penetrate the soil surrounding the root is significant in quantifying the volume of soil from which uptake can occur, as well as the characteristics of the depletion profile in this region [Jungk, 2001]. Further complicating quantification of the uptake contribution of hairs is the temporally dynamic element that is present in reality. Since their effective life in the soil is so short (< 3 days), the active root hair zone is gradually displaced in the direction of root-tip growth, longitudinal to the root axis [Jungk, 2001]. Using a radioactive tracer, *Claassen et al.* showed that concentration at the root surface of the low-mobility nutrient potassium (K) reached a maximum less than one day after the emergence of root hairs, with the depletion zone radius growing from 0.5mm to 3mm over the following 3 days [Claassen

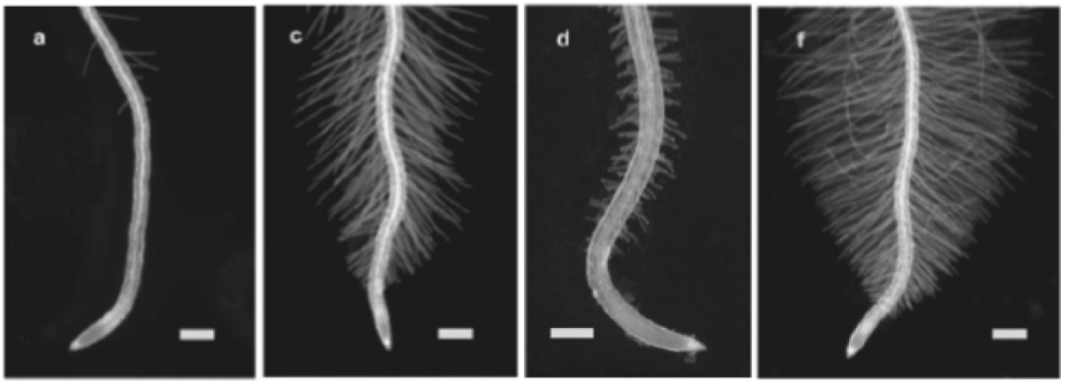

Figure 5.5: Figure from *Muller et al.* showing differences in hair formation between *cpc* and *ttg* mutants of *Arabidopsis thaliana* grown in different P conditions [Müller and Schmidt, 2004]. (a) *cpc* mutant grown in control P conditions, (c) *cpc* mutant grown in P-deficient media, (d) *ttg* mutant grown in control P conditions, (f) *ttg* mutant grown in P-deficient media. $\mathrm{Bar} = 250\mu\mathrm{m}$

et al., 1981]. The suggestion of these findings is that even if hairs remained active longer than a few days, their utility to the plant would be negated by the unavailability of poorly mobile nutrients [Jungk, 2001]. It remains to be determined whether hair senescence is driven by redundancy (when uptake rates become sufficiently small to render hairs ineffective) or whether the initiation of programmed cell death is unconnected to P availability.

Though the enormous increase in surface area afforded to the plant by the production of hairs has long been known to correlate with improved uptake of immobile nutrients [Bole, 1973; Gahoonia and Nielsen, 1998], the mechanisms by which hairs uptake phosphate have been more difficult to elucidate. Work by *Itoh and Barber* showed that discounting the influence of hairs in uptake models leads to systematic underestimation of influx as compared to uptake measured in real plants [Itoh and Barber, 1983]. To experimentally confirm the role of hairs in uptake, *Gahoonia et al* designed a vermiculite-filled growth chamber from which hairs could cross an air gap into a soil volume containing the radioactive phosphorus isotope $^{32}\mathrm{P}$, whilst roots were excluded (see Figure 5.7). Detection of $32\mathrm{P}$ in the aerial tissues after 2 days demonstrated conclusively the contribution of root hairs to total uptake by the plant [Gahoonia and Nielsen, 1998]. When 70% of the hairs from *Secale cereale* plants were able to access the radioactive chamber, it was seen that after 4 days, $^{32}\mathrm{P}$ from this region accounted for 63% of the total P measured in the shoots [Gahoonia and Nielsen, 1998]. Phosphate is thus clearly taken up in substantial quantities by root hairs, driven by an electrochemical gradient across the plasma membrane, maintained by H^+-ATPase. The work of *Moriau et al.* demonstrated that in *Nicotiana plumbaginifolia*, genes linked with H^+-ATPase activity are expressed in substantial levels, with expression peaking in young hairs, and falling off as they mature [Moriau et al., 1999]. This trend correlates with the temporal reduction in P uptake predicted in ageing hairs, as discussed previously.

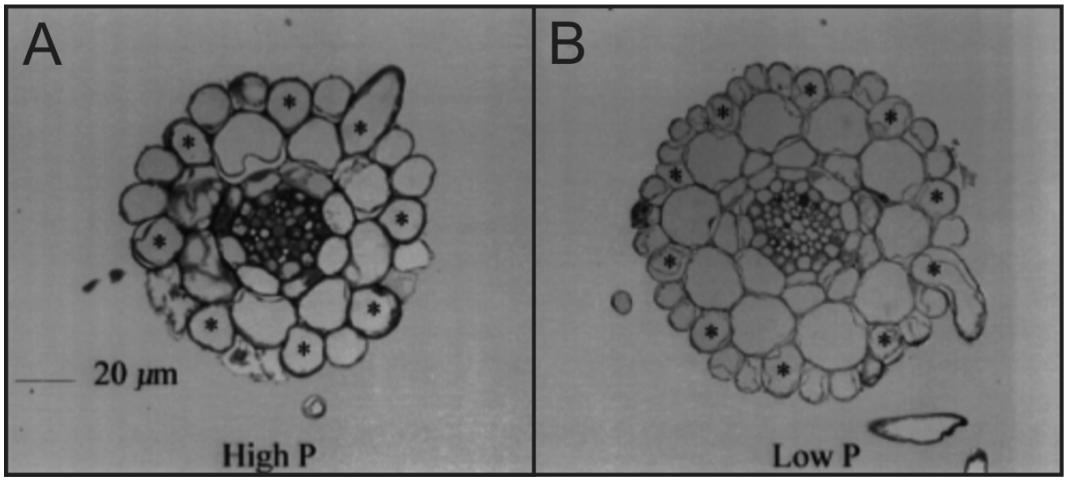

Figure 5.6: Micrographs from *Ma et al.* showing cross sections of *Arabisopsis thaliana* roots grown in different P conditions, taken $3\mathrm{mm}$ from the root apex. Trichoblasts are indicated by asterisks, and it can be seen that low P conditions have altered the trichoblast file count of the root. Magnification is $400\times$, low P media concentration is $1\mathrm{mmol.m}^{-3}$ and high P media concentration is $1000\mathrm{mmol.m}^{-3}$ [Ma et al., 2001].

5.1.3 The importance of hair/soil interactions in determining plant performance in low-P environments

Though split pot and air-gap protocols have helped understand the bulk contribution of hairs to nutrient uptake, virtually all our understanding about root hair morphology has come from roots grown on agar or phytagel plates [Maizel et al., 2011; Yi et al., 2010]. A different approach is microscopy of carefully washed root samples, which dates back at least as far as the work of *Dittmer* in the 1930's [Dittmer, 1937; Haling et al., 2013]. *Haling et al.* used this methodology, combined with measurement of resulting digital images in the open-source package FIJI, to characterise root hair lengths of barley cultivars grown under different degrees of soil compaction [Haling et al., 2013]. Though considering hairs grown in real soil, problematically such a method cannot provide information about explicit hair/soil interaction, and the likelihood of experimental artifacts is extremely high given the fragility of hairs [McCully, 1999]. Although the need to be able to finely examine crop root hair morphology is undoubted in understanding nutrient acquisition, neither destructive washing nor *in vitro* methods can examine the interplay between hairs and the extraordinary structural and biochemical heterogeneity that characterises real soils at all scales [Hinsinger et al., 2009]. However, cryogenic scanning electron microscopy (cryo-SEM) is one technique that has provided qualitative insight into the true complexity of hair/soil interactions, though the technique does not lend itself well to quantification [McCully, 1999; Yu et al., 2013]. By cryogenically cooling rhizosphere samples and sectioning them normal to a root axis, it is possible to use SEM to visualise hairs in the soil environment, as seen in Figure 5.8. The data shows that hairs growing into macropores initially exhibit the straight growth familiar from *in vitro* studies, but that one they begin to

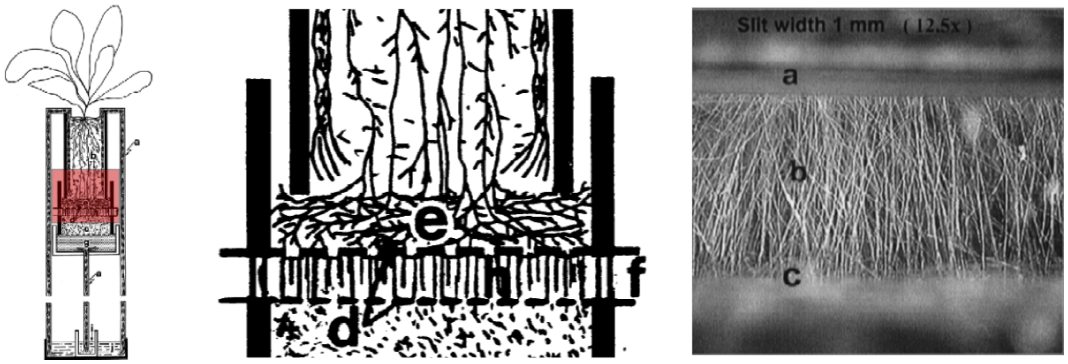

Figure 5.7: Figure showing air gap apparatus of *Gahoonia et al.* for estimation of the root hair contribution to overall plant P uptake [Gahoonia and Nielsen, 1998]. A root mat (e) grows against one side of a pair of meshes (d) which define an air gap (f). Hairs grow through the mesh, crossing the air gap (h) into a region of ^{32}P labelled soil. The micrograph shows root hairs (b) crossing the $1\mathrm{mm}$ air gap between the two meshes (a, c).

interact with soil, curling, distortion and branching result [McCully, 1999]. How such morphology might influence uptake is difficult to ascertain, particularly since the nature of contact with the soil, and with pore water, is likely to have a key influence on uptake kinetics. As discussed previously, attempts to model the influence of root hair traits on nutrient uptake have considered straight hairs within a bulk or highly ordered soil medium [Ma et al., 2001; Roose and Zygalakis, 2010], a situation which is clearly far from capturing even the structural complexity of hair/soil interactions, let alone the high degree of known temporal and spatial heterogeneity in water and nutrient distribution [Ashley et al., 2006; Carminati and Vetterlein, 2012]. Progressing understanding of the contribution different root hair traits make to uptake of immobile nutrients will require methods allowing direct observation of hair and soil interactions, preferably in a manner that allows the predictive power of computational approaches to be brought to bear on the data.

5.2 Guiding principles for experiment design

The technique of synchrotron X-ray computed tomography (SRXCT) holds promise for the investigation of intact rhizosphere structure and the root hairs which form such an important component of this region. The latest generation of SRXT beam-lines facilitate rapid image acquisition ($\approx 5\mathrm{m}$) at voxel resolutions in the range ($\approx 0.1 - 15\mu\mathrm{m}$). It was hypothesised that SRXT imaging coupled with a suitable growth protocol might facilitate first-time 3D imaging of root hairs within the soil environment. Dependent on species, the diameter of root hairs generally lies in the range $\approx 7 - 17\mu\mathrm{m}$ [Dittmer, 1949]. Because field of view (FOV) diameter in imaging is inversely proportional to reconstructed voxel resolution, substantial constraints are placed on the experimental protocol. The field of view must necessarily be very small if hair-

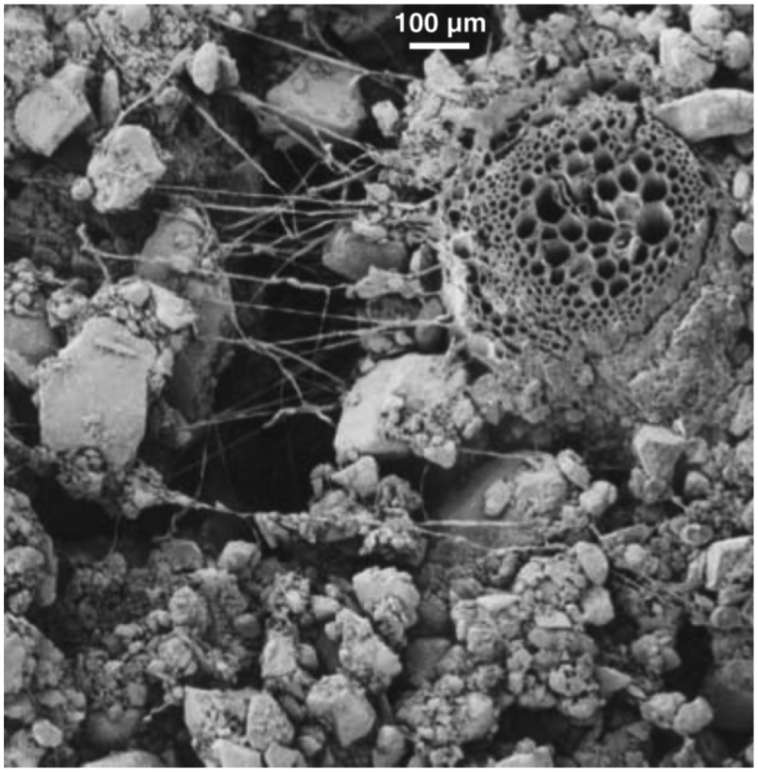

Figure 5.8: A micrograph obstained using cryoscanning electron microscopy, showing the rhizosphere surrounding a root of buckwheat (*Fagopyron esculentum*) [Hinsinger et al., 2005]. A variety of root hair interactions with pores and soil aggregates are clearly visible.

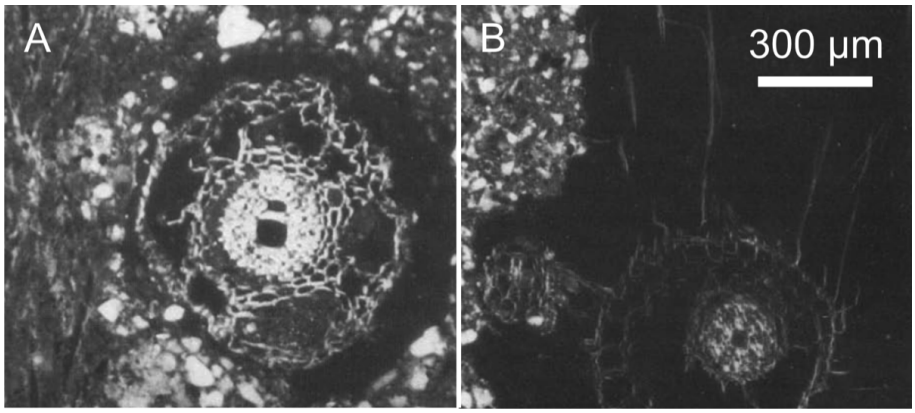

Figure 5.9: Schematic from *van Noordwijk et al.* showing SEM microscopy of sections through freeze-dried wheat roots and rhizosphere soil. (A) Root-soil contact regions seen between soil surfaces and the root exodermis. (B) Root cross section in macropore, with root hairs visible. [Van Noordwijk et al., 1993].

scale features are to be reliably detected in reconstructed data. Furthermore, movement both of the whole sample and of structures within the sample must be minimised. When imaging at resolutions at the $1\mu\mathrm{m}$ scale, as opposed to the lower resolutions at which roots have conventionally been investigated in literature studies, the influence of movements at similar length scales to those of roots, water or soil aggregates becomes more pronounced. Problematically, a living plant growing in uncompacted, hydrated soil represents an inherently unstable, dynamic system, prone to movement. As has been seen in previous work, root growth, root bending, soil consolidation, water movement, and bulk shrinkage due to water evaporation can all introduce substantial movement and associated blurring in images, even when scan times are relatively short ($< 1\mathrm{h}$). Despite many μ-CT systems being capable of $< 5\mu\mathrm{m}$ resolution in *transmission* mode, the low flux constraint at the required spot size necessitates longer scans, during which movement of roots, soil and water can be very pronounced relative to the spatial resolution. SRXCT sources, though not necessarily offering appreciable resolution benefits over benchtop systems, offer greatly improved flux, with the result that acquisition times can be substantially reduced from the hour to the minute scale [Connolley et al., 2007]. When samples are inherently structurally unstable, as is the case with soils and plants, this reduced acquisition time is of great benefit in reducing intra-scan movement.

These factors clearly pointed to the suitability of synchrotron X-Ray CT combined with very small sample sizes for the elucidation of root hair structure and interactions with soil. The X02DA ('TOMCAT') beamline at the Swiss Light Source (Paul Scherrer Institute, Villigen, Switzerland), is one such facility, optimised for tomographic X-Ray imaging at resolutions of $0.36 - 14.8\mu\mathrm{m}$ [Stampanoni et al., 2006]. This range is ideal for investigation of structures at the root hair scale. The beamline acquires radiographs using a detector with 2048×2048 elements, so when imaging at a resolution of $1.5\mu\mathrm{m}$ the maximum field of view diameter is only $3.072\mathrm{mm}$, necessitating extremely small sample sizes compared to previous plant X-ray CT studies in the literature. In order to design a suitable experiment, the following criteria were identified:

1. Selection of a plant variety with suitable root and root hair characteristics for investigation.

2. Development of a growth protocol satisfying the requirements of both plant development and imaging constraints.

3. Acquisition of CT data with sufficient resolution, contrast and quality that root hairs are discernible.

4. Image processing of resulting data, ensuring sufficiently accurate determination and differentiation of distinct phases and structures.

5. Generation of accurate FE volume meshes from defined regions.

6. Derivation of a mechanistic simulation model using robust approaches to modelling of P uptake, soil-surface binding and fluid diffusion kinetics.

7. Derivation of defensible and where possible, experimentally-derived parameters to set initial conditions for the model.

8. Application of equations and initial conditions to the FE model and computation of solutions over a suitable timescale.

9. Post-processing and analysis of simulation data for improved understanding of P movement in the rhizosphere .

10. Application of findings to real-world plant breeding, fertilization and soil management.

5.3 Materials and methods

5.3.1 Selection of a suitable plant variety

Wheat (*Triticum aestivum*) has root hairs with diameter of $\approx 12\mu\mathrm{m}$ [Singh Gahoonia et al., 1997], which given sufficient contrast should be visible at the $1.5\mu\mathrm{m}$ resolution available at X02DA ('TOMCAT'). The relatively fast growth of wheat, coarse primary rooting and substantial agricultural significance were deemed to render it suitable as a candidate species for imaging. Trials conducted using 'Santiago' variety winter wheat (KWS, Thriplow, UK) confirmed that healthy plants could be grown successfully in a Chromi-Abruptic Luvisol sourced from the Sutton Bonington field site at the University of Nottingham ($52°49'52'', -1°15'13''$). Soil chemistry for this soil, derived from an assay at Bangor University (Bangor, UK), is given in Table 5.2 (full experimental procedure is given in Section 8.2.1).

Table 5.2: Soil chemistry of Chromi-Abruptic Luvisol, derived via soil assay.

Nutrient	Bulk D ($kg.l^{-1}$)	C_{sol} ($mol.l^{-1}$)	C_{sor} ($mol.kg^{-1}$)	C_{tot} ($mol.l^{-1}$)	b
PO_4	1.1	$11E^{-6}$	$522.6E^{-6}$	$578.7E^{-6}$	48.87
NH_4	1.1	$471.25E^{-6}$	$2.44E^{-3}$	$2.8E^{-3}$	6.03
K	1.1	$1.11E^{-3}$	$2.28E^{-3}$	$3.0E^{-3}$	2.22

For growth, the necessity of imaging extremely small ($\approx 3\mathrm{mm}$) diameter samples placed substantial constraints on the design of the apparatus. Trials showed that it was possible to grow roots in small soil volumes by clustering $1\mathrm{ml}$ polymer syringe barrels together, filling them with finely sieved soil, then planting seeds to a bulk layer of soil above the barrel openings.

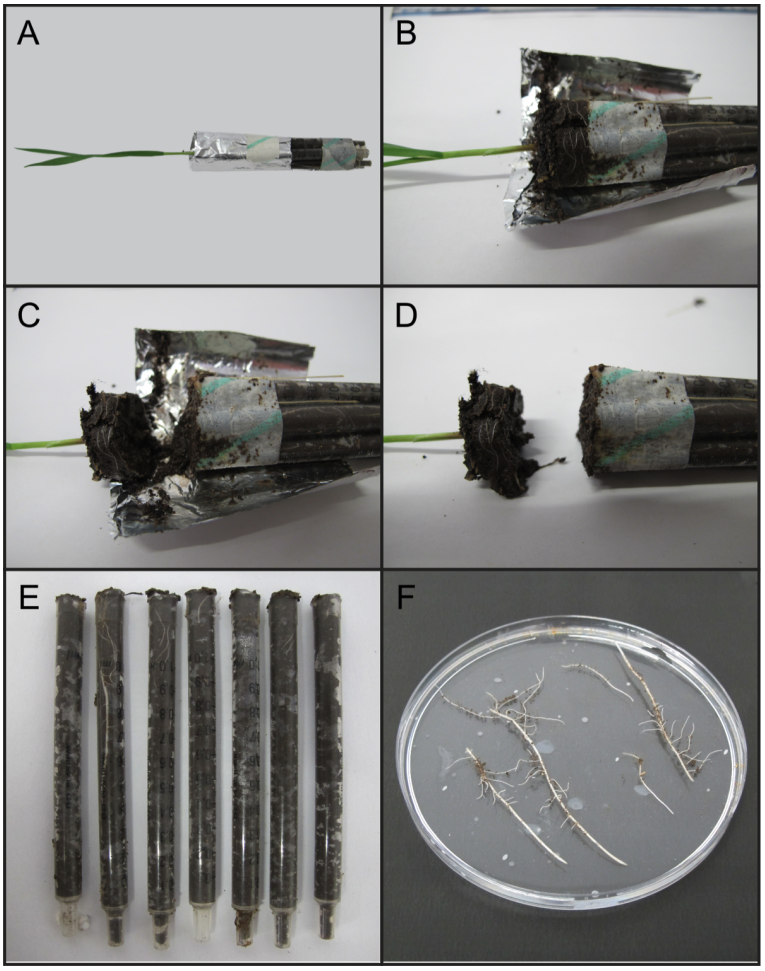

Figure 5.10: The procedure for dismantling growth assemblies prior to imaging. (A) The syringe bundle was removed from exterior tube. (B) The foil collar was removed to expose soil. (C-D) A scalpel was used to excise all material flush with the top of the syringe bundle. (E) Roots were visually identified in the barrels. (F) After imaging, roots can be gently washed from individual barrels to validate structure.

In this manner, growing roots could enter individual cylinders of soil, and following separation of the barrels, single tubes of internal diameter ($\approx 4\text{mm}$) were rendered that satisfied the constraints for imaging. Figure 5.10 shows the protocol for dismantling the growth chambers. Since hairs are known to remain in position up to many days after their internal, cytoplasmic structures have ceased to operate [Fusseder, 1987], imaging within minutes of aerial tissue excision is almost certain to capture the *in vivo* positions.

For the experiment, bundles of seven syringe barrels (with tabs removed) were housed within 50ml standard lab tubes with 16 holes cut into the base to allow hydration and drainage. A collar of aluminium foil was added to each bundle to occlude light and act as a root guide, encouraging growth down the syringe barrels. Each exterior tube was pre-filled with a 20mm depth of perlite granules in order to raise the bundle height and improve drainage. The

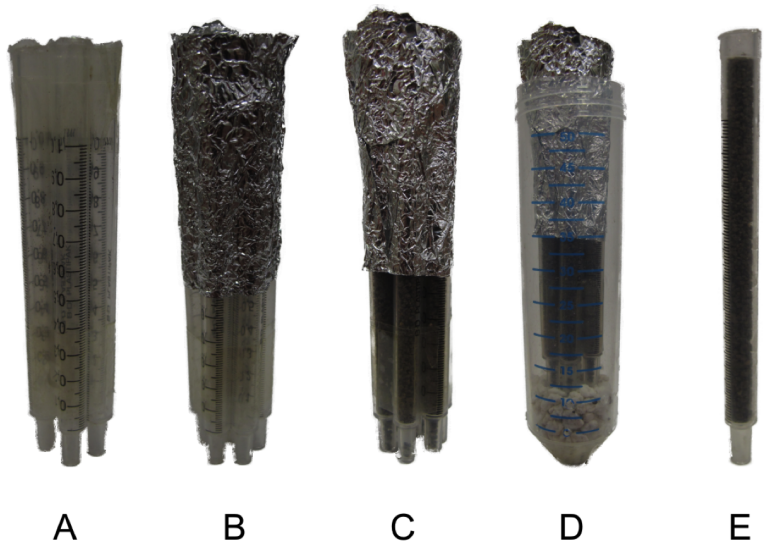

Figure 5.11: Schematic showing assembly of growth chambers. A) bundles of seven $1\mathrm{ml}$ syringe tubes were taped together, B) a foil collar was added as a root guide, C) soil was introduced to the tubes, and seeds planted, D) each bundle was placed in a larger $50\mathrm{ml}$ tube with a layer of perlite added to aid hydration, E) individual tubes were separated immediately prior to imaging.

soils used were a Chromi-Abruptic Luvisol (described previously) and a peat-based compost (Scott's Levington F2+S). Soils were autoclaved according to standard laboratory procedure in order to prevent algal and fungal growth, then sieved using a $1.2\mathrm{mm}$ aperture soil sieve to produce a texture that allowed adequate filling of the tubes without formation of large macropores of a similar length scale to the tube diameter. The soil was treated with the systemic pesticide *Intercept 60 WP* according to standard glasshouse procedure, then sieved between $1.6\mathrm{mm}$ and $1.18\mathrm{mm}$, in order to be introduced easily to the barrels. Details of the apparatus are shown in Figure 5.11

The prepared Luvisol was introduced to tube bundles and lightly compacted by periodically tapping each bundle on a bench top (following *Gregory et al.* [Gregory et al., 2003]), refilling in between compactions to ensure the soil filled the barrels. A $10\mathrm{mm}$ layer of compost was intoduced above the barrel tops in order to provide additional nutrients for improvement of growth. Seeds of *Triticum aestevicum* ('Santiago') were pre-germinated at RT for $48\mathrm{h}$ on damp tissue paper, before being transplanted to the growth assemblies and lightly covered with $5\mathrm{mm}$ of compost. The resulting assembly is shown in Figure 5.11. Plants were grown for 10 days in a controlled growth environment (Fitotron SGR, Weiss-Gallenkamp, Loughborough, UK), being top-watered initially, and subsequently hydrated passively from the base. Day conditions were $16\mathrm{h}$ at $23°\mathrm{C}$ and 60% humidity, night conditions were $8\mathrm{h}$ at $18°\mathrm{C}$ and 55% humidity, with humidity and temperature both ramped up and down between states over 30 minute periods.

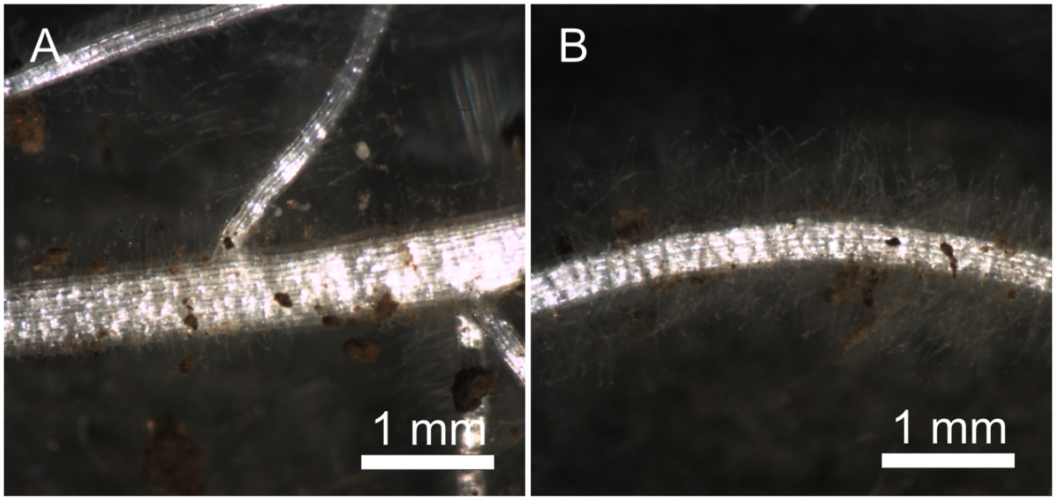

Figure 5.12: (A-B) Macroscope images showing two primary roots of different diameters, grown using the syringe barrel assay. After 10 days growth following germination, root hairs and lateral roots are clearly present.

5.3.2 Validation of hair growth

To validate root hair growth in the assemblies after the 10 day growth period, roots were extracted, washed, and imaged using light microscopy. Each cluster of barrels was carefully removed from the exterior tube, the foil collar removed, and both soil and plant material gently excised flush with the tops of the barrels using a scalpel. The bundle of syringe barrels was dismantled, and individual barrels were examined visually to identify samples which contained roots.

After gently washing the roots from the barrels in a large beaker of water, root segments were transferred to a petri-dish for imaging using both light microscopy and macroscopy. Resulting images are shown in Figure 5.12. Root hairs could be clearly seen in all images, despite the destructive nature of the washing technique used to separate roots from the soil, confirming validating the suitability of the protocol for growth of roots with intact hairs.

5.3.3 Imaging at the SLS

Imaging took place at the TOMCAT beamline on the X02DA port of the Swiss Light Source synchrotron in Villigen, Switzerland. Each cluster of barrels was carefully removed from the exterior tube, and both soil and plant material gently excised flush with the tops of the barrels using a scalpel. Individual barrels were examined visually to identify samples which contained roots (determined by validation of root cross-sections at the cut surface). From this subset of tubes, sections were identified in which the roots were surrounded by soil as opposed to being in contact with the wall. These were the sections selected as the regions of interest for

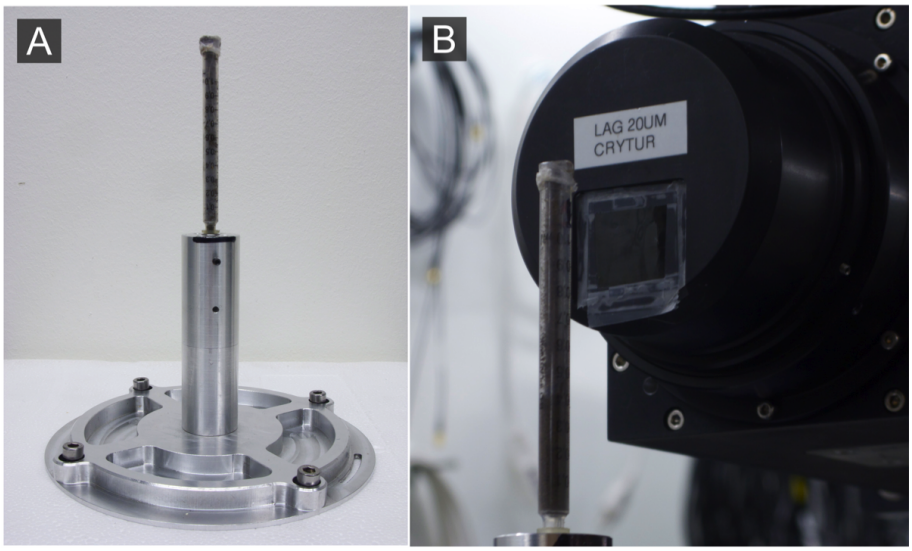

Figure 5.13: (A) A sample stage adaptor designed to hold syringe barrels samples with minimal intra-scan movement. (B) A sample in position prior to SRXCT imaging, with the scintillator visible in the background.

SRXCT imaging. Figure 5.13 shows the setup for imaging individual samples. Time for acquisition of a full set of radiographs was ($\approx 5\mathrm{minutes}$) due to the high available flux, allowing rapid exposure times as compared to μ-CT systems.

5.3.4 Imaging parameters

Figure 5.14 shows the basic layout of the beamline. The samples were imaged using a coherent, monochromatic synchrotron X-ray beam at an accelerating potential of $20\mathrm{KeV}$, with 1501 equiangular projections taken through $180°$. The projections were processed using a multi-node computer cluster in order to produce light and dark corrected sinograms, which were in turn converted to a stack of 2D, 8bit tiff files for analysis.

Image processing

Using the image processing package *FIJI* to view the data [Schindelin et al., 2012], root hairs were clearly visible in the individual 2D images which together comprised the 3D volume. Visual inspection of the data suggested little artifact influence, with no pronounced movement-derived artefacts. The quality, resolution and contrast of the data were of sufficiently high quality that many root hair characteristics could be straightforwardly identified without any image processing or feature extraction.

Though hairs were clearly identifiable, automated extraction of these features from the soil proved challenging, due to the similar attenuation coefficients of soil phases, and the numerous contacts made between hairs and soil structures. Global thresholding and seeded region

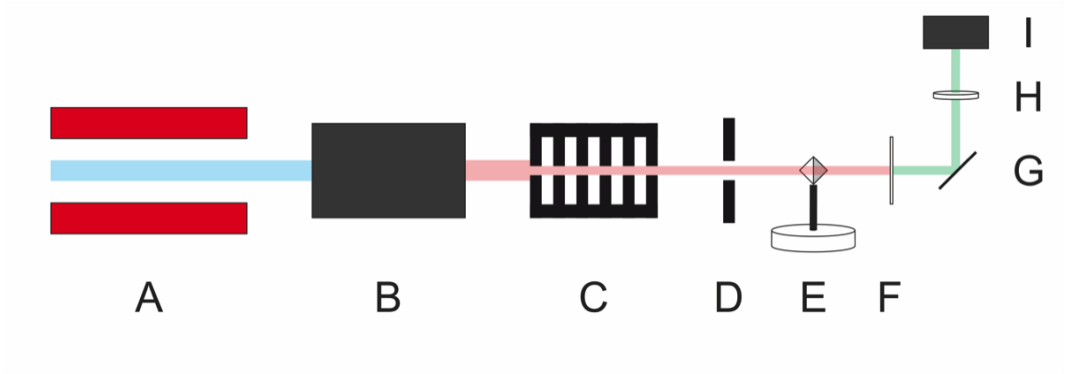

Figure 5.14: Schematic showing the layout of a standard synchrotron tomography beamline. A coherent, monochromatic beam of X-ray photons produced by electromagnetic interference of an accelerated electron beam (A) is filtered to give a monochromatic energy distribution (B). It then travels through a series of attenuators and slits (C) and a fast-shutter assembly (D) before passing through the sample, which sits on a rotating stage (E). The attenuated beam is then converted to visible light by a *scintillator* (F), reflected by a mirror (G) and passes through filters and lenses (H) before radiographs are acquired by a charge coupled device (CCD) array (I).

growth (SRG) methods both failed to provide reliable classification. Given the absence of multiple datasets, the highly original nature of the findings, and the constraints of time, it was deemed that a manual segmentation approach was both necessary and justifiable. Manual segmentation was undertaken using AVIZO 6 Fire software (VSG Inc., Burlington, MA, USA), with a Cintiq 22HD graphics tablet (Wacom Co. Ltd., Saitama, Japan) allowing sensitive and accurate tracing of features. Using the tablet, root hairs were visually identified at the main root surface and traced outwards, following each individual hair and capturing all voxels pertaining to it until the hair reached a terminus or became visually indistinguishable from neighbouring soil phases. Once all hairs that initiated from the epidermis had been traced, it was clear that unclassified hairs still remained within soil pores, with some fragments visible at a distance of $> 1\mathrm{mm}$ from the root surface. These non-continuous fragments were traced where distinguishable, being classified according to a second voxel set.

5.3.5 Defining subset segments for simulations

For the purposes of modeling the diffusion of nutrient species from the aggregates to the root hairs, certain constraints were placed upon the element count of the meshed volume. A trial to benchmark the performance of the IRIDIS 3 supercomputer cluster (University of Southampton, UK) against the most powerful stand-alone computing solution available (32-core AMD workstation with 128GB RAM, supplied by Broadberry Data Systems, Middlesex, UK) found that the stand-alone workstation was able to solve the equations for a larger mesh than the cluster. Though this was found to be due to poor optimisation of COMSOL on the IRIDIS cluster, rather than lack of raw hardware capacity, the present study was limited by these issues

to working within the capabilities of the stand-alone workstation. By running a series of simulations, maintaining otherwise identical parameters but increasing the element count of the mesh each time, an upper limit of 9×10^6 elements was determined, above which there was insufficient RAM available for the solver to build the required matrices.

A segment geometry was chosen as the basic format for sub-sets of data. By defining a segment of a cylinder, the centerline of which is aligned with the root centerline at various positions, future comparisons are possible between regions of identical volume at different positions along the root. Prior to definition of a single segment, the entire dataset was registered using rotational transforms such that the major root axis was parallel to the Z axis. This was achieved by determination of the root centre-point in two slices at different ends of the imaged root section, followed by trivial trigonometric derivation of the transformation angles required to align the line defined by these two points with respect to the Z axis.

A sub-volume was defined as a segment whose centre-line was coincident with the major axis of the root. The segment dimensions are the swept angle in radians (θ_{seg}), segment radius ($\mathrm{r_{seg}}$), and segment depth ($\mathrm{d_{seg}}$). The segment was defined with dimensions $\theta_{seg} = 1.29\mathrm{rad}$, $r_{seg} = 600\mu\mathrm{m}$ and $\mathrm{d_{seg}} = 557\mu\mathrm{m}$. The rhizosphere region from which the segment was defined was chosen for its representative mixture of macro-pore space and aggregates, along with visible hairs. As well as being limited by the solvable element count of the resultant mesh, the dimensions were constrained by the need to avoid lateral roots, volume edges, and regions affected by artefacts.

The root hairs and the root surface within the segment were classified manually according to the previous procedure, whilst the soil phase was segmented automatically using an automated seeded region growth approach, following *Keyes et al.* [Keyes et al., 2013a]. Since the manual nature of the root hair segmentation leads to potential double-classification of voxels at hair/soil contact points, shared voxels had to be classified singly before mesh generation. FIJI was used to assign any such voxels to the root region. Regions pertaining to hairs, root and soil were than combined as distinct volumes into a single volume, and the remaining unclassified voxels were classified as water.

5.3.6 Generating volume meshes

These regions were used to generate a partitioned volume mesh for input to COMSOL though use of the ScanIP software package (Simpleware Ltd., Exeter, United Kingdom). ScanIP offers two meshing algorithms, one producing a mixed tetrahedral and hexahedral mesh (+FEGrid) and the other producing a smoothed all-tetrahedral mesh (+FEFree). *Friedrichs et al.* used ScanIP for meshing of SEM and confocal microscopy data, and compared the performance of the

two algorithms on identical datasets [Friedrichs et al., 2012]. They found the mesh produced by the +FEFree algorithm to be more detailed, but it required ample pre-processing before it could be used successfully in FE packages. Despite the smoothing, the present study required use of the +FEFree algorithm since trials found the element counts and computation times to be prohibitively high when using +FEGrid. Parameters were tuned to maximise quality whilst satisfying the $n < 9 \times 10^6$ elements constraint. The resulting parameters used for final mesh generation are given in Table 5.3.

Table 5.3: Input parameters for +FEFree meshing algorithm in ScanIP, used to mesh segment for input to COMSOL.

Parameter	Value
Coarseness	-50
Smoothing iterations	20
Target min. edge length	-0.0001mm
Target max. edge length	1mm
Target max. error	0.0008mm
Surface change rate	30
Internal change rate	100
Target element count across a layer	0.5
Quality optimisation cycles	5

The mesh was imported into COMSOL (Version 4.2a, COMSOL Inc., Burlington, MA, USA) for solution of the numerical model. The geometry is shown in Figure 5.15

5.3.7 Definition of the explicit model

The model applied to the geometry was derived from that of *Schnepf et al.* [Schnepf et al., 2011], which though in their case was applied to a more geometrically simple case, explicitly considers P uptake and soil-surface binding reactions. Since other approaches in the literature consider these processes on a bulk basis, the model of *Schnepf et al.* was deemed to be the most suitable foundation for the root hair uptake case developed in this work.

5.3.8 Summary of equations

The following is a summary of the equations as used to set up the numerical simulation:

Movement of phosphate in water follows simple fluid diffusion:

$$\frac{\partial C_l}{\partial t} = D\nabla^2 C_l, \tag{5.1}$$

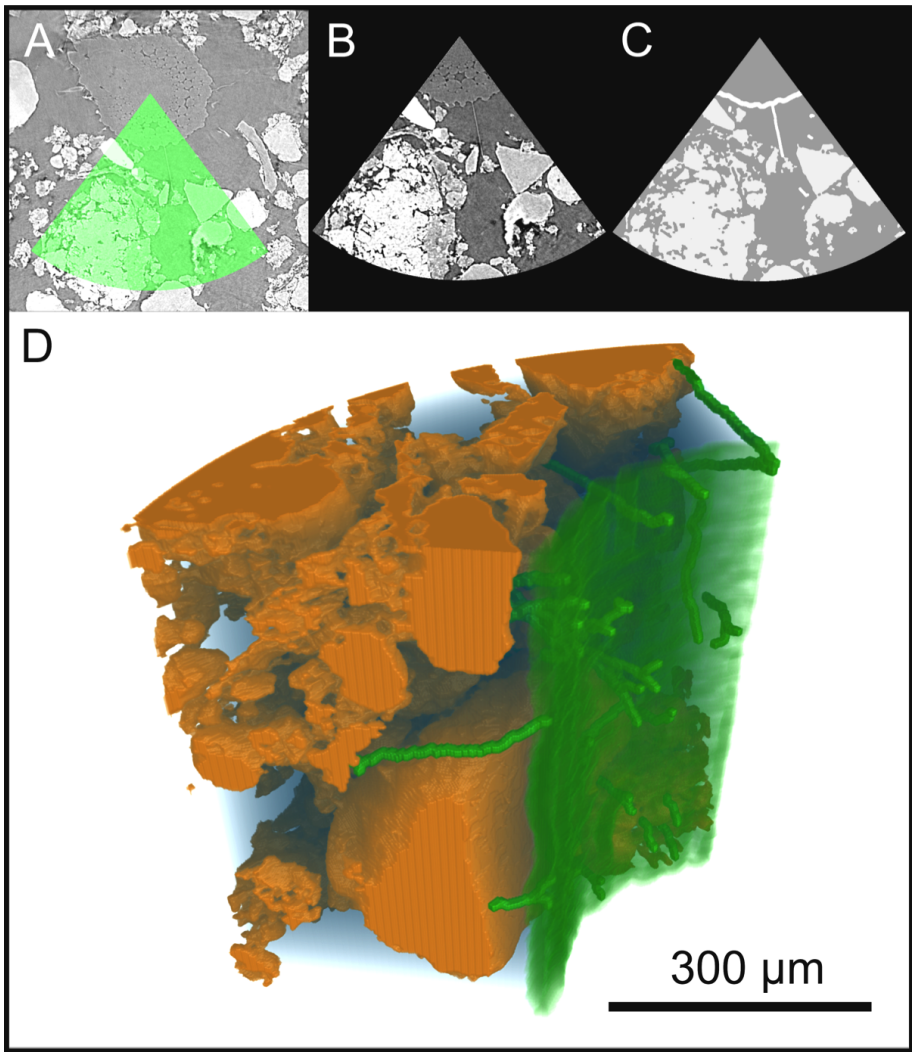

Figure 5.15: Visualisation of the segment used for numerical simulation of P uptake. (A) Initial aligned sub-selection, (B) raw data of the sub-section, (C) classification of root hairs, soil, fluid and root surface regions for volume mesh generation, (D) the resulting three-dimensional model

Where C_l ($\mathrm{mol.m^{-3}}$) is the concentration of P in pore water, and D ($\mathrm{m^2.s^{-1}}$) is the diffusion constant for P in water.

The conservation of mass on the soil surface is represented by the following first order reaction:

$$\frac{dC_a}{dt} = -k_d(C_a - \frac{k_a}{k_d}C_l) \tag{5.2}$$

Where C_a ($\mathrm{mol.m^{-2}}$) is the quantity of bound P per unit of surface area on soil aggregates, k_a ($\mathrm{ms^{-1}}$) is the sorption rate, and k_d ($\mathrm{s^{-1}}$) is the desorption rate.

The uptake boundary condition applied to the root hair and root surfaces is described by Michaelis-Menten kinetics:

$$D\hat{n} \cdot \nabla C_l = -\frac{F_m(C_l - C_{min})}{K_m + (C_l - C_{min})}, \tag{5.3}$$

Where C_{min} ($\mathrm{mol.m^{-3}}$) is the concentration of P in pore water at which plant uptake stops, F_m ($\mathrm{mol.m^{-2}.s^{-1}}$) is the maximal P uptake rate, K_m ($\mathrm{mol.m^{-3}}$) is the concentration at which uptake is half of the potential maximum, and $\hat{\mathbf{n}}$ is a vector normal to the root surface, pointing out of the fluid domain.

The boundary condition between soil surface and fluid phase takes into account the binding reactions, and as such is coupled with equation 5.2:

$$D\hat{n} \cdot \nabla C_l = k_d(C_a - \frac{k_a}{k_d}C_l), \tag{5.4}$$

External surfaces of the domain of integration take the following zero-flux boundary condition:

$$\hat{n} \cdot \nabla C_l = 0 \tag{5.5}$$

At $t = 0$, the soil and all related surface and fluid P concentrations are assumed to be in equilibrium, i.e. $\frac{k_a}{k_d} = \frac{C_{a,0}}{C_{l,0}}$. $C_{l,0}$ is straightforward to determine experimentally, however it is not possible to directly measure the soil surface concentration using standard assaying approaches. The volume concentration, $C_{a(V)}$, can be determined, and then converted into a surface concentration using $C_{a,0} = \frac{C_{a(V)}\rho V}{S}$, where V ($\mathrm{m^3}$) is the soil aggregate volume, S ($\mathrm{m^2}$) is the soil surface area, and ρ ($\mathrm{kg.m^{-3}}$) is the soil bulk density.

Figure 5.16 shows a schematic of a simplified geometry with the model applied.

5.3.9 Experimental approaches for soil model parameterization

The soil chemistry of the Luvisol used in the experiment was analyzed by collaborators from

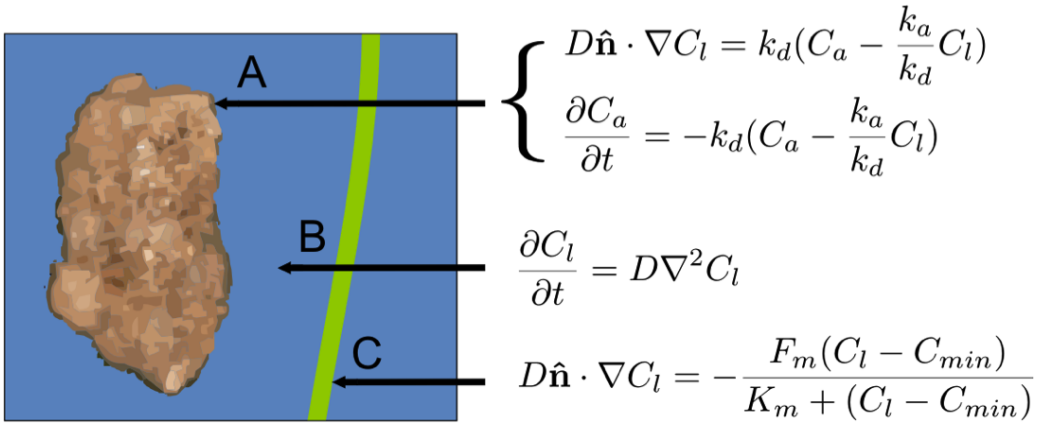

Figure 5.16: Schematic showing soil/root-hair/fluid system, with equations governing P kinetics. (A) The boundary condition (Equation 5.4) and conservation of mass (Equation 5.2) on the soil surface are applied to all soil/fluid interfaces. (B) Simple diffusion (Equation 5.1) governs movement of P in the fluid phase. (C) The uptake boundary condition at the root hair and root surfaces (Equation 5.3) follows Michaelis-Menten kinetics.

University of Bangor, Bangor, UK. By experimentally determining the input parameters for the model rather than using figures derived from the literature, the simulation could be parameterised to approximate as closely as possible the real soil P status. The standard soil assaying protocol used can be found described in detail within Appendix 8.2.1. The list of parameters used in the model are shown in Table 5.4

5.3.10 Numerical modelling

Running the model for a $> 24\text{h}$ period showed that the uptake had dropped to zero by the 10h point. For the next run of the model, the time steps for the simulation were set to give better resolution near to the beginning, in order to better capture the initial stage. Since the initial conditions of the model represent equilibrium, the first mechanism within the rhizosphere once the model begins is the generation of sufficiently strong depletion gradients by root and root hair uptake that P begins to desorb from the soil surfaces. Data were recorded for time points at 0s and $1 \times 10^{-9}\text{s}$, then in steps of 0.1s from $0.1 - 1\text{s}$, steps of 60s from $1 - 600\text{s}$, steps of 600s from $600 - 3600\text{s}$, and steps of 1800s from $3600 - 30600\text{s}$. Three simulations were run, using initial conditions approximating three different agronomic soil P indices (P1, P2, P3). The soil indexing system is a scheme adopted by the UK government in order to regulate P fertiliser use [DEFRA, 2010]. A soil with index P3 contains 39mgP.l^{-1}, a concentration usually deemed sufficient for crop production without additional P application. Soils with indices P2 and P1 (23mgP.l^{-1} and 12mgP.l^{-1} respectively) are generally treated with P fertiliser for crop production.

Table 5.4: Parameters used in the explicit model, derived from a soil assay of the Luvisol growth medium

Parameter	Expression	Value	Units
D	-	10^{-9}	$\mathrm{m}^2.\mathrm{s}^{-1}$
k_m	-	6×10^{-3}	$\mathrm{mol}.\mathrm{m}^{-3}$
F_m	-	5×10^{-8}	$\mathrm{mol}.\mathrm{m}^2.\mathrm{s}^{-1}$
S	-	3.1158×10^{-6}	m^2
V	-	3.4832×10^{-11}	m^3
ρ	-	1.1×10^3	$\mathrm{kg}.\mathrm{m}^{-3}$
θ	-	0.33	-
C_{min}	-	2×10^{-5}	$\mathrm{mol}.\mathrm{m}^{-3}$
C_{tot}	-	0.25×10^{-3}	$\mathrm{mol}.\mathrm{kg}^{-1}$
A	-	0.7975	-
κ	-	1.269×10^{-3}	s^{-1}
C_{sor}	AC_{tot}	1.994×10^{-4}	$\mathrm{mol}.\mathrm{kg}^{-1}$
$C_{a,0}$	$C_{sor}\rho V/S$	2.452×10^{-6}	$\mathrm{mol}.\mathrm{m}^{-2}$
$C_{l,0}$	$\rho(C_{tot} - C_{sor})/\theta$	0.1687	$\mathrm{mol}.\mathrm{m}^{-3}$
k_d	$\kappa(1 - A)$	2.569×10^{-4}	s^{-1}
b	$C_{a,0}/C_{l,0}$	1.453×10^{-5}	m

5.3.11 Analysing results

5.3.12 Exporting data for post-processing

Once the simulation had concluded, results were exported from COMSOL for post-processing. Comma-separated variable (CSV) files containing scalar values of C_a and C_l at grid points defined in Cartesian coordinates were exported for a number of time steps. Files were imported into the post-processing and visualisation package AVIZO 7 Wind (VSG Inc., Burlington, MA, USA). The CSV data for C_a and C_l were interpolated onto grids with the same X, Y, Z dimensions as the original RAW data used to generate the FE mesh, using the *ClusterToGrid* module, then saved as 32-bit RAW files for which the attenuation coefficients mapped the scalar concentration values of the original data at each point. Post-processing of the C_l dataset was completed by applying a logical AND along with a version of the original RAW data in which the fluid phase region had a value 1, and all other regions were 0. To complete post-processing of the C_a dataset, a logical AND was applied along with a version of the original RAW data in which the soil phase region had value 1, and all other regions were 0. To visualise the C_a distribution at various time steps, the finalised voxel data were combined with the root surface and root hair regions segmented previously, allowing C_a to be seen in relation to uptake surfaces.

The C_l dataset was visualised by using *streamlines* set to follow paths of maximum concentration gradient between soil surfaces and uptake surfaces. Of particular interest was the relative area and location of sorbed P from which root hair and root surface uptake occurred. An estimate was derived by seeding streamlines from linearly distributed sets of equally spaced seed points on root hairs and root surfaces (where spacing was δ_0). A total of 10 sets of 80 linearly arranged seed points were defined in a grid pattern on the root surface, and a total of 12 such sets were arranged longitudinally on root hair surfaces at random points on randomly selected hairs. Using the open source software *ParaView* [Ahrens et al., 2005], single streamlines were calculated from each seed point, following the path of maximum concentration gradient back to the soil surfaces. This not only allowed diffusion paths to be visualised, but also the ratio of summated lengths between initiation points and end points to be calculated. This provided a quantifiable measure of how diffuse or localised the uptake of P was from root hairs and the root surface.

In the case where streamlines from a single seed set terminated on the surfaces of different soil aggregates, a false measure of the spread would result from inclusion of the inter-aggregate distances. The following procedure mitigated against this outcome, by statistically rejecting outlying distances between terminal points. Figure 5.17 shows a schematic illustrating the procedure. In this case, 10 streamlines link evenly spaced seed points on the root hair with terminal points on the soil surfaces of two distinct particles, A and B. The intra-terminus distance between two neighbouring points is δ_1. Removing every other terminal point, the intra-terminus distance between two neighbouring points becomes (δ_2). In the case where streamlines have been split between two or more aggregates, very large outlier distances such as (δ_a) will exist. By calculating (δ_1) and (δ_2) for each terminal point, the parameter ($\frac{\delta_2}{\delta_1} - 2$) could be defined for each point, which would be 0 in the idealised case where (δ_1) is the same for every point. By calculating the mean value of ($\frac{\delta_2}{\delta_1} - 2$) for each streamline set, and rejecting any intra-point distances (δ_1) for which ($\frac{\delta_2}{\delta_1} - 2$) is more than two standard-deviations outside the mean, outliers could be rejected (the δ_a case), and the sum of remaining values of (δ_1) used.

5.4 Results

5.4.1 Qualitative observations

A wealth of insights was obtained from the SRXCT data, with initial examination of the raw data clearly demonstrating the heterogeneity of hair-particle interactions. The interactions between hairs and soil aggregates were just as complex as had been suggested by cryo-SEM images [McCully, 1999]. Figure 5.18 shows examples of hairs which traverse macropores towards aggregate surfaces. Figure 5.19 shows examples of hairs which appear to follow closely

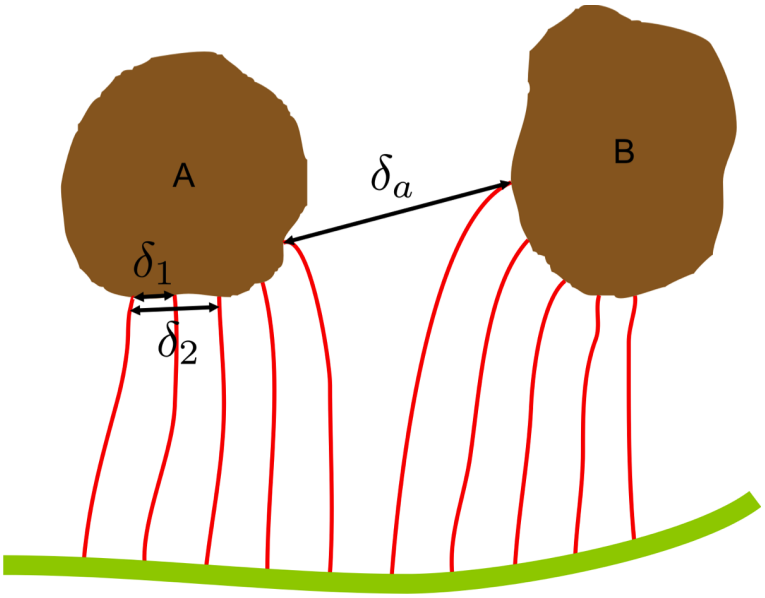

Figure 5.17: Schematic showing parameters for calculating the ratio of depletion zones on soil particles to corresponding uptake zones on root and root hair surfaces. A total of (n) seed points are evenly spaced along a root hair or the root surface (shown in green) with a spacing of (δ_0). Tracing paths back to aggregates along paths of maximum concentration gradient calculated by the numerical model, a set of (n) points on the soil surfaces is defined. The ratio of summated inter-point distances between the soil surface and the root or hair surface is a measure of how spatially focused is the uptake of P. Inter-aggregate distances (δ_a) are rejected using a statistical procedure. For each point on the soil surface, the ratio ($\frac{\delta_2}{\delta_1}$) is calculated. For points where this ratio falls more than two standard deviations outside the mean for the whole set, the inter-point distance is rejected as being an inter-aggregate distance.

the surface contours of soil particles. Figure 5.20 shows examples of hairs which appear to infiltrate fissures and cracks in the soil matrix. Clearly, due to similar attenuation coefficients, reliable distinction of root hair and soil voxels is challenging in the many cases where hairs are in close proximity to soil surfaces.

It was also possible to derive an estimate of root hair density from the segmented geometry. Over the subsection used in the simulation, the root hair density, translated into the commonly reported form, was $\approx 210\mathrm{hairs.mm}^{-1}$. Differing growth protocols, growth periods and sampling positions make direct comparison with figures cited in the literature difficult, but it is clear that this estimate far exceeds the range elucidated for *Triticum aestivum* using root-washing. *Gahoonia et al.* estimated a mean density of $24 - 38\mathrm{hairs.mm}^{-1}$, with samples taken across a range of plants grown for 7 and 14 days [Gahoonia and Nielsen, 1998]. *Itoh and Barber* estimated densities of $56 - 181\mathrm{hairs.mm}^{-1}$ by sampling the roots of 6 different species [Itoh and Barber, 1983]. *Bole* grew 'Chinese Spring' and 'S-615' cultivars of *Triticum aestivum* for 28 days at high and low P indices, and estimated density as $20 - 80\mathrm{hairs.mm}^{-1}$ [Bole, 1973].

In addition to hair and soil interactions, the high resolution and contrast of the SRXCT data also allowed the internal structures of the root to be visualised in detail. Individual cortical cells could be clearly distinguished, as well as cortical spaces extending for varying lengths parallel to the root axis (Figure 5.21). Also visible were the internal structures at branches where lateral roots emerge from the seminal root (Figure 5.22). Though, only initial observations, such non-invasive elucidation of internal structure may aid in improving understanding of root tissue development, adaption and senescence.

By extracting the hairs, soil and root as separate volumes, it was possible to visualise these structures in three dimensions. Figure 5.23 shows a 3D volume rendering of the root with soil phases partially cut away, such that the proliferation of root hairs can be clearly seen. It was to a subsection of this model that the simulation was applied (Figure 5.15).

5.4.2 Results of P uptake simulation

In all three simulations (P1, P2 and P3), cumulative P uptake by root surface and root hairs was comparable, with uptake decreasing to very low values by $> 5\mathrm{h}$ (Figure 5.25). In all cases the root uptake was $\approx 15\%$ greater than for hairs, contradicting the dominant paradigm in the literature, that root hairs dominate P uptake [Barber and Silberbush, 1984; Leitner et al., 2010b; Ma et al., 2001; Tinker and Nye, 2000]. In the model, the surface areas of root surface and root hairs were $1.96 \times 10^{-7}\mathrm{mm}$ and $1.66 \times 10^{-7}\mathrm{mm}$ respectively, giving a root surface area 18% greater than that of the hairs. The difference in P uptake was thus attributable to the difference in surface area between the two entities, rather than the soil volume explored by the

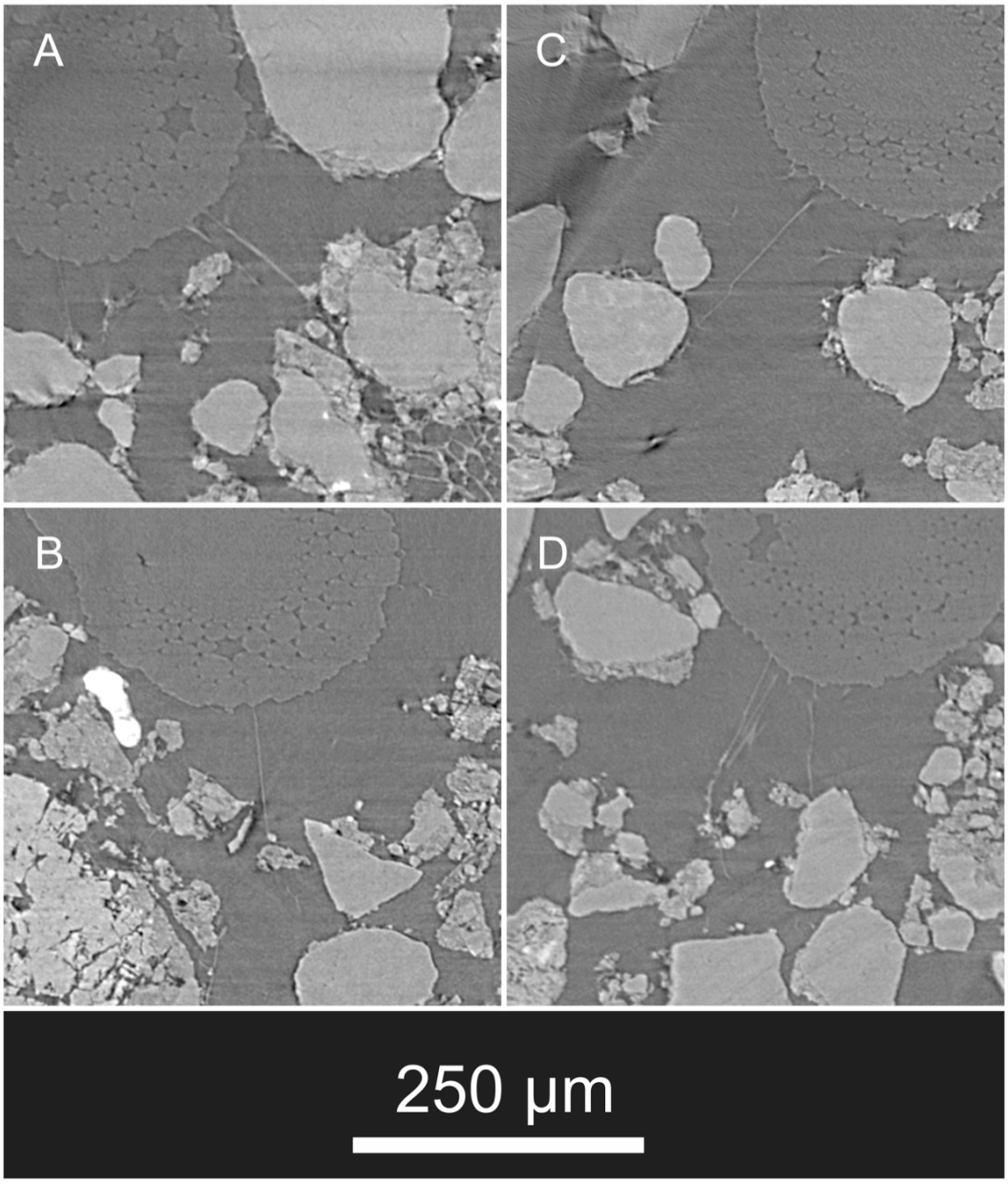

Figure 5.18: (A-D) Examples of hairs traversing soil pore spaces.

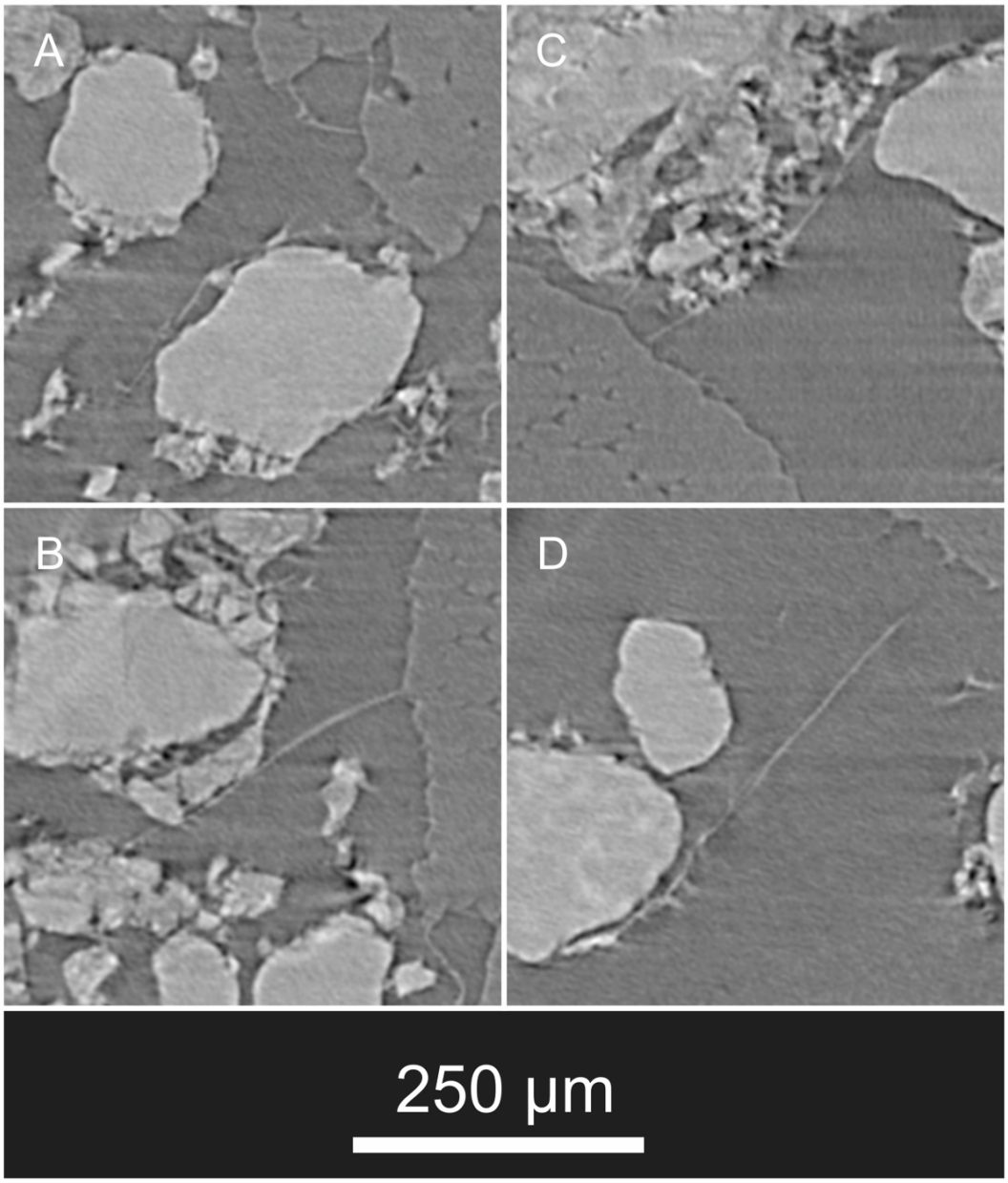

Figure 5.19: (A-D) Examples of hairs closely following soil surface contours.

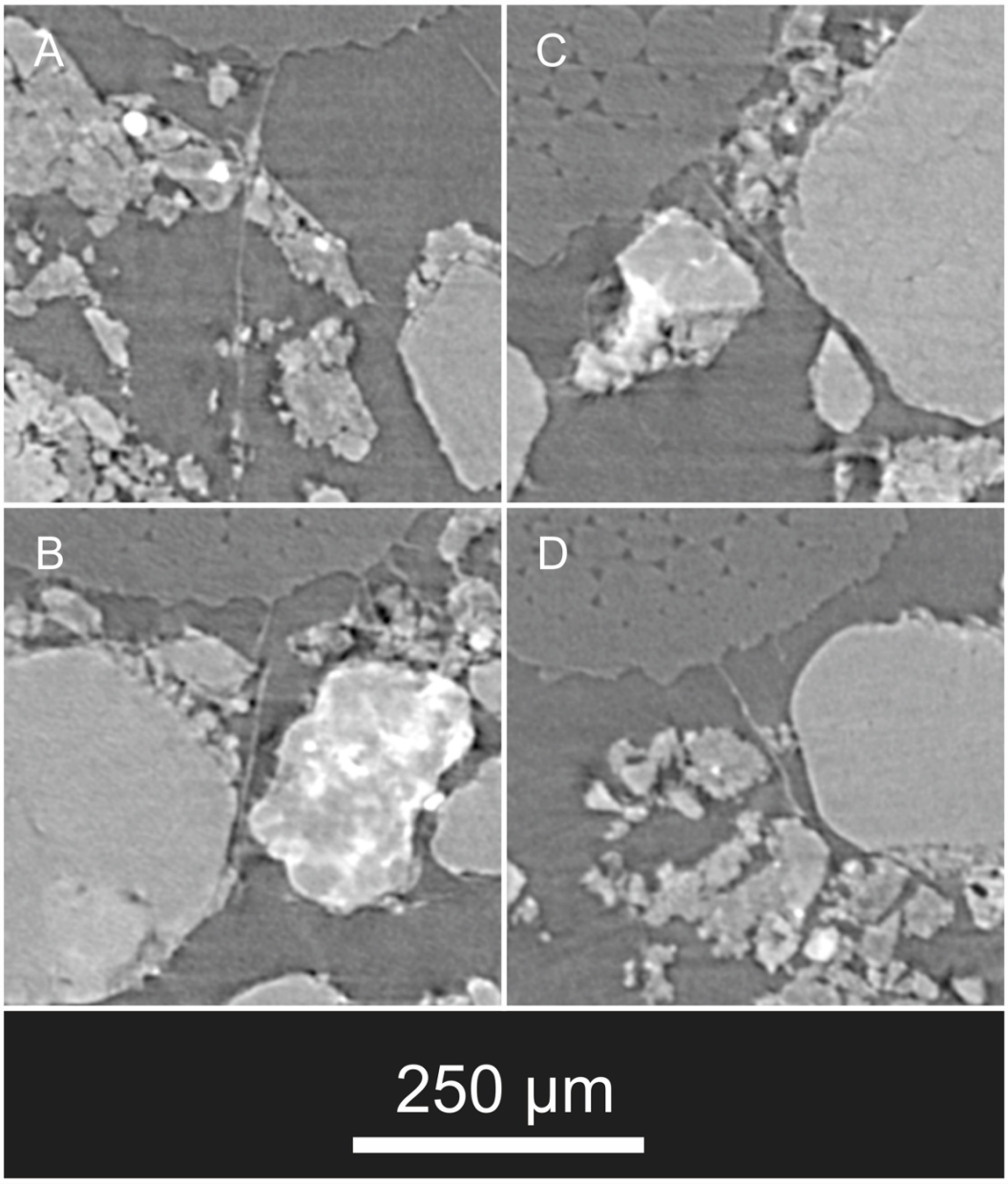

Figure 5.20: (A-D) Examples of hairs infiltrating fissures and intra-aggregate cracks.

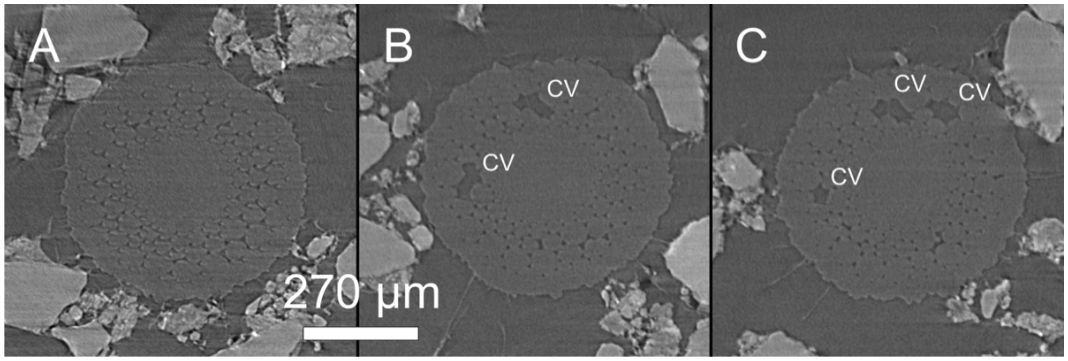

Figure 5.21: Cortical spaces were observed at numerous positions along the main root. (A) An x, y planar section in which no large cortical voids are apparent, (B-C) x, y planar sections showing cortical voids (CV - cortical void).

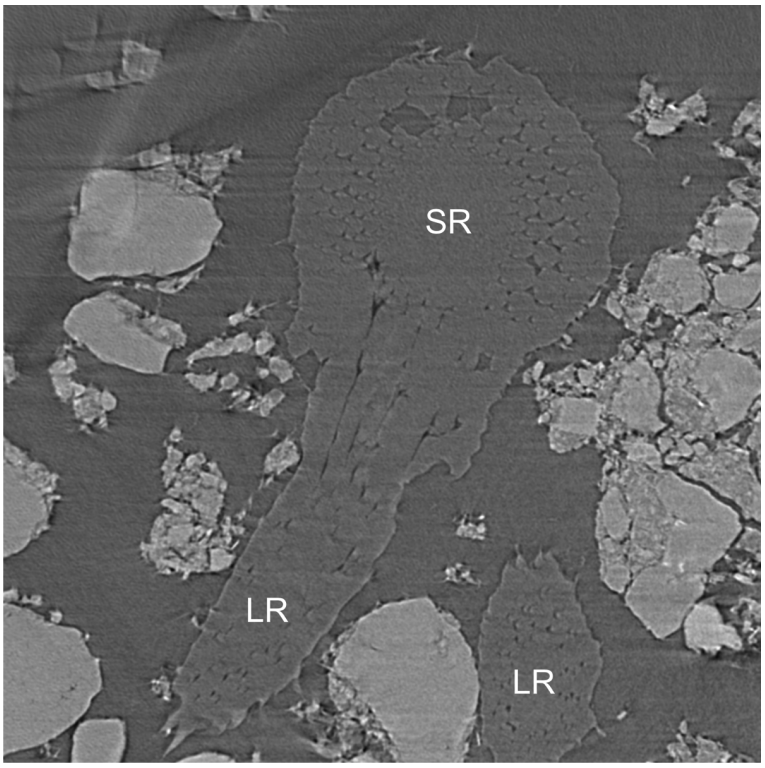

Figure 5.22: Cross section in the x, y plane of the seminal root at a lateral root branching point (SR - seminal root, LR - lateral root.)

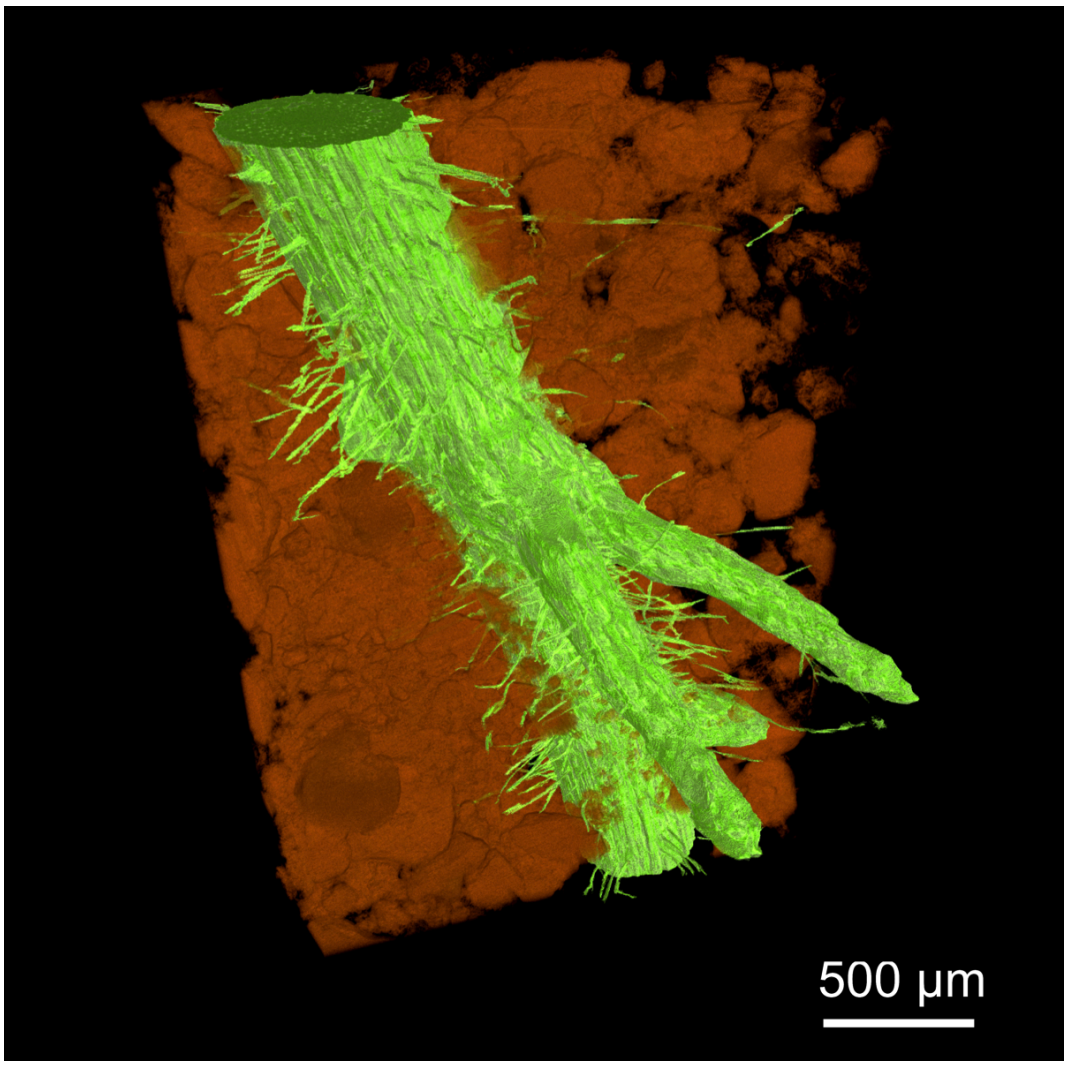

Figure 5.23: Digitally rendered 3D volume with the soil phases partially cut away to reveal a $\approx 3\mathrm{mm}$ section of a juvenile seminal root of *Triticum aestivum* including lateral roots and root hairs.

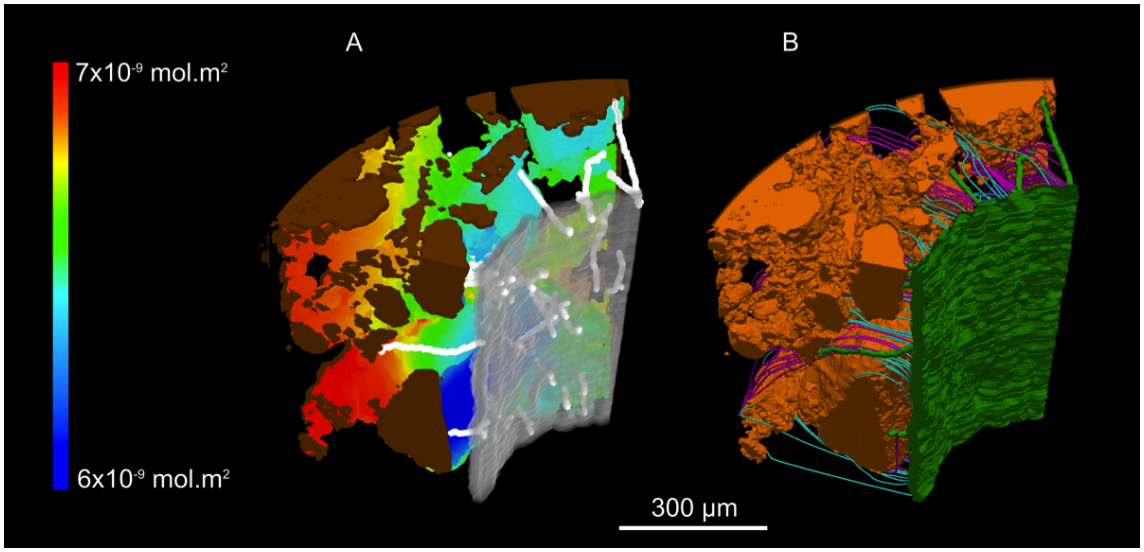

Figure 5.24: (A) Estimated surface concentrations of phosphate (C_a) on the soil particle surfaces after 10h of uptake by root and root hairs, (B) streamlines showing phosphate transport paths from soil surfaces to root hairs (magenta) and root surface (blue).

root hairs. The heterogeneity in C_a of the P remaining on the soil surfaces after 10h is shown in Figure 5.24-A, with the relationship between depletion and proximity to roots and root hairs clearly evident.

The flux of soil P from particle surfaces to root and root hairs was visualised by plotting diffusion streamlines (Figure 5.24-B). Mean ratios of sub-sampled streamline sets, along with standard mean error for root hair and root surfaces are shown in Figure 5.25. The particle surface area from which the root hairs draw P is approximately $2-3$ times greater than their own surface area, whereas for the root surface, the equivalent region on the soil surface is $5-10$ times greater than the uptake surface area. This difference arises through creation of global diffusion gradients by the root surface at a greater length scale than the more localised gradients generated very close to soil particles by the root hairs. The thin geometry and close proximity of hairs to soil particle surfaces results in P fluxes that are substantially more influenced by hair diameter and curvature. Comparing mean streamline lengths relating to root surface and root hair P fluxes confirmed that, dependent on time point, streamline paths were approximately $5-9\%$ longer for the root surface. Additional insight was conferred by the dynamic nature of the error bounds on the mean measure of soil surface to root/root-hair ratios. During the early stages of uptake variation was high, since diffusion in the fluid phase was interacting dynamically with the P binding on soil particle surfaces (i.e. the diffusion profile in soil-pore fluid, driven by uptake, had begun to influence soil particle surfaces, but the binding reactions had not yet reached equilibrium.) Also evident from Figure 5.25 was a period of adjustment in C_a values (via particle to particle interactions) in the $2-3\text{h}$ range, after which equilibrium

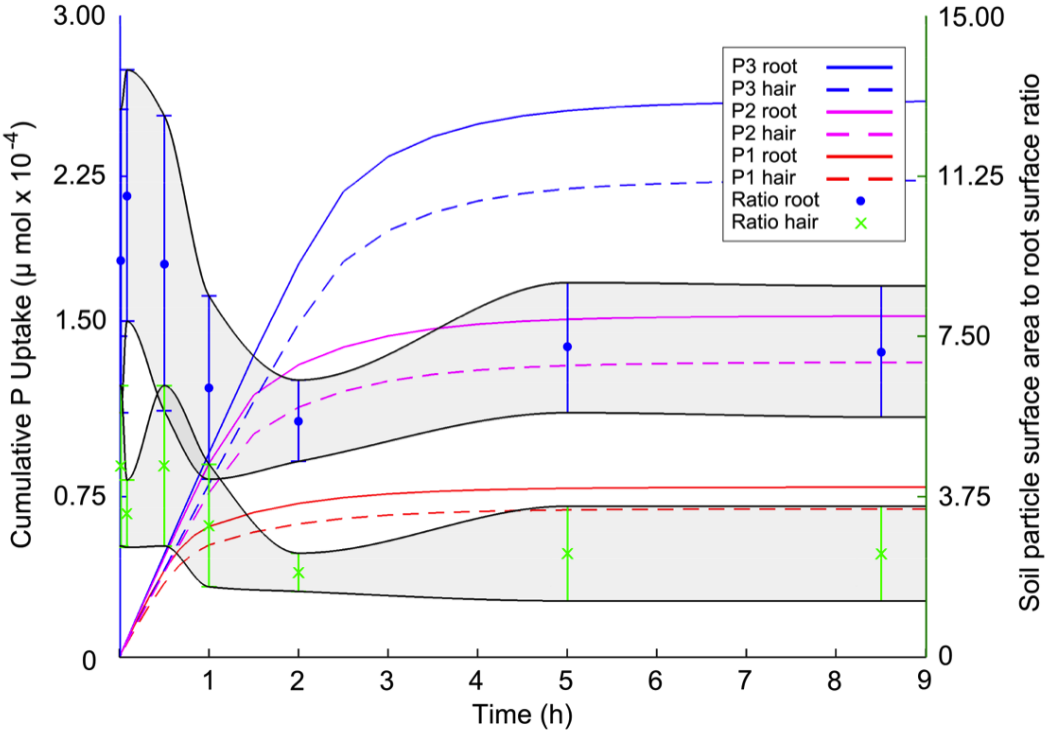

Figure 5.25: Consolidated simulation results (over 10h). Left axis indicates cumulative P uptake, plotted separately for root surface and root hairs, with $C_{a,0}$ values corresponding to phosphate indices P1, P2 and P3. Right axis shows ratios of polyline distance between groups of streamline start points (on soil surfaces) and groups of corresponding end points (on root and root hair surfaces, see Figure 5.17), where streamlines follow maximum C_l concentration gradients (shown in Figure 5.24-B). Plotted points are mean values for all sets, calculated separately for root and root hairs (with standard error in means indicated by error bars.)

was reached across the entire soil-pore and soil-surface domain.

5.5 Discussion

For the first time, it has been possible to bring together the most sophisticated non-invasive imaging techniques and mechanistic uptake models from the literature, completing the workflow from living plant in real soil to estimates of uptake based on explicit simulation. Though other studies have considered these two domains individually, either elucidating root morphology and architecture, or deriving models, this study has shown the explanatory power of bringing both capabilities together. The ability to visualise root architecture non-invasively is an important step in phenotyping for improved root traits, but the addition of modelling also allows us to understand which of these varied traits might be most effective in improving uptake efficiency, and thus yield. Further to generating highly useful data, this study also

serves as a proof of concept, and an encouragement to more researchers to combine imaging and modelling to plant root study at a variety of length-scales.

The study achieved first-time imaging of root hairs in field soils at high resolution, through the combination of a novel growth protocol and the use of a synchrotron X-ray source. The short acquisition times possible due to the very high flux (as compared to benchtop systems) are of great benefit in imaging an unstable system such as roots in soil. By reducing acquisition time to the minute scale as opposed to the hour scale, high quality data were attainable which allowed root hairs to be seen clearly enough to be manually segmented. This allowed root hairs and their interactions with the soil to be seen clearly for the first time in the undisturbed condition. The undisturbed nature of the method also yielded root hair density measurement greatly in excess of the characteristic range of values estimated for soil-grown roots using root-washing approaches. The data allowed parameterisation of a numerical P uptake model with real hair and soil interaction geometry for the first time. Understanding of mechanical interactions and uptake characteristics may have a direct future role in breeding of new varieties with improved hair traits for poor P environments.

The degree of complexity observed in hair/soil interactions does raise challenges in characterising such behaviour by developing a taxonomy for describing interactions. Hairs in the data were easy to identify and trace when clearly traversing larger pores, but where hairs came in close proximity with soil, it often became difficult to trace them reliably. In cases where such hairs can be clearly seen, defining the nature of the apparent 'contact' between hair and soil is complex, since the presence of water films between roots and the soil means that the true contact may not in fact be made, even where hairs follow the contour of a soil particle or infiltrate a fissure. Considering that effective automated extraction algorithms are only starting to be developed for coarse roots, it appears that it may be some time until automated image processing for extraction of hairs from data is possible. In the meantime, now that hairs are clearly able to be visualised using certain X-ray CT setups, a pressing task is qualitatively defining the various possible interactions in a robust manner.

5.6 Conclusions

This study has demonstrated that in situ imaging of living roots in soil is possible using SRXTM, and that consequent resolution of individual root hairs with respect to soil aggregates can be achieved. Root hair interactions with the rhizosphere soil were described in-situ for the first time, with the derived figures for hair density suggesting that current estimates for soil-grown roots (acquired by means of root washing) represent a substantial underestimation. Image segmentation approaches (including those developed in Section 2.2) were used

to generate a 3D model of root hairs and soil aggregates, to which a rhizosphere-scale P uptake model was applied and solved. This approach substantially improved upon existing P uptake models, showing that P uptake by root hairs is a rapid process, occurring on the same timescale as P uptake by the root. Quantification of the zones from which root hairs extract P from the soil suggests that the majority is extracted from soil surfaces immediately adjacent to root hairs, with very little acquired from particle surfaces oriented away from them. These results have major implications regarding how root hairs should be modeled at the plant and crop scale, and indicate that previous modeling studies should be re-visited using an imaging-based, multi-scale homogenization approach. This research also opens up possibilities for assessing how different surface binding reactions and geometries in the soil might influence different rhizosphere processes.

Chapter 6

Towards a paradigm for image based modelling of hairs grown in non-ideal soil states

Chapter 5 demonstrated the feasibility of establishing a workflow incorporating novel SRXCT imaging and image-based modelling. However, towards the goal of a larger scale comparison of genotypes and soil conditions, the workflow was extended to include non-ideal soil states. The comparatively dry soil conditions for which the data in Chapter 5 were acquired meant the absence of a macro-pore fluid fraction. In this chapter, the same growth assay and SRXCT imaging protocols were applied to samples with higher soil water content, revealing issues with hair detection similar to those often encountered in root detection at larger sample scales [Menon et al., 2006]. Rice genotypes provided by collaborators at JIRCAS were assessed alongside the wheat genotype used previously during imaging at the TOMCAT beamline of the SLS synchrotron in Villigen, Switzerland. Qualitative analysis of the data revealed the necessity of applying either contrast enhancement methods (such as those developed in Chapter 3) or growth modelling approaches, due to concealment of hair segments in pore water regions. A hair growth modeling algorithm (*HairGrower*) was developed in order to 'complete' partially visible hairs according to a stochastic regime, taking into account the length distribution of soil-grown hairs, and the rhizosphere structure revealed by SRXCT imaging. Finally, a mesh convergence test was carried out in order to determine optimal parameters for finite element (FE) mesh generation. The entire workflow represents a robust scheme to prepare geometries suitable for future explicit modelling studies, even in cases where soil water states are sub-optimal for hair detection. An overview flowchart of the entire plant to data workflow may be found in schematic form in Appendix 8.7.

6.1 Introduction

Chapter 5 demonstrated that in reconstructed data from SRXCT of samples where no bulk macropore water fraction was present, hairs were easily identifiable in the macropore domain. More challenging to identify were growth paths in regions where hairs made extended contact with aggregate surfaces. In these hair/soil coincident regions, *phase contrast* effects made differentiation between soil/pore boundaries and both hair/pore and hair/soil boundaries difficult to achieve reliably. Automated tracing of such structures is a highly challenging problem in the computer-vision domain, variants of which also exist for substantially simpler cases of feature extraction from μ-CT data of roots from real soils. By way of example, *RooTrak*, a recently published algorithm for automated extraction of coarse roots from μ-CT data [Mairhofer et al., 2012], has proven to be only partially effective at unsupervised extraction of root architectures of first and second order roots. In SRXCT data, the level of complexity of the images is far greater than those for which RooTrak and similar algorithms are designed, suggesting that highly sophisticated, novel approaches from within the computer vision domain will be necessary for development of such methods in future.

Furthermore, water content in soils can vary greatly across temporal and spatial domains, with corresponding influences upon nutrient acquisition by plants [Carminati and Vetterlein, 2012]. Therefore, whereas the study in Chapter 5 investigated root hairs in the absence of macropore water, it is of significant interest to be able to image and model hairs across conditions of differing pore-water content. Such imaging considerably heightens the level of complexity in the image-processing domain, since the attenuation coefficients of water and non-aerenchymous plant matter are extremely similar, with the likely result that contrast between hairs and bulk fluid will be minimal, even given the excellent spatial resolution available using synchrotron SRXCT methods (see Chapter 5).

In order to assess the performance of X-ray CT imaging in such conditions, an experiment was devised to grow wheat and rice (*Oryza sativa*) in partially flooded soil conditions, according to the following guiding hypotheses:

- It is possible to image rice (*Oryza sativa*) at the rhizosphere scale in a similar manner as already demonstrated for wheat.
- It is possible to discern root hairs in reconstructed data for samples in which the soil macropore space is at least partially filled with fluid.
- Novel methods in the image-processing domain can be used to give greater insight into hair nutrient uptake processes.

- Enhancements to the image-based modelling protocol can make computation more tractable and verify accuracy.

6.2 Preparation and imaging of plant samples

6.2.1 Materials and methods

Plant growth

Three plant varieties were chosen for investigation, one wheat genotype (*Triticum aestivum cv. Santiago*) and two contrasting rice genotypes provided by collaborators at JIRCAS, (*Oryza sativa cv. Varyla* and *Oryza sativa cv. Sadri tor Misri*), the latter demonstrating markedly better performance in low-P conditions according to field trials conducted by collaborators at JIRCAS.

Following the protocol outlined in Section 5.3.1, samples were grown suitable for imaging at the TOMCAT beamline on the X02DA port of the Swiss Light Source, Villigen, Switzerland [SLS]. The soil used was a low-P Eutric Cambisol of the Denbigh series, sourced from a field site at the University of Bangor, Gwynedd, UK ($53°13'54''$, $4°0'54''$). Following autoclaving and a $72\mathrm{h}$ desiccation period at $23°\mathrm{C}$, the soil was sieved between an upper bound of mesh aperture $1.18\mathrm{mm}$ and a lower bound of $0.8\mathrm{mm}$ to produce quasi-homogenous aggregates. Soil was introduced to clusters of $7\times$ $1\mathrm{ml}$ syringe barrels, prepared as previously with foil collars to act as root guides. Seeds were heat-treated at $55°\mathrm{C}$ for $72\mathrm{h}$ in order to break dormancy, then pre-germinated on wetted filter paper at $25°\mathrm{C}$ for $72\mathrm{h}$. Seeds were planted to the growth chambers, with a $15\mathrm{mm}$ depth of soil covering each seed, followed by $5\mathrm{ml}$ of water applied to the soil surface. Hydration was maintained via capillary rise from a tray of water, with an additional $3\mathrm{ml}$ top-applied every $72\mathrm{h}$ in order to maintain the soil at a high water content. Plants were grown for varying periods in a controlled growth environment (Fitotron SGR, Weiss-Gallenkamp, Loughborough, UK). Day conditions were $16\mathrm{h}$ at $23°\mathrm{C}$ and 60% humidity, night conditions were $8\mathrm{h}$ at $18°\mathrm{C}$ and 55% humidity, with humidity and temperature both ramped up and down between states over 30 minute periods. In total, 6 replicates of *Santiago*, 6 replicates of *Varyla* and 8 replicates of *Sadri tor Misri* were prepared.

Imaging at $1.5\mu\mathrm{m}$ resolution

Samples were transported for imaging at the SLS, following which a number were prepared and imaged according to the protocol outlined in Section 5.3.3. Due to the constraints of available beamtime, it was necessary to subsample particular samples of interest prior to imaging.

Details for the chosen samples are tabulated in Table 6.1. A single syringe barrel for each of these samples was chosen based on a two stage criterion stipulating that the barrel in question had to contain a root, but must also include a section for which the root was not growing coincident to the barrel wall. For suitable samples, the position of the region of interest (ROI) was recorded relative to a datum point, in order to allow adjustment of the sample stage to the correct height prior to imaging. All growth chambers were dismantled and the resulting discrete barrels assessed for imaging according to this protocol. A total of 10 datasets were acquired in this manner.

Table 6.1: Growth conditions for synchrotron samples

ID	Species	Genotype	Growth (d)	Imaging resolution (μm)
1	*Oryza sativa*	*Varyla*	12	1.5
3_b	*Oryza sativa*	*Varyla*	12	0.6
3	*Oryza sativa*	*Varyla*	12	1.5
6	*Oryza sativa*	*Sadri tor Misri*	12	1.5
8	*Oryza sativa*	*Sadri tor Misri*	12	1.5
17	*Triticum aestivum*	*Santiago*	12	1.5
19	*Triticum aestivum*	*Santiago*	12	1.5
20	*Triticum aestivum*	*Santiago*	12	1.5
21	*Oryza sativa*	*Varyla*	20	1.5
22	*Oryza sativa*	*Varyla*	20	1.5
24	*Triticum aestivum*	*Santiago*	20	1.5

Imaging at $600\mathrm{nm}$ resolution

The rapidity of the reconstruction workflow at TOMCAT allowed single x, y slices of acquired data to be visualised $< 10\mathrm{min}$ following the end of each scan. This presented the potential for registering the root axis position within a dataset by measuring the offset in x and y axes required to align the root surface or centreline with the axis of stage rotation (See Figure 6.1. In such a manner, ROI scans of root and rhizosphere could be acquired at higher resolution, in order to uncover finer-scale root, hair and soil structures. This procedure was carried out for a *Varyla* sample (3) which had been identified during scanning at $1.5\mu\mathrm{m}$ as having a particularly advantageous water content and soil structure for hair visualisation. The beamline optics were adjusted for imaging at a spatial resolution of $600\mu\mathrm{m}$, following which the sample was re-scanned.

6.2.2 Results

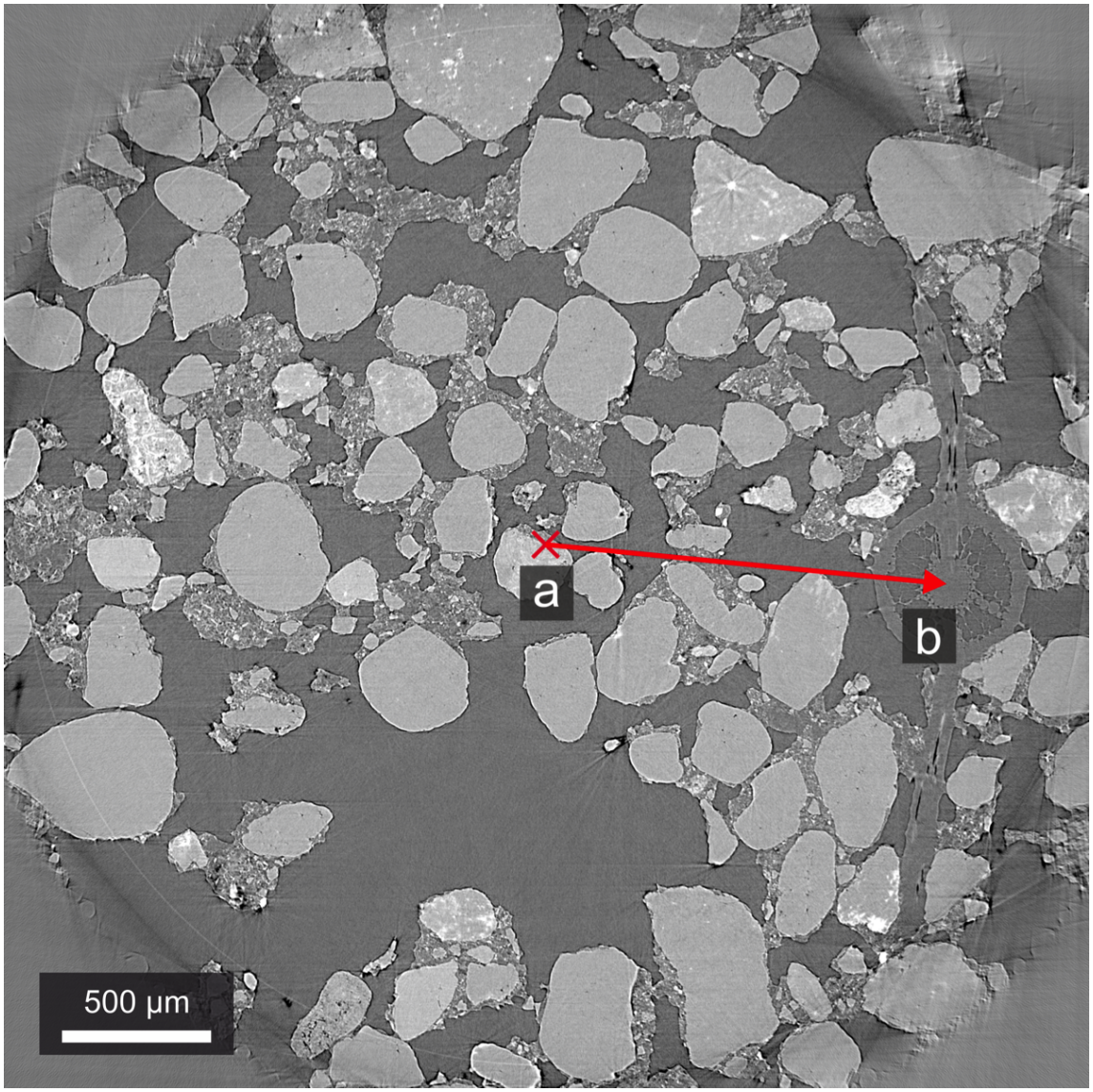

Figure 6.1: Schematic showing the method for registering major root-axes for higher-resolution ROI scanning. Using FIJI, the positions of both centre of rotation (a) and the root axis (b) are determined. Shifting the sample stage through vector $\vec{a}b$ then centres the ROI on the root axis.

Data were quantitatively analysed as in Chapter 5 using FIJI. Figure 6.2 shows representative cross sections through all data acquired at $1.5\mu\mathrm{m}$ resolution. Compared to the data considered in Chapter 5, the water content of the soil was visibly higher. The macropore domain was partially filled with fluid phases, and fluid regions were coincident to root surfaces in many instances. Figure 6.2-G shows that for data of sample 2, the entire root circumference was in contact with fluid, such that the root surface was indistinguishable. In this instance, as discussed previously, only the contrast between fluid and cortical gas phases allowed the position of the root to be identified.

Figures 6.3 and 6.4 show data acquired for a *Varyla* sample (3) at $600\mathrm{nm}$ resolution. Whereas in data considered in Chapter 5, hairs were clearly visible in macropores, and often visible in contact with aggregates, the high macropore fluid content of the soil in data considered here served to conceal hair paths. In Figure 6.4, hairs are highly visible in the gas phase, but immediately become indistinguishable from fluid one the hair transitions from one phase to the other.

The data acquired at $600\mathrm{nm}$ also clearly reveal the heterogeneity of soil aggregate microstructure. Figure 6.5 shows four different soil aggregates each with distinctive internal texture and intra-aggregate pore structure characteristics. Whereas some aggregates have a structure that appears highly homogenous in terms of both attenuation coefficient and porosity at the detection threshold of the data (Figure 6.5-D), others indicate the presence of more complex combinations of constituent phases (Figure 6.5-A).

6.2.3 Results

The data clearly demonstrate the quantity and complexity of rhizosphere morphology information that is accessible using SRXCT techniques. Root structures down to the level of the single cortical cell were clearly visible (Figure 6.3), and the aggregate and fluid distributions around the root could be resolved in unprecedentedly fine detail. However, the multi-phase complexity raises significant challenges as to the optimal way to process data in order to answer pertinent questions about rhizosphere processes. The presence of mixed gas and fluid phases in the macropore space serves to shield root hairs from view. This deleterious contrast between hairs and fluid limited the use of hair segmentation techniques used in Chapter 5, to a class of hair segments positioned fully within the gas phase. In order to prepare data for image-based modelling routines, a more sophisticated approach to hair characterisation was thus necessary. The following section is concerned with development of such a workflow.

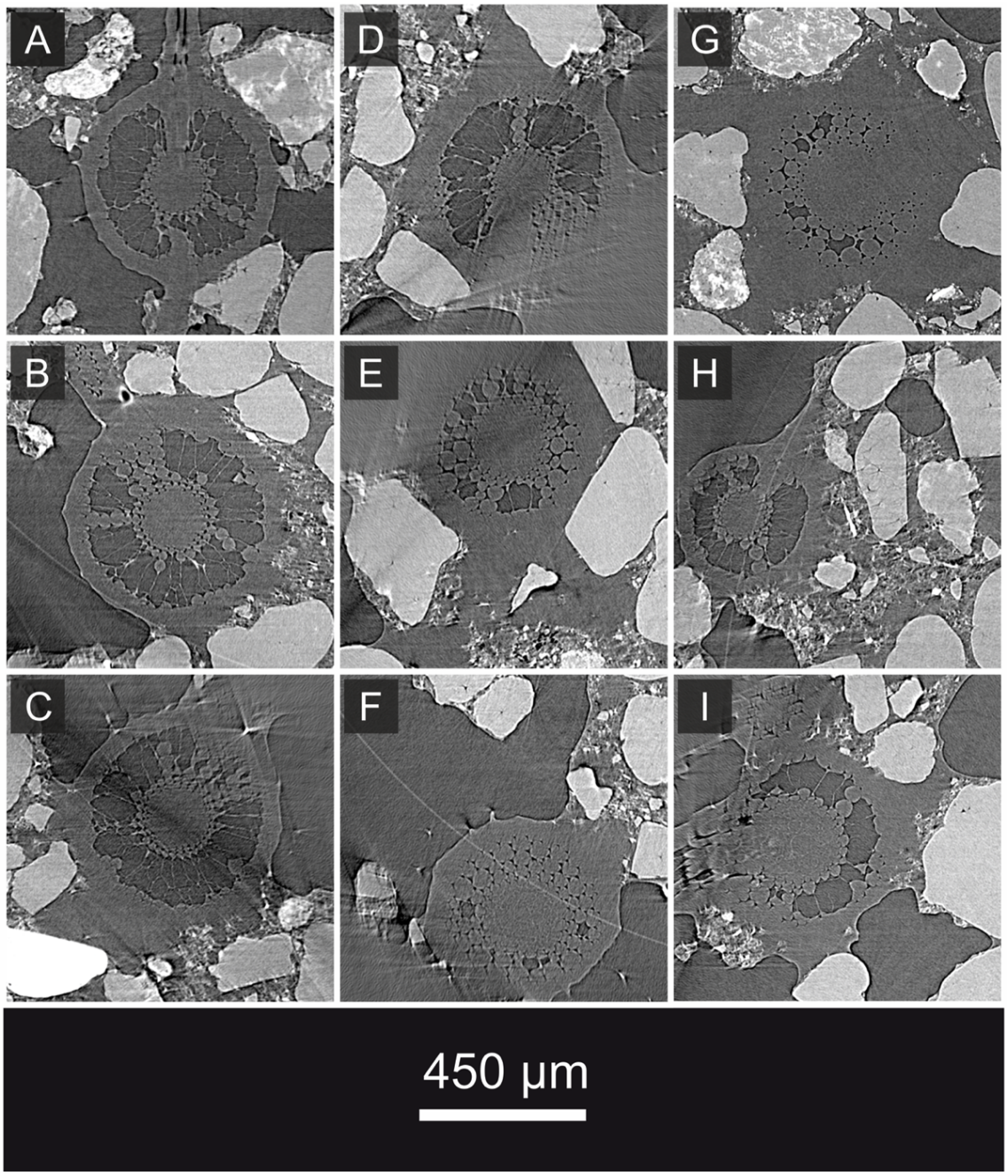

Figure 6.2: Cross sections of primary roots: (A) *Varyla*, 3 (B) *Sadri tor Misri*, 6 (C) *Sadri tor Misri*, 8 (D) *Varyla*, 1 (E) *Santiago*, 17 (F) *Santiago*, 19 (G) *Santiago*, 20 (H) *Sadri tor Misri*, 21 (I) *Santiago*, 24

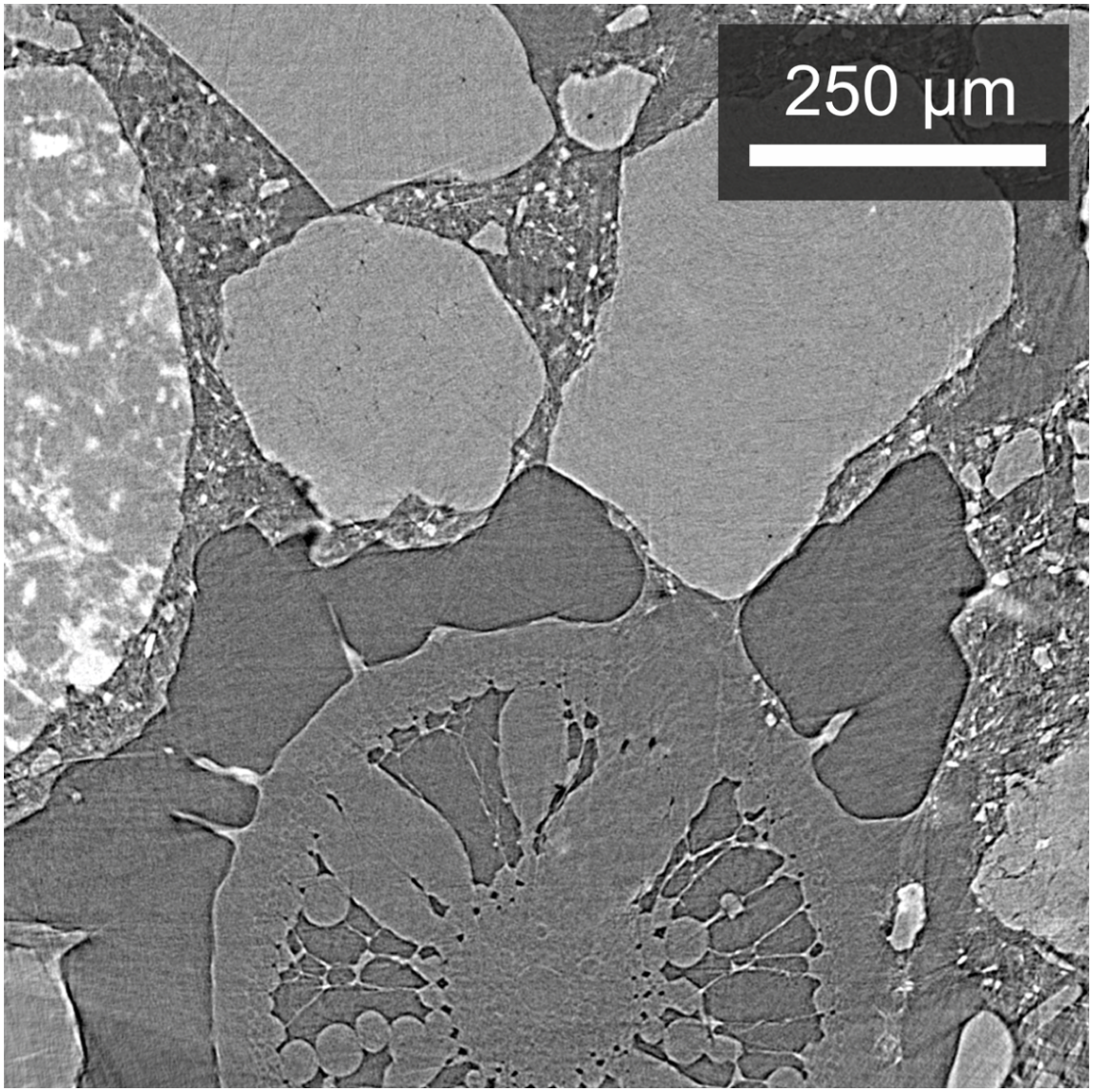

Figure 6.3: Data for sample 3 (*Oryza sativa cv Varyla*), acquired at $600\mathrm{nm}$ spatial resolution. Aerenchyma structure is clearly visible, as are hairs initiating from the root epidermis. A fluid phase is distinguishable in inter-aggregate spaces.

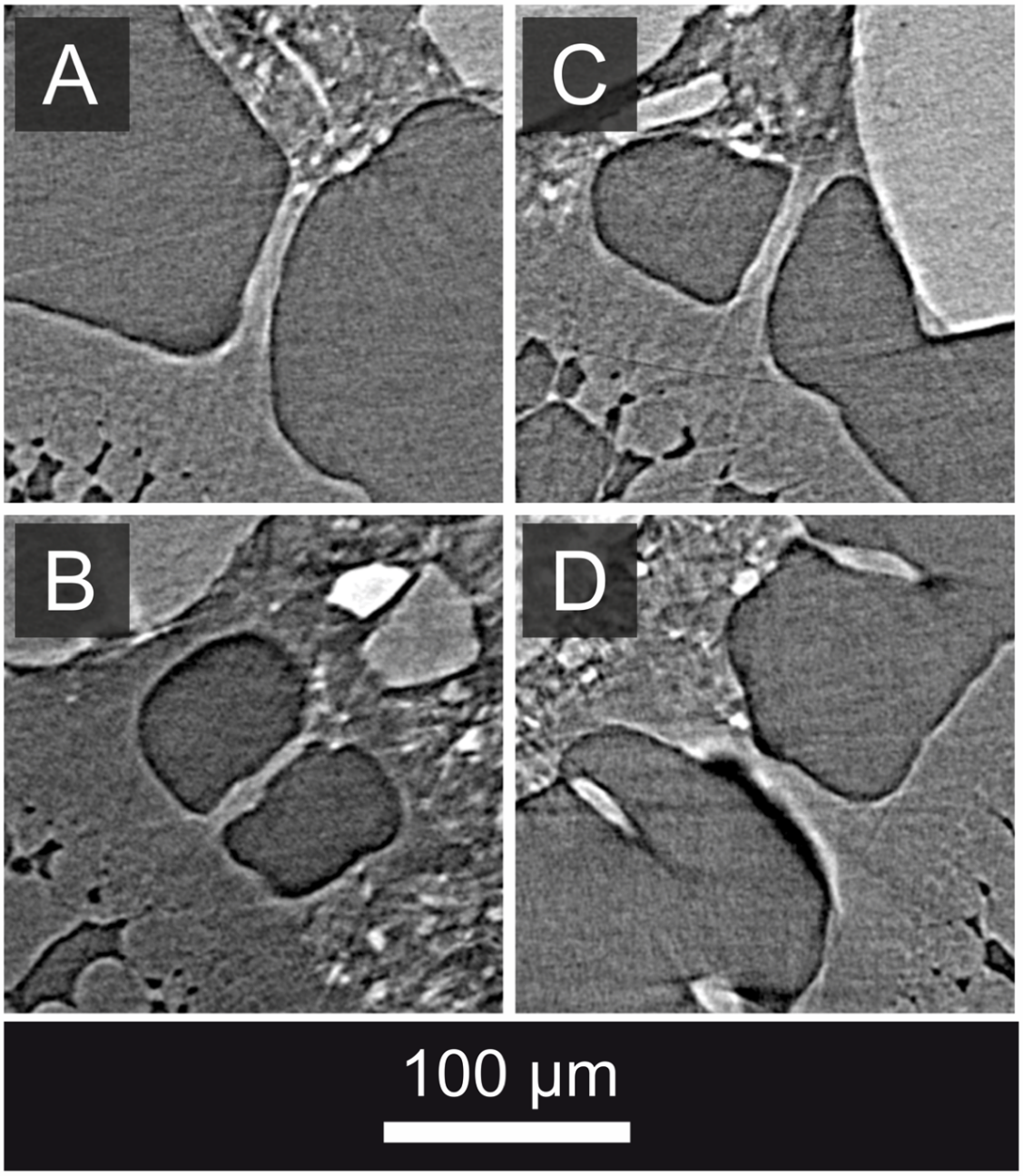

Figure 6.4: Panes A-D show root hairs in sample 3 (*Oryza sativa cv Varyla*) transitioning between gas and fluid phases. The hairs become indistinguishable in fluid due to the matched attenuation coefficients of water and fluid-filled cells

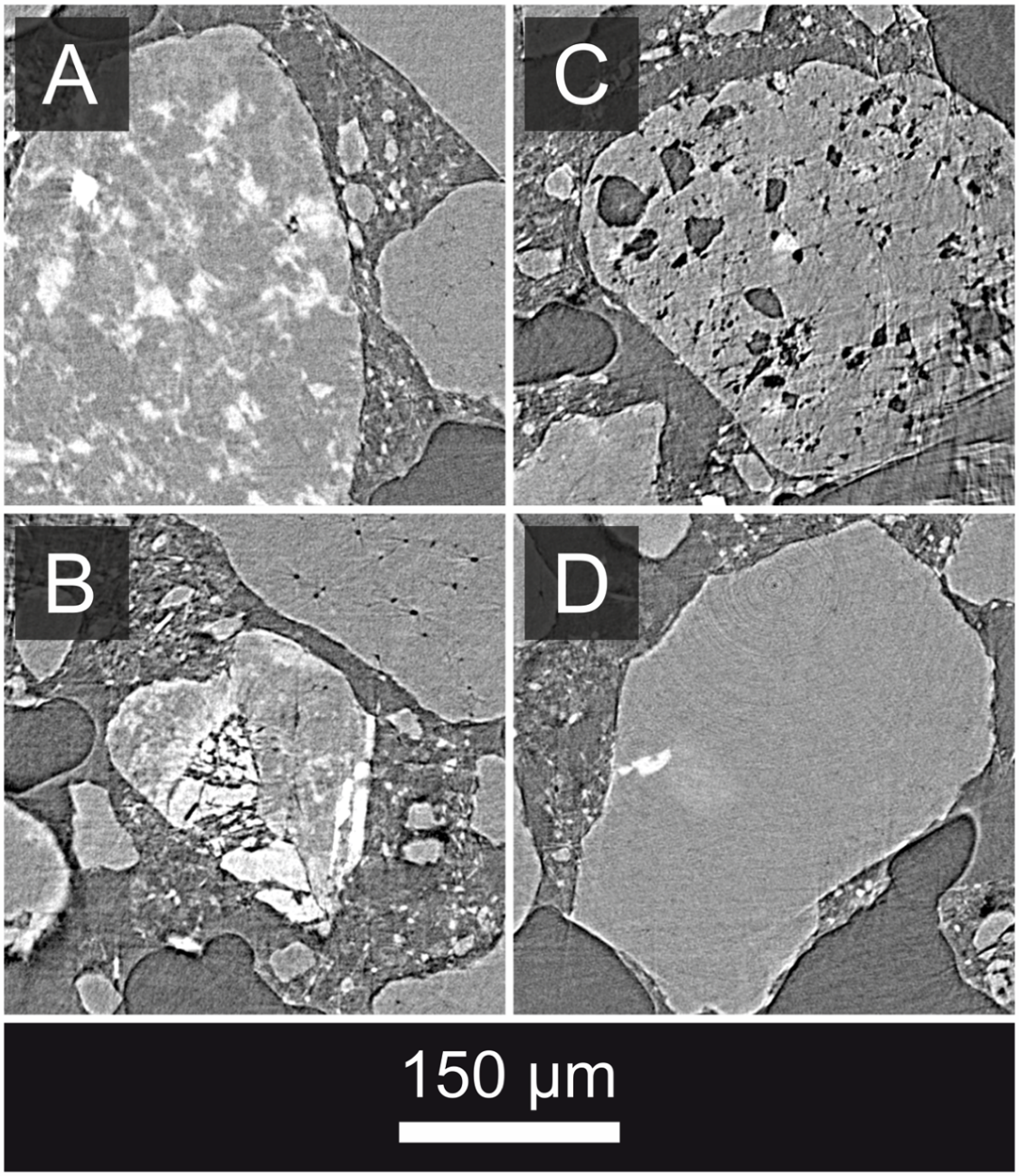

Figure 6.5: Panes A-D show different aggregate structures in sample 3 (*Oryza sativa cv Varyla*). Whereas some (A) have a highly homogenous intra-aggregate attenuation coefficient and pore distribution (given the imaging contrast and resolution), others demonstrate substantially more complex micro-structures

6.3 An improved paradigm for image-based modelling using SRXCT-derived rhizosphere data

The primary requirement in processing any CT data for explicit model parameterisation is the accurate classification of relevant features in 3D, allowing the generation of meshed geometries to which suitable equations can be applied in the simulation domain [Keyes et al., 2013a]. For samples containing a mixture of gas and fluid in the macropore domain, the classification of features represented two particular challenges in addition to those considered in Chapter 5:

- Achieving multiphase soil, gas and fluid segmentation
- Remedying the paucity of image contrast between root hairs and the fluid phase.

This section first considers the segmentation of fluid and soil phases, following which extensive treatment will be given to a novel, image-based paradigm for explicit root hair growth simulation. The preparation of geometries for P-uptake modelling in unsaturated conditions will thus be described.

6.3.1 Methods

Definition of a candidate sample and region of interest

Qualitative analysis of datasets revealed that in most cases, fluid content was too high to allow determination of even incomplete hair paths. Of the data acquired at $1.5\mu\mathrm{m}$ resolution, only that pertaining to sample 3 (*Oryza sativa cv Varyla*) had a majority of visible root length both unaffected by deleterious edge effects, and with an apparent majority of surface area not in direct contact with fluid or soil phases. In the regions where gas-filled macropore space was coincident to the root surface, full and partial hair paths were clearly discernible. On this justification, the dataset was chosen as a basis for workflow development.

A region of interest (ROI) was first sub-selected for image processing. In order to remove regions affected by edge effects, and to generate a geometry which was tractable for feature-extraction and FE meshing processes, a sub-region was cropped from the raw data representing a root length of $1.5\mathrm{mm}$, centred around the mid-point of the dataset in the z axis. Because the major root axis was close to the edge of the dataset in the x axis, it was necessary to crop to within $225\mu\mathrm{m}$ of the root surface in the positive x direction. However, in the negative x direction, and in both directions along the y axis, $1\mathrm{mm}$ of rhizosphere extending radially from the root surface was maintained. Given that the maximum root hair length determined in experimental data was $424\mu\mathrm{m}$ (Appendix 8.3), it can be considered that the ROI entirely enclosed

the root hair zone for $\approx 300^{\circ}$ of the root circumference (as shown in Figure 6.6). The resulting x, y, z dimensions of the dataset were $(1155 \times 1791 \times 1000)$.

Multi-phase segmentation of air, fluid and soil regions

The observed structure of the rhizosphere in the acquired data were more complex than for the data considered in Chapter 5, due to the presence of mixed gas/fluid phases within the macropore domain. Figure 6.7 demonstrates the significant difference in rhizosphere morphology elucidated by comparing data from the two imaging sessions sessions. In Figure 6.7-B, the macropore domain is entirely gas filled, whereas in Figure 6.7-A, it is only partially gas-filled, with the remainder consisting of a mixed fluid/soil phase. In some localised regions, the fluid appears near-homogenous, whereas in others, a heterogenous texture indicates a suspension of higher-density phases.

Robust segmentation of soil phases from μ-CT and SRXCT data is a non-trivial problem, as discussed in depth in Chapter 2. As part of this thesis, an algorithm was successfully applied to segment soil and macropore phases from μ-CT data [Keyes et al., 2013a]. Recently, others have developed alternative schemes for minimisation operator bias in soil segmentation, including techniques based on gradient masking [Schlüter et al., 2010] and indicator kriging [Houston et al., 2013]. Though such methods improve upon user-supervised approaches, they all consider the bi-level segmentation case, such that as presented, none was suitable for extraction of multiple phases from the hydraulically sub-optimal SRXCT data considered here.

Because the grey-level distribution of the data considered is bi-modal, with a lower intensity peak representing the gas phase (Figure 6.8), voxels for aggregates, roots and fluid phases are all encoded within a single, higher-intensity peak. Because image segmentation methods taking into account grey-level value alone will fail, additional operators that take into account morphological characteristics of the data must be used [Schlüter et al., 2010; Vogel and Kretzschmar, 1996].

To this end, a trainable segmentation approach was used, developed by *Kaynig et al.* for the classification of neurons in serial-section transmission electron-microscopy (ssTEM) data [Kaynig et al., 2010]. The approach allows the user to classify regions of pixels belonging to a number of distinct material *classes* (fluid, air, soil) within a single slice of the RAW grey-level CT data, and uses a *random forest* method, following *Breiman*, for classification of voxels in the entire dataset [Breiman, 2001]. The algorithm uses a combination of well-defined image filters (*i.e.* the difference between two Gaussians, the local gradient given by Sobel filtering and the computation of $2x2$ Hessian matrices) to define a range of descriptive parameters for each image pixel. The user trains the *random forest* classifier by manually defining sample sets of voxels

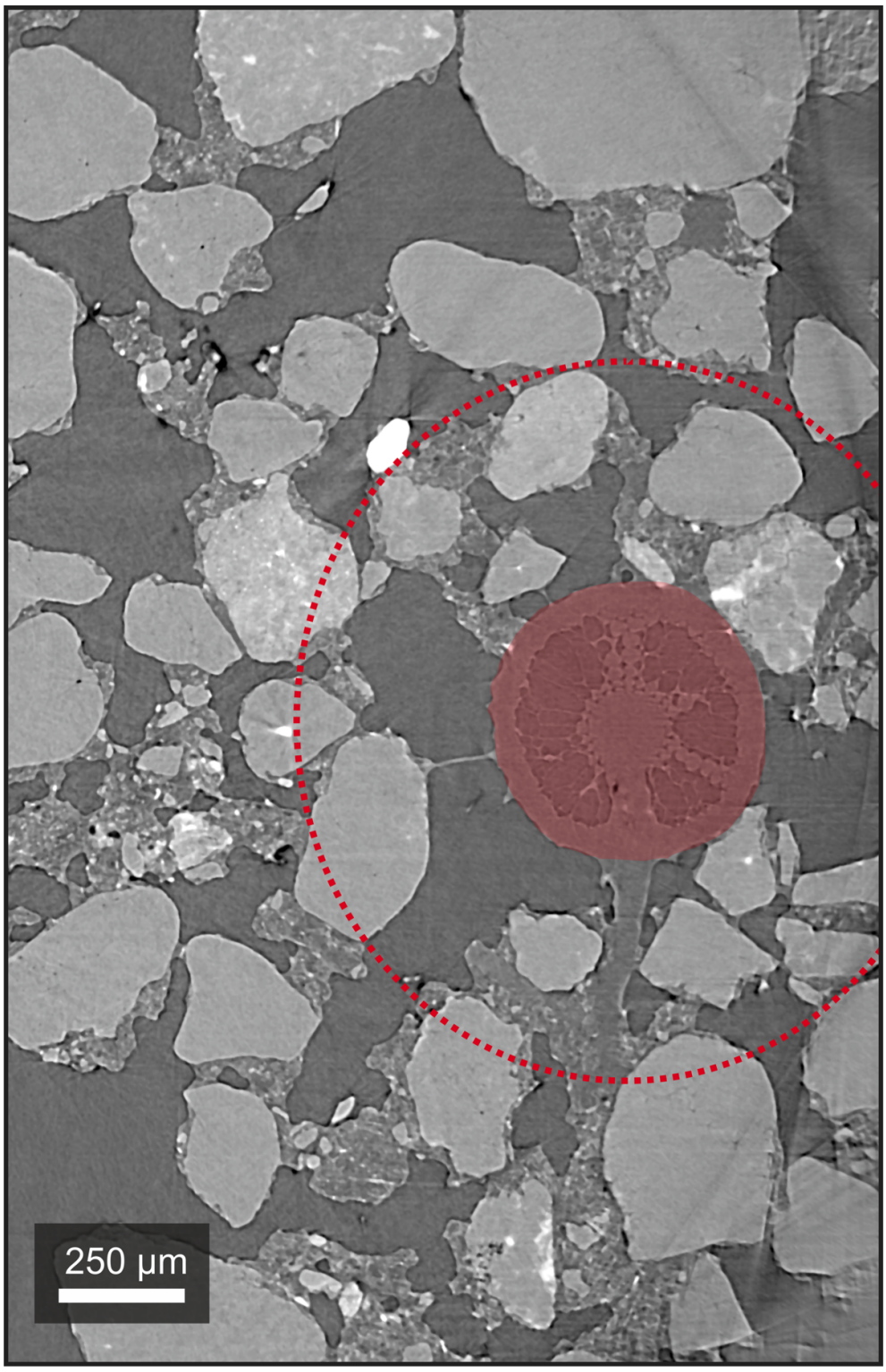

Figure 6.6: The ROI defined for image-processing. The dotted line indicates a distance of $\approx 425\mu\mathrm{m}$ from the root surface, this being the length of the longest hair in the validation data.

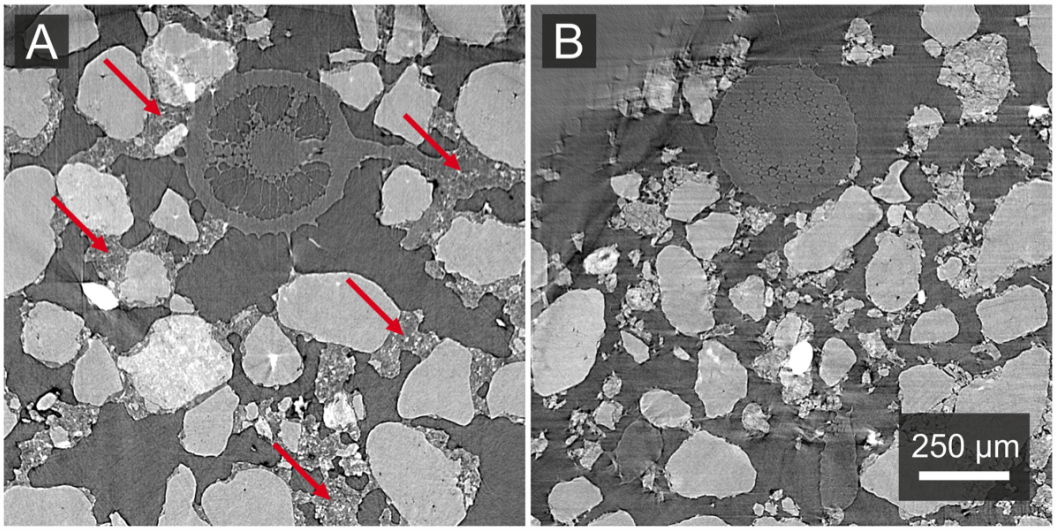

Figure 6.7: Comparing ROIs from data in sample 3 (A) and the wheat sample considered in Chapter 5 (B), the difference in macropore fluid characteristics can be seen. Arrows show representative regions of macro-pore fluid.

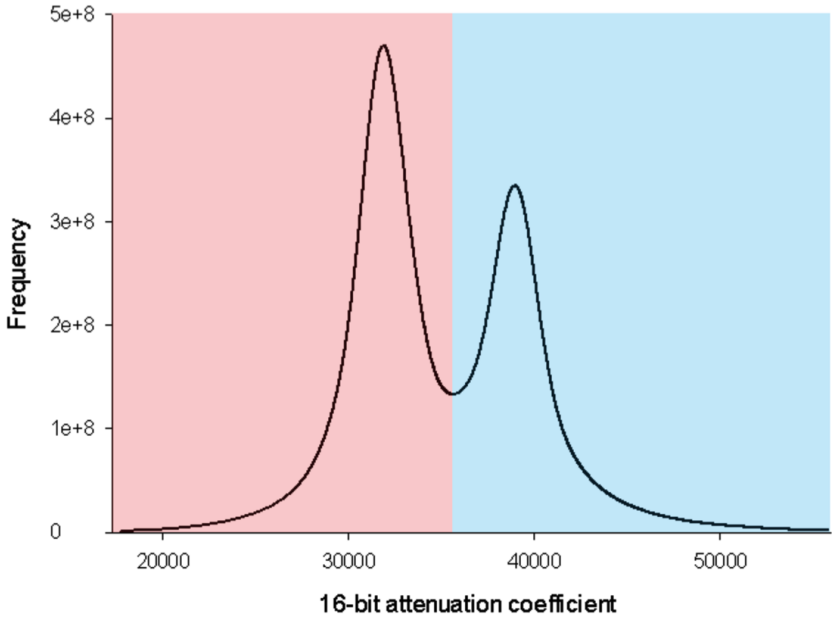

Figure 6.8: A greylevel histogram of the ROI demonstrates why segmentation methods reliant on global greylevel classification are unsuitable. Whereas the lower intensity peak (red region) encodes voxels representing the gas phase only, the fluid, root tissue and soil phases are encoded together within the higher intensity peak (blue region).

for each material class. The statistical method of *bootstrapping* (sampling with replacement) is used to parameterise the classifier, using the descriptive parameters of each user-defined pixel set to establish conditions determining the class to which a given test voxel is most likely to belong. The *random forest* algorithm is then applied to the entire dataset, allocating every voxel to the most probable parent class.

The specific application of the procedure to tri-phase segmentation in this work was to perform two distinct classification steps. First, the algorithm, implemented in FIJI, was used to differentiate between gas and non-gas phases, with the resulting non-gas region then being re-processed in order to separate the fluid from the solid phase. Figure 6.9 shows the stages of this routine. Median filtering with a radius of 6 voxels was applied following each segmentation stage in order to remove speckling artifacts in the classified results, whilst preserving gross surface topology. Distinct, binarised $8-\mathrm{bit}$ RAW files were thus generated for the soil and fluid phases.

Segmentation of roots and root hairs

Visible hair lengths were segmented using AVIZO 6 software, according to the protocol detailed in Section 5.3.4. Figure 6.10 shows the range of possible cases for hair interaction with soil and fluid phases. Of these, two hair sets were defined, one for which the entire length was visible ($\mathbf{H}_{FV}$), as shown in Figure 6.10-D, and the other for which only part of the hair length was visible ($\mathbf{H}_{PV}$), as shown in Figure 6.10-A. The set of hairs with no visible length was not considered in this case, (*i.e.* hairs that initiate in positions where fluid and/or soil are coincident to the root surface), as shown in Figure 6.10-C. Also excluded from consideration were hair segments emerging from the fluid phase for which no ($P_{epidermal}$) could be determined, as shown in Figure 6.10-B. These were excluded on the basis of two factors:

- Only one such hair was observed during qualitative analysis of the dataset.
- Such hairs introduce significant added complexity to the virtual hair growth stage considered later. An algorithm is described for 'growing' hairs with explicit reference to soil structure, but predicting a *reverse* path would require the added constraint that the hair path *must* track back to a root surface. Including such a constraint whilst maintaining stochasticity and a constrained length distribution is significantly more complex than it is for the 'open-ended' hair growth case. Though their inclusion is a clear objective for future work, such cases were not considered here.

For hairs in the set ($\mathbf{H}_{PV}$), the cartesian coordinates of initiation points on the root surface ($P_{epidermal}$) and points at which hairs transitioned to bulk fluid ($P_{interface}$) were recorded explicitly in a CSV file for later use in a simulation procedure. Distinct, binarised $8\mathrm{bit}$ RAW files were thus generated for hair sets ($\mathbf{H}_{FV}$) and ($\mathbf{H}_{PV}$).

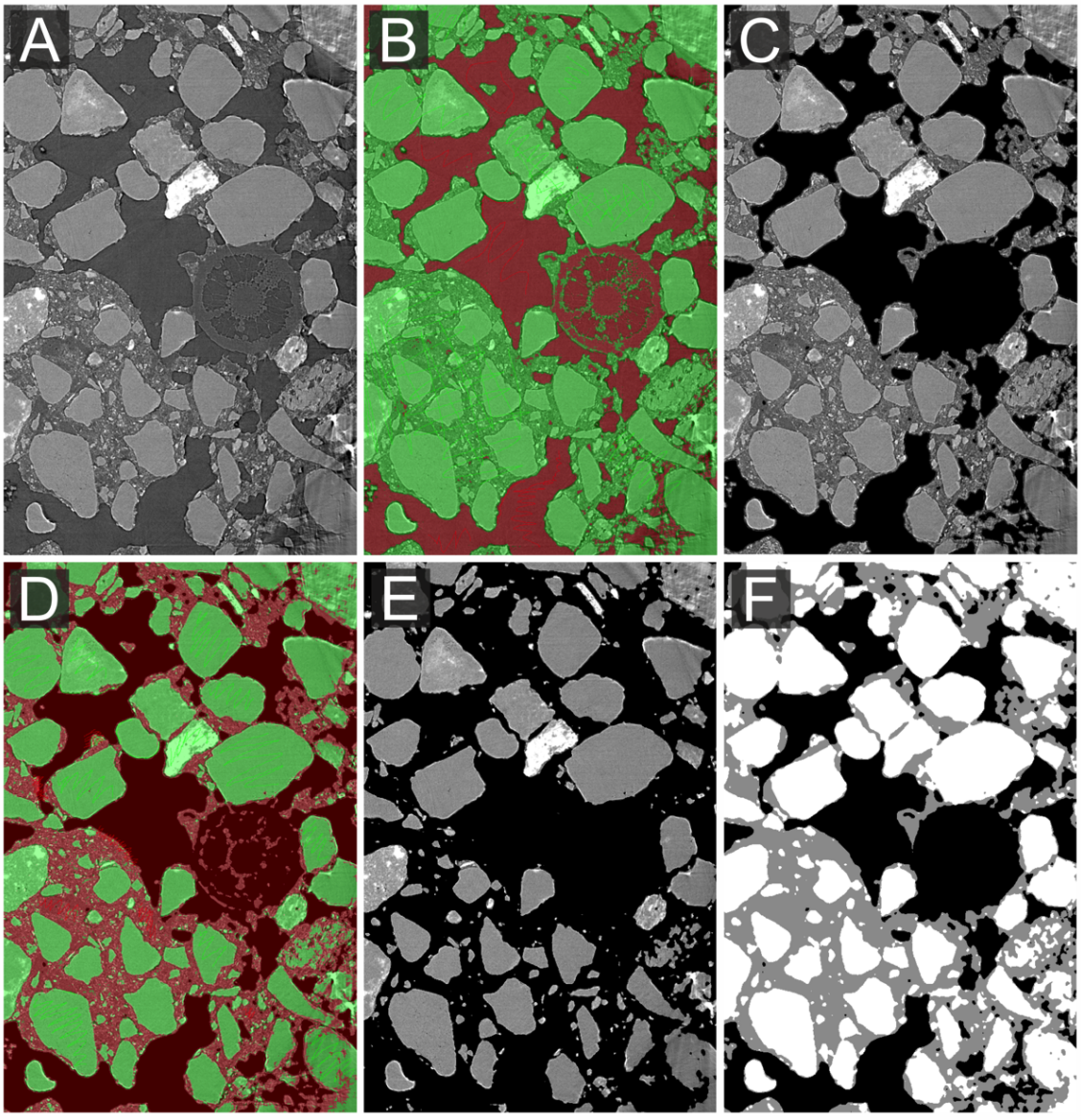

Figure 6.9: The trainable segmentation algorithm is applied to raw data (A) to classify solid and fluid phases as distinct from gas (B). The resulting region (C) is then re-classified to separate the gas and fluid phases (D) leaving isolated soil regions (E). Binarising and recombining the soil and fluid phases results in the output geometry (F).

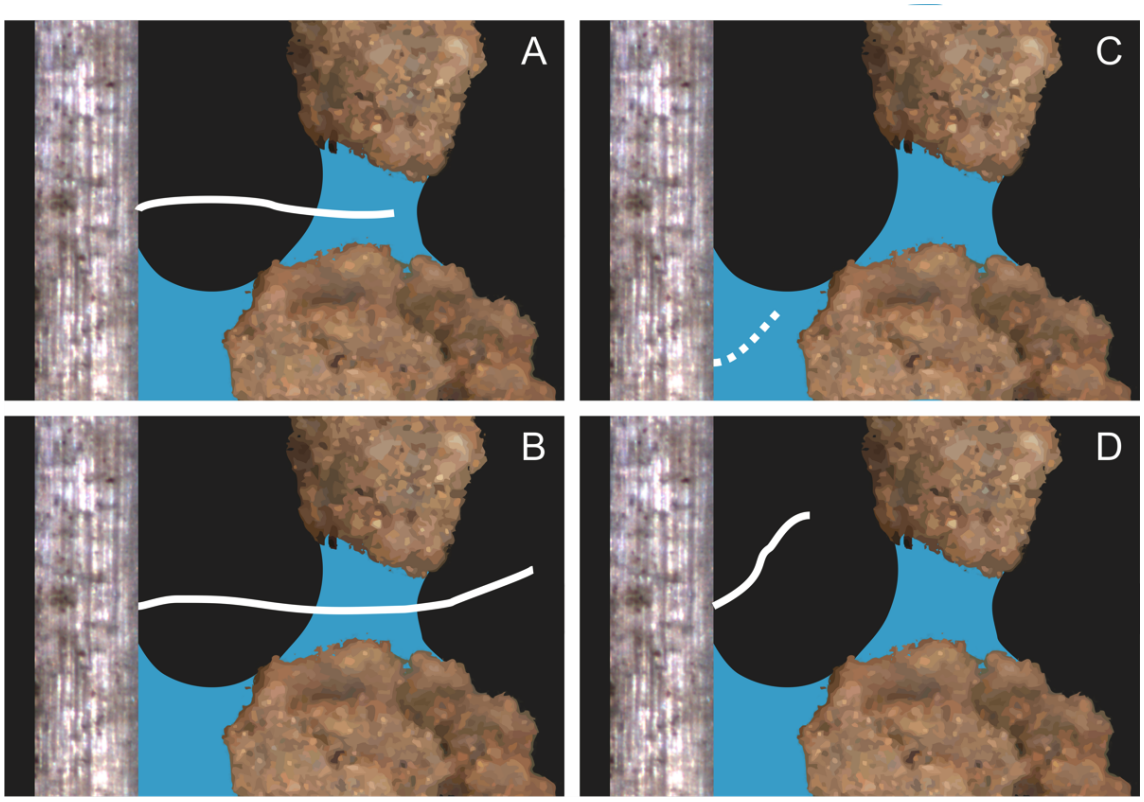

Figure 6.10: Hair path characteristics fall into one of a number of classes, including (A) hairs that cross macropore space, enter fluid and do not re-emerge, (B) hairs that cross macropore space, enter fluid and do re-emerge, (C) hairs that are entirely within the fluid phase, (D) hairs that are entirely within the gas phase.

Roots were segmented within AVIZO 6, using a semi-automated method combining manual classification of root cross-sections and an interpolation procedure. Using a Cintiq 22HD graphics tablet (Wacom Co. Ltd., Saitama, Japan), primary and lateral root cross sections were classified manually at a slice spacing of 20 voxels in the data z axis. An inbuilt interpolation algorithm within AVIZO 6 was then used to generate a 3D volume with a surface fitted to maintain a smooth surface topology following the in-slice user-defined boundaries. The resulting volume was exported as a binarised $8\mathrm{bit}$ RAW file.

Combining segmented regions into a master geometry

After definition of necessary phases (soil, fluid, roots, visible root hairs), the datasets were combined to generate a *master* geometry suitable for:

- The quantification of rhizosphere properties (*i.e.* volume fractions, surface areas, wetted hair length).
- The parameterisation of 3D regions impermeable to hairs (soil, roots), allowing explicit consideration of mechanical impedance effects in a virtual hair growth model.
- Generation of FE meshes, to allow explicit numerical modelling of nutrient acquisition by hairs and roots.

Figure 6.11 shows a volume rendering of the resulting *master* dataset, with cutaways to show internal root structure and soil phases.

Quantifying key rhizosphere morphology parameters

The master dataset can be used to quantify a range of rhizosphere structural properties. Volume fractions of soil aggregates, gas, macropore fluid and roots can be calculated by counting voxels belonging to each phase. Areas of coincidence are also estimated between different phases using the following approach:

- The two phases for which coincidence is to be quantified are extracted from the master dataset as discrete, binarised regions (*i.e.* fluid and root in Figure 6.12-A).
- Within FIJI, a binary dilation operator is applied to one of the regions, adding a 1-voxel-deep layer to the entire surface, such that a single voxel overlap exists across coincident regions.
- Applying a logical AND function to the two regions leaves only the coincident surface region in the form of a 'shell' of a single voxel thickness (Figure 6.12-B).

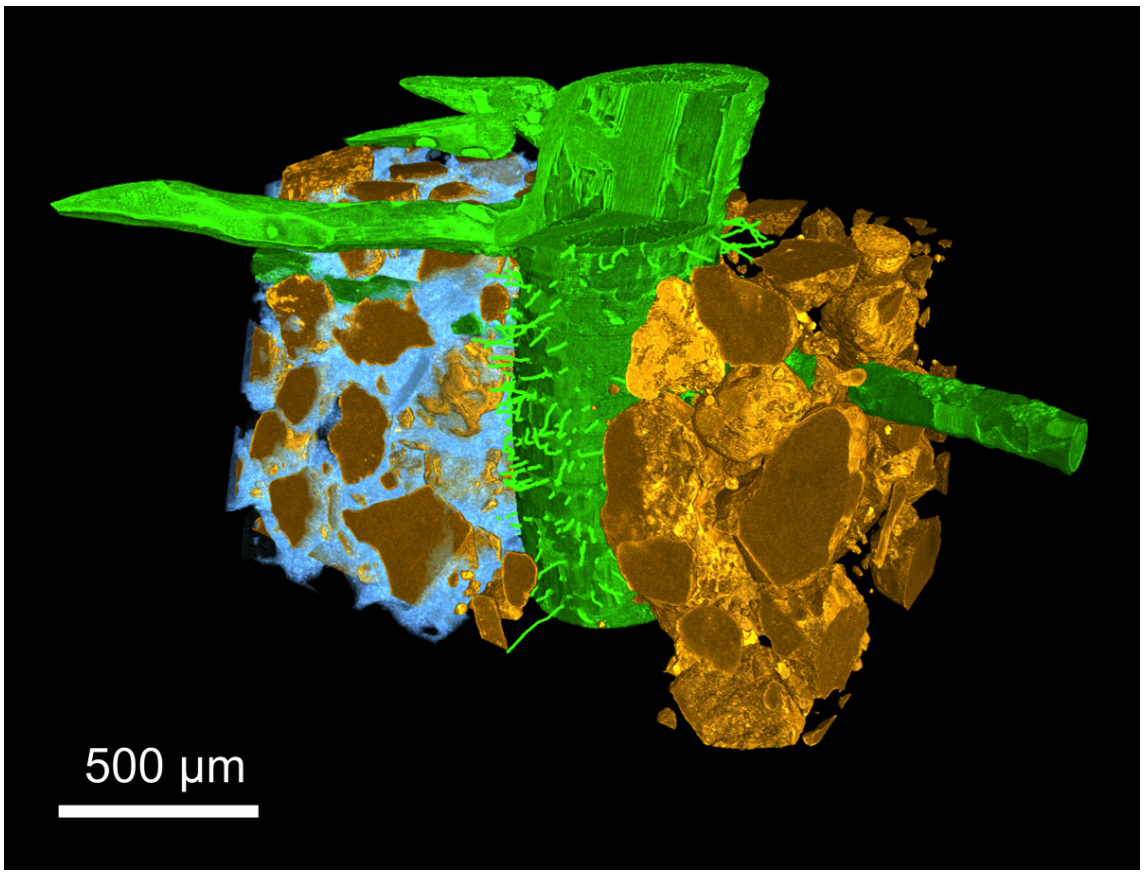

Figure 6.11: 3D rendering of the output from image segmentation procedures, with cutaways to show features. Hairs shown are from sets ($\mathbf{H}_{FV}$) and ($\mathbf{H}_{PV}$). Fluid is only shown in one half of the soil region. Root surfaces have been partially cut away to show internal structure of aerenchyma and stele.

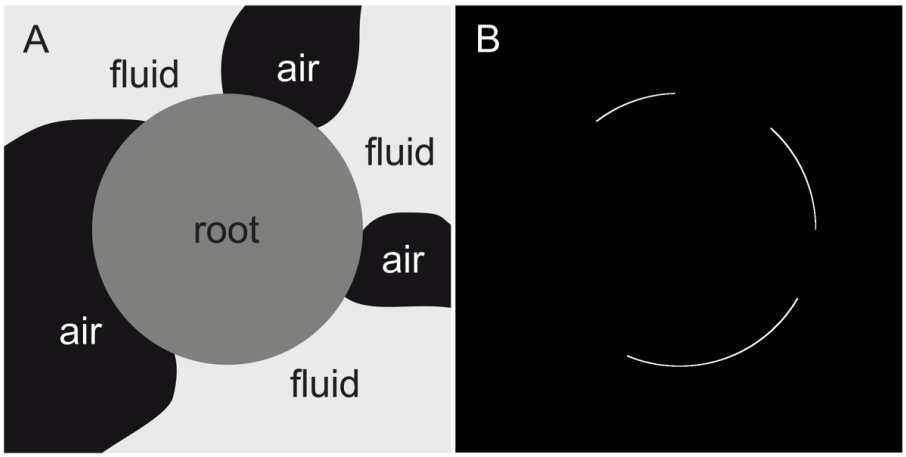

Figure 6.12: Schematic showing the procedure for definition of coincident surface area between different phases. (A) The fluid region is dilated by a single voxel, with a logical AND then applied between fluid and root voxels. (B) The result is a single voxel shell which can be used to estimate contact surface area.

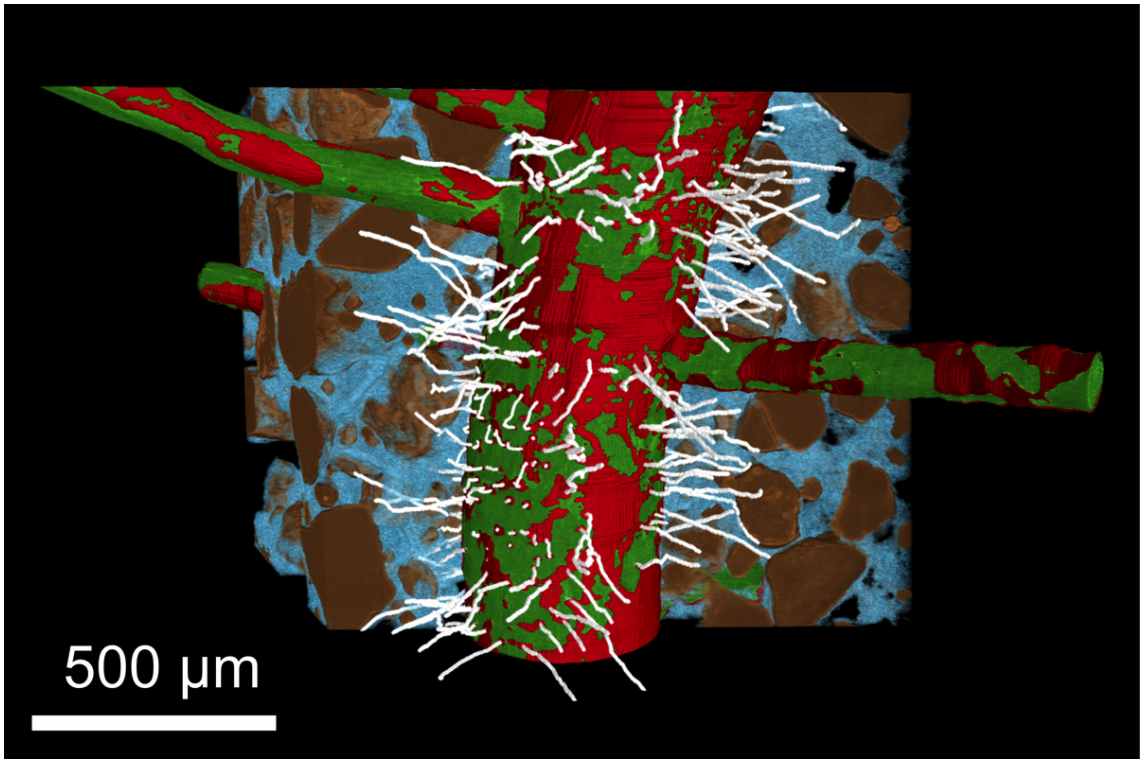

Figure 6.13: Figure showing the region of the root surface which is directly coincident to either soil or fluid phases (red). The hairs are generated using the HairGrower algorithm described in Section 6.4.

In this manner, the surface area of coincident voxel regions can be both visualised and quantified, allowing parameters such as the wetted soil and root surface area to be reported. For the root length shown in Figure 6.11, Figure 6.13 shows the region of the root surface directly coincident to either soil or fluid phases. Over the 1.5mm root length considered in the region of interest (ROI), 32.15% of the total root surface was found to be in immediate contact with soil and water phase. In this region, the determination of hairs was not possible. Along the root length, a total of 276 hairs were classified, of which 221 were only partially visible due to coincidence with macropore fluid, giving a total density of 184hairs/mm. If the same hair density exists over the fluid and soil coincident surface of the root, the root hair density might be as high as 271hairs/mm, far in excess of any estimates from root washing studies.

6.4 Development of *HairGrower*, a novel algorithm for virtual hair growth

6.4.1 Classifying hairs in poor contrast situations

As discussed in Section 6.2.2, it was impossible to resolve hairs in the data once they enter

regions of bulk macropore fluid. The problem is one of image contrast rather than spatial resolution, such that even in data acquired at $600\mathrm{nm}$ resolution, it was not possible to differentiate between hairs and fluid with the naked eye. Three hypothetical solutions to the problem are:

- Enhance contrast by using chemical manipulation of plant or pore water to improve the inherent difference in attenuation coefficients between fluid and root hairs.
- Enhance contrast in the imaging domain through exploitation of phase contrast effects, including full phase retrieval.
- Use computational approaches in the image-processing domain to complete missing components of hair architecture.

A trial was carried out using an adaption of the a contrasting protocol developed in Chapter 3, with imaging carried out at the SRXCT beamline at the DIAMOND light source at Harwell, UK. Hardware limitations meant that samples received much greater doses of ionising radiation than in previous experiments (see Appendix 8.4). This resulted in a degree of cortical damage and motion artifacts which precluded any meaningful assessment of effectiveness in this case. Robust assessment of phase-contrast applications in root hair imaging is a primary aim for future SRXCT imaging experiments.

The remainder of this chapter is given to development of a hair modelling paradigm, *Hair-Grower*, which allows the generation of virtual hair completions in data affected by poor contrast between hairs and macropore fluid.

6.4.2 Virtual completion of root hairs using unsupervised, computational methods

Though the high volume fraction of macropore fluid in the majority of datasets precludes meaningful assessment of hair morphology, approaches in the simulation domain can potentially allow models to be parameterised by virtual completion of partially visible hairs. As discussed in Section 1.5.3, previous approaches to modelling of root systems at scales from the root hair [Ma et al., 2001] to the entire root system [Diggle, 1988; Leitner et al., 2010a; Lynch et al., 1997; Pagès et al., 2004] have made use of growth simulation schemes in order to provide geometric parameterisation for root/soil models. Because these models consider root growth in a bulk soil volume without a explicitly represented structure, root deflection arising from the complex physical and biochemical properties of real soils is typically simulated according to a stochastic regime [Dunbabin et al., 2013]. The stochastic character of root growth is thought to be determined both by environment and genetics [Postma et al., 2013], and in growth models it has tended to be tuned using a variety of scalar indices representing the magnitude of various effects, such as deflection due local compaction and the influence gravitropism on root angles [Lynch et al., 1997]

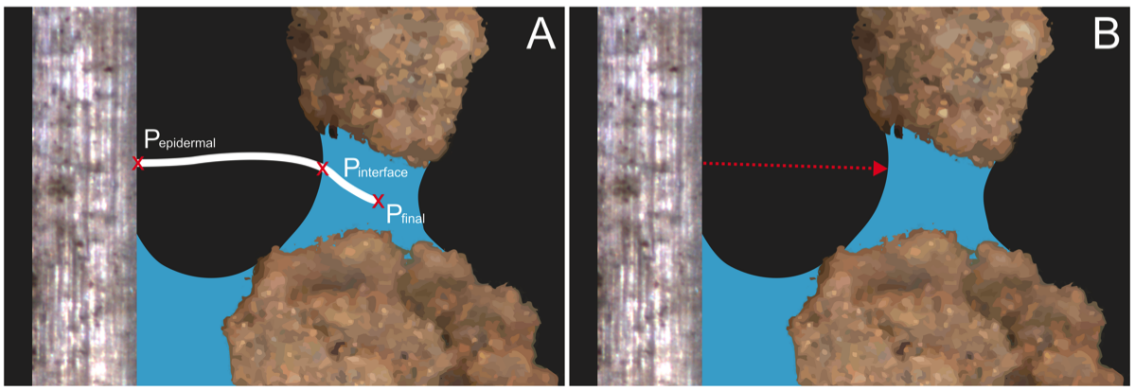

Figure 6.14: For each hair, a certain set of characteristic entities can be defined (A). $P_{epidermal}$ is the location at which the hair initiated from the root epidermis. $P_{interface}$ is the point at which the hair transitions from gas to fluid phase. P_{final} is the point at which the hair terminates (concealed within fluid in most cases). (B) Shows the vector ($P_{epidermal}\vec{P}_{interface}$) used to approximate existing length and direction.

As seen, data acquired using synchrotron μ-CT contains highly detailed information regarding the spatial arrangement of soil phases, macropore fluid, major root axes, and to a degree (dependent on macropore fluid characteristics), the paths of fully and partially visible hairs in the rhizosphere. Problematically for image-based nutrient uptake modelling, in which the fluid provides the ion transport continuum between bound soil nutrients and plant uptake surfaces, the inability to resolve hairs in fluid means that only hair lengths that do not contribute to uptake can be considered. In the absence of a hair growth simulation procedure, the only models that could be parameterised would be those considering uptake by root surfaces alone, or by hairs of the set ($\mathbf{H}_{PV}$) in a fully saturated regime (as considered in Chapter 5). Though this is a standard assumption in explicit models [Barber and Silberbush, 1984], it would be preferable to be able to combine the fine 3D structural insight afforded by synchrotron imaging with the benefits of virtual root modelling. In future, prediction of P uptake characteristics can then be achieved explicitly at the hair scale for non-idealised saturation conditions.

Analysis of the data showed that for the ROI considered, 80.0% of hairs were only partially visible due to coincidence with macropore fluid. However, it was feasible to quantify the length of each hair in the set ($\mathrm{H_{PV}}$), as well as the coordinates of each epidermal initiation point ($P_{epidermal}$), and the corresponding point at which the hair enters the fluid phase $P_{interface}$ (see Figure 6.14). In this manner the spatial distribution of all partially visible hairs on the root surface could be defined, as well as the existing length ($L_{existing}$) and an approximate direction vector of growth at the point of fluid entry for each hair ($P_{epidermal}\vec{P}_{interface}$). Though any number of genetic and biochemical factors could ostensibly be considered, the remaining parameterisation requirements for a minimal model of physical interactions are:

- The manner in which hairs deviate as a result of mechanical interaction with the major

component phases (soil aggregates, fluid, gas) of the rhizosphere.

- The final length (L_{final}) to which each hair must be grown, such that a required growth length for each hair ($L_{virtual}$) can be defined as $L_{virtual} = L_{final} - L_{existing}$.

By defining a value of $L_{virtual}$ for each hair, together with a set of rules governing the nature of interaction with different rhizosphere phases, growth of a virtual hair set within a suitable computational environment could be achieved.

Setting up the growth model

The growth algorithm was written in MATLAB (Mathworks, Natick, Mass, US), selected as a high-level environment facilitating straightforward prototyping and debugging of code during development. The top-level overview of the algorithm is as follows:

- Import or define all necessary parameters, including (i) initiation and termination points of partially-visible hairs, (ii) experimentally determined full hair lengths, (iii) soil, root, water and air phases as 3D entities, (iv) parameters to determine stochastic growth procedure.
- Fit a distribution to the experimental hair length data, then use survival analysis sampling to apply a discrete value of $L_{virtual}$ to each hair.
- Use a stochastic growth routine to define a virtual continuation path for each hair, such that the final total length matches the value of L_{final} defined via survival analysis. The growth path should take into account necessary deflection around soil aggregate and root phases.
- Write the virtual continuation paths of all completed hairs to an output file suitable for meshing as an input for numerical modelling.

As with other virtual growth paradigms, the design of the algorithm follows a modular form, such that later improvements to various processes can be added or substituted in. The operation of the algorithm is now described in detail (the entire code can be found in Appendix 8.6).

Parameterising the nature of physical hair interactions with the rhizosphere.

To most closely approximate the real growth characteristics of hairs, observations from the SRXCT data were used to guide algorithm design. Qualitative analysis of root hair data from the TOMCAT beamline indicated the following characteristics of root hair and rhizosphere interactions:

- In the macropore domain, SRXCT data suggested that hairs are most often found to cross pores without gross deviation. This is likely a consequence of the uni-axial nature of hair growth, driven as it is by radially constrained turgor pressure and tip-focused deposition of new cell wall material [Gilroy and Jones, 2000; Sieberer et al., 2005]. It should be noted that *in vitro* de-polymerisation of endoplasmic micro-tubules (EMTs) has been observed to cause waviness in hairs of *Arabidopsis thaliana* [Sieberer et al., 2005], and such EMT array regulation may be responsible for the curling of hairs around rhizo-bacteria which represents the initiation of symbiotic nodule formation in leguminous plants [Esseling and Emons, 2004; Hadri and Bisseling, 1998; Kijne, 1992]. However, for rice and wheat grown in sterilised soil, such influences on hair morphology can be precluded.
- When hairs make contact with soil aggregates, a complex array of morphologies can result. In Chapter 5, it was observed that once a hair contacts the surface of an aggregate, the impedance to growth necessitates deviation, following which the hair either re-enters the macropore space, or maintains contact with the aggregate, following the surface profile. A single hair can make a number of such interactions with discrete aggregates.

In the absence of a temporally resolved study, it unclear is to what extent the observed morphology of a hair represents the path actually transcribed by the tip during growth, since water and soil movement may alter the position of a hair subsequent to development. It is conceivable that a hair grown in saturated macropore space could be deposited against an aggregate surface via hydraulic effects (*i.e. surface tension*) if the fluid later drains away under the influence of redistribution processes. What is nonetheless clear is that hair pathways are confined to either the macropore domain, or, in a minority of incidences, intra-aggregate cracks. It follows that a hair growth model which explicitly considers hair/aggregate interactions should constrain growth to within pore spaces of at least the diameter of the growing hairs.

Parameterising hair length distributions

An important parameter requiring external validation is the length to which hairs should be grown during a growth simulation procedure. Because only partial length data is gained from analysis of the CT data, it is necessary to estimate the required values of L_{final} for each hair in the set ($\mathbf{H}_{PV}$) using a complementary methodology. Various studies in the literature have estimated mean hair lengths using phytagel assays or washed root segments [Dittmer, 1949; Haling et al., 2013], but have not reported the distribution of lengths in the sample set. At the root system scale, models have been similarly parameterised using measurements taken from detailed drawings of root systems acquired in the field via planar sectioning [Kutschera, 2009; Schnepf et al., 2012]. In this study, it is preferable to parameterise hair length against a distribution of lengths rather than a mean value, in order to more accurately capture the real characteristics of hair morphology in the rhizosphere.

Given known values of $L_{existing}$ for the partially visible hair set in the CT data, corresponding values for $L_{virtual}$ can be sampled through the application of *survival analysis* statistics. Considering the application of this principle to root hair length, if a distribution of experimentally derived L_{final} values is known, it is possible to calculate the probabilities of a hair with length $L_{existing}$ reaching different values of L in the range $L_{existing} \geq L \leq L_{max}$, where L_{max} is the maximum possible value of L.

Validation data for soil-grown hairs can be achieved through image-based measurement of carefully washed root segments in FIJI, following [Haling et al., 2013]. Root washing methods entail experimental artifacts as a consequence of mechanical damage [McCully, 1999], but there is a paucity of alternative validation protocols for soil-grown roots. A protocol for estimation of hair length distributions following *Haling et al.* can be found in Appendix 8.3.

Statistical hair length sampling

In order to select appropriate values of $L_{virtual}$ for each hair, methods from the field of survival analysis statistics are used. Survival analysis considers the probability of an individual from a sample set surviving to a certain age, given that both the individual's existing age and the distribution of terminal ages for the population is known. If a distribution of experimentally derived L_{final} values is known, it is thus possible to sample completion lengths ($L_{virtual}$) for each hair in the set, such that the distribution of resulting lengths matches that of the validation data. Though it would be feasible to calculate the mean of the validation data, and apply this same value of L_{final} to every hair, the use of a distribution allows for a consideration of hair morphology more closely representing the real condition. Input parameters necessary for the application of survival analysis are:

- An array containing ($P_{epidermal}$) and ($P_{interface}$) coordinates for each visible hair section in the segmented CT data.
- An array of experimentally derived hair lengths.

The first stage is the estimation of discrete existing hair lengths ($L_{existing,n}$) using a trignometric, straight-line approximation between $P_{epidermal,n}$ and $P_{interface,n}$. Because hairs in macropore space are observed to have near-zero tortuosity, this is considered a reasonable assumption.

In order to generate a continuous probability distribution from the experimental data, allowing application of survival analysis theory, characteristic parameters α and β were fitted in to the Weibull probability density function (PDF) using MATLAB, defined as,

$$y = f(l|\alpha, \beta) = \beta(\frac{l^{(\beta-1)}}{\alpha^{\beta}})e^{-(\frac{l}{\alpha})^{\beta}}, \tag{6.1}$$

where α is the *scale parameter* and β is the *shape parameter*.

Methods from survival analysis were then used to estimate the likelihood of each of the n hairs in the set ($\mathbf{H}_{PV}$) reaching a final length ($L_{tot,n} = L_{existing,n} + L_{virtual,n}$), given both the distribution of final lengths ($g(\alpha, \beta)$), and the observed partial length ($L_{existing,n}$). For any length (l) in the range ($L_{existing} \leq l \leq L_{max}$), two key entities are defined; the *survival function* (SF),

$$S(l) = P(L_{tot} > l), \tag{6.2}$$

and its complementary function, the *lifetime distribution function* (LDF),

$$F(l) = P(L_{tot} \leq l), \tag{6.3}$$

which is the probability that a random variable (L_{tot}) with a known probability distribution will be less than or equal to (l). This takes the form of a cumulative distribution function (CDF), which can be computed in MATLAB from the fitted PDF (Equation 6.1). Being the complement of the survival function, the LDF can also be defined as,

$$F(l) = 1 - S(l), \tag{6.4}$$

and where the derivative of $F(l)$ can be computed, it is also possible to define the corresponding PDF $f(l)$, where,

$$f(l) = \frac{d}{dl}F(l), \tag{6.5}$$

The probability (P) of a hair reaching each length in the range $L_{existing} \leq l_{test} \leq L_{max}$, given a set value of $L_{existing}$ is given by first computing a PDF of *future lifetime* according to the equation:

$$P(L_{virtual}|L_{existing}) = \frac{f(L_{existing} + L_{virtual})}{S(L_{existing})} \tag{6.6}$$

Where $f(L_{existing} + L_{tot})$ is the PDF of ($L_{existing} + L_{virtual}$) over the range ($L_{existing} \geq l_{test} \geq L_{max}$), according to Equation 6.5.

Using Equation 6.4, $S(L_{existing})$ can be written in the form $(1 - F(l))$, where as discussed, ($F(l)$) is the CDF of ($L_{existing}$). Both CDF and PDF are computed in MATLAB, using the α and β values derived by fitting Equation 6.1 to the experimentally derived hair length data. Because each partially-visible hair has a distinct value of $L_{existing}$, it is necessary to define an individual PDF of future lifetime for each hair.

Discrete P values were calculated using a FOR loop which iterates over Equation 6.6, using a 1D array of $L_{virtual}$ values over the range ($L_{existing} \leq l_{test} \leq L_{max}$), with a step size ($dx$), set in this instance to ($dx = 0.1$). Thus a total of ($\frac{L_{max}-L_{existing}}{0.1}$) discrete values of P are calculated. Randomised sampling of the resulting array allowed a value of L_{tot} to be selected for the given hair. The required growth length to be added to the partial hair by the *HairGrower* algorithm was then trivially given by,

$$L_{virtual,n} = L_{tot,n} - L_{existing,n} \tag{6.7}$$

Repeating this procedure for all the hairs in the set ($\mathbf{H}_{PV}$), defined from the SRXCT data allowed complete definition of the final lengths required to parameterise the virtual growth procedure which follows.

Full description of the *HairGrower* algorithm

The hair growth steps of the algorithm are presented graphically in Figure 6.16, using a simplified 2D representation of the real 3D case. Figure 6.15 shows a flow-chart overview of the algorithm.

The growth algorithm uses a binarised, 3D representation of soil and root phases as a geometric input (Figure 6.17), allowing the growth to be simulated via explicit mechanical interactions within the rhizosphere. An 8bit RAW file with voxel dimensions (x_{CT}, y_{CT}, z_{CT}) is imported into MATLAB, in which voxels representing root and soil phases have a value of 255, and air and fluid phases have a value of 0. This is read into a 3D array of size (x_{CT}, y_{CT}, z_{CT}), such that each element has a corresponding index value of either 255 or 0. A zero array (*dummy*) with the same coordinates is defined, to which are written the hair paths that are the output of the algorithm.

The growth algorithm functions iteratively on each hair. A step length (L_{step}) for each iteration is defined by the user, though if $L_{step} \geq L_{virtual}$, the step length is automatically defined as ($L_{step} = L_{virtual}/2$). A step number is defined as ($n_{steps} = L_{virtual}/L_{step}$), which is the number of growth iterations required to complete the hair. The initial growth vector for the hair is defined as the product of L_{step} and the unit vector in the direction of the visible hair segment.

The next stage in the algorithm is to determine in which direction the next iteration should be made from the initial point (P_{init}), relative to the previous line segment. The chosen point (P_{seed}) becomes the initiation point for the following iteration, and the process continues until the number of iterations reaches n_{steps}.

For the first iteration, P_{init} is defined as the hair entry point to the fluid phase ($P_{interface}$).

The position of P_{seed} is determined by interrogating a large number (n_{points}) of test points (P_{test}) for validity of certain criteria. Because the step length is constrained, all test points must necessarily lie on the surface of a sphere with radius L_{step}, centred on P_{init}. The placing of evenly distributed points on a sphere is a well known mathematical problem, since for large values of n_{points}, there exists no exact formula allowing the coordinates of the points to be defined [Kuijlaars and Saff, 1997]. As a result, approximations must be used. Most commonly, this is achieved by either simulating the equilibrium positions of repelling points constrained to a spherical surface [Tatham, 2012], or by distributing points along a spiral transcribed on the surface of a unit sphere [Kuijlaars and Saff, 1997]. Methods based on the spiral approach are computationally much faster than those requiring simulation, and of these the *Golden Section spiral* provides more even packing of points than the *Saff & Kuijlaars* method, with the added benefit of accommodatng any number of points. Using this method, a total of n_{points} points are defined on a unit sphere, with the coordinates multiplied by (L_{step}) and translated such that the centre of the circle is coincident with P_{init}. This provides the coordinates of n_{points} test points surrounding P_{init}, for which corresponding array values ($\psi_{x_{test,n},y_{test,n},z_{test,n}}$) are known.

Sampling of a single point in order to initalise P_{init} for the next iterative step is performed according to the following criteria:

- Points are rejected for which the vector ($P_{init}\vec{P}_{test}$) forms an angle of more than 90° to that of the vector ($P_{epidermal}\vec{P}_{interface}$). This is to prevent the possibility of a hair deviating by more than 90° from the visible growth direction.
- Points are rejected for which any coordinate is outside the range of the dataset. In other words, the coordinates of each test point must satisfy all the criteria,

$$(0 \leq x_{test} \leq x_{CT}), (0 \leq y_{test} \leq y_{CT}), (0 \leq z_{test} \leq z_{CT}) \tag{6.8}$$

- Points are rejected for which index value satisfies the constraint ($\psi_{x_{test,n},y_{test,n},z_{test,n}} = 255$), as defined by the imported SRXCT data, since such points lie within the location of either soil or root phases.

Un-rejected test points are next grouped according to the angle between the vectors ($P_{init}\vec{P}_{test}$) and ($P_{epidermal}\vec{P}_{interface}$). This angle ($\alpha_{test,n}$) is calculated for each point, and points then grouped into four sets:

1. $0^\circ \leq \alpha_{test} < 15^\circ$
2. $15^\circ \leq \alpha_{test} < 30^\circ$
3. $30^\circ \leq \alpha_{test} < 50^\circ$

4. $50° \leq \alpha_{test} \leq 90°$.

The uni-axial, turgor-driven extension of hairs means that growth is likely to continue in a direction close to the existing orientation, unless mechanical impedance constrains the growth path. Selection of a new P_{seed} thus always begins with the set of smallest angle, moving to the next if the preferred set is empty. If no suitable point exists in any set, hair growth is terminated and the algorithm moves to consider the subsequent hair. Selection of points within any non-zero set where $n_{points} > 1$ is randomised in order to model the stochasticity observed in real hair growth [Dunbabin et al., 2013; Postma et al., 2013].

Once a new P_{seed} has been initialised in this manner, values of elements in the *dummy* array that lie along the vector (P_{init} to P_{seed}) are switched from 0 to 255. When all growth steps for an individual hair are completed, the result is a continuous, skeletonised hair path represented by elements of value 255 in the dummy array. This array is exported as a RAW file at the conclusion of the growth algorithm, and the skeletonised paths dilated in FIJI using binary operators, giving a hair diameter which is correct relative to the spatial resolution of the SRXCT data.

Building virtual and SRXCT-derived geometries into a single model

Following export of the 8bit RAW file containing skeletons of the virtual root paths, a sequence of image-processing operations was implemented in FIJI to achieve two objectives:

- Incorporate all phases into one *master* volume for input to an FE mesh generation process.
- Extract relevant morphological data from the master volume, in order to quantify rhizosphere characteristics relevant to nutrient uptake (such as wetted hair length, wetted root surface area and volumetric fluid content).

Examples of hair morphologies generated by repeat iterations of the *HairGrower* algorithm, using the same parameters are shown in Figure 6.18. The stochastic element of the algorithm is evident, causing the length and path for each hair to vary over progressive iteration.

Quantifying statistics relevant to P transport in the rhizosphere

In addition to the hair densities and wetted root surface areas quantified in Section 6.3.1, wetted hair lengths were reported for each virtual hair set. As only wetted hair surfaces will have access to soil P, it is hypothesised that the ratio of wetted/un-wetted hair length might correlate with hair P uptake. Lengths were estimated by counting voxels of skeletonised hair sets and applying a scaling factor as described with relation to RSA in Section 4.3.1 of Chapter 4. Voxel counts for wetted hair segments were acquired in FIJI by applying a logical AND to find the

coincident voxels between output hair skeletons and the macropore fluid phase region. When applied to measure total hair length of 10 separate HairGrower iterations, the mean value was 101.95% of that used to initialise HairGrower, at a RSD of $< 1\%$ (see Equation 6.9). The voxel counting method was thus validated for measurement of wetted hair lengths.

The variation in total grown hair length was small, with a relative standard deviation (RSD) of only 3.6% over 10 HairGrower iterations. Relative standard deviation is given by,

$$RSD = \frac{\overline{x}}{s}, \tag{6.9}$$

where ($\overline{x}$) is the mean length value of total hair length, and (s) is the standard deviation for the 10 iterations. The small degree of variation observed is partly a result of the random sampling used to determine hair lengths, and partly due to the small number of hairs in each iteration that cease extension before reaching (L_{tot}). The latter condition can occur during the simulated growth of a single hair if all test values of (P_{seed}) fail at least one of the criteria for acceptance.

Over 10 iterations of HairGrower, given the total volumetric macropore fluid content of 21.5%, 50% of the total hair length was found to be in the fluid phase. The RSD for total *wetted* hair length was 4.1%, compared to 3.6% for the total grown length, suggesting that at $1.5\mathrm{mm}$ root-section scale, the stochasticity of hair growth does not markedly influence the total hair length implicated in P uptake. However, when a small sub-segment of the root was considered (as in Chapter 5), the RSD over 10 iterations increased markedly. The segment had a swept angle of $50°$, aligned with the root centreline, with a radius of $550\mu\mathrm{m}$ and covering a z length of $0.25\mathrm{mm}$. The enclosed volume of rhizosphere was ($\approx 1/100$) of that enclosed by the master ROI. Over 10 iterations of HairGrower, 43.7% of the total hair length in the segment was found to be in the fluid phase. RSD values for the total and wetted lengths were 7.9% and 26.7% respectively, revealing that at length-scale of the segment, an order of magnitude smaller than that of the ROI, variation in wetted length was substantially greater.

6.5 Discussion and conclusion

By applying an explicit hair growth model, 3D rhizosphere models could be generated. These improved on the models developed in Chapter 5 by allowing realistic macropore water distributions to be considered, whilst also allowed prediction of virtual hair geometries according to validated length distributions and a stochastic tip-extension scheme. The growth model considered the spatial arrangement of soil aggregates and the lengths and growth vectors of partially visible hairs, in order to capture as much of the known morphology as possible. The work in this chapter has thus described a modular workflow for acquiring data, processing extractable structure into 3D geometries, and generating informed estimates of 'missing' compo-

nents according to the best available approximations derived using complementary methods.

Each element of this modular workflow can be improved in future, should more robust methodologies be developed. In line with the motivations for Section 2.2, user-invariant segmentation methodologies are preferable to supervised methods where available. In this work, a review of the literature revealed a paucity of image-processing methods suited to the soil and hair complexity revealed in the reconstructed data. Future work within the computer vision domain will likely result in algorithms for multi-phase segmentation and filament tracing in such data, at which point such methods can easily be substituted into the presented workflow.

Generating 3D models allowed hair statistics to be estimated. *Java* scripts written for the FIJI image processing utility allowed automated quantification of hair density, wetted root hair lengths, wetted root surface area, and macropore water content . Future modelling studies implemented using image-derived geometries will thus be able to relate P uptake characteristics directly to rhizosphere structure parameters. Using these approaches, it was found that variation in wetted hair length is sensitive to the length scale considered. A systematic assessment of different length scales may in future assist in establishing the scale at which heterogeneity in the rhizosphere must be considered. It may prove possible to establish correlations between uptake characteristics (as predicted using a numerical modelling regime as laid out in Chapter 5) and these image-derived parameters, in which case the parameters might be used to predict nutrient transport characteristics without the need for modelling and the associated computational resources. Appendix 8.5 outlines the method and results of a mesh convergence test, applied to a small ($200 \times 200 \times 200$voxel) subset of the 3D model generated in this chapter. The results established a set of mesh generation parameters necessary for robust application of the *Schnepf et al.* model implemented in Chapter 5, in order to inform the use of the FEFree+ meshing algorithm in ScanIP during future modeling studies [Schnepf et al., 2011]. Furthermore, fitting curves to simulation metadata from the Iridis 4 supercomputer cluster allowed the element count in the meshed geometry to be related to both the time period and memory resources required for solution of the model.

Although a full comparative modelling study was beyond the scope of this work, acquisition of further SRXCT data and subsequent analysis using the plant-to-model workflow established in Chapters 5 and 6 will allow the influence on P uptake of hair morphology, soil structure and water distribution to be predicted. The structural detail that the workflow reveals will allow this to be achieved to a greater degree of accuracy than has previously been possible using idealised models with no explicit consideration of rhizosphere heterogeneity. If the influence of hair traits on nutrient acquisition can be robustly predicted at the hair scale via explicit

numerical models, upscaling methods such as *homogensation* can be applied to improve the accuracy of models at larger scales. Using such methods, the influence of hairs can be included non-explicitly in models at the whole-plant RSA scale, themselves parameterised accurately using using large-scale μ-CT imaging protocols of the kind developed in Chapter 4.

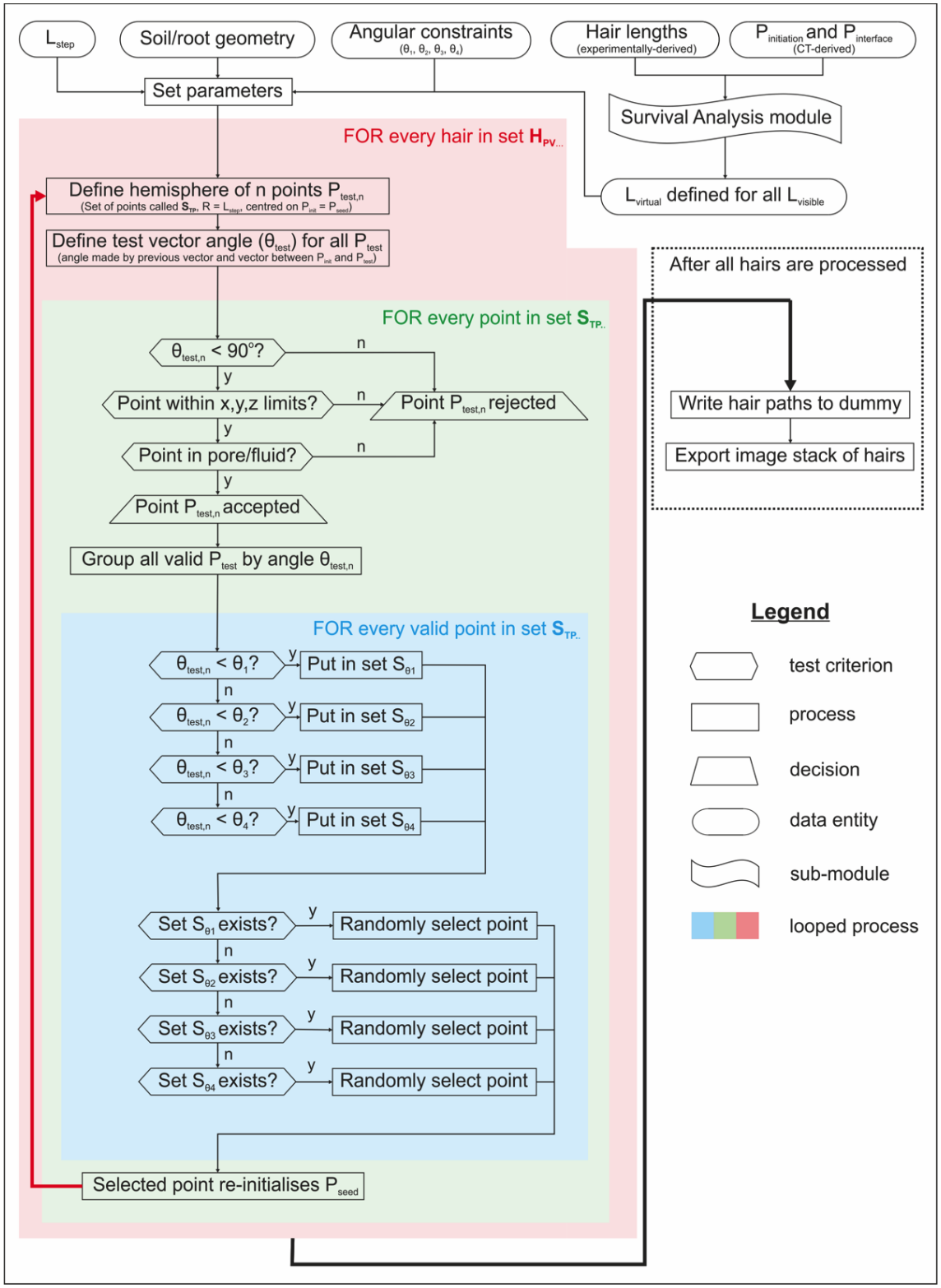

Figure 6.15: Flow diagram outlining the top-level operation of the *HairGrower* algorithm.

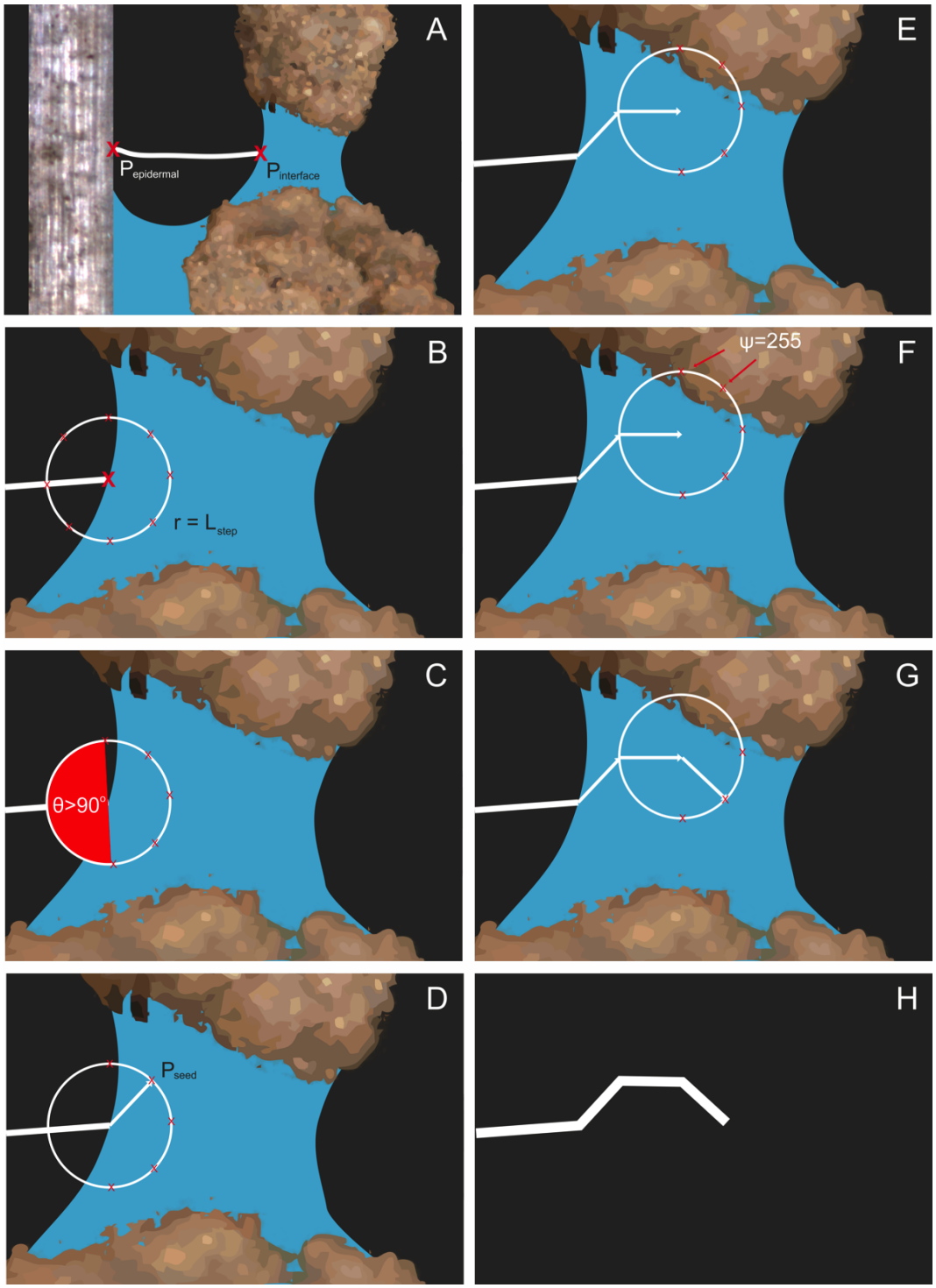

Figure 6.16: The steps taken by the HairGrower algorithm to complete a single root hair. (A) The vector $\vec{P_{epidermal}P_{interface}}$ is defined. (B) A test array of points is defined around $P_{interface}$. (C) Points requiring more than $90°$ of deviation are disallowed. (D) A new seed is randomly selected from the remaining point set, so long as other constraints are met. (E) A new array of test points is defined. (F) Points corresponding to soil and root phases are disallowed. (G) A point meeting all validation criteria is randomly selected. (H) Once the full length ($L_{total,n}$) for the hair is reached, the 3D path is written to an output file.

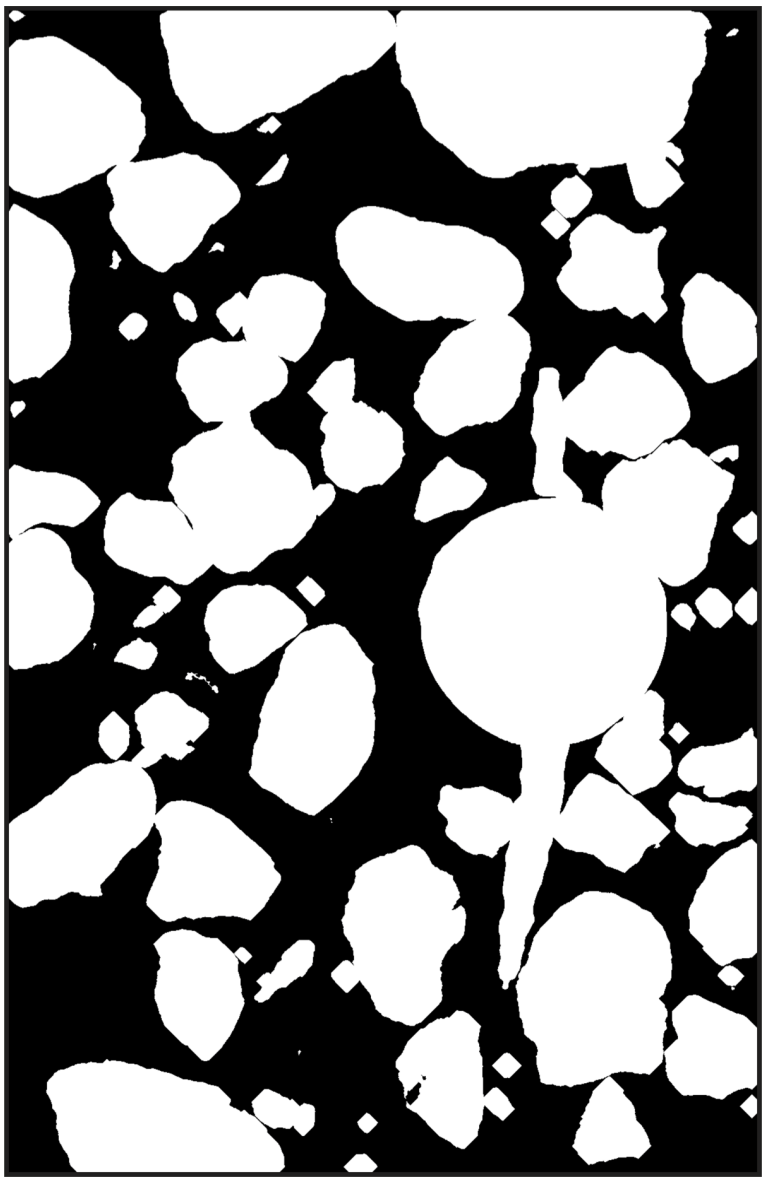

Figure 6.17: Middle slice of the geometric input data for the *HairGrower* algorithm. Root and soil regions are binarised with 8-bit grey-level value of 255, whilst macro-pore regions have a value of 0.

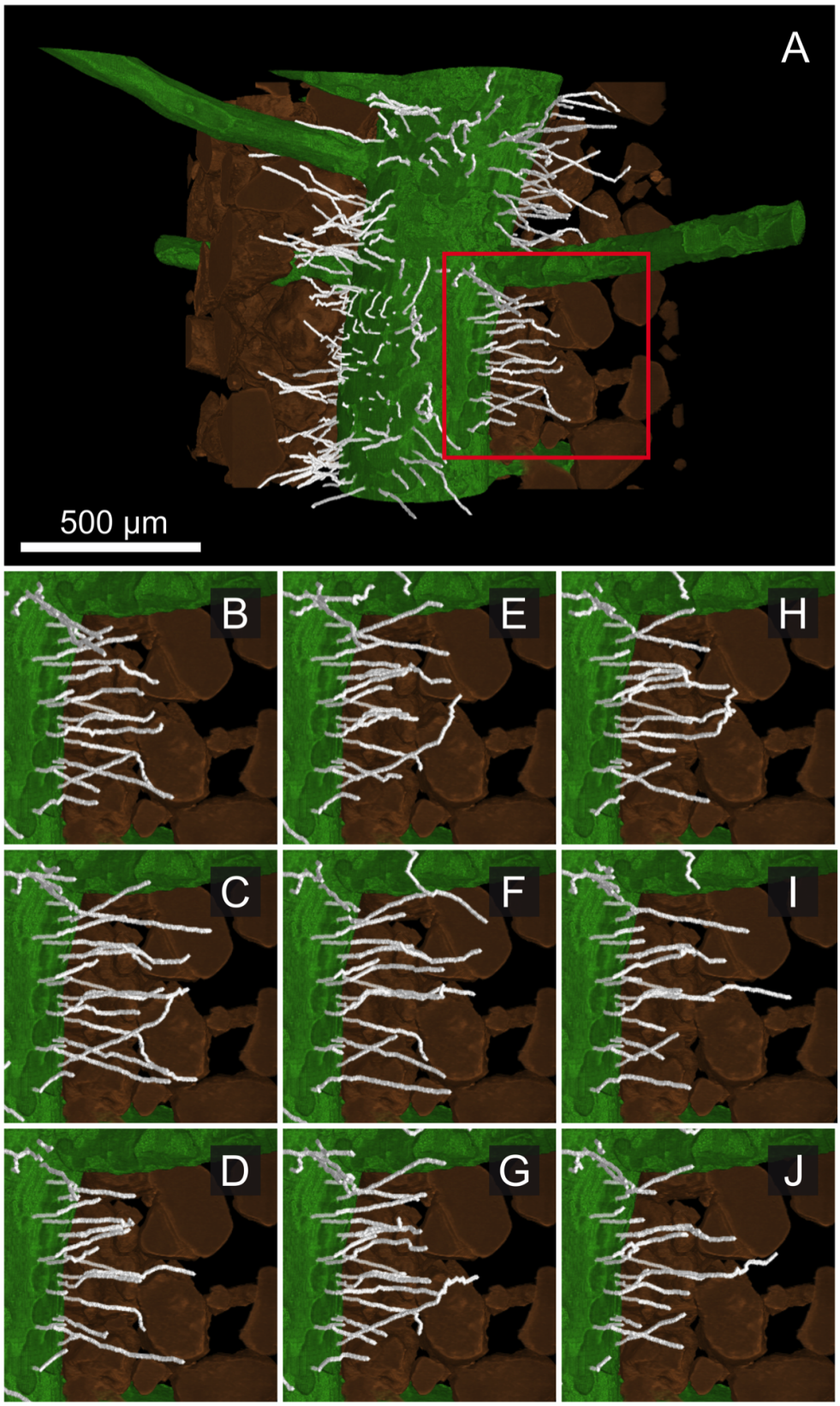

Figure 6.18: (A) An example of a completed hair population generated by the *HairGrower* algorithm. For the subregion indicated in red, frames (B-J) show the virtual hair morphologies for 9 further iterations. The stochasticity of the algorithm is evidenced by the different length distributions and paths generated despite identical input parameters.

Chapter 7

Final Conclusions

The work presented in this thesis has considered improvements to existing work in the domain of plant root imaging and modelling. A review of the pertinent literature reveals that both phenotyping and modelling efforts have been hampered by a paucity of methods for reliable assessment of root system and soil complexity at a range of scales. The more accurate understanding of root system traits and the parameterisation of numerical models will be reliant on the ability to observe the real arrangement of RSA within the field soil environment. Existing methods for direct observation either constrain the plant physically, or represent conditions of mechanical impedance and chemistry that bear little relation to those of field soil.

μ-CT techniques offer the potential for non-destructive investigation of plant roots in the real soil environment. Unfortunately studies often give little technical justification for imaging and reconstruction parameters, and the system scales considered are dominated by samples in the $2 - 10\mathrm{cm}$ diameter range. In order to better understand the roles of specific soil and root structural traits in nutrient acquisition, the ability to investigate both the mature RSA scale and the rhizosphere scale are important. Robust and well described methods are also necessary in order to reduce as far as possible the influence of user bias in image analysis.

This thesis has considered the application of novel methods within the μ-CT imaging, digital image-processing and image-based modelling domains:

Imaging domain

In the imaging domain, new methods have been described for the imaging of unprecedentedly large root systems of rice (*Oryza sativa*), and the imaging of root hairs at the $\mu\mathrm{m}$ scale in rice and wheat (*Triticum aestivum*). The large-scale imaging protocol extended the sample diameter range for plant-scale imaging to $> 20\mathrm{cm}$, with good capture of primary roots allowing root

lengths and angles to be compared between different genotypes. The small scale SRXCT assay and imaging protocol has allowed undisturbed root hair morphology to be examined *in vivo* within the rhizosphere. A workflow has been developed which allows qualitative analysis of hair-to-soil interactions, quantification of key hair traits, and the parameterisation of numerical P uptake models for the first time at the hair scale. At the canonical sample scale of well-cited μ-CT studies ($2 - 10\mathrm{cm}$), mature chemical contrasting methods drawn from clinical XCT were assessed for architecture extraction for the first time. The methodogy developed was trialled using two iodinated contrast media, with optimum concentrations determined for use in plant root μ-CT. Use of the media in conjunction with imaging allowed physiological detail such as the vascular structure of rhizobial nodules to be revealed for the first time. Calibration of attenuation coefficient against iodine concentration also suggested that chemical contrasting methodologies might in future be used for temporally resolved detection of preferential vascular flow in roots.

Imaging-processing domain

Imaging of root hairs in non-optimal soil water states revealed an inability to resolve hair structures within macropore water. In order to generate geometries which could be used to analyse the rhizosphere, a paradigm for virtual hair growth was developed, allowing partially-visible hairs to be completed according to an explicit, stochastic regime. Experimentally derived hair length distributions of soil-grown roots were used to allow random sampling of specific hair completion lengths for individual hairs. The model incorporated as much information from the SRXCT data as possible, including mechanical impedance due to hair-and-aggregate interaction, and the existing growth vectors and lengths of partially visible hair segments. Models generated using this approach were used to predict the influence of length scale on the heterogeneity of wetted hair length, thought to be a key parameter influencing P uptake.

In the domain of soil segmentation, a method was developed for user-invariant extraction of connected macropore volumes from μ-CT data. Estimation of soil porosity from μ-CT data has often been highly dependent on user-supervised selection of parameters, leading to the potential for large differences in pore volume estimates made by different users from the same data. By combining a seeded region growth (SRG) algorithm with a user-invariant selection of a tuning parameter based on image data, a protocol for unsupervised soil segmentation was defined.

Image-based modelling domain

By applying a numerical model to rhizosphere geometry elucidated by SRXCT, it was possible to consider the undisturbed arrangement of hairs and soil aggregates within a modelling

paradigm for the first time. The results suggested that previous models may have overestimated the influence of hairs compared to that of the root, with the study suggesting comparable uptake of soil P by both regions. By quantifying streamline sets following paths of maximal concentration gradient in macropore water, the more focused, localised uptake of P by hairs was revealed, as compared to the root surface. The dynamic adjustment of inter-terminal distances in streamline sets seeded from hairs and the roots also provided insight into the nature of uptake. Three periods were suggested: (i) the progressive interference with aggregates of depletion fronts through pore fluid, (ii) a period of aggregate-to-aggregate redistribution of P, and (iii) an equilibrium condition in which the spatial arrangement of depletion gradients ceased to change temporally. With a workflow now in place for a full-scale modelling study of hair distributions in rhizosphere soil at field water capacity, much greater insight into the dynamics of P uptake and transport kinetics will be possible.

7.0.1 Future work

A number of final suggestions are made as to work which will follow on or complement the developments and results laid out in this thesis:

- With a workflow now in place to image, quantify, visualise and model rhizosphere-scale nutrient acquisition processes, a comparative study of crop genotypes with suspected trait differentiation at the hair scale is an obvious short-term goal.
- Future SRXCT studies will allow the potential for the visualisation of hairs in pore water using either chemical contrasting or phase contrast methods to be assessed. If such techniques make resolution of hairs in the fluid phase possible, the complexity of the image-processing required to extract hair paths might be significantly reduced.
- Fungal mycorrhizae exist at a similar scale to that of hairs, but extend over much greater distances within the soil. With the ability to resolve hairs using SRXCT established, there is clear justification to develop a complementary assay for the isolated growth of mycorrhizae in soil volumes of similar scales. Such work would allow parameterisation of mycorrhizal P uptake models in the same manner as achieved for root hairs, extending our understanding of mycorrhizal importance in low-P agricultural contexts.
- The suitability of clinical contrast media established for plant use has been demonstrated. Protocols should now be defined for their application in revealing different facets of root behaviour. Different media, loading and imaging strategies are likely to be optimal for investigation of (i) RSA in poor-contrast situations, (ii) elucidation of internal root physiology, and (iii) temporally-resolved phloem flow characteristics.

- A clear impediment to the more accurate parameterisation of numerical models at the hair scale is a lack of understanding regarding nutrient distribution. In this study initial soil P concentration was homogenous, determined via chemical assaying. A better approach would be to map concentration distributions in soil using *in situ* methods, in order to allow parameterisation of initial conditions. Future application of X-ray absorption near edge structure (XANES) fluorescence spectroscopy may allow the spatially-resolved speciation of sorbed P and other nutrients at the single-aggregate scale. In this manner, image-based concentration mapping could allow less idealised initial conditions to be considered in future models.

Chapter 8

Appendices

8.1 Estimation of root angles in contrasting rice genotypes using a rhizobox protocol

8.1.1 Growth conditions

Four genotypes of rice *Oryza sativa* were chosen from among participating varieties in a JIRCAS field trial, *Kaladri*, *Sadri tor Misri*, *ARC* and *Binyalawan*. Plants were grown in rhizo-boxes with dimensions $30\mathrm{cm} \times 30\mathrm{cm} \times 2\mathrm{cm}$, constructed of transparent polycarbonate with a removable front-plate, and wrapped in foil to occlude light. The boxes were filled with soil, according to two conditions. Three replicates of each genotype were grown in a low-P soil (0P), with a single replicate grown in the same soil treated with P fertiliser up to an equivalent soil P content of $50\mathrm{kg.Ha}^{-1}$ (50P). Hydration during the growth period was maintained via capillary rise from a tray of water, with occasional top-watering. Plants were grown in a glasshouse, with temperature ranging from $20 - 32^{\circ}\mathrm{C}$ over the growth period.

After a growth period of 35 days, the boxes were dismantled to allow quantification of root system parameters (Figure 8.1), according to the a protocol following *Bengough et al.* [Bengough et al., 2004]:

- The front plates were first removed to expose the root system.
- A rigid foam board with a uniform grid arrangement of $20\mathrm{mm}$ metal pins, at a spacing of $20\mathrm{mm}$, was pressed against the soil.
- The rhizobox was gently inverted, allowing the root system and soil to be transferred to the foam board.
- With the board lifted to a near-vertical angle, a gentle stream of water was used to manually remove the bulk of the soil.

- A single representative coarse and fine primary root respectively were excised next to the seed and transferred to a sample tube containing RO H_2O (in order to allow later characterisation of root hair morphology).
- Soil adhering to the remaining roots was removed using a stream of water combined with gentle mechanical manipulation.
- The root system was photographed orthogonal to the plane of the foam board, in order to allow approximate quantification of rooting angles.

8.1.2 Results

Figure 8.2 shows root architecture data for one repeat of all genotypes in both 0P and 50P conditions, with the metal pins protruding from the foam board allowing the growth angles of primary roots to be approximated for each sample. Though visual inspection appears to confirm that root angle distributions differ substantially across different genotypes, root angles were quantified using the acquired 2D images in order to allow comparison with μ-CT derived values.

Measurement of root angles made the assumption that the root path between the seed and the furthest visible extent of the root could be approximated as a straight line. By manually defining the position of the seed (P_{seed}), and the position of each discernible primary root at a position near the tip (P_{tip}), a vector ($\vec{P_{seed}P_{tip}}$) could be defined to describe the approximate growth path of each root. It was then possible to define the distribution of root angles with respect to the soil surface horizon. Carrying out this procedure for all samples, histograms of primary root angle were generated.

Figure 8.3 shows root angle distributions for each of the genotypes in the P0 condition (*ARC, Binyalawan, Kaladri, Sadri tor Misri*), with genotypic trends clearly evident. Whereas *ARC* shows heavy weighting towards steep rooting, *Sadri tor Misri* exhibits a a far more even distribution of angles across the range $0 - 90°$. *Kaladri* root angles were similar to those for *ARC*, though with less heavy weighting towards steep roots. *Binyalawan* exhibited a characteristic peak centred around $60°$ for all repeats.

8.2 Parameterisation of P sorption characteristics via soil assaying

8.2.1 Solution and solid phase P concentrations (C_{sol} and C_{sor}).

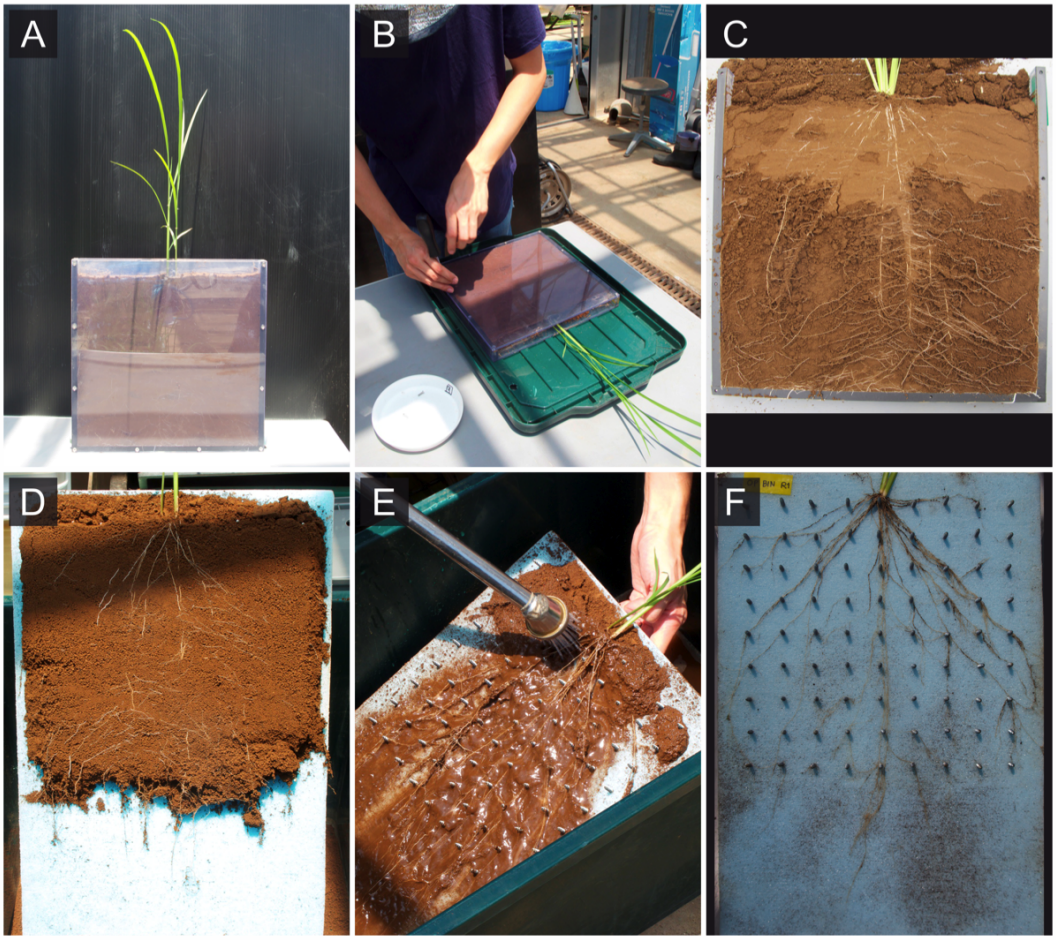

Figure 8.1: (A) Plants were grown in rhizoboxes. (B-D) By removing the face-plate, a board with an array of extruding metal pins could be gently pressed into the soil, with the entire root system gently transferred from the box to the board. (E) Gentle washing of the soil from the root system allowed the root angles to be maintained by the pins. (F) Photographing the root system orthogonal to the board plane provides images suitable for digital root angle estimation.

Pore water was extracted from replicated $20\mathrm{g}$ batches of soil, according to the centrifuge-drainage method of *Giesler and Lundström*, then analysed to determine P concentration following *Murphy and Riley* [Giesler and Lundström, 1993; Morphy and Riley, 1962].

To elucidate the relationship between C_{sol} and C_{sor}, a sorption isotherm was constructed following the approach of *Barber* [Barber, 1995]. $1\mathrm{g}$ quantities of desiccated soil were mixed with $5\mathrm{ml}$ volumes of KH_2PO_4 labelled with the radioactive Phosphorus isotope 33-P, which has an activity of $\mathrm{kBq.ml^{-}1}$. 33-P concentrations of 0.01, 0.05, 0.1, 0.25, 0.5 and $1\mathrm{mM}$ were used, with $24\mathrm{h}$ of shaking at $200\mathrm{rev.min^{-1}}$ prior to centrifuging at $24 \times 10^3\mathrm{g}$. The C_{sol} of the supernatant was determined by liquid scintillation counting with a Wallac 1404 counter (Perkin-Elmer, Boston, MA, USA). Having calculated C_{sol} at each 33-P concentration, Sigmaplot v11 (Systat Software Inc., San Jose, CA, USA) was used to fit a Langmuir adsorption isotherm to the data,

enabling C_{sor} to be calculated for the pore water equilibrium P concentration determined initially.

8.2.2 Buffer power (b)

The buffer power ratio of the soil was estimated for the equilibrium condition using the equation:

$$b = \frac{dC_{tot}}{dC_{sol}} \tag{8.1}$$

Where:

$$C_{tot} = (C_{sol} \times \theta) + (C_{sor} \times \gamma) \tag{8.2}$$

And θ and γ are soil volumetric water content and soil bulk density respectively.

8.2.3 P soil adsorption constant (k_a)

A similar approach was used for determination of k_a. As before, $1\mathrm{g}$ samples of soil were shaken with $5\mathrm{ml}$ volumes of $^{3}3\mathrm{P}$ labelled $\mathrm{KH_2PO_4}$ (at concentrations of 0.25 and $0.05\mathrm{mM}$), with C_{sol} of 33-P measured after equilibration periods of 0, 0.25, 0.5, 1, 2, 4, 8, 12 and 24 hours. C_{sor} of 33-P was determined as previously, with absorption and desorption constants (k_a and k_d) calculated by plotting C_{sor} vs time and fitting the following equation:

$$C_a = C_{tot}A(1 - e^{-\kappa t}) \tag{8.3}$$

It is assumed that adsorption kinetics at the soil surface can described by a linear equation of the form found in Equation 5.2. Given the data derived previously for C_{sor} with respect to time, k_a and k_d can be determined using the following equation:

$$\rho C_{tot} = \rho C_{sor} + \theta C_l \tag{8.4}$$

Where θ is the dimensionless water capacity, ρ is the bulk soil density, C_{sor} is the sorbed soil bulk concentration ($\mathrm{mol.kg^{-1}}$) and C_{tot} is the total concentration ($\mathrm{mol.kg^{-1}}$). Multiplying equation 5.2 by $\frac{S}{V}$ (the ratio of soil surface area to solid phase volume, determined from CT data), and using equation 8.4, an equation for C_{sor} is obtained:

$$\frac{dC_{sor}}{dt} = -(k_d + \frac{k_a S}{\theta V})C_{sor} + \frac{k_a S}{\theta V}C_{tot} \tag{8.5}$$

Setting the intial condition $C_{sor} = C_{tot}A(1 - e^{-kt}$, this equation has the general solution:

$$C_{sor} = C_{tot}A(1 - e^{-\kappa t}) \tag{8.6}$$

Where $A = \frac{k_a S/V}{k_d \theta + k_a S/V}$ and $\kappa = k_d + \frac{k_a S}{\theta V}$ are determined by a fitting procedure, using only the two lowest concentrations and fitting data in MATLAB (Mathworks, Natick, MA, USA). The resulting curves are shown in Figure 8.4.

8.3 Parameterisation of hair length distributions via washing of soil-grown roots

To parameterise a hair length distribution for the *HairGrower* algorithm, sections were sampled from sections of soil grown primary roots. Root sections grown in low-P soil were sampled during destructive assessment of plants grown in Section 4.5. The sections were gently washed to remove soil, and after plating of sections on microscope slides, hairs lengths were estimated following the approach of *Haling et al.*, using a microscope to image root surface sections. Stitching together resulting images (Figure 8.5) and importing them into FIJI allowed hair lengths to be measured using poly-lines defined using a graphical tablet. In order to avoid regions most severely affected by washing artifacts, only five ($1 \times 1\mathrm{mm}$) regions in each image were used for length measurement, being chosen by the user as the most densely populated by hairs.

8.4 Root damage caused by excess ionising radiation during SRXCT imaging

A chemical-contrasting protocol developed in Chapter 3 was trialled using the SRXCT beamline at the DIAMOND light source at Harwell, UK. Leaf sections of mature plants (rice (Rice (*Oryza sativa cv Sadri tor Misri/Oryza sativa cv Varyla*) and wheat (*Triticum aestivum cv Santiago*)) were excised and submerged for $24\mathrm{h}$ in solutions of either Gastrografin 370 at a 25% dilution or strong Lugol's solution (iodine and potassium iodide) at 10% dilution. Reconstructed slices through the data for rice and wheat showed no evidence of chemical contrast enhancement in either stele or hairs, but did reveal extensive root damage and movement artifacts (Figure 8.6). Excessive X-ray flux to the samples had resulted from a technical fault in the sample stage, requiring that centre of rotation for each scan be determined manually. As a result, the samples were subjected to $\approx 15\mathrm{m}$ of exposure to the X-ray beam, as opposed to the $\approx 5\mathrm{m}$ that was characteristic of imaging carried out at the SLS. The degree of damage caused rendered it impossible to distinguish whether the lack of contrast resulted from radiation damage, or from unsuitability of the chemical contrasting protocol.

Carefully washing root sections from samples and imaging using light macroscopy in the scanned region validated the existence of damage to the cortical tissue (Figure 8.7. Clearly,

these results suggest an upper limit to the exposure of the plant to SRXCT radiation before disadvantageous artifacts begin to result.

8.5 Convergence testing of an image-derived sub-geometry using a numerical P-uptake model

The computing resources required for numerical solution of am explicitly-considered P uptake model are proportional to the element count of the meshed geometry. It is thus advantageous to optimise mesh quality in order to avoid un-necessarily fine elements. In order to determine the threshold of convergence for the P uptake model of *Schnepf et al.* defined in Section 5.3.8, a small reference geometry was used to run a range of computational tests.

A small ROI was selected (shown in Figure 8.8), a cubic geometry with an edge length of 200voxels ($300\mu\text{m}$), including a single hair of length $300\mu\text{m}$ and diameter $14\mu\text{m}$. Prior to the meshing stage, a number of variants of the geometry were generated in order to assess the influence of voxel binning on both model convergence time and simulation results. Figure 8.9 shows slices through the resulting datasets, binned to edge lengths of 200, 100, 50, 40, 33, 29, 25 and 22 voxels respectively. As in Section 5.3.6, the +FEFree algorithm within the ScanIP software package (Simpleware Ltd., Exeter, United Kingdom) was used for mesh generation. The voxel-binned datasets were all meshed using the same parameters, detailed in Table 8.1. The parameters were scaled for each dataset in order to compensate for the larger voxel sizes as the degree of binning was progressively increased. In addition, the original un-binned dataset was meshed using 4 different parameter sets (detailed in Table 8.2) selected to produce iteratively finer meshes. The parameters used were defined by adjustment of a global *coarseness* parameter, which determined the values of individual parameters shown in Table 8.2. *Python* scripting was used to automate the process of file import, mesh generation and export for batch operation.
Following generation of meshed geometries, the P uptake model described in Section 5.3.8 was applied to each geometry using LiveLink for COMSOL and MATLAB, allowing all model parameters to be defined in MATLAB script form. MATLAB could then be used to batch-import COMSOL model files exported from ScanIP, apply the various elements of the model (*i.e.* timescale, boundary conditions and initial parameters), and batch export files ready for import to the Iridis 4 cluster. This protocol circumvents the graphical interface (GUI), allowing a large number of different geometries to be prepared using the same physics and initial conditions in a timely and accurate manner [Trott and Matthias, 2010].

The models were solved using the high power computing (HPC) nodes of the Iridis 4 cluster at the University of Southampton. Depletion of P was compared for all geometries by com-

Table 8.1: Parameters used to mesh binned geometries 1-8.

Parameter	Value
Smoothing iterations	20
Target min. edge length	0.00135mm
Target max. edge length	0.015mm
Target max. error	0.015mm
Target element count across a layer	0.5
Quality optimisation cycles	10
Surface change rate	100
Internal change rate	40

puting the surface integral of C_a on the soil surfaces with respect to time. Figure 8.11 shows the resulting depletion curves for all geometries, which reveal that excellent convergence was obtained for geometries 10-12, with close convergence obtained for geometry 9. For all the geometries that had been binned prior to meshing, the initial angle of the C_a/t curves became progressively steeper as the degree of binning increased. With a $\approx 20\%$ variation in the time taken to exhaust C_a between the geometries, the parameters which satisfied the convergence condition (10, 11 and 12) are preferable.

In order to approximate the largest tractable input geometry, metadata exported from Iridis was used to plot the relationships between element count and both convergence time and RAM usage (Figure 8.10). Table 8.3 shows metadata for all computations. Using equations of best-fit lines for each plot, maximum tractable element counts were estimated for the available resources computational resources. With RAM limited to 256GB and the maximum runtime limited to 60h, the maximum element count was estimated as 12.6×10^6, thus defining the target maximum element count for mesh generation.

8.6 Full MATLAB code for the *HairGrower* algorithm

```
%##########################################
%#                                        #
%#  HAIRGROWER v1 (with WeibullFit add-on)  #
%#                                        #
%##########################################

% Hairgrower is a program to grow semi-virtual root hairs.  It uses
% synchrotron CT data as an input, as well as hair washout data (or
```

```
% alternative hair length data.)

% Hairs are grown from SEED POINTS.  These are provided in a csv file that
% should be named:

% "pointsdata.csv"

% This csv file has the start and end points of each existing hair in the
% data.  The start points are where hairs initiate at the root surface, and
% the end points are the positions where hairs are no longer visible due to
% water content (hairs are usuall invisible in CT data when water is present.)
% The SEED POINTS are the positions of these end points.

% A GROWTH VECTOR is defined (approximated as the vector between start and
% end point, since hairs are usually near-straight.)

% HAIRGROWER assigns a continuation length to each of these hairs using a
% distribution fitted to experimental data.  The process for this is
% contained in the WEIBULLFIT algorithm, which begins this script.

% Once an array of continuation lengths (one for each hair) has been
% defined, all information required for HAIRGROWER is complete.

% The script virtually 'grows' a skeletonied path for each hair.  This is
% done using an iterative process, contrained by a user-defined preferred
% angle, a step length which scales with continuation length, and a
% binarised soil dataset, dilated by a few times from its actual size.

% Hairs will attempt to grow within a certain angle to the previous step
% vector(beginning with the seed vector), but are allowed increase this
% angle up to 90 degrees if necessary.

% Growth is not permitted into regions with a greylevel greater
% than a certain threshold value (soilthresh) which represents
% the solid phase.  Growth is also not permitted into xyz space
% which lies outside the limits of the input volume.

% Data is output in the form of a tiff stack, which can be used for
% post-processing.

%#########################################################################

%%%%%%%%%%%%%%%%%%%%%%%%%%
%*** CLEAR VARIABLES *** %
%%%%%%%%%%%%%%%%%%%%%%%%%%

clear ptsxyz;
```

```
clear dummy;
clear LengthComparison;
clc

%%%%%%%%%%%%%%%%%%%%%%%%%%%%%%
%*** READ IN TIFF STACK *** %
%%%%%%%%%%%%%%%%%%%%%%%%%%%%%%

% The initial step is to read in a stack of tiffs.  This should represent
% the soil phase.  It is sensible to dilate the soil phase by 1/2 the
% final desired hair diameter (to avoid soil/hair overlaps when the hairs
% are eventually dilated.)
%%%%%%%%%%%%%%%%%%%%%%%%%%%%%%%%%%%%
%*** 2 - NON DIALOG IMAGE INPUT *** %
%%%%%%%%%%%%%%%%%%%%%%%%%%%%%%%%%%%%

fprintf('Beginning to read in dataset');
fprintf('\n');

% Set the target file, and the filename of the tiff stack (with wildcards
% for enumeration).

fileFolder = fullfile('H:\Matlab_work_for_simulations_10_07_13');
dirOutput = dir(fullfile(fileFolder,'HairGrowerInputGeometry*.tif'));
fileNames = {dirOutput.name}';
numFrames = numel(fileNames);  % The number of tiffs

I = imread(fileNames{1});

% Preallocate the array

% sequence = zeros([size(I) numFrames],class(I));
% sequence(:,:,1) = I;

% Create image sequence array

for p = 2:numFrames

    sequence(:,:,p) = imread(fileNames{p});

end

% Find dimensions in xyz of input data

datasetx = size(sequence,1);
datasety = size(sequence,2);
datasetz = size(sequence,3);
```

```
fprintf('Dataset read in successfully')
fprintf('\n');

%~~~~~~~~~~~~~~~~~~~~~~~~~~~~~~~~~~~~~~~~~~~~~~~~~~~~~~~~~~~~~~~~~~~~~~~~~~~~%
% ~~~~~~~~~~~~~~~~~~~~~~~~END OF FILE IMPORT SEQUENCE~~~~~~~~~~~~~~~~~~~~~~~~~%
%~~~~~~~~~~~~~~~~~~~~~~~~~~~~~~~~~~~~~~~~~~~~~~~~~~~~~~~~~~~~~~~~~~~~~~~~~~~~%

clear PointsInput;

fprintf('Beginning Weibull fitting and length assignment process')
fprintf('\n');

% This is the input data and will usually have been manually assessed.
% Each hair has two rows, and the x/y/z values of the start point are on
% indices (n,2-4), with end points on indices (n+1,2-4).  Index (n,1) is
% the number (for n = odd).

PointsInput = csvread('pointsdata.csv');

InputSize = size(PointsInput,1);  % This is TWICE the number of hairs.

clear hairlengths;

CountHair = 1;

% Build an array of hair lengths (using trignometric approximation).

for ir=1:2:InputSize

    xlength = PointsInput(ir,2) - PointsInput(ir+1,2);
    ylength = PointsInput(ir,3) - PointsInput(ir+1,3);
    zlength = PointsInput(ir,4) - PointsInput(ir+1,4);
    hairlength = (1.5*sqrt((xlength^2)+(ylength^2)+(zlength^2))); % Scale data to
        actual length (um) from data coordinates
    hairlengths(CountHair,1) = hairlength;
    DATACOMPARISONDEBUG(CountHair,1) = hairlength;

    CountHair = CountHair+1;



end

%%%%%%%%%%%%%%%%%%%%%%%%%%%%%
%*** WEIBULLFIT PROCESS *** %
%%%%%%%%%%%%%%%%%%%%%%%%%%%%%
```

```
% The WeibullFit algorithm fits a Weibull distribution to the experimental
% validation data (from washout / hydroponics or otherwise).  It then uses
% this distribution to assign a 'random' length to each discrete hair from
% the CT data.

% Import the validation data.

Lengths = csvread('MicroscopeData.csv');

% Fit Weibull parameters to data

WblParams = wblfit(Lengths);
WBLalpha = WblParams(1);
WBLbeta = WblParams(2);
LGTH = 0:20:460;

% The Weibull parameters.

WeibullFit(1,1) = WBLalpha;
WeibullFit(1,2) = WBLbeta;

% Output a histrogram of the validation length data.

% figure(1)
%
% hist(Lengths,20)
% axis([0 500 0 50])

%~~~~~~~~~~~~~~~~~~~~~~~~~~~~~~~~~~~~~~~~~~~~~~~~~~~~~~~~~~~~~~~~~~~~~~~~~~~~
%~~~~~~~~~~~~~~~~~~~~~~~~~#*** MAJOR LOOP *** #~~~~~~~~~~~~~~~~~~~~~~~~~~~~~~
%~~~~~~~~~~~~~~~~~~~~~~~~~~~~~~~~~~~~~~~~~~~~~~~~~~~~~~~~~~~~~~~~~~~~~~~~~~~~

% This is the major loop.  All remaining processes are contained within it,
% including hair growth.  The number of runs is the number of unique hair
% geometries that will be produced (make sure there are enough folders
% named

for WeibRuns = 1:10

% A failure counter is initiated to check for hair growth failures in the later
    growth stage

FailCount = 0;

%continuation algorithm
```

```
%measured length

dx=0.1;

gamma=[0:dx:max(Lengths)];

IterData(1,1) = WBLalpha;
IterData(1,2) = WBLbeta;
IterData(1,3) = sum(Lengths);
IterData(1,4) = sum(Lengths)/length(Lengths);

countBIG = 0; % The count of runs through the whole dataset
countSMALL = 0; % The count of individual hairs

for hr=1:size(hairlengths);

    l0=hairlengths(hr);

probability=zeros(1,length(gamma));

for ir=1:length(gamma)
    probability(ir)= wblpdf(l0+gamma(ir),WBLalpha,WBLbeta)/(1- wblcdf(l0,WBLalpha,
        WBLbeta));
end

cdf=dx*cumsum(probability);

%plot(gamma,cdf)
%  rand > [0 , cdf(1:end-1)]

WBLy = dx*sum(rand > [0 , cdf(1:end-1)]);

FinalLengths(hr) = WBLy + hairlengths(hr);

DATACOMPARISONDEBUG(hr,2) = WBLy;
DATACOMPARISONDEBUG(hr,3) = hairlengths(hr);
DATACOMPARISONDEBUG(hr,4) = WBLy + hairlengths(hr);

countBIG;

countSMALL = countSMALL+1;

HairWeibCount = num2str(countSMALL);
WeibFullMess = strcat('Fitting virtual length to hair :', HairWeibCount);
fprintf(WeibFullMess);
fprintf('\n');
WeibPercComp = num2str(round((countSMALL/(InputSize/2))*100));
```

```
WeibPercMeter = strcat('Percentage completion :', WeibPercComp);
fprintf(WeibPercMeter);
fprintf('\n');

end

WblParamsVIRTUAL = wblfit(FinalLengths);
WBLalphaVIRTUAL = WblParamsVIRTUAL(1);
WBLbetaVIRTUAL = WblParamsVIRTUAL(2);
WeibullFit(WeibRuns,3) = WBLalphaVIRTUAL;
WeibullFit(WeibRuns,4) = WBLbetaVIRTUAL;

WBLXaxis = [1:10:500];
WBLXaxis = transpose(WBLXaxis);

RunID = num2str(WeibRuns);

CSVName = 'FinalLengths_';

CSVExtension = '.csv';

CSVFileName = strcat(CSVName, RunID, CSVExtension);

csvwrite(CSVFileName,FinalLengths);

for g=1:(length(PointsInput)/2)

    comparison(g,1)= hairlengths(g);
    comparison(g,2)= FinalLengths(g);
    comparison(g,3)= FinalLengths(g)-hairlengths(g);

end

fprintf('Finished Weibull processes')
fprintf('\n');

%%%%%%%%%%%%%%%%%%%%%%%%%%%%%%%%%%%%%%
%*** READ IN / GENERATE OTHER DATA ***%
%%%%%%%%%%%%%%%%%%%%%%%%%%%%%%%%%%%%%%

%%%%%%%%%%%%%%%%%%%%%%%%%%%%%%%%%%
%*** 2 - NON DIALOG BOX METHOD *** %
%%%%%%%%%%%%%%%%%%%%%%%%%%%%%%%%%%

clear PointsInput;

PointsInput = csvread('pointsdata.csv');
```

```
clear FinalLengths;

FinalLengths = csvread(CSVFileName);

InputSize = size(PointsInput,1);

clear hairdata;

CountHair = 1;

%%%%%%%%%%%%%%%%%%%%%%%%%%%%%%%%%%%%%%%%%%%%%%%%%%%%%%%%%%%%%%%%%%%%%%%%%%%%

%%%%%%%%%%%%%%%%%%%%%%%%%%%%%%%%%%%%%%%%%%%%
%*** BUILDING THE HAIR DATA ARRAY *** %
%%%%%%%%%%%%%%%%%%%%%%%%%%%%%%%%%%%%%%%%%%%%

% This is the array which contains the necessary information for completion
% of each hair, and also serves as the initiating data.

% The array 'hairdata' has one row for each hair, and includes xyz
% coordinates of initiation and end point of the visible section, as well
% as the length of each hair.

for i=1:2:InputSize

    hairdata(CountHair,1) = PointsInput(i,2);
    hairdata(CountHair,2) = PointsInput(i,3);
    hairdata(CountHair,3) = PointsInput(i,4);
    hairdata(CountHair,4) = PointsInput(i+1,2);
    hairdata(CountHair,5) = PointsInput(i+1,3);
    hairdata(CountHair,6) = PointsInput(i+1,4);
    hairdata(CountHair,7) = FinalLengths(CountHair); % the total desired distance
        for each hair

    CountHair = CountHair+1;

end

% x and y values are swapped to put points in MATLAB coordinate system

hairdata(:,[1 2]) = hairdata(:,[2 1]);
hairdata(:,[4 5]) = hairdata(:,[5 4]);

%%%%%%%%%%%%%%%%%%%%%%%%%%%%%%%%%%%%%%%%%%%%
%*** BUILD ZERO ARRAY FOR OUTPUT ***%
%%%%%%%%%%%%%%%%%%%%%%%%%%%%%%%%%%%%%%%%%%%%
```

```
% the zero matrix to which virtual hair skeletons will be written
%(by replacing 0 with 255 along hair paths)

dummy = zeros(datasetx, datasety, datasetz);

%%%%%%%%%%%%%%%%%%%%%%%%%%%%%%%%%%%%%%%%%%%%%%%%
%*** DEFINITION OF VARIABLES / CONSTANTS ***%
%%%%%%%%%%%%%%%%%%%%%%%%%%%%%%%%%%%%%%%%%%%%%%%%

%%%%%%%%%%%%%%%%%%%%%%%%%%%%%%%%%%
%*** 1 - NON DIALOG BOX METHOD *** %
%%%%%%%%%%%%%%%%%%%%%%%%%%%%%%%%%%

targetangle = 15; % the desired maximum angle of 'wiggle' that the hair is allowed
    to have in the absence of obstacles.
numtest = 400; % the number of test points generated on the test sphere
soilthresh = 200; % the threshold of greylevel value above which the hair cannot
    grow.

targetangle = targetangle / 57.2957795 ; % convert target to radians
numbhairs = size(hairdata,1); % finds the number of hairs from the hairdata csv

%~~~~~~~~~~~~~~~~~~~~~~~~~~~~~~~~~~~~~~~~~~~~~~~~~~~~~~~~~~~~~~~~~~~~~~~~~~~~~~~
%~~~~~~~~~~~~~~~~~~~~~~~~~# *** HAIR LOOP *** #~~~~~~~~~~~~~~~~~~~~~~~~~~~~~~~~
%~~~~~~~~~~~~~~~~~~~~~~~~~~~~~~~~~~~~~~~~~~~~~~~~~~~~~~~~~~~~~~~~~~~~~~~~~~~~~~~

% DEFINE VECTOR FOR THE VISIBLE PORTION OF THE HAIR

% The outer loop iterates through each hair and builds a completion onto it
% based on the input length data and parameters.

TotalHairLength = 0;

ThisIsHair = 0;

for d=1:numbhairs

    % Print progress information to output

    ThisIsHair = ThisIsHair + 1;
    PercentComplete =(ThisIsHair/numbhairs)*100;
    TIH = num2str(ThisIsHair);
    PC = num2str(round(PercentComplete));
    message1 = strcat('Now processing hair : ', TIH);
    message2 = strcat('Percentage complete : ', PC);
    fprintf(message1);
```

```
fprintf('\n');
fprintf(message2);
fprintf('\n');

tic

% Clear all relevant variables which change each time the loop iterates.

clear numsteps;
clear ptsxyz;
clear p;
clear vectxdim1
clear vectydim2
clear vectzdim3
clear vectIS
clear ISlength
clear targetlength
clear growthlength
clear numsteps

% Read in initiation and end point positions from the 'hairdata' master array

initx=hairdata(d,1); %initialise initx to the value in import data.
inity=hairdata(d,2); %initialise inity to the value in import data.
initz=hairdata(d,3); %initialise initz to the value in import data.

seedx=hairdata(d,4); %initialise seedx to the value in import data.
seedy=hairdata(d,5); %initialise seedy to the value in import data.
seedz=hairdata(d,6); %initialise seedz to the value in import data.

% Find x/y/z components of the vector between initiation and end of
% visible portion

vectxdim1 = seedx-initx;
vectydim2 = seedy-inity;
vectzdim3 = seedz-initz;

% Define vector from initiation to end of visible portion (IS)

vectIS = [vectxdim1,vectydim2,vectzdim3];

% And find the length.

ISlength = (1.5*sqrt(((vectxdim1)^2)+((vectydim2)^2)+((vectzdim3)^2)));  %
    Scale length from data coordinates to actual length

DATACOMPARISONDEBUG(d,5) = ISlength;
```

```
% Read in the target length from the master data array.  This is the
% final total length to which the hair will be grown.

targetlength=hairdata(d,7);

DATACOMPARISONDEBUG(d,6) = targetlength;

% Calculate the required simulated growth length past the end of the
% visible section.

growthlength = ((targetlength-ISlength)/1.5);

DATACOMPARISONDEBUG(d,7) = growthlength*1.5;

% Adapt steps for low growth lengths to make sure tiny growth lengths
% do not cause code to fail.  This prevents step lengths being <1.  If
% the growth length is <2, step length is 1, if growth length <8, step
% lenght is 2, and for all other growth lengths, step length is 8.

if (growthlength < 2)

steps = 1;

elseif (growthlength < 8)

    steps = 2;

else

    steps = 8;

end

% Calculate the integer number of iterations required to reach the
% required length

numsteps = round(growthlength/steps);

%%%%%%%%%%%%%%%%%%%%%%%%%%%%%%%%%%%%
%*** BUILDING THE TEST SPHERE  ***%
%%%%%%%%%%%%%%%%%%%%%%%%%%%%%%%%%%%%

% The code assigns quasi-equally spaced points on a unit-sphere surface
% according to the golden-spiral method.  This unit sphere is then scaled
% by radius to the step size.  It is from these points that a growth
% destination is chosen, depending on various constraints of angle,
```

```
% greyscale and length.

StepCtr = 0; % A counter

% Assigns quasi-equally spaced points on a unit-sphere surface according to the
     golden-spiral method.

 for j=1:numsteps,

    StepCtr = StepCtr+1;

    numpts= 2*numtest; % initialises for twice as many points as required (
        since half will be removed later).
    radius=steps; % sets radius to user defined step value.
    inc = pi * (3-sqrt(5));
    off = 2/numpts;

    k = 0:numpts-1;
    y = k * off - 1 + (off/2);
    r = sqrt(1 - (y.^2));
    phi = k * inc;

    p = [cos(phi).*r; y ;sin(phi).*r]'; % 'p' is an an (n,3) matrix of x,y,z,
        values of the n surface points

    p = radius*p ; % scales the unit sphere to the step size.

    p(:,1)=p(:,1)+seedx; % aligns the scaled sphere to the seed location (S)
    p(:,2)=p(:,2)+seedy; % aligns the scaled sphere to the seed location (S)
    p(:,3)=p(:,3)+seedz; % aligns the scaled sphere to the seed location (S)

    % p is an array of xyz positions for all surface points.  It is
    % also where all true/false criteria for the different checks are
    % kept.

    p=round(p); % turns x,y,z values of surface points to integers in order to
        read greylevel values.

%%%%%%%%%%%%%%%%%%%%%%%%%
%*** IN RANGE CHECK ***%
%%%%%%%%%%%%%%%%%%%%%%%%%

% If the point lies within the dataset, it will be given a value 1 in
% the 6th column, otherwise the value will be zero (valid).  This has
% the effect of constraining the later growth to within the dataset as
% out-of-data points cannot be chosen as the next growth destination.
```

```
for k=1:numpts;

    if (p(k,1) >= datasetx)

        p(k,6) = 1;

    elseif (p(k,2) >= datasety)

        p(k,6) = 1;

    elseif (p(k,3) >= datasetz)

        p(k,6) = 1;

    elseif (p(k,1) < 1)

        p(k,6) = 1;

    elseif (p(k,2) < 1)

        p(k,6) = 1;

    elseif (p(k,3) < 1)

        p(k,6) = 1;

    else

        p(k,6)=0;

    end

end

%%%%%%%%%%%%%%%%%%%%%%%%%
%*** GREYLEVEL CHECK ***%
%%%%%%%%%%%%%%%%%%%%%%%%%

% The next check is whether the surface point lies within the soil
% phase or not.  The soil threshold value is user defined and has the
% variable name 'soilthresh'

for l=1:numpts; % loop to check validity of greylevels for each surface point

    greyx = p(l,1); % the x coordinate of the randomly selected surface point
    greyy = p(l,2); % the y coordinate of the randomly selected surface point
    greyz = p(l,3); % the z coordinate of the randomly selected surface point
```

```
    if p(l,6) == 0;

    testgrey = sequence(greyx,greyy,greyz); % find greylevel in dataset for
        this surface point

        if testgrey<soilthresh

            p(l,4)=1; % sets in-range values to 1 if the point is in valid
                range

        elseif testgrey == soilthresh

            p(l,4)=0; % sets out-of-range values to 0 if point is outside valid
                 range

        elseif testgrey > soilthresh

            p(l,4)=0;

        end

    else

    % if the point is outside the dataset range, set its greyscale
    % truth value to that of soil (0)

    p(l,4)=0;

    end


end

%%%%%%%%%%%%%%%%%%%%%
%*** ANGLE CHECK ***%
%%%%%%%%%%%%%%%%%%%%%

% CHECK IF ANGLE BETWEEN CURRENT VECTOR AND INITAL VECTOR IS IN ALLOWABLE
% RANGE AND IF SO ADD A NUMBER TO 5th COLUMN IN P.
% THE NUMBER (1-4) DENOTES THE BAND INTO WHICH THE VECTOR ANGLE FALLS
% RELATIVE TO THE INITIAL (VISIBLE) VECTOR

for s=1:numpts; % loop over all surface points to check validity of angle

testvectx = p(s,1) - seedx; % specify x dist between each surface point and the
     circle centre (S)
```

```
testvecty = p(s,2) - seedy; % specify y dist between each surface point and the
     circle centre (S)
testvectz = p(s,3) - seedz; % specify z dist between each surface point and the
     circle centre (S)

growvect = [testvectx,testvecty,testvectz]; % creates the vector of the test
    segment

DistToCentre = sqrt((testvectx^2)+(testvecty^2)+(testvectz^2));

vectangle = atan2(norm(cross(vectIS,growvect)),vectIS*growvect'); % the angle
    between the test segment and the initial vector from input data

%Write the angles and the distances into the SurfacePointArray file for
    debugging purposes

p(s,8) = vectangle;
p(s,9) = DistToCentre;

        if vectangle<targetangle

                p(s,5)=1; % sets column 5 of p to 1 if vector is in range

            elseif vectangle<(2*targetangle)

                p(s,5)=2; % sets column 5 of p to 2 if vector is within two
                    times the target

            elseif vectangle<(3*targetangle)

                p(s,5)=3; % sets column 5 of p to 3 if vector is within three
                    times the target

            elseif vectangle<1.57

                p(s,5)=4; % sets column 5 of p to 4 if vector is within 90
                    degrees of the preceding vector

            else

                p(s,5)=0; % sets column 5 of p to 0 if vector is out of range (
                    i.e. outside the hemisphere)

        end

 end
```

```
    counttest1 = 0; % initialise the counter for surface points within the
        first choice of angle
    counttest2 = 0; % initialise the counter for surface points within the
        second choice of angle
    counttest3 = 0; % initialise the counter for surface points within the
        third choice of angle
    counttest4 = 0; % initialise the counter for surface points within the
        fourth choice of angle

    clear angleis1;
    clear angleis2;
    clear angleis3;
    clear angleis4;
    clear testgrey;
    clear testangle;
    clear testrange;

%%%%%%%%%%%%%%%%%%%%%%%%%%%%%%%%%%%%
%*** CATEGORISE POINTS BY ANGLE ***%
%%%%%%%%%%%%%%%%%%%%%%%%%%%%%%%%%%%%

% Place points from the p array into different arrays named 'angleisn'
% where n is from 1 to 4, depending on which bin the vector between the
% seed and that point falls wrt the initial vector angle.

for o=1:numpts;

        testgrey=p(o,4); % for each surface point in array p, report if the
            greylevel is in range (1) or out of range (0)
        testangle=p(o,5); % for each surface point in array p, report if the
            angle is in first (1) 2nd (2) 3rd (3) or 4th (4) choice band.
        testrange=p(o,6); % for each surface point, report if it lies outside
            the dimesnions of the input data (1=bad) or inside (0=good)

    if ((testgrey==1)&&(testangle==1)&&(testrange~=1)) % xyz values of any
        point with allowable greylevel and first choice angle are put into (n,3)
         array angleis1

            counttest1=counttest1+1; % the counter to correctly allocate the
                row number for each value.

            angleis1(counttest1,1)=p(o,1);
            angleis1(counttest1,2)=p(o,2);
            angleis1(counttest1,3)=p(o,3);

        elseif ((testgrey==1)&&(testangle==2)&&(testrange~=1)) % xyz values of
            any point with allowable greylevel and second choice angle are put
```

```
            into (n,3) array angleis2

            counttest2=counttest2+1;

            angleis2(counttest2,1)=p(o,1);
            angleis2(counttest2,2)=p(o,2);
            angleis2(counttest2,3)=p(o,3);

        elseif ((testgrey==1)&&(testangle==3)&&(testrange~=1)) % xyz values of
            any point with allowable greylevel and third choice angle are put
            into (n,3) array angleis3

            counttest3=counttest3+1;

            angleis3(counttest3,1)=p(o,1);
            angleis3(counttest3,2)=p(o,2);
            angleis3(counttest3,3)=p(o,3);

        elseif ((testgrey==1)&&(testangle==4)&&(testrange~=1)) % xyz values of
            any point with allowable greylevel and fourth choice angle are put
            into (n,3) array angleis4

            counttest4=counttest4+1;

            angleis4(counttest4,1)=p(o,1);
            angleis4(counttest4,2)=p(o,2);
            angleis4(counttest4,3)=p(o,3);

    end

end

%%%%%%%%%%%%%%%%%%%%%%%%%%%%%%%%%%%%%%%%%%%%%%%%%%%%%%%%%%%%%%%%%%%%%%%%%%%%%%%
%*** CHECK WHETHER THE ANGLE ARRAYS EXIST, AND COUNT POINTS IN EACH ARRAY  ***%
%%%%%%%%%%%%%%%%%%%%%%%%%%%%%%%%%%%%%%%%%%%%%%%%%%%%%%%%%%%%%%%%%%%%%%%%%%%%%%%

% clear the arrays and variables related to determining existence and
% size of 'angleisn' arrays.

    clear isthere1;
    clear isthere2;
    clear isthere3;
    clear isthere4;
    clear sizeangle1;
    clear sizeangle2;
    clear sizeangle3;
    clear sizeangle4;
```

```
 isthere1 = exist('angleis1'); % returns a value of 1 if the array exists.
 isthere2 = exist('angleis2'); % returns a value of 1 if the array exists.
 isthere3 = exist('angleis3'); % returns a value of 1 if the array exists.
 isthere4 = exist('angleis4'); % returns a value of 1 if the array exists.

 % check if there are any points in each of the arrays, from first
 % to fourth choice.  If so, return the number of points.

 if (isthere1==1)

 sizeangle1 = size(angleis1,1); % reports number of points within the first
     choice of angle band (< targ).

 end

 if (isthere2==1)

 sizeangle2 = size(angleis2,1); % reports number of points within the second
      choice of angle band (< 2*targ).

 end

 if (isthere3==1)

 sizeangle3 = size(angleis3,1); % reports number of points within the third
     choice of angle band (< 3*targ).

 end

 if (isthere4==1)

 sizeangle4 = size(angleis4,1); % reports number of points within the 4th
     choice of angle band (< 90 deg).

 end

 %%%%%%%%%%%%%%%%%%%%%%%%%%%%%%%%%%%%%%%%%%%%%%%%%
 %*** NEXT GROWTH POINT SELECTION PROCESS  ***%
 %%%%%%%%%%%%%%%%%%%%%%%%%%%%%%%%%%%%%%%%%%%%%%%%%

% Chooses a new seed point from one of the subarrays 'angleisn'
% working iteratively from the most desirable to least desirable
% angle.  The first array with a valid point will have one of them
% randomly chosen.

 if (isthere1==1) % if any first choice points exist...
```

```
    RaNumArr = randperm(sizeangle1);
    rnum = RaNumArr(randi(size(RaNumArr,2))); % select a random row
        from the array of first choice points

    newseedx = angleis1(rnum,1); % sets new seed x value for next
        iteration
    newseedy = angleis1(rnum,2); % sets new seed y value for next
        iteration
    newseedz = angleis1(rnum,3); % sets new seed z value for next
        iteration

elseif (isthere2==1) % otherwise, if any second choice points exist...

    RaNumArr = randperm(sizeangle2);
    rnum = RaNumArr(randi(size(RaNumArr,2))); % select a random row
        from the array of first choice points

    newseedx = angleis2(rnum,1); % sets new seed x value for next
        iteration
    newseedy = angleis2(rnum,2); % sets new seed y value for next
        iteration
    newseedz = angleis2(rnum,3); % sets new seed z value for next
        iteration

elseif (isthere3==1) % otherwise, if any third choice points exist...

    RaNumArr = randperm(sizeangle3);
    rnum = RaNumArr(randi(size(RaNumArr,2))); % select a random row
        from the array of first choice points

    newseedx = angleis3(rnum,1); % sets new seed x value for next
        iteration
    newseedy = angleis3(rnum,2); % sets new seed y value for next
        iteration
    newseedz = angleis3(rnum,3); % sets new seed z value for next
        iteration

elseif (isthere4==1) % otherwise, if any fourth choice points exist...

    RaNumArr = randperm(sizeangle4);
    rnum = RaNumArr(randi(size(RaNumArr,2))); % select a random row
        from the array of first choice points

    newseedx = angleis4(rnum,1); % sets new seed x value for next
        iteration
    newseedy = angleis4(rnum,2); % sets new seed y value for next
        iteration
```

```
            newseedz = angleis4(rnum,3); % sets new seed z value for next
                iteration

    end

% Break out of loop if there is no point found (due to going out of
% domain)


    %%%%%%%%%%%%%%%%%%%%%%%%%%%%%%%%%%%%%%%%%%%%%%%%%%%%
    %*** WRITE POINTS TO THE MASTER OUTPUT ARRAY ***%
    %%%%%%%%%%%%%%%%%%%%%%%%%%%%%%%%%%%%%%%%%%%%%%%%%%%%

    % The start and end point of the vector just described will be
    % written to a master array, which is used to write out the output
    % images after the hair growth algorithm is finished.

    if ((isthere1==1)||(isthere2==1)||(isthere3==1)||(isthere4==1)) % if any of
         them are 1....

    vectxdim = newseedx-seedx; % find length in x dir between init and seed
    vectydim = newseedy-seedy; % find length in y dir between init and seed
    vectzdim = newseedz-seedz; % find length in z dir between init and seed

    ptsxyz(j,1)=newseedx;
    ptsxyz(j,2)=newseedy;
    ptsxyz(j,3)=newseedz;
    ptsxyz(j,4)=seedx;
    ptsxyz(j,5)=seedy;
    ptsxyz(j,6)=seedz;
    ptsxyz(j,7)=(sqrt(((vectxdim)^2)+((vectydim)^2)+((vectzdim)^2))); % the
        distance of the step to this found point from the seed.

    %%%%%%%%%%%%%%%%%%%%%%%%%%%%%%%%%%%%%%%%%%%%%%%%%%%%
    %*** SET UP VARIABLES FOR NEXT ITERATION ***%
    %%%%%%%%%%%%%%%%%%%%%%%%%%%%%%%%%%%%%%%%%%%%%%%%%%%%

    % seed(xyz) is now the newly found surface value, and the new
    % initiation (xyz) is that of the seed point from which it was
    % found.

    seedx=newseedx; % update new initial x value to the seed point of current
        iteration
    seedy=newseedy; % update new initial y value to the seed point of current
        iteration
    seedz=newseedz; % update new initial z value to the seed point of current
        iteration
```

```
% Break out of loop if there is no point found (due to going out of
  % domain)

        else

        FailCount = FailCount + 1;

        ERR1 = 'Could not find a suitable point for hair number : ';
        ERR2 = num2str(ThisIsHair);
        ERR3 = '. Failed on step :';
        ERR4 = num2str(StepCtr);

        ErrMess = strcat(ERR1, ERR2, ERR3, ERR4);
        fprintf(ErrMess)
        fprintf('\n');

        Step_Failure_Error_Log(FailCount, 1) = ThisIsHair;
        Step_Failure_Error_Log(FailCount, 2) = StepCtr;
        Step_Failure_Error_Log(FailCount, 3) = seedx;
        Step_Failure_Error_Log(FailCount, 4) = seedy;
        Step_Failure_Error_Log(FailCount, 5) = seedz;

            break

        end

    end

        %%%%%%%%%%%%%%%%%%%%%%%%%%%%%%%%%%%%%%%%%%%%%%%%%%%%%%%%%%%%%%%%%%%%%%%
        %*** WRITE OUT FOUND VALUES FOR GROWTH STEP TO DUMMY MATRIX ***%
        %%%%%%%%%%%%%%%%%%%%%%%%%%%%%%%%%%%%%%%%%%%%%%%%%%%%%%%%%%%%%%%%%%%%%%%

        istherептsxyz = exist('ptsxyz');

        if (istherептsxyz==1)

        ThisHairLength = 0;

        numgrwsteps=size(ptsxyz,1);

        clear hairvals;
        clear xcomp
        clear ycomp
        clear zcomp
        clear writevec
        clear xang
```

```
clear yang
clear zang
clear startptx
clear startpty
clear startptz
clear xcompstp
clear ycompstp
clear zcompstp

iterstep = 1; % set length of each step to half of the longest inter-point
    distance

xunitv = [1,0,0]; % set up x unit vector
yunitv = [0,1,0]; % set up y unit vector
zunitv = [0,0,1]; % set up y unit vector

for t=1:numgrwsteps

    xcomp=ptsxyz(t,1)-ptsxyz(t,4);
    ycomp=ptsxyz(t,2)-ptsxyz(t,5);
    zcomp=ptsxyz(t,3)-ptsxyz(t,6);

    stepl = ptsxyz(t,7); % set length of growth vector

    writevec = [xcomp, ycomp,zcomp]; % the vector for segment n (linking
        seed and surface point)

    xang = atan2(norm(cross(xunitv,writevec)),xunitv*writevec'); % find
        angle between x axis and writevec (rads)
    yang = atan2(norm(cross(yunitv,writevec)),yunitv*writevec'); % find
        angle between y axis and writevec (rads)
    zang = atan2(norm(cross(zunitv,writevec)),zunitv*writevec'); % find
        angle between z axis and writevec (rads)

    numvcsteps = round(stepl/iterstep); % establish the number of write
        steps required given the radius size of the test sphere

    startptx = ptsxyz(t,4);
    startpty = ptsxyz(t,5);
    startptz = ptsxyz(t,6);

    TotalHairLength = TotalHairLength + stepl;
    ThisHairLength = ThisHairLength + stepl;

    for q=1:numvcsteps

        xcompstp = ceil((q*iterstep)*cos(xang)); % find x component of
```

```
                growvect at the ith step
            ycompstp = ceil((q*iterstep)*cos(yang)); % find y component of
                growvect at the ith step
            zcompstp = ceil((q*iterstep)*cos(zang)); % find y component of
                growvect at the ith step

            hairvals(q,1) = ((startptx) + xcompstp); % write x value of point
                to be written to (numcvsteps,3) array "hairvals"
            hairvals(q,2) = ((startpty) + ycompstp); % write y value of point
                to be written to (numcvsteps,3) array "hairvals"
            hairvals(q,3) = ((startptz) + zcompstp); % write y value of point
                to be written to (numcvsteps,3) array "hairvals"

        end

        dummy(startptx,startpty,startptz)=255;

        for m=1:numvcsteps

            dummy(hairvals(m,1), hairvals(m,2), hairvals(m,3)) = (255); % for
                each xyz coordinate in hairvals, set the value at the
                corresponding lcoation in dummy matrix to 255

        end

    end

    % Write out hair lengths to an array where column is the run, and
    % row is the hair (for debugging purposes)

    HairLengthsIndividual(d, WeibRuns) = ThisHairLength*1.5;

    else

    continue

    end

    toc

end

fprintf('Starting to write TIF data to file');
fprintf('\n');

OuTpUt = 'OUTPUT_';
```

```
NumRun = num2str(WeibRuns);

FiLeNaMe = strcat(OuTpUt, NumRun);

OverWriteQuery = exist(FiLeNaMe);

if (OverWriteQuery==7)

cd(FiLeNaMe);

delete *.tif;

else

    mkdir(FiLeNaMe);

    cd(FiLeNaMe);

end


for i=1:datasetz;

     a=num2str(i);

     filename = 'output';

     fltype = '.tif';

     filename = strcat(filename,a,fltype);

     imwrite(dummy(:,:,i),filename,'WriteMode','append','Compression','none');

end

fprintf('Finished TIF output');
fprintf('\n')

cd ..;

% Report the total hair length for the entire dataset into a row of array
% "TotalHairLengthArr"

TotalHairLengthArr(WeibRuns) = TotalHairLength*1.5;


RunNumber = num2str(WeibRuns);
```

```
MenSage = '
    Error_log_of_failed_hairs_with_failure_step_and_xyz_of_seed_at_failure_WEIBRUN_'
    ;
MsGwBr = strcat(MenSage, RunNumber);
csvwrite(MsGwBr, Step_Failure_Error_Log);

clc

end

csvwrite('List_of_total_hair_lengths_for_runs', TotalHairLengthArr);
csvwrite('
    List_of_Weibull_parameters_of_virtual_datasets_for_comparison_with_those_from_washout_fit
    ', WeibullFit);
csvwrite('Lists_of_discrete_hair_lengths_one_column_per_HairGrower_run',
    HairLengthsIndividual);

WeibullFit = csvread('
    List_of_Weibull_parameters_of_virtual_datasets_for_comparison_with_those_from_washout_fit
    ');
```

8.7 Flowchart of the SRXCT rhizosphere imaging workflow

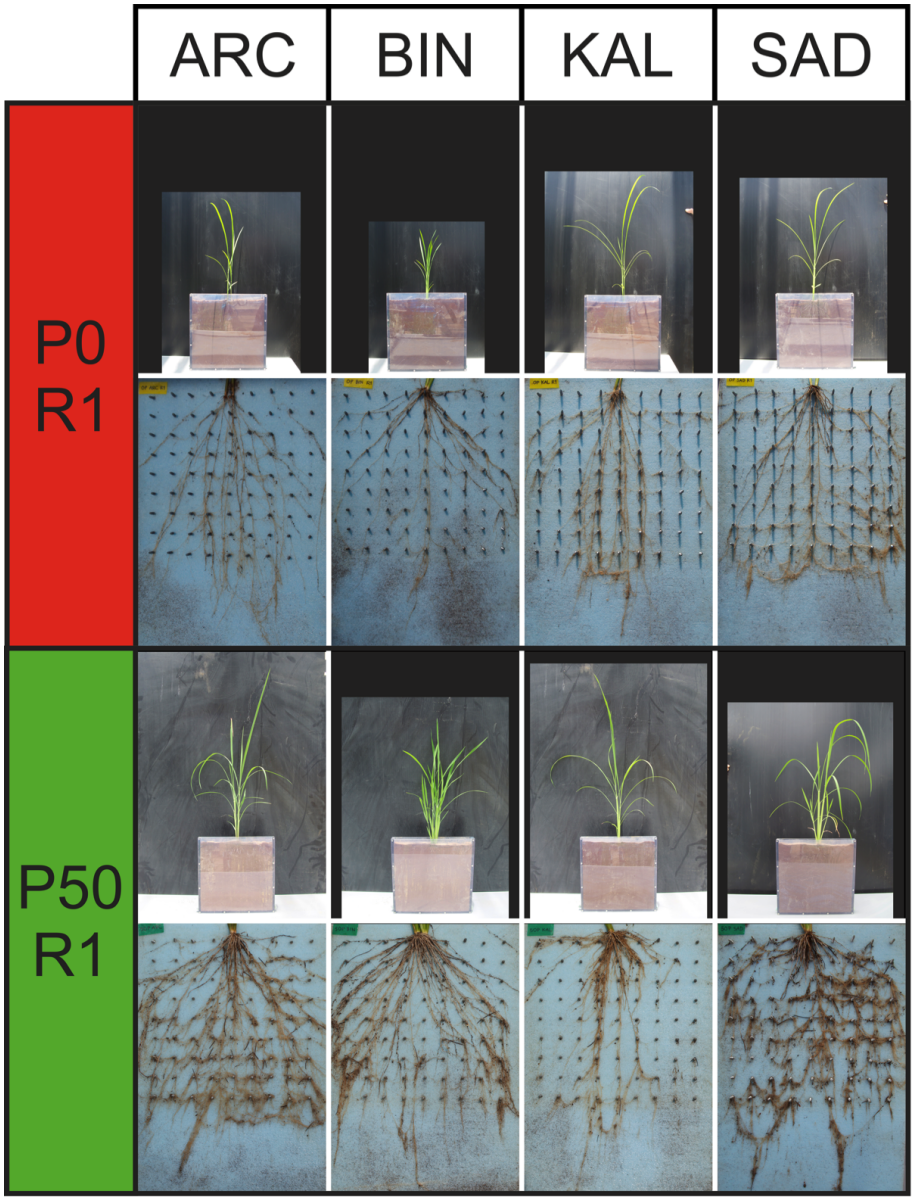

Figure 8.2: Rhizobox-grown root architecture of 30 day old rice plants of differing genotypes. ARC =, BIN = *Binyalawan*, KAL =, KAS =, N4 =, SAD = *Sadri tor Misri*. Samples are shown from low-P soil and identical soil treated before planting with P fertiliser up to an equivalent soil content of $50\mathrm{Kg\ P.Ha^{-1}}$. There is a clear up-regulation of fine rooting in the high-P soil condition compared to the samples in low-P soil.

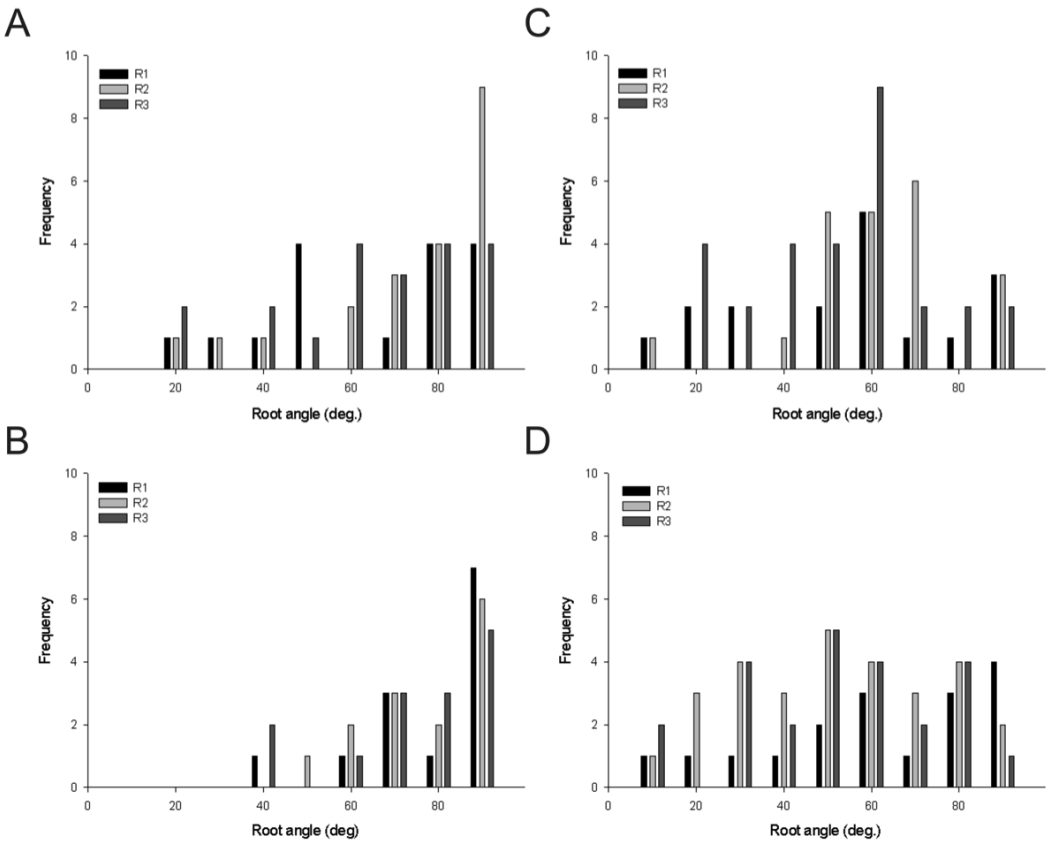

Figure 8.3: Histograms of primary root angle for (A) KAL, (B) ARC, (C) BIN and (D) STM in low-P soil. Data from three replicates (R1, R2, R3) are shown.

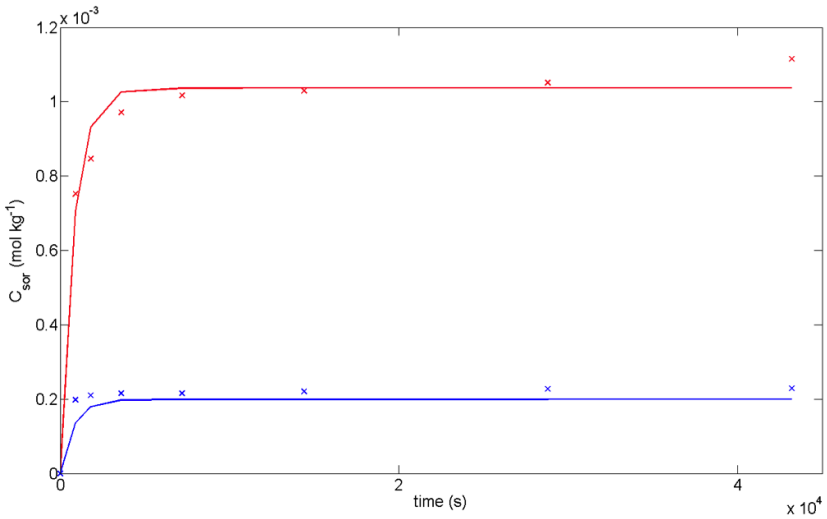

Figure 8.4: Determination of A and κ via curve fitting of C_{sor} vs t, using experimental data from the two lowest concentrations of ^{3}3P labelled $\mathrm{KH_2PO_4}$.

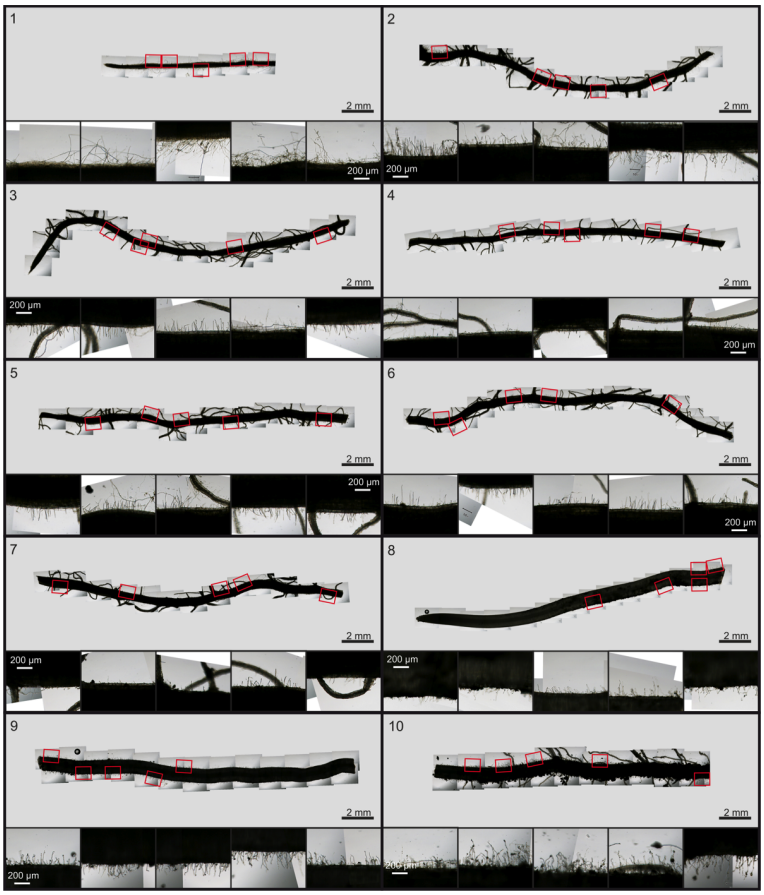

Figure 8.5: Data used for sampling of soil-grown root hair lengths. One fine primary and one coarse primary were sampled following gentle washing of rhizobox-grown roots in the low-P condition, but before manual removal of soil from roots. Each was cut into a number of subsections of $\approx 2cm$ for analysis, at a 2cm spacing from tip to the basal region. Frames (1-7) represent fine primary subsections, and frames (8-10) represent coarse primary subsections. The entire length of each subsection was imaged using an Olympus BX50 microscope and a $4\times$ magnification. After stitching all images together, 5 subregions were defined for each subsection, each representing a distance of 1mm on the root surface. All hairs in subregions which were in sharp focus were measured in FIJI to generate a set of 220 hair lengths.

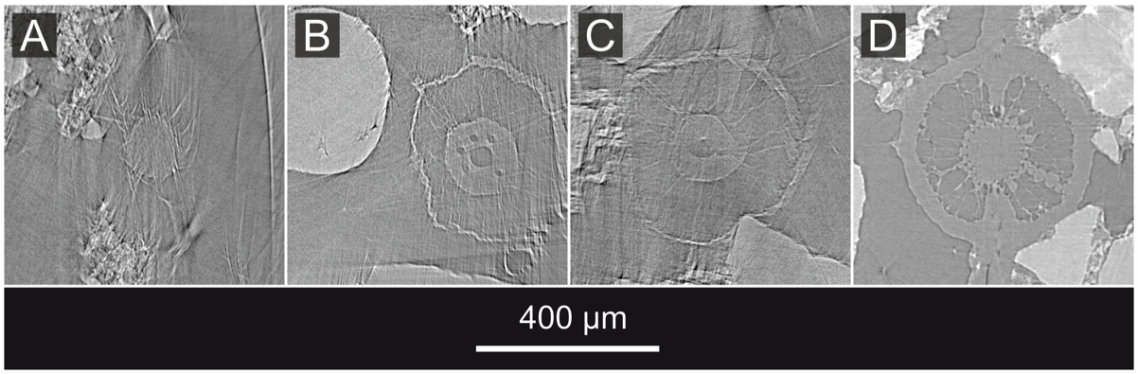

Figure 8.6: Frames (1-3) show movement artifacts and cortical damage caused by excessive exposure of samples to X-rays during sample set-up. (A) Wheat (*Triticum aestivum cv Santiago*) (B) Rice (*Oryza sativa cv Sadri tor Misri*) (C) Rice (*Oryza sativa cv Varyla*) (D) Comparison data of undamaged rice root *Oryza sativa cv Varyla* acquired at the SLS synchrotron

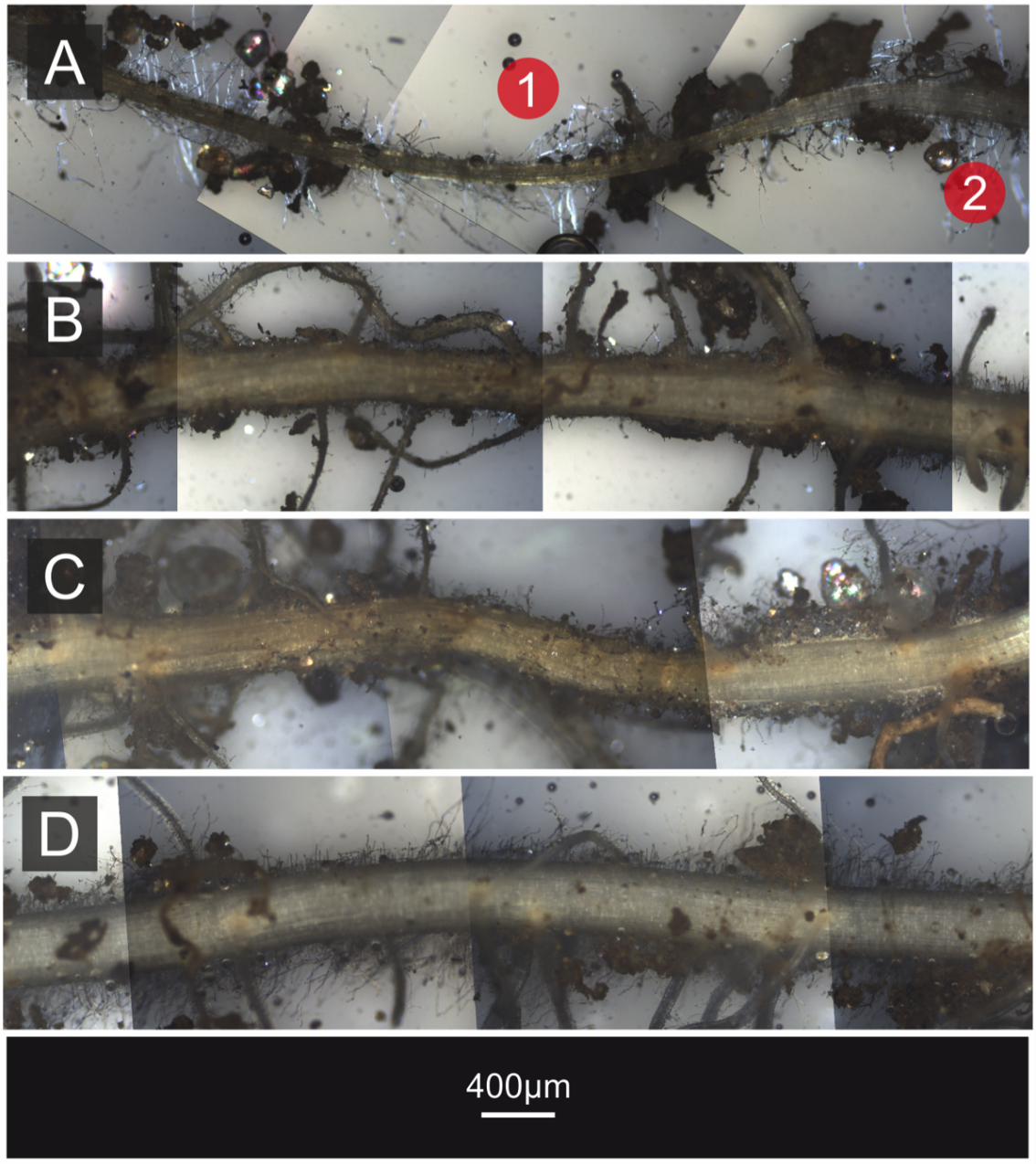

Figure 8.7: Macroscope images showing damage to roots due to excessive X-ray flux during sample set-up. (A) Wheat (*Triticum aestivum cv Santiago*, comparing damaged (1) and undamaged (2) regions. (B) Rice (*Oryza sativa cv Varyla*). (C) Rice (*Oryza sativa cv Sadri tor Misri*) (D) Control sample of rice (*Oryza sativa cv Varyla*) for comparison.

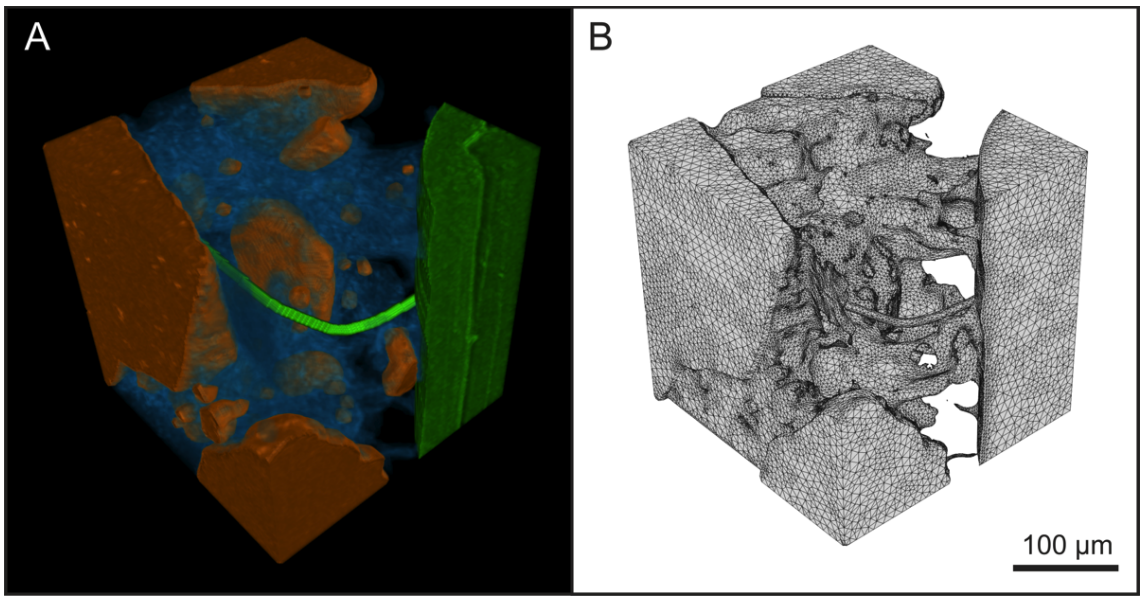

Figure 8.8: (A) The geometry used for the convergence test. (B) Mesh output file from ScanIP.

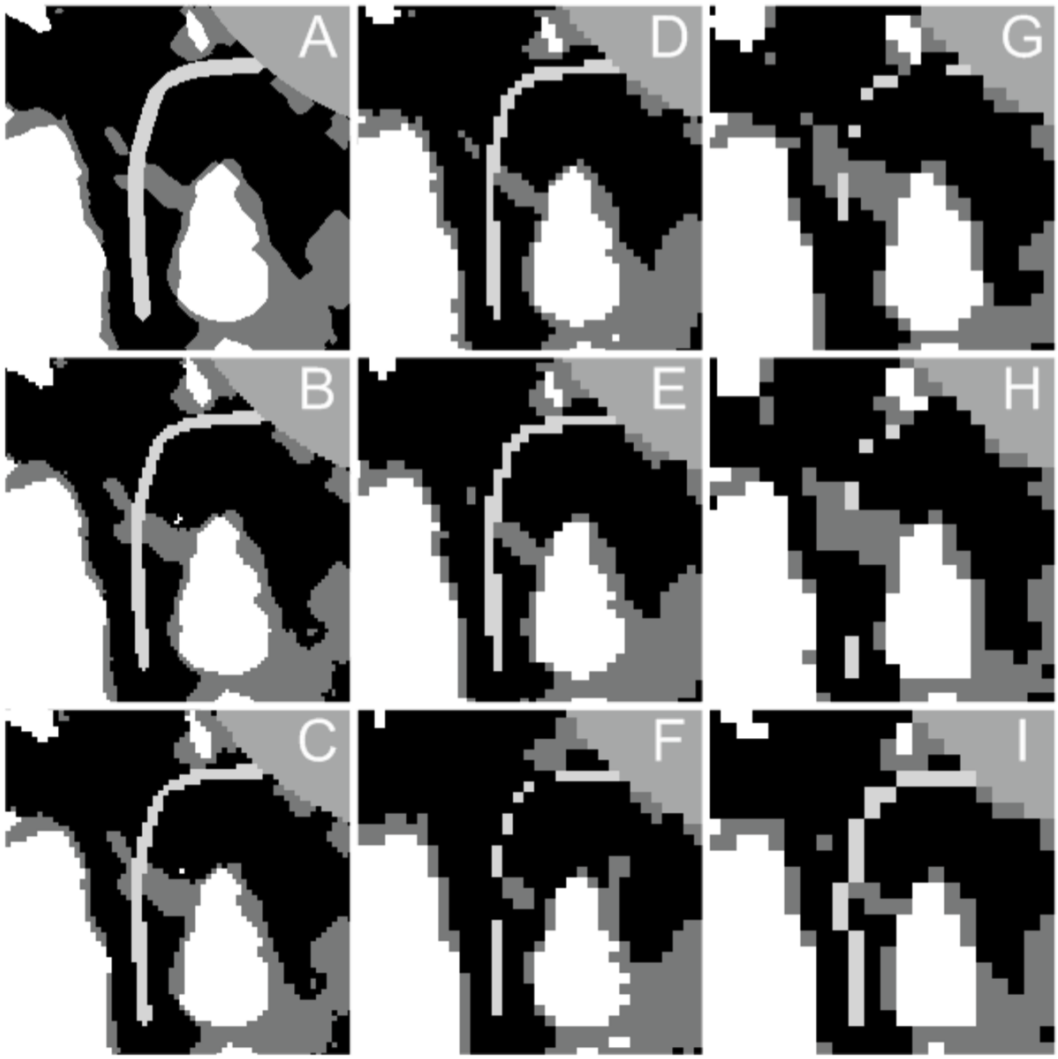

Figure 8.9: xy slices through the geometry used for the convergence test, showing the influence of progressive voxel binning on topology. Edge lengths from (A-I) are (in voxels): 200, 100, 67, 50, 40, 33, 29, 25, 22.

Table 8.2: Parameters used to mesh un-binned geometries 9-12

ID	Min Edge L. (mm)	Max Edge L. (mm)	Target Max. Err. (mm)	Els. Acr. Layer (d)	Qual. Opt. Cyc.	Surface change rate	Internal change rate
9	0.00135	0.015	0.015	0.5	10	100	40
10	0.00285	0.00015	0.00015	0.8	5	40	30
11	0.0018	0.0042	0.00015	0.9	5	20	30
12	0.000744	0.00296	0.000148	1.08	5	68	29

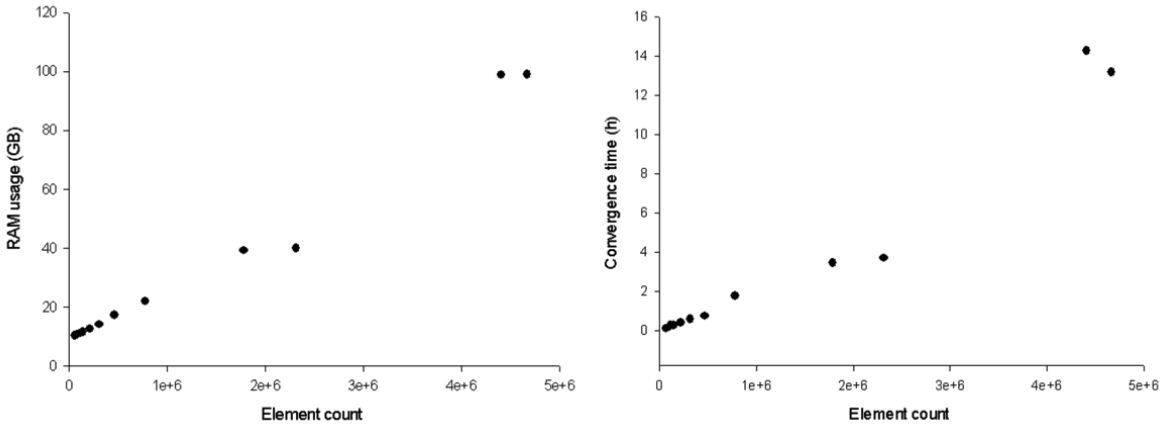

Figure 8.10: Plotting metadata from the Iridis 4 cluster for all simulations allowed broad relationships to be established between element count and both RAM utilisation and convergence time.

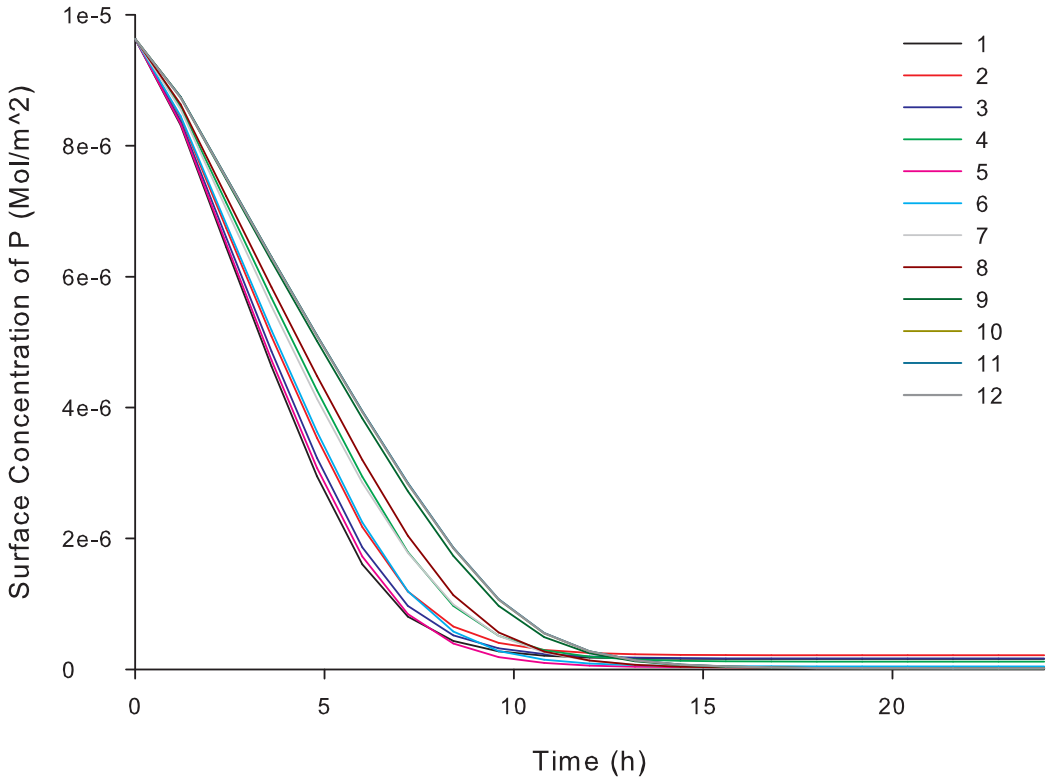

Figure 8.11: Plots of soil-bound P with respect to time are shown for all meshed geometries. Convergence was reached for meshes 10-12, with other mesh parameters leading to variation in predicted depletion profile.

Table 8.3: Iridis metadata

ID	Edge length (vox.)	Convergence time (h)	RAM usage (GB)	Element count
1	22	0.01	10.24	6.32×10^4
2	25	0.13	10.66	8.78×10^4
3	29	0.26	11.03	1.14×10^5
4	33	0.25	11.39	1.45×10^5
5	40	0.40	12.47	2.16×10^5
6	50	0.57	14.00	3.12×10^5
7	67	0.73	17.19	4.66×10^5
8	100	1.75	21.88	7.78×10^5
9	200	3.68	39.90	2.32×10^6
10	200	3.44	39.13	1.79×10^6
11	200	14.26	98.81	4.41×10^6
12	200	13.17	98.96	4.67×10^6

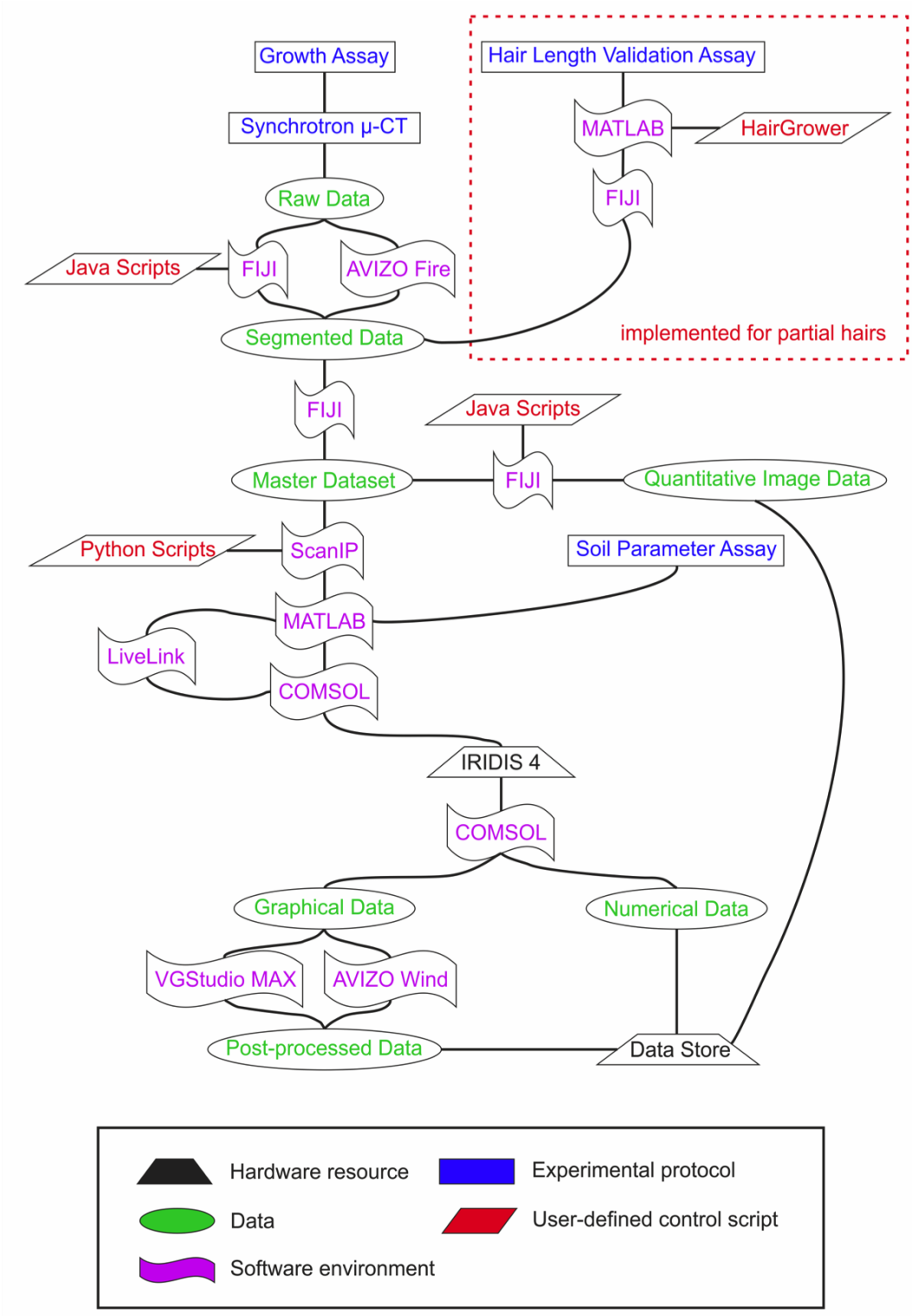

Figure 8.12: Flowchart showing all steps of the rhizosphere imaging and modelling protocol

Glossary

The following is a glossary of terms used, defined in the context of their use in the domain of this work:

- **Artifact** - Spurious features in reconstructed data. Artifacts result from non-ideal physical effects in the source, sample, and detector, leading to deviance in the reconstructed data away from the true representation of the attenuation profile in the sample.
- **Boolean random set** - A stochastic approach to generation of virtual pore domains with distributions of effective radii and throat sizes which approximate those of real soil, allowing modelling of pore-domain processes without the requirement for imaging methods.
- **Bootstrapping** - A resampling method, using repeated sampling of a parent dataset to estimate its degree of error. For a dataset for which the error is unknown, multiple resampling allows it to be compared to the resulting 'bootstrapped' data, thus giving a measure of the likely error.
- **Compton scattering** - An X-ray attenuation mode generally dominant at higher energies to *photoelectric absorption*, in the range ($\approx 500 > \approx 1 \times 10^4 \mathrm{keV}$). Rather than being absorbed, photons are deflected by atomic electrons.
- **cryo-SEM** - A method for preparing samples for scanning electron microscopy, using cryogenic temperatures to stabilise the sample structure, allowing sectioning and imaging.
- **Euler Poincaré characteristic** - A dimensionless descriptor of a topological space. The Euler Poincaré characteristic describes shape and character of a space as a function of, but without explicit reference to, specific properties (such as vertices or faces), allowing comparison between different spaces (such as connected macro pore domains).
- **Gaussian difference** - Using the *Gaussian* operator to filter the same image using two difference standard deviation values, then subtracting one from the other produces an

image in which preferentially suppressed frequencies in the image are filtered out. Because image noise has a high spatial frequency, the difference of Gaussians (DoG) method can suppress noise whilst revealing useful spatial detail such as edges.

- **Golden section spiral** - A spiral for which the distance from the origin increases by a factor of the *Golden Ratio* for every $90°$ of rotation. The golden section spiral forms the basis of a computationally highly-efficient method for approximating the evenly-spaced distribution of points on the surface of a sphere.
- **Hessian matrix** - A square matrix of second-order PDE's of a function ($f(x, y)$) at a point. Point-wise determination of a $2x2$ Hessian matrix forms the basis of a number of feature detection algorithms, since it allows curvature in image features to be quantified.
- **Homogenisation** - Modelling of complex heterogenous systems can be simplified by considering a unit cell on the smallest length scale of significance, characterising behaviour of governing equations within this domain, then upscaling to larger scales. Homogenisation theory allows the contribution of individual features at the unit cell scale to be considered at higher scales, without the requirement to explicitly consider them. The computational load required for solution of a model can thus be drastically reduced.
- **Hydraulic lift** - The redistribution of water in the soil by the plant. Water absorbed in a horizon at higher water potential is leached into soil at lower water potential in order to improve mobility of nutrrients.
- **K-edge filtering** - A method for filtering an X-ray spectrum to generate a quasi-monochromatic effect. The characteristic emission peak of a target material is matched to the characteristic absorption of a filter. Through careful selection of energy, target and filter materials, energies around the desired K-peak can be preferentially absorbed.
- **Morphology** - A description of the form and structure of a biological entity.
- **Neural network** - An approach in computer modelling using a synthetic approximation of the nervous system of the brain. Neural networks are often used in developing trainable pattern recognition algorithms.
- **Non-dimensionalisation** - A technique used to simplify equations, or uncover characteristic behaviour of a mathematically-described system, achieved using variable-substitution to remove physical units.
- **Pedo-transfer function** - A function for translating between variables, used in soil science to infer difficult-to-measure soil properties from known properties.
- **Photoelectric absorption** - The dominant X-ray attenuation up to energies of around ($\approx 500\text{keV}$).

- **Poly-line** - A line defined by straight segments joining a number of discrete points to form a quasi-curve.
- **Puddling** - A method used to prepare soil for rice culture, in which structure is removed by mechanical shearing at 100% soil saturation.
- **Random Forest** - A method for trainable, computational decision-making, in which a large number of decision trees (the 'forest') are trained using a set of classes, with these criteria used by each tree to assign each test sample to its most likely parent class. The modal decision between those of all the trees for a given sample is chosen as the target class.
- **Reconstruction** - The computational process by which a series of angular projections is converted into a 3D volume of voxels.
- **Resin-infusion tomography** - A process by which a sample is infused with hard-setting epoxy resin, before being mechanically sectioned and investigated, often using light microscopy.
- **Rhizosphere** - The small region surrounding plant roots in which the majority of nutrient transport processes take place, and in which the greatest diversity of soil fauna is found.
- **Scintillator** - A thin wafer of material which emits visible light when irradiated by X-rays. On an SRXCT beamline, a scintillator turns the attenuated X-ray beam into light, which is captured using a light-sensitive charge coupled detector (CCD).
- **Segmentation** - An image analysis process by which voxels in CT data are isolated and assigned to a particular material class.
- **Sobel filtering** - An image processing function, used in edge detection. The Sobel operator approximates the gradient in image intensity function, allowing transition rate in attenuation coefficient between image regions to be quantified.
- **Spatial resolution** - The smallest resolvable feature size in reconstructed CT data. Spatial resolution is a function of detector, source, sample and reconstruction characteristics.
- **Streamlines** - Curves which are parallel to the direction of the concentration gradient in the fluid at a point in space.
- **Topology** - A description of the relationships between different elements in a branching system.
- **Trophomorphogenesis** - A term used to describe the plasticity of a root system in response to environmental constraints.

- **Voxel** - The smallest geometric unit of a 3D dataset.
- **XANES** - X-ray Absorption Near Edge Structure absorption spectroscopy. A technique using absorption peaks of incident X-rays to map chemical species in materials in a spatially resolvable manner.

Bibliography

No Title.

R Adams and L Bischof. Seeded region growing. *Pattern Analysis and Machine Intelligence, IEEE Transactions on*, 16(6):641–647, 1994.

J Ahrens, B Geveci, and C Law. Paraview: An end user tool for large data visualization. *the Visualization Handbook. Edited by CD Hansen and CR Johnson. Elsevier*, 2005.

M Amato and J T Ritchie. Spatial distribution of roots and water uptake of maize (Zea mays L.) as affected by soil structure. *Crop Science*, 42:773–780, 2002.

Junhua Ao, Jiabing Fu, Jiang Tian, Xiaolong Yan, and Hong Liao. Genetic variability for root morph-architecture traits and root growth dynamics as related to phosphorus efficiency in soybean. *Functional Plant Biology*, 37(4):304–312, 2010. ISSN 1445-4416.

F Asch, M Dingkuhn, A Sow, and A Audebert. Drought-induced changes in rooting patterns and assimilate partitioning between root and shoot in upland rice. *Field Crops Research*, 93 (2):223–236, 2005.

M K Ashley, M Grant, and A Grabov. Plant responses to potassium deficiencies: a role for potassium transport proteins. *Journal of Experimental Botany*, 57(2):425–436, January 2006. doi: 10.1093/jxb/erj034. URL `http://jxb.oxfordjournals.org/content/57/2/425.abstract`.

ASTM. Standard Guide for Computed Tomography (CT) Imaging, 2008.

M. S. Aulakh, R. Wassmann, H. Rennenberg, Fink, and S. Pattern and Amount of Aerenchyma Relate to Variable Methane Transport Capacity of Different Rice Cultivars. *Plant Biology*, 2: 182–194, 2000. ISSN 14358603. doi: 10.1055/s-2000-9161.

A G Aylmore. Use of computer-assisted tomography in studying water movement around plant roots. *Advances in Agronomy*, 49:1–54, 1993.

Antony Bacic, Susan F Moody, and Adrienne E Clarke. Structural Analysis of Secreted Root Slime from Maize (Zea mays L.). *Plant Physiology*, 80(3):771–777, 1986.

R Bagshaw, L V Vaidyanathan, and P H Nye. The supply of nutrient ions by diffusion to plant roots in soil. *Plant and Soil*, 37(3):627–639, 1972.

S A Barber. *Soil nutrient bioavailability: a mechanistic approach*. Wiley, 1995.

S A Barber and M Silberbush. Plant root morphology and nutrient uptake. *ASA Special Publication - American Society of Agronomy*, 49:65–87, 1984.

S A Barber, J M Walker, and E H Vasey. Mechanisms for Movement of Plant Nutrients from Soil and Fertilizer to Plant Root. *Journal of Agricultural and Food Chemistry*, 11(3):204–207, 1963.

Philippe C Baveye, Magdeline Laba, Wilfred Otten, Liesbeth Bouckaert, Patricia Dello Sterpaio, Rohit R Goswami, Dmitri Grinev, Alasdair Houston, Yaoping Hu, Jianli Liu, Sacha Mooney, Radoslaw Pajor, Steven Sleutel, Ana Tarquis, Wei Wang, Qiao Wei, and Mehmet Sezgin. Observer-dependent variability of the thresholding step in the quantitative analysis of soil images and X-ray microtomography data. *Geoderma*, 157(1–2):51–63, 2010.

A Glyn Bengough, B M McKenzie, P D Hallett, and T A Valentine. Root elongation, water stress, and mechanical impedance: a review of limiting stresses and beneficial root tip traits. *Journal of Experimental Botany*, 62(1):59–68, January 2011. doi: 10.1093/jxb/erq350. URL `http://jxb.oxfordjournals.org/content/62/1/59.abstract`.

A.G. Bengough, D.C. Gordon, H. Al-Menaie, R.P. Ellis, D. Allan, R. Keith, W.T.B. Thomas, and B.P. Forster. Gel observation chamber for rapid screening of root traits in cereal seedlings. *Plant and Soil*, 262:63–70, 2004. ISSN 0032-079X. doi: 10.1023/B:PLSO.0000037029.82618.27.

W Bergmann. Uber die Beeinflussung der Wurzelbehaarung von Roggenkeimpflanzen durch verschiedene AuBenfaktoren. *Z. Pflanzenernahr. Dung. Bodenk*, 80:218–224, 1958.

G M Berntson and F I Woodward. The root system architecture and development of Senecio vulgaris in elevated CO2 and drought. *Functional Ecology*, 6:324–333, 1992.

K K S Bhat, P H Nye, and J P Baldwin. Diffusion of phosphate to plant roots in soil. *Plant and Soil*, 44(1):63–72, 1976.

Ian J Bingham and Lianhai Wu. Simulation of wheat growth using the 3D root architecture model SPACSYS: Validation and sensitivity analysis. *European Journal of Agronomy*, 34(3): 181–189, 2011. ISSN 1161-0301.

J B Bole. Influence of root hairs in supplying soil phosphorus to wheat. *Canadian Journal of Soil Science*, 53:169–175, 1973.

A M Bonser, J Lynch, and S Snapp. Effect of phosphorus deficiency on growth angle of basal roots in Phaseolus vulgaris. *The New phytologist*, 132:281–288, 1996. ISSN 0028-646X. doi: 10.2307/2558450.

Nyle C Brady and Ray R Weil. *The nature and properties of soils.* Number Ed. 11. Prentice-Hall Inc., 1996. ISBN 0132431890.

Leo Breiman. Random forests. *Machine learning*, 45(1):5–32, 2001. ISSN 0885-6125.

L K Brown, T S George, L X Dupuy, and P J White. A conceptual model of root hair ideotypes for future agricultural environments: what combination of traits should be targeted to cope with limited P availability? *Annals of Botany*, November 2012. doi: 10.1093/aob/mcs231. URL http://aob.oxfordjournals.org/content/early/2012/11/19/aob.mcs231.abstract.

S S O Burgess, M A Adams, N C Turner, and C K Ong. The redistribution of soil water by tree rot systems. *Oecologia*, 115:306–311, 1998.

K Butterbach-Bahl, H Papen, and H Rennenberg. Scanning electron microscopy analysis of the aerenchyma in two rice cultivars. *Phyton*, 40(1):43–55, 2000.

Ragan M Callaway, Steven C Pennings, and Christina L Richards. PHENOTYPIC PLASTICITY AND INTERACTIONS AMONG PLANTS. *Ecology*, 84(5):1115–1128, May 2003. ISSN 0012-9658. doi: 10.1890/0012-9658(2003)084[1115:PPAIAP]2.0.CO;2. URL http://dx.doi.org/10.1890/0012-9658(2003)084[1115:PPAIAP]2.0.CO2.

Andrea Carminati and Doris Vetterlein. Plasticity of rhizosphere hydraulic properties as a key for efficient utilization of scarce resources. *Annals of Botany*, December 2012. doi: 10.1093/aob/mcs262. URL http://aob.oxfordjournals.org/content/early/2012/12/11/aob.mcs262.abstract.

Andrea Carminati, AhmadB. Moradi, Doris Vetterlein, Peter Vontobel, Eberhard Lehmann, Ulrich Weller, Hans-Jörg Vogel, and SaschaE. Oswald. Dynamics of soil water content in the rhizosphere. *Plant and Soil*, 332(1-2):163–176, 2010. ISSN 0032-079X. doi: 10.1007/s11104-010-0283-8. URL http://dx.doi.org/10.1007/s11104-010-0283-8.

Humberto F Causin, Gonzalo Roqueiro, Ezequiel Petrillo, Verónica Láinez, Liliana B Pena, Cintia F Marchetti, Susana M Gallego, and Sara I Maldonado. The control of root growth by reactive oxygen species in¡ i¿ Salix nigra¡/i¿ Marsh. seedlings. *Plant science*, 183:197–205, 2012. ISSN 0168-9452.

M C Champoux, G Wang, S Sarkarung, D J Mackill, J C O'Toole, N Huang, and S R McCouch. Locating genes associated with root morphology and drought avoidance in rice via linkage to molecular markers. *TAG Theoretical and Applied Genetics*, 90(7):969–981, 1995.

Ying Long Chen, Vanessa M Dunbabin, Johannes A Postma, Art J Diggle, Jairo A Palta, Jonathan P Lynch, Kadambot H M Siddique, and Zed Rengel. Phenotypic variability and

modelling of root structure of wild Lupinus angustifolius genotypes. *Plant and soil*, 348(1-2): 345–364, 2011. ISSN 0032-079X.

Cathrine Christiansen. X-ray contrast media—an overview. *Toxicology*, 209(2):185–187, 2005.

N Claassen, L Hendriks, and A Jungk. Erfassung der Mineralstoffverteilung im wurzelnahen Boden durch Autoradiographie. *Zeitschrift für Pflanzenernährung und Bodenkunde*, 144(3): 306–316, 1981.

Thomas Connolley, Derek Nash, Jean-Yves Buffière, Faisal Sharif, and Peter Edward McHugh. X-ray micro-tomography of a coronary stent deployed in a model artery. *Medical Engineering & Physics*, 29(10):1132–1141, 2007.

Yoan Coudert, Christophe Périn, Brigitte Courtois, Ngan Giang Khong, and Pascal Gantet. Genetic control of root development in rice, the model cereal. *Trends in Plant Science*, 15(4): 219–226, 2010.

J W Crawford, S Verrall, and I M Young. The origin and loss of fractal scaling in simulated soil aggregates. *European Journal of Soil Science*, 48:643–650, 1997.

D J Crotty, R L McKinley, and M P Tornai. Experimental spectral measurements of heavy K-edge filtered beams for x-ray computed mammotomography. *Physics in Medicine and Biology*, 52:603–616, 2007.

J H Dane. *Methods of Soil Analysis. Part 4. Physical Methods*, volume 5 of *Soil Science Society of America Book Series*. 2002.

Masako Dannoura, Yuji Kominami, Naoki Makita, and Hiroyuki Oguma. *Flat Optical Scanner Method and Root Dynamics Measuring Roots*. Springer Berlin, Heidelberg, 2012.

P R Darrah, D L Jones, G J D Kirk, and Tiina Roose. Modelling the rhizosphere: a review of methods for 'upscaling' to the whole-plant scale. *European Journal of Soil Science*, 57:13–25, 2006.

S. K. De Datta and P. K. Sharma. Puddling Influence on Soil, Rice Development, and Yield1, 1985. ISSN 03615995.

Gerlinde B De Deyn and Wim H Van der Putten. Linking aboveground and belowground diversity. *Trends in ecology & evolution (Personal edition)*, 20:625–633, 2005. ISSN 01695347. doi: 10.1016/j.tree.2005.08.009.

Sophie de Dorlodot, Brian Forster, Loïc Pagès, Adam Price, Roberto Tuberosa, and Xavier Draye. Root system architecture: opportunities and constraints for genetic improvement of crops. *Trends in Plant Science*, 12(10):474–481, 2007.

DEFRA. Fertiliser Manual, 2010.

M del Fresno, M Vénere, and A Clausse. A combined region growing and deformable model method for extraction of closed surfaces in 3D CT and MRI scans. *Computerized Medical Imaging and Graphics*, 33(5):369–376, 2009.

P Dery and B Anderson. Peak Phosphorus, 2007.

A R Dexter. Soil physical quality Part I. Theory, effects of soil texture, density and organic matter, and effects on root growth. *Geoderma*, 120:201–214, 2004.

A J Diggle. ROOTMAP—a model in three-dimensional coordinates of the growth and structure of fibrous root systems. *Plant and Soil*, 105(2):169–178, 1988. ISSN 0032-079X.

B Dinkelaker, G Hahn, V Römheld, G A Wolf, and H Marschner. Non-destructive methods for demonstrating chemical changes in the rhizosphere I. Description of methods. *Plant Soil*, 155:67–70, 1993.

H J Dittmer. A quantitave study of the subterranean members of three field grasses. *American Journal of Botany*, 25(9), 1938.

Howard J Dittmer. A Quantitative Study of the Roots and Root Hairs of a Winter Rye Plant (Secale Cereale). *American Journal of Botany*, 24(7):417–420, 1937.

Howard J Dittmer. Root Hair Variations in Plant Species. *American Journal of Botany*, 36(2): 152–155, 1949.

M C Drew, P H Nye, and L V Vaidyanathan. The supply of nutrient ions by diffusion to plant roots in soil. *Plant and Soil*, 30(2):252–270, 1969.

V M Dunbabin, S McDermott, and A G Bengough. Upscaling from rhizosphere to whole root system: modelling the effects of phospholipid surfactants on water and nutrient uptake. *Plant and Soil*, 2005.

Vanessa M Dunbabin, Johannes A Postma, Andrea Schnepf, Loïc Pagès, Mathieu Javaux, Lianhai Wu, Daniel Leitner, Ying L Chen, Zed Rengel, and Art J Diggle. Modelling root–soil interactions using three–dimensional models of root growth, architecture and function. *Plant and Soil*, pages 1–32, 2013. ISSN 0032-079X.

J J Esseling and A M C Emons. Dissection of Nod factor signalling in legumes: cell biology, mutants and pharmacological approaches. *Journal of microscopy*, 214(2):104–113, 2004.

M Ewens and R A Leigh. The effect of nutrient solution composition on the length of root hairs of wheat (Triticum aestivum L.). *Journal of Experimental Botany*, 36:713–724, 1985.

Suqin Fang, Xiaolong Yan, and Hong Liao. 3D reconstruction and dynamic modeling of root architecture in situ and its application to crop phosphorus research. *The Plant journal : for cell and molecular biology*, 60:1096–1108, 2009. ISSN 1365-313X. doi: 10.1111/j.1365-313X.2009.04009.x.

L A Feldkamp, L C Davis, and J W Kress. Practical cone-beam algorithm. *Optical Society of America*, 1:612–619, 1984.

A H Fitter, T R Stickland, M L Harvey, and G W Wilson. Architectural analysis of plant root systems. *New Phytologist*, 118:375–382, 1991.

Richard J Flavel, Christopher N Guppy, Matthew Tighe, Michelle Watt, Ann McNeill, and Iain M Young. Non-destructive quantification of cereal roots in soil using high-resolution X-ray tomography. *Journal of Experimental Botany*, 63(7):2503–2511, 2012.

D Fohse and A Jungk. Influence of phosphate and nitrate supply on root hair formation of rape, spinach and tomato plants. *Plant and Soil*, 74(359-368), 1983.

Laure S Fournier, Charles Andre Cuenod, Cedric De Bazelaire, Nathalie Siauve, Christophe Rosty, Phuong Lan Tran, Guy Frija, and Olivier Clement. Early modifications of hepatic perfusion measured by functional CT in a rat model of hepatocellular carcinoma using a blood pool contrast agent. *European Radiology*, 14:2125–2133, 2004.

L Friedrichs, M Maier, and C Hamm. A new method for exact threedimensional reconstructions of diatom frustules. *Journal of Microscopy*, 248(2):208–217, 2012.

Qiushi Fu, Lailiang Cheng, Yangdong Guo, and Robert Turgeon. Phloem Loading Strategies and Water Relations in Trees and Herbaceous Plants. *Plant Physiology*, 157(3):1518–1527, 2011.

A Fusseder. The longevity and activity of the primary root of maize. *Plant and Soil*, 101:257–265, 1987.

T S Gahoonia and N E Nielsen. A method to study rhizosphere processes in thin soil layers of different proximity to roots. *Plant Soil*, 135:143–146, 1991.

Tara Singh Gahoonia and Niels Erik Nielsen. Direct evidence on participation of root hairs in phosphorus (³²P) uptake from soil. *Plant and Soil*, 198(2):147–152, 1998.

J S Geelhoed, S L J Mous, and G R Findenegg. Modeling Zero Sink Nutrient Uptake By Roots With Root Hairs From Soil: Comparison of Two Models. *Soil Science*, 162(8):544–553, 1997.

D M Gibeaut, J Hulett, G R Cramer, and J R Seemann. Maximal Biomass of Arabidopsis thaliana Using a Simple, Low-Maintenance Hydroponic Method and Favourable Enfironmental Conditions. *Plant Physiology*, 115:317–319, 1997.

R Giesler and U Lundström. Soil solution chemistry: effects of bulking soil samples. *Soil Science Society of America Journal*, 57(5):1283–1288, 1993.

Simon Gilroy and David L Jones. Through form to function: root hair development and nutrient uptake. *Trends in Plant Science*, 5(2):56–60, 2000.

C A Glasbey, G W Horgan, and J F Darbyshire. Image analysis and three dimensional modelling of pores in soil aggregates. *Soil Science*, 42:479–486, 1991.

H C J Godfray, J R Beddington, I R Crute, L Haddad, D Lawrence, J F Muir, J Pretty, S Robinson, S M Thomas, and C Toulmin. Food security: the challenge of feeding 9 billion people. *Science*, 327(5967):812–818, 2010.

N Gonzalez, G T S Beemster, and D Inzé. David and Goliath: what can the tiny weed Arabidopsis teach us to improve biomass production in crops? *Current opinion in plant biology*, 12(2):157–164, 2009.

D J Greenland and H C Pereira. Soil damage by intensive arable cultivation: temporary or permanent. *Philosophical Transaction of the Royal Society*, 281:193–208, 1977.

P J Gregory and P Hinsinger. New approaches to studying chemical and physical changes in the rhizosphere: an overview. *Plant and Soil*, 211:1–9, 1999.

P J Gregory, D J Hutchison, D B Read, P M Jenneson, W B Gilboy, and E J Morton. Non-invasive imaging of roots with high-resolution X-ray micro-tomography. *Plant and Soil*, 255:351–359, 2003.

P J Gregory, J S I Ingram, and M Brklacich. Climate change and food security. *Philosophical Transactions of The Royal Society*, 360:2139–2148, 2005.

P J Gregory, A G Bengough, D Grinev, S Schmidt, W Thomas, T Wojciechowski, and I M Young. Root phenomics of crops: opportunities and challenges. *Functional Plant Biology*, 36:922–929, 2009.

M C J Grevers, E De Jong, and R J St Arnaud. The characterization of soil macroporosity with CT scanning. *Canadian Journal of Soil Science*, 69:629–637, 1989.

A E Hadri and T Bisseling. *Responses of the plant to Nod factors*, pages 403–416. Kluwer Academic Publishers, Dordrecht, 1998.

J M Hainsworth and A G Aylmore. The use of computer- assisted tomography to determine spatial distribution of soil water content. *Australian Journal of Soil Research*, 21:435–443, 1983.

Rebecca E Haling, Lawrie K Brown, A Glyn Bengough, Iain M Young, Paul D Hallett, Philip J White, and Timothy S George. Root hairs improve root penetration, root–soil contact, and phosphorus acquisition in soils of different strength. *Journal of experimental botany*, 64(12): 3711–3721, 2013. ISSN 0022-0957.

François Hallouard, Nicolas Anton, Philippe Choquet, André Constantinesco, and Thierry Vandamme. Iodinated blood pool contrast media for preclinical X-ray imaging applications – A review. *Biomaterials*, 31(24):6249–6268, 2010.

M A Hamza and L A G Aylmore. Soil solute concentration and water uptake by single lupin and radish plant roots. I. Water extraction and solute accumulation. *1992*, 145:187–196, 1992.

L Han, P Dutilleul, S O Prasher, C Beaulieu, and D L Smith. Assessment of common scab-inducing pathogen effects on potato underground organs via computed tomography scanning. *Phytopathology*, 98(10):1118–1125, 2008.

T Hartig. Ueber die Bewegung des Saftes in den Holzpflanzen. *Bot. Zeit.*, 16:329–342, 1858.

M J Hedley and J W B Stewart. Method to measure microbial phosphate in soils. *Soil Biology & Biochemistry*, 14:377–385, 1982.

D A Heeraman, J W Hopmans, and V Clausnitzer. Three dimensional imaging of plant roots in situ with x-ray computed tomography. *Plant and Soil*, 189(2):167–179, 1997.

G D Herder, G Van Isterdael, T Beeckman, and I De Smet. The roots of a new green revolution. *Trends in plant science*, 15(11):600–607, 2010.

Philippe Hinsinger, George R Gobran, Peter J Gregory, and Walter W Wenzel. Rhizosphere geometry and heterogeneity arising from root-mediated physical and chemical processes. *New Phytologist*, 168(2):293–303, 2005.

Philippe Hinsinger, A Glyn Bengough, Doris Vetterlein, and Iain M Young. Rhizosphere: biophysics, biogeochemistry and ecological relevance. *Plant and soil*, 321(1-2):117–152, 2009. ISSN 0032-079X.

G W Horgan. Mathematical morphology for analysing soil structure from images. *European Journal of Soil Science*, 49(2):161–173, 1998.

A N Houston, S Schmidt, A M Tarquis, W Otten, P C Baveye, and S M Hapca. Effect of scanning and image reconstruction settings in X-ray computed microtomography on quality and segmentation of 3D soil images. *Geoderma*, 207–208(0):154–165, 2013. ISSN 0016-7061. doi:

http://dx.doi.org/10.1016/j.geoderma.2013.05.017. URL http://www.sciencedirect.com/science/article/pii/S0016706113001717.

S Itoh and S A Barber. Phosphorus uptake by six plant species as related to root hairs. *Agronomy*, 75:457–461, 1983.

P M Jenneson, W B Gilboy, E J Morton, and P J Gregory. An X-ray micro-tomography system optimised for the low-dose study of living organisms. *Applied Radiation and Isotopes*, 58: 177–181, 2003.

M G Johnson, D T Tingey, D L Phillips, and M J Storm. Advancing fine root research with minirhizotrons. *Environmental and Experimental Botany*, 45:263–289, 2001.

B Jones and K Ljung. Subterranean space exploration: the development of root system architecture. *Current Opinions in Plant Biology*, 15(1):97–102, 2011.

D L Jones. Organic acids in the rhizosphere. *Plant and Soil*, 205:25–44, 1998.

K W Joy. Translocation in Sugar-beet. *Journal of Experimental Botany*, 15(3):485–494, 1964.

Albrecht Jungk. Root hairs and the acquisition of plant nutrients from soil. *Journal of Plant Nutrition and Soil Science*, 164(2):121–129, 2001.

A Kaestner, E Lehmann, and M Stampanoni. Imaging and image processing in porous media research. *Advances in Water Resources*, 31(9):1174–1187, 2008.

Anders Kaestner, MArtin Scneebli, and Frank Graf. Visualising three-dimensional root networks using computed tomography. *Geoderma*, 136:459–469, 2006.

Verena Kaynig, Thomas Fuchs, and Joachim M Buhmann. Neuron Geometry Extraction by Perceptual Grouping in ssTEM Images. *Microscopy*, 0:2902–2909, 2010. ISSN 10636919. doi: 10.1109/CVPR.2010.5540029.

I Kemmochi and H Maru. Nondestructive discrimination of cabbage [Brassica oleracea capitata] plants infected with verticillium wilt using contrast media and an X-ray apparatus. *Journal of the Japanese Society for Horticultural Science*, 73:484–490, 2004.

R A Ketcham and W D Carlson. Acquisition, optimization and interpretation of X-ray computed tomographic imagery: applications to the geosciences. *Computers and Geosciences*, 27: 381–400, 2001.

S D Keyes, R P Boardman, A Marchant, T Roose, and I Sinclair. 'A robust approach for determination of the macro-porous volume fraction of soils with X-ray computed tomography and an image processing protocol. *European Journal of Soil Science*, Awaiting p, 2013a.

S. D. Keyes, R. P. Boardman, a. Marchant, T. Roose, and I. Sinclair. A robust approach for determination of the macro-porous volume fraction of soils with X-ray computed tomography and an image processing protocol. *European Journal of Soil Science*, 64(3):298–307, June 2013b. ISSN 13510754. doi: 10.1111/ejss.12019. URL `http://doi.wiley.com/10.1111/ejss.12019`.

G S Khush. Green revolution: preparing for the 21st century. *Genome*, 42(4):646–655, 1999.

G S Khush. Green revolution: the way forward. *Nature Reviews Genetics*, 2(10):815–822, 2001.

J W Kijne. *The Rhizobium infection process*, pages 349–398. Chapman and Hall, New York, 1992.

J Kittler and J Illingworth. Minimum error thresholding. *Pattern Recognition*, 19(1):41–47, 1986.

R Kodesôova, N Vignozzi, M Roho\vokova, T Hájková, M Kočárek, M Pagliai, J Kozák, and J Šim\vunek. Impact of varying soil structure on transport processes in different diagnostic horizons of three soil types. *Contaminant Hydrology*, 104:107–125, 2009.

E J W Koekkoek and H Booltink. Neural network models to predict soil water retention. *European Journal of Soil Science*, 50(3):489–495, 1999.

G Krasilnikoff, T Gahoonia, and E N Nielsen. Variation in phosphorus uptake efficiency by genotypes of cowpea (Vigna unguiculata) due to differences in root and root hair length and induced rhizosphere processes. *Plant and Soil*, 251:89–91, 2003.

R Kuchenbuch and A Jungk. A method for determining concentration profiles at the soil–root interface by thin slicing rhizosphere soil. *Plant Soil*, 68:391–394, 1982.

A. B. J. Kuijlaars and E. B. Saff. Distributing many points on a sphere, 1997. ISSN 0343-6993.

Anke Kuppardt, Doris Vetterlein, Hauke Harms, and Antonis Chatzinotas. Visualisation of gradients in arsenic concentrations around individual roots of Zea mays L. using agar-immobilized bioreporter bacteria. *Plant and soil*, 329(1-2):295–306, 2010. ISSN 0032-079X.

M Kutilek and D R Nielsen. Interdisciplinarity of hydropedology. *Geoderma*, 138(3-4):252–260, 2006.

Lore Kutschera and Erwin Lichtenegger. *Wurzelatlas mitteleuropäischer Ackerunkräuter und Kulturpflanzen*, volume 1. DLG Verlag Frankfurt., 1960.

U. Kutschera. Darwin's Philosophical Imperative and the Furor Theologicus, 2009. ISSN 1936-6426.

HANS Lambers, M W Shane, M D Cramer, S J Pearce, and E J Veneklass. Root Structure and Functioning for Efficient Acquisition of Phosphorus: Matching Morphological and Physiological Traits. *Annals of Botany*, 98(4):693–713, 2006.

D Leitner, S Klepsch, A Kniess, and A Schnepf. The algorithmic beauty of plant roots - an L-System model for dynamic root growth simulation. *Mathematical and Computer Modelling of Dynamical Systems*, 16:575–587 ST – The algorithmic beauty of plant root, 2010a.

D Leitner, S Klepsch, M Ptashnyk, A Marchant, G J Kirk, A Schnepf, and T Roose. A dynamic mdoel of nutrient uptake by root hairs. *New Phytologist*, 185(3):792–802, 2010b.

D G Lewis and J P Quirk. Phosphate diffusion in soil and uptake by plants. *Plant and Soil*, 26 (1):99–118, 1967.

J Lipiec, J Kus, A Słowinska-Jurkiewicz, and A Noselawicz. Soil porosity and water infiltration as influenced by tillage methods. *Soil and Tillage Research*, 89:210–220, 2006.

S J Livesley, C L Stacey, P J Gregory, and R J Buresh. Sieve size effects on root length and biomass measurements of maize (Zea mays) and Grevillea robusta. *Plant Soil*, 207:183–193, 1999.

E Lombi and J Susini. Synchrotron-based techniques for plant and soil science: opportunities, challenges and future perspectives. *Plant and Soil*, 320:1–35, 2009.

E Lombi, K G Scheckel, R D Armstrong, S Forrester, J N Cutler, and D Paterson. Speciation and Distribution of Phosphorus in a Fertilized Soil. *Soil Sci. Soc. Am. J.*, 70(6):2038–2048, 2006.

Melinda Lontoc-Roy, Pierre Dutilleul, Shiv O Prasher, Liwen Han, Thomas Brouillet, and Donald L Smith. Advances in the acquisition and analysis of CT scan data to isolate a crop root system from the soil medium and quantify root system complexity in 3-D space. *Geoderma*, 137(1-2):231–241, 2006.

José López-Bucio, Alfredo Cruz-Ramırez, and Luis Herrera-Estrella. The role of nutrient availability in regulating root architecture. *Current Opinion in Plant Biology*, 6(3):280–287, 2003.

G F Lorens, J M Bennett, and L B Loggale. Differences in drought resistance between two corn hybrids. I. Water relations and root length density. *Agronomy journal*, 79(5):802–807, 1987.

John Lussenhop and Robert Fogel. Observing soil biota in situ. *Geoderma*, 56:25–36, 1993.

J P Lynch. Turner review no. 14. Roots of the second green revolution. *Australian Journal of Botany*, 55(5):493–512, 2007.

Jonathan Lynch. Root architecture and plant productivity. *Plant Physiology*, 109:7–13, 1995.

Jonathan P Lynch and Kathleen M Brown. New roots for agriculture: exploiting the root phenome. *Philosophical Transactions of the Royal Society of London - Series B: Biological Sciences*, 367: 1598–604, 2012. ISSN 14712970. doi: 10.1098/rstb.2011.0243.

Jonathan P Lynch, Kai L Nielsen, Robert D Davis, and Andrei G Jablokow. SimRoot : Modelling and visualization of root systems. *Plant and Soil*, 188:139–151, 1997. ISSN 0032079X. doi: 10.1023/A:1004276724310.

Z Ma, D G Bielenberg, K M Brown, and J P Lynch. Regulation of root hair density by phosphorus availability in Arabidopsis thaliana. *Plant, Cell & Environment*, 24(4):459–467, 2001.

Stefan Mairhofer, Susan Zappala, Saoirse R Tracy, Craig Sturrock, Malcolm Bennett, Sacha J Mooney, and Tony Pridmore. RooTrak: Automated Recovery of Three-Dimensional Plant Root Architecture in Soil from X-Ray Microcomputed Tomography Images Using Visual Tracking. *Plant Physiology*, 158(2):561–569, 2012.

Alexis Maizel, Daniel von Wangenheim, Fernán Federici, Jim Haseloff, and Ernst H K Stelzer. Highresolution live imaging of plant growth in near physiological bright conditions using light sheet fluorescence microscopy. *The Plant Journal*, 68(2):377–385, 2011. ISSN 1365-313X.

T R Malthus. *An essay on the principle of population, as it affects the future improvement of society: with remarks on the speculations of mr. Godwin, mr. Condorcet, and other writers*. 1798.

B Mambani and R Lal. Response of upland rice varieties to drought stress. *Plant and Soil*, 73 (1):73–94, 1983.

H. Marschener. Role of root growth, arbuscular mycorrhiza, and root exudates for the efficiency in nutrient acquisition, 1998. ISSN 03784290.

Margaret McCully. ROOTS IN SOIL, Unearthing the Complexities of Roots and their Rhizospheres. *Annual Review of Plant Physiology and Plant Molecular Biology*, 50:695–718, 1999.

J D McElgunn and C M Harrison. Formation, elongation, and longevity of barley root hairs. *Agronomy Journal*, 61:79–81, 1969.

M Menon, B Robinson, S E Oswald, Anders Kaestner, K C Abbaspour, E Lehmann, and R Schulin. Visualisation of root growth in heterogeneously contaminated soil using neutron radiography. *European Journal of Soil Science*, 58(3):802–810, 2006.

Gerhard Michael. The control of root hair formation: suggested mechanisms. *Journal of Plant Nutrition and Soil Science*, 164(2):111–119, 2001.

Sacha J Mooney. Three-dimensional visualization and quantification of soil macroporosity and water flow patterns using computed tomography. *Soil Use and Management*, 18:142–151, 2002.

Christopher J Moran, Alain Pierret, and A W Stevenson. X-ray absorption and phase contrast imaging to study the interplay between plant roots and soil structure. *Plant and Soil*, 223: 99–115, 2000.

Luc Moriau, Baudouin Michelet, Pierre Bogaerts, Laurence Lambert, Alain Michel, Mohammed Oufattole, and Marc Boutry. Expression analysis of two gene subfamilies encoding the plasma membrane H+-ATPase in Nicotiana plumbaginifolia reveals the major transport functions of this enzyme. *The Plant Journal*, 19(1):31–41, 1999.

J Morphy and J P Riley. A modified single solution method for determination of phosphate in natural water. *Anal Chimica Acta*, 27:31–36, 1962.

Stephen R Mudge, Anne L Rae, Eugene Diatloff, and Frank W Smith. Expression analysis suggests novel roles for members of the Pht1 family of phosphate transporters in Arabidopsis. *The Plant Journal*, 31(3):341–353, 2002.

Margarete Müller and Wolfgang Schmidt. Environmentally Induced Plasticity of Root Hair Development in Arabidopsis. *Plant Physiology*, 134(1):409–419, 2004.

J D Murray. Michaelis–Menten theory: detailed analysis and the pseudo-steady state hypothesis. *Math. Biol*, 19:116–117, 1993.

P Mylona, K Pawlowski, and T Bisseling. Symbiotic nitrogen fixation. *Plant Cell*, 7:869–885, 1995.

P H Nye. The effect of the nutrient intensity and buffering power of a soil, and the absorbing power, size and root hairs of a root, on nutrient absorption by diffusion. *Plant and Soil*, 25(1): 81–105, 1966.

P H Nye and P B Tinker. *Solute movement in the soil-root system*, volume 4. Univ of California Press, 1977.

Karen S Osmont, Richard Sibout, and Christian S Hardtke. Hidden Branches: Developments in Root System Architecture. *Annual Review of Plant Biology*, 58(1):93–113, 2007.

N Otsu. A threshold selection method from gray-level histograms. *IEEE TRansactions on Systems, Man and Cybernetics*, 9(1):62–66, 1979.

W Paddock and P Paddock. *Famine-1975!* Weidenfeld and Nicolson, 1968.

Loïc Pagès, Gilles Vercambre, Jean-Louis Drouet, François Lecompte, Catherine Collet, and Jacques Le Bot. Root Typ: a generic model to depict and analyse the root system architecture. *Plant and Soil*, 258:103–119, 2004. ISSN 0032079X. doi: 10.1023/B:PLSO.0000016540.47134.03.

M Pagliai and M De Nobili. Relationships between soil porosity, root development and soil enzyme activity in cultivated soils. *Geoderma*, 56:243–256, 1993.

J B Passioura. A mathematical model for the uptake of ions from the soil solution. *Plant and Soil*, 18(2):225–238, 1963.

G A Pavliotis and A M Stuart. Multiscale methods, volume 53 of Texts in Applied Mathematics, 2008.

J Perret, S O Prasher, A Kantzas, and C Langford. Three-dimensional quantification of macropore networks in undisturbed soi cores. *Soil Science Society of America*, 63(6):1530–1543, 1999.

J S Perret, M E Al-Belushi, and M Deadman. Non-destructive visualisation and quantification of roots using computed tomography. *Soil Biology and Biochemistry*, 39:391–399, 2007.

R Peterson and Melissa Farquhar. Root hairs: Specialized tubular cells extending root surfaces. *The Botanical Review*, 62(1):1–40, 1996.

A D Peuke, M Rokitta, U Zimmermann, L Schreiber, and A Haase. Simultaneous measurement of water flow velocity and solute transport in xylem and phloem of adult plants of Ricinus communis over a daily time course by nuclear magnetic resonance spectrometry. *Plant, Cell & Environment*, 24(5):491–503, 2001.

Alain Pierret, Yvan Capowiez, Christopher J Moran, and Andrè Kretzschmar. X-ray computed tomography to quantify tree rooting spatial distributions. *Geoderma*, 90:307–326, 1999.

Alain Pierret, Christopher J Moran, and Claude Doussan. Conventional detection methodology is limiting our ability to understand the roles and functions of fine roots. *New Phytologist*, 166:967–980, 2005.

L F Pires, O O S Bacchi, K Reichardt, and L C Timm. Application of gamma-ray computed tomography to analysis of soil structure before density evaluations. *Applied Radiation and Isotopes*, 63(4):505–511, 2005.

G Poludniowski, G Landry, F DeBlois, P M Evans, and F Verhaegen. SpekCalc: a program to calculate photon spectra from tungsten anode x-ray tubes. *Physics in Medicine and Biology*, 54 (19):433–438, 2009.

Johannes A Postma, Ulrich Schurr, and Fabio Fiorani. Dynamic root growth and architecture responses to limiting nutrient availability: linking physiological models and experimentation. *Biotechnology Advances*, (0), 2013. ISSN 0734-9750. doi: http://dx.doi.org/10.1016/j.biotechadv.2013.08.019. URL `http://www.sciencedirect.com/science/article/pii/S0734975013001535`.

N D Prionas, S Ray, and J M Boone. Volume assessment accuracy in computed tomography: a phantom study. *Journal of applied clinical medical physics/American College of Medical Physics*, 11(2):3037, 2010.

M Ptashnyk, T Roose, D L Jones, and G J D Kirk. Enhanced zinc uptake by rice through phytosiderophore secretion: a modelling study. *Plant, cell & environment*, 34(12):2038–2046, 2011.

K G Raghothama. Phosphate transport and signaling. *Current Opinion in Plant Biology*, 3(3): 182–187, 2000.

C Rappoldt. The application of diffusion models to an aggregated soil. *Soil Science*, 150:645–661, 1990.

T L Roberts and W M Stewart. Inorganic Phosphorus and Potassium Production and Reserves. *Better Crops*, 86(2), 2002.

David Robinson. Optimal relations between root length and nutrient inflow rate in plant root systems, 1988. ISSN 00225193.

M Rokitta, A Peuke, U Zimmermann, and A Haase. Dynamic studies of phloem and xylein flow in fully differentiated plants by fast nuclear-magnetic-resonance microimaging. *Protoplasma*, 209(1):126–131, 1999.

V Romheld and H Marschner. Iron deficiency stress induced morphological and physiological changes in root tips of sunflower. *Physiol. Plant.*, 53:354–360, 1981.

T Roose and A C Fowler. A mathematical model for water and nutrient uptake by plant root systems. *Journal of theoretical biology*, 228(2):173–184, 2004.

T Roose, A C Fowler, and P R Darrah. A mathematical model of plant nutrient uptake. *Journal of Mathematical Biology*, 42(4):347–360, 2001.

Tiina Roose and K C Zygalakis. A dual porosity model for the uptake of nutrients by root hairs, 2010.

P A Sanchez, K D Shepherd, M J Soule, F M Place, R J Buresh, A M N Izac, A U Mokwunye, F R Kwesiga, C G Ndiritu, and P L Woomer. Soil fertility replenishment in Africa: An investment in natural resource capital. *Replenishing soil fertility in Africa*, (replenishingsoi):1–46, 1997.

J Schindelin, I Arganda-Carreras, E Frise, V Kaynig, M Longair, T Pietzsch, S Preibisch, C Rueden, S Saalfeld, and B Schmid. Fiji: an open-source platform for biological-image analysis. *Nature Methods*, 9(7):676–682, 2012.

Steffen Schlüter, Ulrich Weller, and Hans-Jörg Vogel. Segmentation of X-ray microtomography images of soil using gradient masks. *Computers & Geosciences*, 36(10):1246–1251, 2010. ISSN 0098-3004.

H Schmidt, T Eickhorst, and R Tippkotter. Monitoring of root growth and redox conditions in paddy soil rhizotrons by redox electrodes and image analysis. *Plant Soil*, 341:221–232, 2011.

A Schnepf, D Leitner, and S Klepsch. Modeling phosphorus uptake by a growing and exuding root system. *Vadose Zone Journal*, 11(3), 2012. ISSN 1539-1663.

Andrea Schnepf, Tiina Roose, and Peter Schweiger. Impact of growth and uptake patterns of arbuscular mycorrhizal fungi on plant phosphorus uptake - a modelling study, 2008.

Andrea Schnepf, Davey Jones, and Tiina Roose. Modelling Nutrient Uptake by Individual Hyphae of Arbuscular Mycorrhizal Fungi: Temporal and Spatial Scales for an Experimental Design. *Bulletin of Mathematical Biology*, 73(9):2175–2200, 2011.

M Schottelndreier and U Falkengren-Grerup. Plant induced alteration in the rhizosphere and the utilisation of soil heterogeneity. *Plant and Soil*, 209:297–309, 1999.

Sergey Shabala, Vadim Demidchik, Lana Shabala, Tracey A Cuin, Susan J Smith, Anthony J Miller, Julia M Davies, and Ian A Newman. Extracellular Ca2+ Ameliorates NaCl-Induced K+ Loss from Arabidopsis Root and Leaf Cells by Controlling Plasma Membrane K+-Permeable Channels. *Plant Physiology*, 141(4):1653–1665, 2006.

Björn J Sieberer, Tijs Ketelaar, John J Esseling, and Anne Mie C Emons. Microtubules guide root hair tip growth. *New Phytologist*, 167(3):711–719, 2005.

C A Sierra, J I Del Valle, and S A Orrego. Accounting for fine root mass sample losses in the washing process: a case study from a tropical montaine forest of Colombia. *Journal of Tropical Ecology*, 19:599–601, 2003.

M Silberbush and S A Barber. Sensitivity of simulated phosphorus uptake to parameters used by a mechanistic-mathematical model. *Plant and Soil*, 74:93–100, 1983.

Jagdish Singh and Aditya Daftary. Iodinated Contrast Media and Their Adverse Reactions. *Journal of Nuclear Medicine Technology*, 36(2):69–74, 2008.

T Singh Gahoonia, D Care, and N E Nielsen. Root hairs and phosphorus acquisition of wheat and barley cultivars. *Plant and Soil*, 191(2):181–188, 1997.

E A Sivers and M D Silver. Performance of X-Ray computed tomographic imaging systems. *Materials Evaluation*, 48:706–713, 1990.

G J Sivewright and P J Elliott. Interactive region and volume growing for segmenting volumes in MR and CT images. *Informatics for Health and Social Care*, 19(1):71–80, 1994.

A J M Smucker, S L McBurney, and A K Strivastava. Quantitative separation of roots from compacted soil profiles by the hydropneumatic elutriation system. *Agronomy Journal*, 7:500–503, 1982.

M Stampanoni, A Groso, A Isenegger, G Mikuljan, Q Chen, A Bertrand, S Henein, R Betemps, U Frommherz, P Böhler, D Meister, M Lange, and R Abela. Trends in synchrotron-based tomographic imaging: the SLS experience. pages 63180M–63180M. Proc. SPIE, 2006.

J B Stewart, C J Moran, and J T Wood. Macropore sheath: quantification of plant root and soil macropore association. *Plant and Soil*, 211:59–67, 1999.

W Stuppy, J A Maisano, M W Colbert, P J Rudall, and T B Rowe. Three-dimensional analysis of plant structure using high-resolution X-ray computed tomography. *TRENDS in Plant Science*, 8(1), 2003.

United States Geological Survey. Phosphate Rock Data Sheet, 2011.

Lincoln Taiz and Eduardo Zeiger. *Plant Physiology*, volume 1. Sinauer Associates inc, Los Angeles, 3 edition, 2002.

S Tatham. No Title, 2012. URL `S.Tathum,"ConstructingPolyhedrafromRepellingPointsonaSpher "http://www.chiark.greenend.org.uk/&sim,sgtatham/polyhedra.`

Michael L Thompson, Piyush Singh, Steven Corak, and Warren E Straszheim. Cautionary notes for the automated analysis of soil pore-space images. *Geoderma*, 53(3–4):399–415, 1992.

P B Tinker and P H Nye. *Solute Movement in the Rhizosphere*. Oxford University Press, 1 edition, 2000.

E W Tollner, E L Ramseur, and C Murphy. Techniques and approaches for documenting plant root development with X-ray computed tomography. Technical report, Soil Science Society of America, 1994.

Saoirse R Tracy, Jeremy A Roberts, Colin R Black, Ann McNeill, Rob Davidson, and Sacha J Mooney. The X-factor; visualising undisturbed root architecture in soils using X-ray computed tomography. *Experimental Botany*, 61(2):311–313, 2010.

David W Trott and K Gobbert Matthias. Finite element convergence studies using COMSOL 4.0 a and LiveLink for MATLAB. Technical report, 2010.

D L Turcotte, J D Pelletier, and W I Newman. Networks with Side Branching in Biology. *Theoretical Biology*, 193:577–592, 1998.

M Van Noordwijk, D Schoonderbeek, and M J Kooistra. Root-soil contact of field-grown winter wheat. *Geoderma*, 56(1):277–286, 1993.

C P Vance, C Uhde-Stone, and D L Allan. Phosphorus acquisition and use: critical adaptations by plants for securing a nonrenewable resource. *New Phytologist*, 157:423–447, 2003.

H J Vogel and Andrè Kretzschmar. Topological characterization of pore space in soil - sample preparation and digital image processing. *Geoderma*, 73:23–38, 1996.

K Watanabe, T Mandang, S Tojo, F Ai, and B K Huang. *Nondestructive root-zone analysis with X-ray CT scanner.* American Society of Agricultural Engineers, St-Joseph, MI, USA, 1992.

B T Watson. Rapid Propagation of Changes in Velocity of Translocation along the Phloem Pathway of Helianthus annuus L. *Annals of Botany*, 40(4):659–667, 1976.

Michelle Watt, Wendy K Silk, and John B Passioura. Rates of root and organism growth, soil conditions, and temporal and spatial development of the rhizosphere. *Annals of botany*, 97: 839–855, 2006. ISSN 0305-7364. doi: 10.1093/aob/mcl028.

W W Wenzel, G Wieshammer, W J Fitz, and M Puschenreiter. Novel rhizobox design to assess rhizosphere characteristics at high spatial resolution. *Plant and Soil*, 237:37–45, 2001.

Philip J White, Timothy S George, Peter J Gregory, a Glyn Bengough, Paul D Hallett, and Blair M McKenzie. Matching roots to their environment. *Annals of botany*, 112:207–22, 2013. ISSN 1095-8290. doi: 10.1093/aob/mct123.

Carel W Windt, Edo Gerkema, and Henk Van As. Most Water in the Tomato Truss Is Imported through the Xylem, Not the Phloem: A Nuclear Magnetic Resonance Flow Imaging Study[W][OA]. *Plant Physiology*, 151:830–842, 2009. doi: 10.1104/pp.109.141044.

M Wissuwa, A M Ismail, and S Yanagihara. Effects of zinc deficiency on rice growth and genetic factors contributing to tolerance. *Plant Physiology*, 142(2):731–741, 2006.

G C Wright, R C G Smith, and J M Morgan. Differences between two grain sorghum genotypes in adaptation to drought stress. III. Physiological responses. *Crop and Pasture Science*, 34(6): 637–651, 1983.

Chu WU, Xing WEI, HaiLong SUN, and ZhengQuan WANG. Phosphate availability alters lateral root anatomy and root architecture of Fraxinus mandshurica Rupr. seedlings. *Journal of Integrative Plant Biology*, 47(3):292–301, 2005. ISSN 1744-7909.

Duncan G Wynn, Gareth Humphries, Véronique Morisson-Iveson, James Nairne, Ian M Newington, Joanna Passmore, and Lars-Göran Wistrand. The synthesis and evaluation of unsymmetrical dimeric X-ray contrast agents. *Tetrahedron Letters*, 52(24):3068–3071, 2011. ISSN 0040-4039.

Y Xing and Q Zhang. Genetic and molecular bases of rice yield. *Annual review of plant biology*, 61:421–442, 2010.

Zhengyi Yang, Helen Downie, Emil Rozbicki, Lionel X Dupuy, and Michael P MacDonald. Light Sheet Tomography (LST) for in situ imaging of plant roots. *Optics express*, 21(14): 16239–16247, 2013. ISSN 1094-4087.

Keke Yi, Benoît Menand, Elizabeth Bell, and Liam Dolan. A basic helix-loop-helix transcription factor controls cell growth and size in root hairs. *Nature genetics*, 42(3):264–267, 2010. ISSN 1061-4036.

I M Young, J W Crawford, and C Rappoldt. New methods and models for characterising structural heterogeneity of soil. *Soil and Tillage Research*, 61(1-2):33–45, 2001.

Zhiming Yu, Hanmin Chen, Yanli Tong, and Ping Wu. Analysis of Rice Root Hair Morphology Using Cryo-Scanning Electron Microscopy. In *Rice Protocols*, pages 243–248. Springer, 2013. ISBN 1627031936.

L Zolobowska and F Van Gijsegem. Induction of lateral root structure formation on petunia roots: A novel effect of GMI1000 Ralstonia solanacearum infection imparied in HRp mutants. *Molecular Plant-Microbe Interactions*, 19:597–606, 2006.

A K N Zoysa, P Loganathan, and M J Hedley. A technique for studying rhizosphere processes in tree crops: soil phosphorus depletion around camellia (Camellia japonica L.) roots. *Plant and Soil*, 190:253–265, 1997.

K C Zygalakis, G J D Kirk, D L Jones, Wissuwa T, and T Roose. A dual porosity model for the uptake of nutrients by root hairs. *New Phytologist*, 192(3):676–688, 2011.